

University of Nottingham
UK | CHINA | MALAYSIA

Research and development of polyurethane icephobic composite coatings

Halar Memon, B.Eng., MSc.

Thesis submitted to the University of Nottingham for the degree of Doctor of Philosophy

September 2021

Abstract

Ice accretion over critical engineering structures could lead to costly hazards, and ice prevention is an energy-intensive activity, thus making the applications complicated and inefficient. A more promising and specific strategy is to deploy passive ice protection approaches such as durable coatings that allow the super-cooled droplets to slide off before icing (anti-icing), or that detaches the developed ice completely (de-icing). The main aim of this project was to research and develop new types of polyurethane-based icephobic coatings for potential applications in the aerospace and wind energy industries. The experimental work was planned to offer balanced research outputs on the fundamental aspects of icephobicity studies and to impart the acquired knowledge for the fabrication and investigation of novel durable icephobic materials/surfaces.

At first, fundamental studies relating to surface icephobicity and icephobicity were carried out. A systematic reduction of ice adhesion with the decrease in surface roughness was demonstrated across all the studied material types, i.e. metallic surfaces and polymeric coatings with different surface wettability. If the surface bears a similar surface roughness, then wettability plays a deciding role in reducing the ice adhesion. A surface with higher roughness provides an increased number of possible ice anchoring points and the ice anchoring mechanism was further validated under in-situ icing observation. Furthermore, the variation in response to surface characteristics in icephobicity evaluation methods was also investigated. Centrifugal and horizontal push (shear) methods suggested a linear relationship of ice adhesion strength with surface roughness, whereas the tensile (normal) method indicated an inverse curvilinear relationship with contact angle hysteresis. Apart from the de-icing evaluation, water

droplet freezing delay suggested a direct correlation with surface roughness and the visual examination of frost accumulated samples suggested a reduction in ice densification on the smoothened surfaces, indicating a weakened bond between the ice/solid interfaces. The results offer crucial information on the pre-selection of testing regimes to accurately measure the performance of icephobic materials.

In the second part, several polyurethane-based nanocomposite, fibre-reinforced, and liquid-infused coatings were developed and investigated to understand the deteriorating behaviour of the coatings under impinging erosion tests and the subsequent impact on ice adhesion. The durability analysis on polyurethane composite coatings indicated that the incorporation of fillers was effective in reducing the number of possible ice anchoring points, and after the impingement, the icephobic performance was retained by either lowering surface roughness or by minimising surface deterioration. The reinforcement was effective such that the change in surface roughness was reduced by a factor of 4, compared to the pure polyurethane coatings under erosion impact. To provide an exceptional icephobic response, glycerol-infused fibre-reinforced polyurethane (GIFRP) coatings was proposed by mimicking the fibrous structure of cetacean skin. Instead of hosting the lipid proteins, the coatings were infused with glycerol, a known cryoprotectant to induce the supercooling of water, a strategy inspired by chionophiles, to prevent freezing. The inclusion of glycerol delayed water droplet freezing duration by 659%, while negligible frost accumulated on the fabricated coatings in the anti-icing tests. In addition to the promising anti-icing performance, the incorporation of fibrous structure has proven to be beneficial for infused-liquid replenishment and the slow-releasing capabilities of GIFRP coatings. Minimised surface deterioration and the

continued presence of glycerol on GIFRP coatings demonstrated a small increase in ice adhesion from 0.22 kPa to 0.77 kPa after the erosion tests, one of the lowest values reported in literature after substantial surface damage. The concept inspired by cetacean skin and the cryoprotective features of chionophiles was instrumental in keeping the ice adhesion under 1 kPa after erosion impact.

Parts of this thesis have been published or presented in the following:

Journal Papers

1. **H. Memon,** J. Liu, N. Weston, J. Wang, D. De Focatiis, K.-S. Choi, X. Hou, In-situ icing and water condensation study on different topographical surfaces, Cold Reg Sci Technol, 165 (2019) 102814.

DOI: 10.1016/j.coldregions.2019.102814

2. **H. Memon,** J. Liu, D.S. De Focatiis, K.-S. Choi, X. Hou, Intrinsic dependence of ice adhesion strength on surface roughness, Surf. Coat. Technol., 385 (2020) 125382.

DOI: 10.1016/j.surfcoat.2020.125382

3. **H. Memon**, D.S.A. De Focatiis, K.-S. Choi, X. Hou, Durability enhancement of low ice adhesion polymeric coatings, Prog. Org. Coat., 151 (2021) 106033

DOI: 10.1016/j.porgcoat.2020.106033

4. **H. Memon**, D.S.A. De Focatiis, K.-S. Choi, X. Hou. Toward Exceptional Icephobicity with Chionophile-inspired Durable Biomimetic Coatings, ACS Appl. Polym. Mater., 3 (2021) 4184-4194

DOI: 10.1016/j.porgcoat.2020.106033

5. **H. Memon**, K. Mirshahidi, K.A. Zarasvand, K. Golovin, D.S.A. De Focatiis, K.-S. Choi, X. Hou. Comparative study on the influence of surface characteristics on de-icing evaluation, J. Mater. Sci., (2021) 1-16

DOI: 10.1007/s10853-021-06407-x

6. J. Liu, J. Wang, L. Mazzola, **H. Memon**, T. Barman, B. Turnbull, G. Mingione, K.-S. Choi, X. Hou, Development and evaluation of poly (dimethylsiloxane) based composite coatings for icephobic applications, Surf. Coat. Technol., 349 (2018) 980-985.

DOI: 10.1016/j.surfcoat.2018.06.066

7. J. Liu, J. Wang, **H. Memon**, Y. Fu, T. Barman, K.-S. Choi, X. Hou, Hydrophobic/icephobic coatings based on thermal sprayed metallic layers with subsequent surface functionalization, Surf. Coat. Technol., 357 (2018) 267-272.

DOI: 10.1016/j.surfcoat.2018.10.002

8. J. Wang, **H. Memon**, J. Liu, G. Yang, F. Xu, T. Hussain, C. Scotchford, X. Hou, Effect of surface adsorption on icing behaviour of metallic coating, Surf. Coat. Technol., 380 (2019) 125068.

DOI: 10.1016/j.surfcoat.2019.125068

9. T. Mahmut, **H. Memon**, F. Xu, I. Ahmed, X. Hou, Electrospun nanofibre membrane based transparent slippery liquid-infused porous surfaces with icephobic properties, Colloids Surf. A Physicochem. Eng. Asp., 585 (2019) 124177.

DOI: 10.1016/j.colsurfa.2019.12417

Acknowledgements

Accepting the offer to embark on a doctorate at the University of Nottingham was one of the most rewarding experiences for me and a life-changing decision. I started simple and gullible, and I am leaving as stronger and wiser as ever. For this, I would like to seize these few lines to express my utmost thanks and gratitude to my supervisors, my parents and the unforgettable acquaintances I made during this successful PhD thesis.

First and foremost, I would like to warmly thank Dr. Xianghui Hou, to whom I am highly grateful for accepting me as his student and being patient with me during the multiple phases of this PhD. He was extremely patient and kind and I am indebted to him for dedicating countless hours to develop my writing and research skills and for nourishing my professional aptitude. His emotional support and diligent involvement to ensure the success of this PhD were indeed unrelenting and highly appreciable. I would like to further extend my warmest gratitude to co-supervisors Prof. Kwing-So Choi and Prof. Davide de Focatiis for their thorough supervision, great assistance, and constant help. The realisation of this thesis would not have been possible without their support.

Second, I dedicate this humble work to my dear parents, who always found comfort in supporting me throughout my academic journey, gave me ample confidence and encouragement and never ceased to support me. This PhD has certainly come about with moments of achievement and glory, however, it has also brought about several hardships, which I wouldn't have easily surpassed if it hadn't been for my parents' moral support. I am also happy for being able to conduct my studies abroad and explore the European continent from the UK to its far east. These trips were instrumental in improving my

personality and brewing new ideas that significantly changed my outlook not only on the problems I encountered during my PhD but also on life as a whole.

Furthermore, I am grateful to the Faculty of Engineering at the University of Nottingham for awarding me a studentship to conduct this PhD and for the funding available for my research expenses. I also reiterate my thanks for the confidence that was placed in me to carry out research for the CleanSky 2 Joint Undertaking project under the European Union's Horizon 2020 research and innovation programme [grant agreement No CS2-AIR-GAM-2014-2015-O1. Cf. Art.29.4 of [A2]]. My research stay in Canada was also partially supported by the Graduate School Travel Prize and I am deeply grateful for the generous support provided by the University of Nottingham and Prof. Kevin Golovin at the University of British Columbia, Canada.

I am thankful to Dr. Barbara Turnbull for allowing me to use her lab during my studies, which constituted a crucial part of my thesis, the ice adhesion strength tests. I also thank Dr Junpeng Liu for dedicating time to train me with lab equipment and accelerating my research journey. Finally, I acknowledge the use of the University of Nottingham's facilities at the Nanoscale and Microscale Research, supported by the Engineering and Physical Sciences Research Council [grant number EP/L022494/1].

At last, to my supervisors and parents, thank you for believing in me.

Contents

Page

Chapter 1 Introduction **1**

1.1 Project background……..... 1

1.2 Problem statement.…… 3

1.3 The definition of icephobic materials and surfaces……... 8

1.4 Aims and objectives……..…….…… 9

Chapter 2 Literature review **12**

2.1 Background ……..... 12

2.2 Defining key factors affecting icephobicity.……. 14

2.2.1 Hydrophobicity-induced icephobicity……... 15

2.2.2 Influence of surface roughness on icephobicity……...……. 26

2.2.3 Mechanism of ice breakage on elastomers……..... 33

2.3 Effects of environmental conditions on ice nucleation and hydrophobicity……. 37

2.4 Design strategies of icephobic surfaces/coatings …….……..... 39

2.4.1 Superhydrophobicity…….…… 39

2.4.2 Infusion of lubricating liquids…...……..…….. 41

2.4.3 Lower surface roughness……..……..…….. 43

2.4.4 Passive coatings for hybrid ice protection…….……..……. 45

2.5 Evaluation methods of ice adhesion strength…… 46

2.6 Challenges……..…… 52

Chapter 3 Methodologies **57**

3.1 Substrates and raw materials..…….. 58

3.2 Preparation of metallic surfaces…….……... 59

3.3 Preparation of pure polymeric coatings…… 61

3.4 Nanocomposite Coatings…..…….……..……. 61

3.4.1 Hydrophobic coatings ……...……... 61

3.4.2 Superhydrophobic coatings…….……...…….. 62

3.4.3 Nanodiamond incorporated polyurethane coatings …….. 63

3.4.4 Graphene incorporated polyurethane coatings…….. 63

3.5 Fibre-reinforced composite coatings…….……..…… 65

3.6 Liquid-infused coatings……..…..……. 65

3.7 Surface/particle functionalisation…….…….…….….. 65

3.8 Surface characterisation…....…….. 67

3.8.1 Scanning electron microscopy...…...…….……..…… 67

3.8.2 Surface roughness measurement and 3D profilometry…… 68

3.8.3 Thickness measurement…… 69

3.9 Evaluation of hydrophobicity...…….…… 69

3.10 Anti-icing methods…….…… 71

3.10.1 Water droplet freezing delay test …….…… 72

3.10.2 Static anti-icing tests …… 72

3.10.3 Dynamic anti-icing tests…… 73

3.10.4 Anti-icing test after an overnight water immersion…….. 74

3.10.5 In-situ icing and de-icing observation…...…… 74

3.11 De-icing methods……..……. 75

3.11.1 Centrifugal method (CAT)…… 75

3.11.2 Horizontal push method (HPM)…… 78

3.11.3 Normal tensile method (NTM)…..…… 79

3.11.4 Electro-thermal de-icing evaluation …….…… 80

3.12 Surface durability…… 81

3.12.1 Shore hardness tests……. 81

3.12.2 Water impinging erosion tests (WIETs)...……. ……. 82

Chapter 4 Variations of response with surface characteristics in icephobicity evaluation methods 83

4.1 Introduction…….…….. 83

4.2 Responses variation with surface characteristics in different de-icing methods... 85

4.2.1 Comparative analysis of de-icing methods...…….……... 85

4.2.2 Correlation of contact angle hysteresis on ice adhesion……..... 87

4.2.3 Ice adhesion strength of POTS coated surfaces.…….…….. 91

4.2.4 Effect of heat conduction on ice detachment ……..……..... 92

4.3 Responses variation with surface characteristics in different anti-icing evaluation techniques…… 95

4.3.1 Water droplet freezing delays…….…….. 95

4.3.2 Frost accumulations……...……... 97

4.4 Comparative analysis of different icephobicity evaluation methods…… 100

4.5 Summary……...……..……..…... 108

Chapter 5 Influence of surface characteristics on ice adhesion and ice anchoring 110

5.1 Introduction…….…….. 110

5.2 Microstructural analysis of the surfaces and coatings……. 111

5.3 Influence of surface roughness and wettability on ice adhesion…….…….. 114

5.3.1 Stainless steel surfaces…….. 114

5.3.2 Aluminium surfaces…….. 115

5.3.3 Polymeric surfaces…… 117

5.3.4 An overview of the influence of surface roughness on ice adhesion…… 121

5.4 Effect of hydrophobic-functionalised surfaces on ice adhesion…… 123

5.5 In-situ icing observation and ice anchoring on different topographical surfaces. 124

5.5.1 In-situ wetting behaviors……... 124

5.5.2 In-situ growth and retracting behaviours……..……..…... 127

5.6 Mechanism of heterogeneous formation of ice.……..…..……. 135

5.7 Summary……..……. 137

Chapter 6 Development of durable reinforced polyurethane coatings 139

6.1 Introduction…….…….. 139

6.2 Microstructural observation of the reinforced coatings.……..……. 141

6.2.1 Pure PU-5 coatings…… 141

6.2.2 Nanocomposite coatings…… 142

6.2.3 Fibre-reinforced coatings…… 144

6.3 Effect of incorporated fillers on coating hardness……..... 144

6.4 Inclusion of high weight percentages of fillers……..……..……. 145

6.4.1 PU nanocomposite coatings…….. 146

6.4.2 Fibrous PU coatings…….. 147

6.5 Impact of water erosion tests on ice adhesion strength..……..……. 149

6.5.1 Evaluation of as-prepared coatings…….. 149

6.5.2 Post-impingement tests……. 150

6.6 Durability enhancement mechanisms……... 152

6.7 Summary ……..……..…….. 157

Chapter 7 Development of skin-inspired durable ultra-low ice adhesion coatings **159**

7.1 Introduction…….…….. 159

7.2 Bio-inspired coating structure design …….....……..…….. 161

7.3 Microstructural analysis..……..……. 165

7.4 Evaluation of Shore hardness…… 167

7.5 Icephobic performance of fibre-reinforced liquid infused coatings…….…… 167

7.5.1 Evaluation of static anti-icing properties…….. 167

7.5.2 Dynamic frost formation……...……..... 169

7.5.3 Effect of overnight water immersion on frost accumulation……..... 172

7.5.4 Impact of erosion on de-icing properties...……..……..…….. 173

7.6 Bio-inspired coating durability and liquid retention mechanisms……..... 175

7.7 Summary……... 182

Chapter 8 Conclusions and future work **184**

8.1 Conclusions…….…….. 184

8.2 Future work……..……. 189

References **193**

Appendix A (supplementary data) **227**

Appendix B (complete list of results) **231**

List of figures **Page**

1.1	Airplane icing accidents 1987 – 2009 (Adapted from reference [1]).	2
2.1	Wettability models in (a) Cassie-Baxter state, and (b) fully wetted Wenzel state [37].	15
2.2	Ice adhesion strength as a function of (a) $\bar{\theta}_{adv}$ and (b) $\bar{\theta}_{e}$ (adapted from reference [50]).	19
2.3	Ice adhesion strength as a function of Contact angle hysteresis (CAH) (adapted from reference [50]).	20
2.4	Ice adhesion strength as a function of (a) $1+\cos\bar{\theta}_{e}$ (b) $1+\cos\theta_{rec}$ (adapted from reference [50]).	21
2.5	Ice adhesion strength as a function of $1+\cos\theta_{rec}$ [65].	22
2.6	Ice adhesion strength as a function of (a) θ_{rec} (b) CAH [6].	24
2.7	Ice adhesion strength as a function of (a) $1+\cos\theta_{rec}$ and (b) I^{*} [66].	25
2.8	Ice adhesion strength vs. (a) water contact angles and (b) root-mean-square (adapted from reference [85]).	28
2.9	Interfacial cavitation process [2].	33
2.10	Cross-link density vs. ice adhesion strength [66].	35
2.11	PDMS+PDMS-PEG coatings practical work of adhesion [35].	36
2.12	A comparison of WCAs in terms of ambient temperatures and humidity [120].	38
2.13	Droplets sliding on pristine polymer (left sample) and nanoparticles mixed polymer (right sample) [127].	40
2.14	Comparison of ice adhesion strength in terms of (a) materials and (b) sub-zero temperatures [125].	42
2.15	Behaviour of water droplet impingement on (a) hydrophilic, (b) hydrophobic, and (c) super-hydrophobic surfaces (adapted from reference [3]).	44
2.16	Fabrication method of (a) functionalized graphene and (b) anti-icing coating (adapted from reference [19]).	45
2.17	Typical setup of ice adhesion centrifuge setup (adapted from reference [6]).	47
2.18	Force transducer ice removal method [50].	48
2.19	Typical arrangement of DMA probe ice adhesion test [2].	49
2.20	Shear lap joint method: (a) test conditions, (b) 3D representation, and (c) section view of the ice mould [65].	50

3.1	(a) Guyson F1200 Sandblaster and (b) Chemat spin-coater KW-4A.	59
3.2	(a) The HERMILE labortechnik Z 200 A and (b) Sauter TI test stand with the Sauter HBA durometer.	66
3.3	(a) The FEI Quanta 650 ESEM system and (b) Polaron SC7640 vacuum sputter equipment.	67
3.4	(a) A Zeta-20 non-contact optical profiler and (b) schematic diagram of the same equipment.	68
3.5	The FTÅ200 goniometer.	70
3.6	The Peltier cooling plate used for the majority of the anti-icing tests.	71
3.7	The water droplet icing delay test setup (created using biorender.com).	72
3.8	A depiction of static anti-icing test setup (created using biorender.com).	73
3.9	(a) The setup of dynamic anti-icing tests and (b) the custom-built 6-seater metal rotor.	74
3.10	The Peltier cooling plate used in the in-situ icing observations.	75
3.11	The design environmental chamber.	76
3.12	Ice formation on a sample surface, (b) the details of the centrifugal testing method, and (c) the actual picture of the centrifuge (adapted from reference [171]) (figure created using biorender.com).	78
3.13	A focused image of the horizontal push method, together with ice samples.	79
3.14	(a) the normal tensile de-icing method (adapted from reference [173]) and (b) the schematic principle of the tensile method.	80
3.15	The electro-thermal de-icing test setup.	81
3.16	A depiction of water impinging erosion test setup (created using biorender.com).	82
4.1	Ice adhesion strength vs. surface roughness using (a) the horizontal push method, (b) the centrifugal method, and (c) the tensile method. The dotted square indicates samples with similar surface roughness and the dotted line indicates a change (an increase) in ice adhesion strengths below a certain surface roughness range.	86
4.2	Ice adhesion strength and CAH vs. surface roughness on the (a) aluminium substrates, (b) SS substrates, and (c) TPU-BN coatings obtained using the NTM method. The red arrows indicate the ice adhesion strength data points and the blue arrows indicate the contact angle hysteresis data points.	89

4.3	Ice adhesion before and after the surface functionalisation of (a) the SS-SB samples (b) Al-SB samples, and (c) TPU-5 coatings (Before Func.: incorporated with pristine hBNs, After Func.: incorporated with POTS functionalised hBNs). The red arrows indicate the contact angle hysteresis data points and the blue arrows indicate the ice adhesion strength data points.	92
4.4	Ice heating melt tests on (a) the SS substrates, (b) the aluminium substrates, and (c) TPU-BN coatings. The red arrows indicate the ice adhesion strength data points and the blue arrows indicate the time to detach data points.	94
4.5	Droplet freezing delays tests on the (a) aluminium substrates, (b) TPU-BN coatings, and (c) stainless steel substrates. The red arrows indicate the ice adhesion strength data points and the blue arrows indicate the water droplet freezing data points. (d) The droplet freezing delays are plotted against the ice adhesion values, measured using the CAT method.	96
4.6	Static ice accumulation tests on the (a) aluminium samples, (b) stainless steel, and (c) TPU-BN coatings. The red arrows indicate the ice adhesion strength data points and the blue arrows indicate the ice accumulation data points. (d) The static ice accumulations are plotted against the water droplet delays.	98
4.7	Frost densification on the SS substrates after (a) 10, (b) 20 and (c) 30 minutes.	99
4.8	Static ice accumulation tests on the (a) aluminium samples, (b) stainless steel, and (c) TPU-BN coatings. The red arrows indicate the ice adhesion strength data points and the blue arrows indicate the ice accumulation data points. (d) The static ice accumulations are plotted against the water droplet delays.	102
5.1	The microstructure of (a) aluminium, (b) stainless steel, and (c) TPU-BN samples, from the roughest sample on the left side to the smoothest sample on the right. The as-received metallic samples were roughened using sandblasting and smoothened using grinding and polishing. The TPU coatings were roughened by increasing the nanoparticle concentration in the coating matrixes. All images have the same scale bar.	112
5.2	Microstructural image of PDMS coatings.	113
5.3	SEM images of (a) Al-AR substrates and (b) SHS-40 coatings.	114
5.4	Ice adhesion strength on the stainless steel substrates with different surface roughnesses. The red arrows indicate the ice adhesion strength data points and the blue arrows indicate the contact angle hysteresis data points.	115

5.5	Ice adhesion strength on the aluminium substrates with different surface roughnesses. The red arrows indicate the ice adhesion strength data points and the blue arrows indicate the contact angle hysteresis data points.	116
5.6	Ice adhesion strength on the pure polymeric surfaces with different surface roughnesses. The red arrows indicate the ice adhesion strength data points and the blue arrows indicate the contact angle hysteresis data points.	117
5.7	Ice adhesion strength on the pure polymeric surfaces with a different shore hardness.	118
5.8	Ice adhesion strength on the TPU nanocomposite coatings with different surface roughnesses. The red arrows indicate the ice adhesion strength data points and the blue arrows indicate the contact angle hysteresis data points.	119
5.9	Ice adhesion strength on variable surface roughness of superhydrophobic coatings. The red arrows indicate the ice adhesion strength data points and the blue arrows indicate the contact angle hysteresis data points.	121
5.10	Overview of ice adhesion strength versus variable surface roughnesses.	122
5.11	Ice adhesion strength: application of low surface energy chemical.	124
5.12	In-situ water condensation on Al-AR substrates at 3 ^{o}C and 97% humidity (a) Top view and (b) side view.	125
5.13	In-situ condensation on the SHS-20 coatings at 4 ^{o}C and 98% humidity (a) at start and after (b) 10 seconds, and (c) 20 seconds. (d) A magnified image at 100% humidity conditions. The arrows point to the water condensation along the surface voids.	126
5.14	In-situ icing retraction on Al-AR samples after (a) 0, (b) 20, (c) 60, (d) 80, (e) 140, and (f) 160 seconds. The anchored ice is indicated by circles and the ice anchoring points/process during the ice retraction are denoted by arrows. The ice retraction starts in sub-figures (a) and (b), the first layer of anchored ice is shown in sub-figures (c) and (d), and the second layer of ice anchoring and the anchored ice are indicated in sub-figures (e) and (f), respectively.	129
5.15	In-situ icing retraction on SS-S3 samples after (a) 0, (b) 40, (c) 60, and (d) 80 seconds. The circles in sub-figure (b) indicate the possible ice anchoring points during the ice retraction process.	130
5.16	In-situ icing retraction on SHS-40 samples after (a) 0, (b) 40, (c) 60, and (d) 80 seconds.	131
5.17	Ice anchoring mechanism on SHS-20 surface after (a) 3, (b) 6, (c) 9, (d) 12, (e) 15 and (f) 18 seconds.	132
5.18	In-situ icing retraction on TPU-10BN samples after (a) 0, (b) 40, (c) 60, and (d) 80 seconds.	134

6.1	Microstructural images of before and after WIETs on the (a) pure PU, (b) PU-ND-3, (c) PU-GR-3, (d) PU-KV-3, and (e) PU-CF-3 coatings. All images have the same scale bar.	143
6.2	Effect of fillers on the Shore D hardness of polymer coatings.	145
6.3	(a) 3D profile and (b) 2D image of PU-ND-40 coatings and (c) 3D profile and (d) 2D image of PU-KV-20 coatings after WIETs.	146
6.4	Microstructural images of (a) PU-ND-20 and (b) PU-KV-20 coatings after WIETs.	147
6.5	(a) PU-KV-20 and (b) PU-CF-20 coatings after WIETs (same scale bar). Possible material damage around the incorporated (c) Kevlar and (d) carbon fibres (same scale bar).	148
6.6	Ice adhesion strength in comparison to (a) Shore D hardness values, surface roughness (b) before and (c) after WIETs. (d) Ice adhesion strength before and after WIETs.	151
6.7	(a) Stress waves generated after the impact of a water droplet/sand particles (The mechanism is adapted from [242]) and the stress waves on (b) a pristine polymer and (c) a fibre-reinforced polymer (figure created using biorender.com).	154
7.1	(a) The microstructural design of the developed coatings, mimicked by the anatomy of a cetacean mammal skin and inspired by the cryoprotective properties of wood frog and red flat dark beetles, (b) the microstructural image of GIFRP coatings and the same coating after the erosion tests, including a 3D picture, and (c) the sectional view of PU-20gly coatings (after it is cut) and their 3D profile (created using Biorender.com).	163
7.2	(a) Water droplet icing delay and (b) de-icing results before and after the erosion tests on developed and the aluminium samples.	168
7.3	(a) The accumulative data on static frost accumulation before and after 24 hours of the overnight water impression tests (experimental details are provided at the end), together with the photos of samples during the tests, (b) the dynamic frost accumulation measurements at 30 rpm speeds and the relevant pictures of samples before and after the OWI tests, (c) the distinctions drawn between the dynamic frost accumulations tests at two rotational speeds and a comparison is made with static frost accumulations tests.	170
7.4	Microstructural images of pure PU (a), PU-20gly (b), and (c) PU-20CF coatings and the same coatings after the erosion tests, together with the 3D profiles. All images have the same scale bar.	174
7.5	Liquid replenishment process on GIFRP coatings via diffusion after the glycerol pockets were wicked away (created using Biorender.com).	180

List of tables **Page**

3.1	List of the prepared metallic samples and their surface treatments.	60
3.2	List of pure polymeric and functional coatings and their compositions.	62
3.3	The reinforced/liquid-infused PU coatings and their compositions.	64
7.1	A comparison of ice adhesion strength and durability of the recent icephobic coatings.	176

Glossary

Terms		Description (units)
θ_{adv}	-	Advancing water contact angle (^{o})
θ_{rec}	-	Receding water contact angle (^{o})
AFP	-	Anti-freeze proteins
Alumina	-	Aluminium oxide
Al	-	Aluminium
Al2024 T4	-	Aluminium 2024 temper 4
ARF	-	Ice adhesion reduction factor
CAH	-	Water contact angle hysteresis
CAT	-	Centrifugal method
CFM	-	Cubic Feet per Minute
CF	-	Carbon fibres
CNTs	-	Carbon nanotubes
CVD	-	Chemical vapour deposition
DMA	-	Dynamic mechanical analyser
DMF	-	N,N-Dimethylformamide
DMPA	-	Dimethylolpropionic acid
ESEM	-	Environmental scanning electron microscope
GSED	-	Gaseous secondary electron detector
Gly	-	Glycerol
GIFRP	-	Glycerol-infused fibre-reinforced polyurethane coatings
GOs/GRs	-	Graphene
HD	-	High definition
hBNs/BN	-	Hexagonal boron nitride particles
HPM	-	Horizontal push method
KV	-	Kevlar fibres
kV	-	Kilovolts
kHz	-	Kilohertz

kPa	-	KiloPascal
LLL	-	Liquid-like layers
LP	-	Liquid parafin
LFD	-	Low-vacuum secondary electron detector
Micron	-	micrometre
Nano-SiO_2	-	Silicon oxide nanoparticles
ND	-	Nanodiamond
nm	-	Nano-metre
NPs	-	Nanoparticles
NTM	-	Normal tensile method
OG	-	Organogel
OWT	-	Overnight water immersion tests
PDA	-	Polydopamine
PDMS	-	Polydimethylsiloxane
PEMA	-	Poly(ethyl methacrylate)
PEG	-	Polyethylene glycol
PFCS	-	Perfluorodecyl trichlorosilane
POSS	-	Polyhedral oligomeric silsesquioxanes
PTFE	-	Polytetrafluoroethylene
PU	-	Polyurethane
R_a	-	Average surface roughness (μm)
R&D	-	Research and development
RH	-	Relative humidity (%)
RT	-	Room temperature (^oC)
RMS	-	Surface mean roughness (μm)
RPM	-	Revolutions per minute
SAMs	-	Self-assembled monolayers
SB	-	Sandblasted
SiC	-	Silicon carbide
SiO_2	-	Silicon dioxide (silica) particles
SEM	-	Scanning electron microscope

SLIPS	-	Slippery liquid-infused polymeric surfaces
SHS	-	Superhydrophobic surface
SS	-	Stainless steel
TPU	-	Thermoplastic polyurethane
TS PU	-	Thermoset polyurethane
W_e	-	Equilibrium work of adhesion (N/m)
W_p / W_a	-	Practical work of adhesion (N/m)
WCAs	-	Water contact angles (^{o})
WIETs	-	Water impinging erosion tests
μl	-	Micro-litre
μm	-	Micrometer

Chapter 1

Introduction

1.1 Project background

Ice accretion is a major and potentially life-threatening multibillion-dollar problem [1]. From 1981 to 2009, there were 750 reported accidents with more than 800 fatalities in aviation history, primarily due to ice accretion over aircraft skin, as summarised in figure 1 [2]. The reduced number of accidents over the years suggests improvements in technology, however, icing has been a costly inconvenience to engineering applications and normally requires a great deal of energy resources to de-ice, which makes the applications complicated and inefficient. Ice protection systems have attracted increasing interest since 1950 [3] owing to their crucial applications in aerospace, marine and offshore installations, power transmission lines, wind turbines, photovoltaic devices, motor vehicles, communication towers and so on [4-6]. But well correlated icephobic evaluation methods and their relations to ice protection are yet to be devised and remain elusive. Icephobic studies are particularly important for the safety of aircraft as the ice accretion on the aircraft wings disrupt the aerodynamic shape of the airframe i.e. high variation in lift controls, which was the case in the unfortunate incident which occurred during Flight 3407 in Buffalo [7]. In-flight icing occurs primarily: just after take-off; just before landing; during climbing/descent, for example between 2800-6100 metres [8], where small water droplets with diameters ranging up to 500 μm collide with the cold skin of aircraft and form ice, thus compromising flight safety [9]. The build-up of ice

over the wings under harsh conditions is currently controlled by de-icing systems such as hot bleed air or electro-thermal heating methods. Technologies currently in use or at the laboratory scale for aircraft de-icing and anti-icing include: electro-impulse system; electrical heating; shape memory alloys based de-icing technology; weeping wing technology based on de-icing fluids. These technologies are being evaluated qualitatively and parameters such as environmental issues, electromagnetic interference, and power consumption (percentage of bleed air usage) are being investigated. These systems have limited applicability over the leading edges as these are (1) intensive power consumption, and (2) the ice melted by heating re-attaches to other parts of wing i.e. runback ice [10], which again is crucial to the aerodynamic structure and to lift controls.

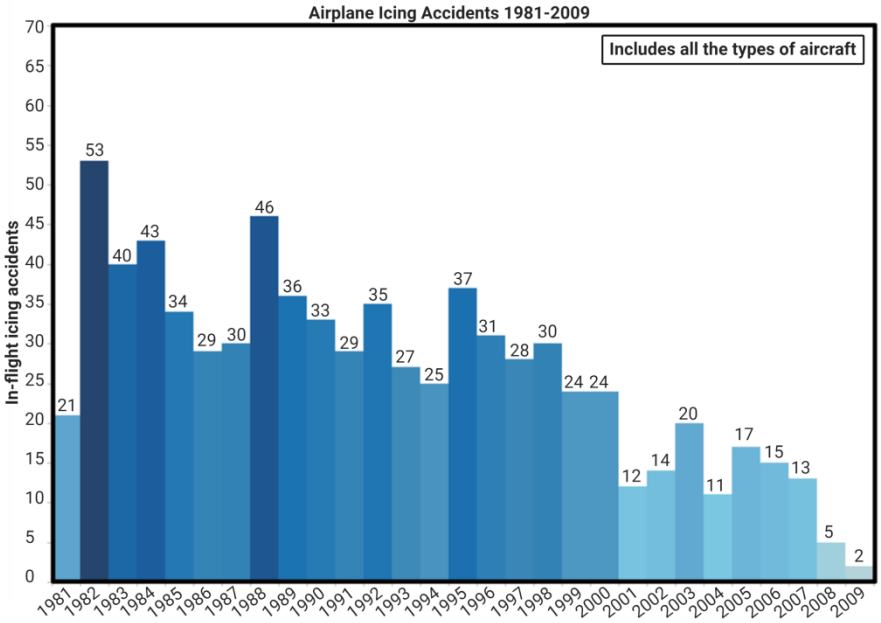


Figure 1.1: Airplane icing accidents 1981 – 2009 (Adapted from reference [2]).

A more promising and specific strategy is to deploy passive ice protection approaches such as durable coatings with/without auxiliary support that allow the super-cooled droplets to slide off before icing (nucleation and crystallisation), or that detaches the

developed ice completely with the help of light vibrational forces created by either the surrounding air or by operative machines. The passive ice protection approach will also significantly mitigate the cost issues that are currently present when spraying chemicals (i.e. sacrificial coatings) periodically to de-ice the aircraft before take-off. Many materials have been introduced to induce passive icephobicity based on hydrophobicity [11], roughness asperities [12], elastic modulus [13], chemical modification of the surface [14], bionic coatings [15], the use of anti-freezing proteins (AFPs) [16], and the incorporation of nanoparticles. However, most of the attempts are experimental in nature and no clear correlations related to icephobicity were identified. Additionally, polymeric surfaces and coatings have been a popular choice of researchers for passive ice protection and many reports have indicated low ice adhesion strength on polymeric coatings and surfaces [17]. Polydimethylsiloxane (PDMS) and polyurethane (PU) based coatings also played a role in the development of hydrophobic surfaces and these surfaces were instrumental for hydrophobicity-induced icephobicity. Thus, it is essential to study and define the key factors affecting icephobicity, and to review the related studies to interpret the true definition of icephobic materials and surfaces.

1.2 Problem statement

Two main strategies were identified to induce icephobicity and were investigated in this thesis. At first, fundamental studies relating to surface icephobicity and icephobicity evaluation methods were carried out, then, the two strategies, which were empirical in nature, were realised to ascertain the fundamental studies and to induce enhanced icephobic performance needed to produce durable icephobic surfaces. The strategies

included the inception of new design ideas and the development of new materials and surfaces.

The idea of deploying superhydrophobic surfaces for icephobic performance was studied and widely experimented [18, 19]. Surface superhydrophobicity would minimise the water contact area to prevent the ice from forming a stronger bond (also referred to as hydrophobicity-induced icephobicity) [20]. This phenomenon favours diversion to homogeneous nucleation or results in a loosely formed (unanchored) ice. It is reported that superhydrophobic surfaces have promising icephobic performance down to -20 ~ -30 ^{o}C [7]. However, under high humidity conditions, the icephobicity of superhydrophobic surfaces is deteriorated due to the capillary action of surface asperities and micro condensation which leads to ice build-up or to the changes of the wetting model from Cassie-Baxter configuration to Wenzel configuration. For example, high-speed impingement of water droplets would wet the rough asperities of the surface and form micro condensation of water [21]. Under sub-zero temperature, the micro condensation forms a thin layer of ice which effectively nullifies the superhydrophobicity of surfaces. Thus, the hypothesis of hydrophobicity-induced icephobicity has limited applications and is not utilizable in the cases of (a) the micro-frost formation under high humidity conditions [22], (b) maintaining high receding angles at sub-zero temperatures [23], (c) mechanical interlocking between ice and high complex surface roughness asperities of the superhydrophobic surface [24], and (d) increased hydrogen bonding (-OH) with interfacial molecules [25]. All these factors become the main hurdles in the deployment of the superhydrophobic surface in icephobic applications and these ideas were put to the

test in this thesis, in order to understand their intrinsic relationship between wettability and ice adhesion.

Surface roughness plays a crucial role in imparting icephobicity and superhydrophobicity onto a solid surface. Superhydrophobicity is also the synergetic result of low surface energy and rough asperities [26]. Surface texturing or patterning has been long debated to achieve icephobicity [27, 28] and some promising results were reported in anti-icing applications (e.g. droplet freezing delays, etc.) [8]. It is reported that ice nucleation can be prevented or significantly delayed by deploying surface roughness patterning close to or smaller than the critical ice nuclei size (1.2 nm – 2 nm) [29]. The rate of ice nucleation over a surface is governed by the interfacial correlation factor [30] and the factor depends on homogenous and heterogeneous nucleation barriers. It is important to control or minimise the heterogeneous nucleation rate, which is mainly influenced by foreign particles present in the water and on the surface, by the interfacial energies between the surface and interacting liquids/solids, and by surface geometries. By favouring the homogenous nucleation on the surface, the need to control the effective contact area as required by superhydrophobicity-induced icephobicity methods could be eliminated. Surfaces with different surface roughness and wettability conditions were investigated to understand the influence of surface roughness on ice adhesion. The microstructural mechanism of ice formation and retraction was also studied using newly-adapted in-situ icing studies.

The icephobic performance and other attributes of icephobic coatings have been investigated. Limited studies have been conducted on the durability of the coatings and their ability to maintain icephobic performance after erosion impact. On the other hand,

liquid infused coatings in general pose performance challenges such as coating durability and liquid retention inside the material matrix. Most studies have either conducted icing/de-icing cycles, chemical stability and/or durability evaluation using mechanical methods (such as abrasion resistance, indentations, scratch tests, and sandblasting etc.). The key application areas of icephobic coatings are in aerospace and wind energy, both of which involve severe water droplet erosion (average rainfall rate 25 mm/h, ~2 mm droplets, and at ~200 m/s speed). The icephobic materials need to resist the surface damage (morphological and/or topographical) that can deteriorate the icephobic performance. In this work, the incorporation of micro-fibres and nanoparticles was driven by the need to enhance durability in surface icephobicity under erosion impact even after non-ignorable material damage, and a new coating design was proposed which is inspired by the anatomy of cetacean skin. The purpose of these new coatings was to mimic the elastic and mechanical response of the skin and to provide a liquid-like flexible surface (infused with a cryoprotectant) to induce extraordinary icephobicity.

Despite the research area's long history, there is no standardised method to measure ice adhesion. The lack of a standardised method means that each research group publishes their own measured data and the comparison of data is difficult due to variation in icing sample preparation, measured magnitudes, applied forces and interfacial contact areas. For example, ice adhesion measured on established de-icing methods varies by several orders of magnitude [1] and stress distributions across the interface area are not uniform [31]. Variation in ice formation also leads to uneven ice layers which may result in non-uniform loads during the de-icing tests. From a fracture mechanics point of view, different shear and peel stresses are exerted on crack tips, and the crack formation and

propagation entirely depends on the load case and orientation for a particular measurement technique [32]. Thus, there is a need to compare the de-icing evaluation methods and to understand their fracture mechanics and dependencies. In this thesis, a comparative study of de-icing and anti-icing methods is provided. Firstly, the ice adhesion strength was measured using three established de-icing methods using the same ice contact area to study the variations of response with surface characteristics of the samples, such as surface roughness and wettability. Secondly, the preliminary results were conducted to observe if the surface characteristics have a similar quantifiable impact on the de-icing and anti-icing evaluation methods. The conclusions could be applied to define an appropriate testing method for the evaluation of icephobic surfaces and coatings.

In conclusion, the emphasis of this thesis was centred on the ice-solid interface mechanisms, the establishment of effective correlations, proposing novel surface and material designs, and the development and investigation of durable icephobic coatings to reduce the substrate/ice adhesion.

To provide detailed rationales behind the problems stated above, the thesis includes seven chapters, together with the supplementary information to support the main investigation and discussion. Chapter 2 covers an extensive literature review of factors defining icephobicity, mechanisms at ice/solid interfaces, design strategies of icephobic coatings, icephobicity evaluation methods, and an overview of associated challenges within the icephobic coatings. Chapter 3 includes the materials and preparation methods, followed by the surface characterisation techniques and icephobicity and durability evaluation methods used in this thesis. Chapter 4 is dedicated to providing a comparative study of

de-icing and anti-icing methods. The variations in ice adhesion response with the surface characteristics offer the crucial information on the pre-selection of testing mechanisms. The results obtained in chapter 4 are the result of a collaboration between the University of Nottingham and the University of British Columbia, Canada. The intrinsic dependence of ice adhesion on surface roughness and variable surface wettability is discussed in chapter 5. Chapter 6 discusses the durability enhancement method to improve the mechanical response of the developed coatings to rigorous impinging impacts. Similar methods were also used in chapter 7, to evaluate a new concept of durable liquid-infused coatings, inspired by cetacean skin and chionophiles. Finally, the conclusions of the thesis are summarised and further recommendations are proposed in chapter 8.

1.3 The definition of icephobic materials and surfaces

Based on the information reviewed, icephobic materials and surfaces could be defined as:

1) Materials with low surface energies i.e. having high water contact angles and low contact angle hysteresis. The contact angle hysteresis of droplets is important to understand the sliding of the super-cooled droplets and avoid ice nucleation of super-cooled droplets on the surface.

2) Materials with smoother morphology i.e. having fewer possible ice anchoring points on the surface. This may lead to a weaker interaction at the ice-surface interfaces. Smooth morphology will also be beneficial for the durability of coatings and may provide consistent hydrophobic performance, as currently higher roughness (peak-void valley) is used for superhydrophobicity. Thus, the roughness of peaks (air trapping technique) is damaged by the shear removal of ice and affects the performance of coatings.

3) Materials with low elastic modulus i.e. the elastic modulus of the material should be lower than that of the ice itself. It is shown in the literature that a softer elastic material loosens the grip of the comparably hard ice and paves way for the ice to slides off easily. The process is called interfacial cavitation and works by introducing cavities or cracks in the ice structure.

4) Materials with good durability to sustain the severe water impingement conditions and mitigate and/or resist microstructural damages. The coatings may generate fewer cracks on the surface by distributing the stress waves generated by the impinging droplets better in a polymeric matrix. The fewer cracks means the reduction of possible ice anchoring points, the reduction of stress concentrations that accelerate the surface deterioration, and a lowering of the probability of mechanical interlocking of ice, thus, paving an easy removal of ice.

5) Materials with anti-icing performance to delay the freezing of water droplets and to minimise the formation of ice/frost on the surface. It should take a longer time for a water droplet to freeze, and less frost should form on the surface in high humidity conditions.

1.4 Aims and objectives

The PhD project aims to research and develop new types of polyurethane icephobic materials and composite coatings for potential applications in the aerospace and wind energy industries. In addition to the development of icephobic materials, there was also a need to compare the established icephobicity evaluations methods to better articulate the obtained anti-icing and de-icing results.

The selection of PU as the matrix material for the coatings was made in connection to its wide availability as well as the promising properties, such as smoothness and flexibility, which are desired to impart icephobicity. PU is also a relatively durable material, as compared to other studied icephobic candidate materials, and could be further reinforced to meet the surface durability requirements of high erosion conditions for icephobic applications. However, PU is a hydrophilic material and mainly possesses a rigid surface which could hinder the induction of interfacial cavitation and may produce a stiffer ice anchor in the case of surface damage. Therefore, an extensive selection of PU variants is required that can induce interfacial cavitation without compromising the material durability and be adaptable to surface/filler functionalisation.

The objectives of the PhD project are proposed as follows,

- The selection of PU candidate matrices that demonstrates key performance as per specified criteria for icephobic materials, the fabrication of PU coatings, and the surface modification of the coatings that could aid in enhancing icephobicity:
    - Mixing techniques to ensure required blending and curing of polymers, dispersions of nanoparticles, and solvent evaporation etc.;
    - The functionalisation of fillers to further aid icephobicity of the coatings;
- To characterise the developed coatings to ascertain surface morphologies and the evaluation of icephobicity and hydrophobicity including conducting the in-situ microstructural water condensation and icing studies of the condensation/icing formation and of ice retraction behaviour;

- To conduct a comparative study of anti-icing and de-icing methods, quantifying the material-dependent response of these methods, and identifying appropriate methods for de-icing and anti-icing evaluation;
- To constitute a fundamental study to quantify the influence of surface characteristics on ice adhesion and ice anchoring;
- To devise strategies for durable icephobic coating designs that offer promising anti-icing and de-icing performance by incorporating nano-and micro-particles, fibres, and the infusion of anti-icing liquids to impart icephobic performance and enhance the overall durability;
- To perform durability tests, including a repeat icephobicity evaluation after the material damage, to ascertain durability of the reinforced coatings.

Chapter 2

Literature review

2.1 Background

In-flight icing compromises flight safety by building up ice layers that are formed due to the continued impinging of water droplets on cold aircraft skin [33]. These ice layers distort the aerodynamic characteristics, such as lift, drag and moment, thus severely jeopardising flight safety and efficiency [34]. In the case of wind turbines, the slight formation of ice over the blades changes the aerodynamic profile, whereas a significant accumulation of ice brings down the power generation capacity of the turbines as the lift would be significantly reduced over the blades [35]. On top of that, the current de-icing/anti-icing methods are significantly energy-intensive [36]. Furthermore, the existing de-icing methods, in the aircraft, for example, employ an internal piping network which severely complicates the aircraft architecture, and limited/crucial areas are covered, such as leading edges [37]. Continued ice accumulation or runback ice, i.e. ice that reforms after melting from the covered area, in the uncovered areas may also pose a dangerous situation as it drastically disturbs the aerodynamic loading conditions. Thus, there is a need for a specific passive ice protection system, such as durable coatings with/without auxiliary support that slides the super-cooled droplets before icing (nucleation/crystallization) or detaches the developed ice easily, such as with the help of low-intensity vibrations created by either surrounding air or operative machines.

One such attempt could be the deployment of icephobic coatings, and icephobicity had been induced on these coatings based on the modification of surface characteristics and

inherent material properties. Different strategies can also be employed to induce icephobic performance: such as delaying droplet freezing time; introducing freezing point depressants; lubricating the surface; resisting the formation of frost; reducing the ice adhesion force or work of adhesion [38-40]. The most widely debated approach is reducing the ice adhesion by minimising the anchoring of water on the surface and increasing contact angles of water. Furthermore, the ice nucleation on the surface also depends on a variety of other external factors, including atmospheric conditions [41]. For example, under high-humidity or supersaturation conditions, the bouncing effect of super-cooled droplets is ineffective due to saturation, which promotes enhanced contact time and non-bouncing Wenzel droplets.

Most of the attempts made to address the icephobic challenge or to induce icephobic performance are empirical in nature and no clear correlations related to icephobicity with respect to surface characteristics have been clearly identified. Therefore, it is essential to understand and define the key factors affecting icephobicity and review the relevant studies to interpret the true definition of icephobic materials and surfaces. In this chapter, an attempt was made to evaluate the current progress on the key factors and mechanisms affecting icephobicity. A comprehensive literature review was conducted to understand the influence of: hydrophobicity; surface roughness; interfacial bonding mechanisms; environmental conditions on icephobic performance. These key characteristics could be further exploited to understand their degree of influence on icephobicity, which could be used to impart lasting icephobic performance in the development of icephobic nanocomposite coatings. The nanocomposite coatings offer a unique combination of providing a softer matrix, which could aid for easy release of ice and the surface

characteristics and mechanical properties can be fine-tuned by the incorporation of nanoparticles. Furthermore, the evaluation methods of ice adhesion strength are also reviewed in detail in this chapter. An in-depth assessment of these methods gives an idea about the existence and limitations of different equipment used for the ice adhesion measurements, considering there is no standardised method to measure ice adhesion strength yet.

2.2 Defining key factors affecting icephobicity

A significant portion of icephobic material development studies involved the use of surface wettability and roughness to induce icephobic performance, mainly due to a minimised interfacial contact between the water/ice and the surface. However, the use of these materials has its limitations and may not retain the icephobic performance under certain environmental conditions or a change in the wettability model if the surface roughness is altered. Additionally, the influence of surface roughness is also pivotal, as it plays an important role in ice nucleation and possible ice anchoring during the ice formation. Furthermore, in an event of anchored ice on a softer interface, the surface could also pave an easy path for ice to detach due to mismatch in strain under stress due to a large moduli difference in soft elastomers and ice surfaces. Thus, in this section, the theory of hydrophobicity and the application of hydrophobicity in icephobicity are debated at length. Furthermore, the influence of surface roughness on icephobicity and the mechanism of ice slippage on elastomeric surfaces are discussed.

2.2.1 Hydrophobicity-induced icephobicity

Theory of hydrophobicity

Wettability of the substrate or the interaction of water with the substrate is defined by two distinctive methods: (a) Cassie-Baxter Model and (b) Wenzel model. In other words, a fully wetted substrate is defined by the Wenzel Model: i.e. water molecules are in direct contact with the substrate and completely wets the surface. On the other hand, when a water droplet is partially suspended on air, for example, trapped between the water droplet and substrate asperities, and substrate asperities (direct contact), then the wetting conditions are defined by the Cassie-Baxter Model, and the probability of water molecules anchoring is low. The visual explanation of these models can be found in figure 2.1 [42].

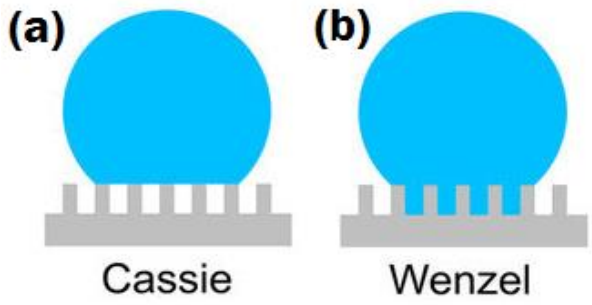


Figure 2.1: Wettability models in (a) Cassie-Baxter state, and (b) fully wetted Wenzel state [42].

Water droplets in their transition composite state resist wetting on a surface having low surface energy [21]. Substrates that show high water contact angles (either static, advancing or receding angles above 150^{o}) are considered superhydrophobic and hypothetically suspended water droplets in the transition composite state [43, 44]. The rolling off of water droplets from these surfaces is likely to happen due to the weak

interaction of water droplets with the substrate surface. The small voids on the surface are often defined as surface roughness or texture, and certain surface roughness leads to increased water repellency due to increased trapping of air in the surface void valley. However, the surface roughness may not be always effective for higher water repellency as the interaction of liquid droplets also relies on the interfacial energies of solid-liquid interfacial phases [45, 46]. If the topography and energy are unfavourable, then liquid droplets will completely wet the specific surface and follow the Wenzel state [21] as shown in figure 2.1(b). The droplet in the Wenzel configuration has a stronger adhesion, characterised to have low receding contact angles, and an enhanced area coverage for liquid-solid interaction [21]. Thus, in order to reduce ice adhesion, it is favourable to initiate the ice nucleation in the Cassie-Baxter state and the anchoring of water could be reduced by the use of micro/nano textures or smoother surfaces/morphologies [21].

To achieve icephobicity, water droplets must resist the transformation into the Wenzel state that could be induced by either the condensation of moisture [47, 48] or by the relative motion of incoming water droplets (i.e. kinetic energy) [49]. To assert this claim, Weber number, a dimensionless parameter, is employed to report the dynamics of the impact of impinging water droplets. The Weber number W_n is the ratio of impinging kinetic energy of a water droplet per unit volume ($\rho V^2/2$) to the capillary pressure (γ_{LV}/r) [50]. Weber number is defined as:

$$W_n = \rho V^2 r/\gamma_{LV} \tag{2.1}$$

Where V is impact velocity, r is drop radius, γ_{LV} and ρ are surface tension and density of water, respectively. Owning to the controlled boundary conditions, the experiments to calculate the Weber number could only be performed in a laboratory. Thus, equation 2.1

can be rewritten concerning potential energy (i.e. gravitational force) g at a height h [51] as:

$$W_n = \rho ghr/\gamma_{LV} \quad (2.2)$$

Water contact angles are often associated with surface wettability i.e. hydrophobicity of the surface and are often coupled for a comparison with the measured ice adhesion strength in the tabular listing or plot pictorials as a function of the water contact angles [52-54]. However, these comparisons did not always follow a correlated trend [55]. With the comparable water contact angles for a few selected samples, the results of measured ice adhesion strength varied by a factor of 10. Typically, the water contact angles are inversely proportional to ice adhesion strength [55].

A solid surface contact with the water droplets inherently possesses unique properties for the different types of interactions. For example, to induce sliding of the sessile liquid droplet, an angle at which a water droplet slides does not correlate with the static water contact angle. Notably, the sliding of water droplets off a surface at a certain angle is a shearing process and behave differently as compared to that of the static water contact angles [56]. Furmidge proposed an equation (equation 2.3) using the spontaneous movement of a sessile droplet to predict the minimum angle of the title (α) [57]:

$$(mg/w)\sin(\alpha) = \gamma_{LV}(\cos\theta_{rec} - \cos\theta_{adv}) \quad (2.3)$$

Where θ_{rec} and θ_{adv} are the receding and advancing water contact angles, respectively. w is the width of the droplet (in 90^o direction to the droplet sliding) and m is the mass of the droplet. From equation 2.3, it is clear that the tilt angle is directly proportional to a dimensionless liquid-solid interaction parameter in the form of $(\cos\theta_{rec} - \cos\theta_{adv})$,

categorised as contact angle hysteresis (CAH), rather than a single value of water contact angle [55].

Hydrophobic surfaces in icephobic applications

The water repellency (or wettability) of a substrate can alternatively be considered from a thermodynamic scenario that accounts for free energies connected with the elimination and formation of interfacial areas [55]. Thus, the reversible free energy of the creation and destruction of interfaces can be narrated as the equilibrium work of adhesion (W_e) of liquid droplets on the material surface and it can be quantified using Young-Dupré Equation (equation 2.4) [58, 59]:

$$W_e = \gamma_{LV}(1 + \cos\theta_e) \tag{2.4}$$

Here, it is clear that the dimensionless factor $(1 + \cos\theta_e)$, where θ_e is Young's equilibrium water contact angle and the angle directly correlates with equilibrium work of adhesion, W_e [55]. However, in literature, there are many terms that describe W_e, such as the thermodynamic work of adhesion, the basic work of adhesion, or the fundamental work of adhesion [60] etc.

Typical processes may not be described using the idealised Young-Dupré equation having the equilibrium contact angle but instead, the adhesion work could be calculated as suggested by Gao and McCarthy [56, 61] and defined as:

$$W_p = \gamma_{LV}(1 + \cos\theta_{rec}) \tag{2.5}$$

Where θ_{rec} is the receding contact angle and the dimensionless factor $(1 + \cos\theta_{rec})$ directly correlates with practical work of adhesion, W_p. Mittal [62] coined the term practical or physical work of adhesion as it is the genuine work required to annihilate the

bond between solid and liquid. Quantitatively, $(1 + \cos\theta_e)$ is always smaller than $(1 + \cos\theta_{rec})$, thus W_e is always smaller than W_p. To further study the impact of θ_{rec}, an approximately linear correlation between contact angle hysteresis (CAH) in the form of $(\theta_{adv} - \theta_{rec})$ and the measured ice adhesion strength was reported by Kulinich and Farzaneh [52]. It was found that most of the differences in CAH were noted due to θ_{rec} and the water droplets were in either the partially wetted composite Cassie-Baxter model (high θ_{rec}) [63] or the fully wetted Wenzel model (low θ_{rec}) [64].

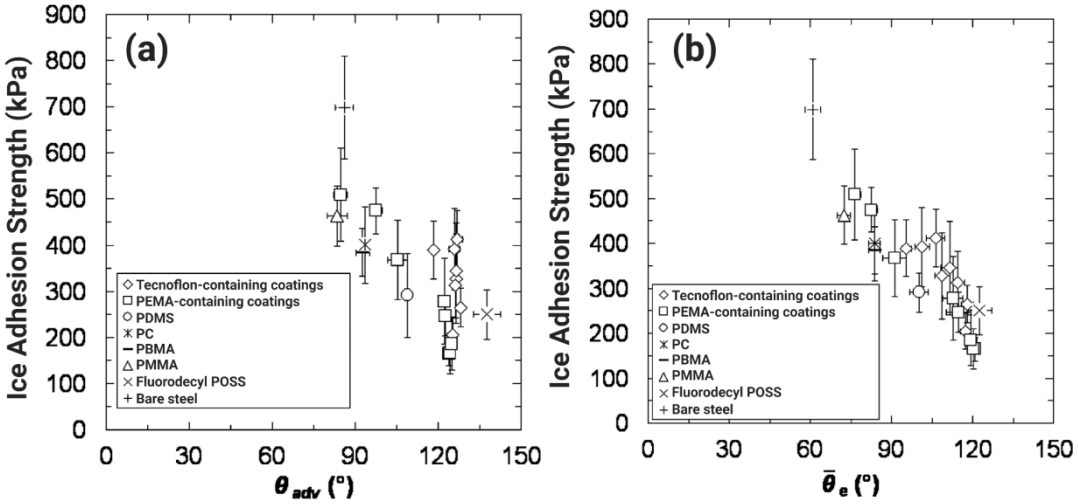


Figure 2.2: Ice adhesion strengths as a function of (a) $\bar{\theta}_{adv}$ and (b) $\bar{\theta}_e$ (adapted from reference [55]).

The measured ice adhesion strength (kPa) were plotted as a function of θ_{adv} i.e. advancing contact angle and used as a near approximation of the static water contact angle [65] (figure 2.2a). In order to reflect the effect of equilibrium static contact angle θ_e on ice adhesion, the equilibrium-like static contact angle $\bar{\theta}_e$ was measured by the vibrating droplets, regardless of their initial positions. The droplets gave a unique and instantaneous contact angle somewhere in between the measured θ_{adv} and θ_{rec} [66].

The reason for using equilibrium-like static contact angles is that the droplets can maintain long-lived metastable conditions and this makes it difficult to measure the static equilibrium contact angle [45]. Theoretically, the static equilibrium-like contact angle, $\bar{\theta}_e$ can be measured [45]:

$$\cos\bar{\theta}_e = 0.5(\cos\theta_{adv} + \cos\theta_{rec}) \quad (2.6)$$

Given this equation, the ice adhesion against the static equilibrium-like contact angles $\bar{\theta}_e$ was studied and shown in figure 2.2b. From the figure, it is clear that both of the plotted graphs indicate a negative slope (i.e. inverse relationship) [27] and the data gives some correlation with ice adhesion strength.

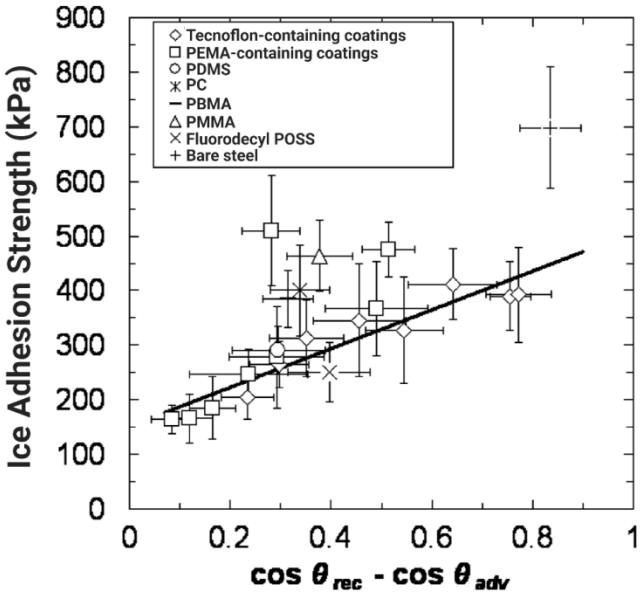


Figure 2.3: Ice adhesion strength as a function of Contact angle hysteresis (CAH) (adapted from reference [55]).

To identify links among the parameters, the CAH parameter ($\cos\theta_{rec} - \cos\theta_{adv}$) was plotted with ice adhesion strength and a linear relationship with the ice adhesion was observed (figure 2.3) [55]. However, many samples having high θ_{adv} (i.e. $\theta_{adv} > 100^o$)

showed a higher ice adhesion than anticipated, thus, it was sufficient enough to assume that the adhesion of ice does not always correlate with CAH [55].

Another plausible assumption made from figure 2.3 is that the linear correlation slope does not pass through the origin, which means that even if CAH is close to zero, ice will still adhere to the surface and this gives the idea that the reduction of the CAH model is not a valid approach to induce low ice adhesion strength [67].

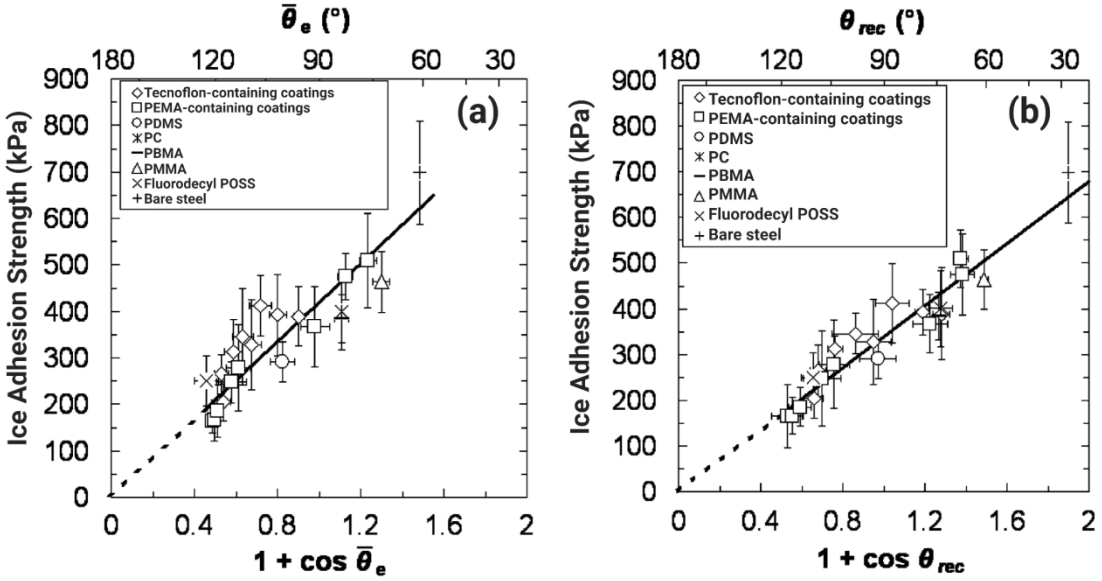


Figure 2.4: Ice adhesion strength as a function of (a) $1 + cos\bar{\theta}_e$ (b) $1 + cos\theta_{rec}$ (adapted from reference [55]).

In order to find a better correlation, ice adhesion strength was plotted as a function of liquid tensile phenomena and practical work of adhesion as shown in figure 2.4 [55]. It was concluded that $1 + \cos\theta_{rec}$ provided a better correlation and is a near-perfect fit to the measured data. It was also assumed that when $\theta_{rec} \approx 120^{o}$, ice adhesion strength tended to be minimal [68] and ice adhesion can be further reduced by the introduction of surface textures in micro-and nanoscale to successfully repel/maintain the ice in the

composite Cassie-Baxter ice state [55], mitigating the possibility of ice anchoring on the surface.

It is clear from figure 2.5 that one superhydrophobic coating (i.e. Sol-Gel fluorinated + aerosil 1d with the textured surface) is significantly different in comparison with other results. Susoff et al. [69] claimed that the CAH has more promising utilization in terms of texture surfaces (i.e. showing a high static angle and the relatively small receding angle simultaneously). They analysed and plotted six types of coatings with regard to ice adhesion strengths and against receding water contact angles of the tested samples. They indicated some linear correlations, notably in the case of smoother surfaces [70]. However, the slope of the correlations did not pass through the origin as observed by Mueler's assumption as shown in figure 2.5. Erbil et al. [27] also used similar plots and found a linear relationship among all the tested samples.

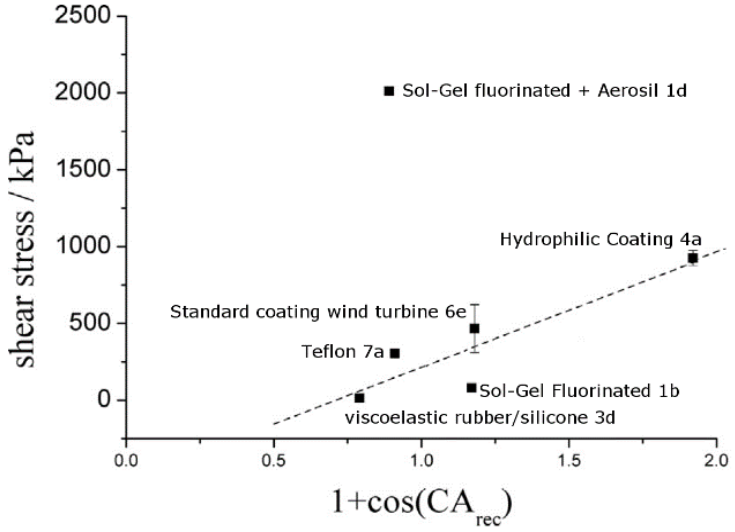


Figure 2.5: Ice adhesion strength as a function of $1 + cos\theta_{rec}$ [70].

Janjua et al. [10] plotted the measured ice adhesion strength as a function of receding contact angles and CAH as shown in figure 2.6a and 2.6b, and indicated that two

different surfaces can have similar ice adhesion strengths with different receding angles (105^o and 55^o, respectively). Although the relation between the practical work of adhesion and the ice adhesion strengths was not given, they corroborated the data with respect to CAH and found CAH to be the dominant parameter in determining ice adhesion strength as shown in figure 2.6b. They further claimed that the receding contact angle, which indicated the intricate dependence on time, would be more effective than advancing and static water contact angle since it is a measurement of de-wetting [10].

Kim et al. [24] noted that the surface retention force is a strong function of the water contact angle hysteresis. They further suggested that the minimisation of the CAH will result in minimising the critical size of water droplets retained on the surface. This phenomenon will enable the condensed water droplets to slide off the surface and ensure efficient removal before freezing [24]. They further interpreted that by reducing the CAH, the ice adhesion could be reduced and the frost formation could be delayed by creating an extremely smooth surface, especially in the case of high humidity conditions [24].

Apart from these comparisons, Golovin et al [71] coined another dimensionless parameter I^*, which is the ratio of ice adhesion strength with interfacial slippage (τ_{ice}^{slip}) to the value without the interface slippage ($\tau_{ice}^{no-slip}$) as shown in equation 2.7.

$$I^* = \frac{\tau_{ice}^{no-slip}}{\tau_{ice}^{slip}} = \frac{C}{\sqrt{\rho^{CL}}} \tag{2.7}$$

Where C is a constant and ρ^{CL} is the cross-linked density of the elastomer. The method of elastomers with interfacial slippage is discussed in more detail in the latter part of this

chapter. The value of *C* was calculated by precise sample preparation to control the cross-linked density, and the measured I^* was in good agreement with equation 2.7 [71].

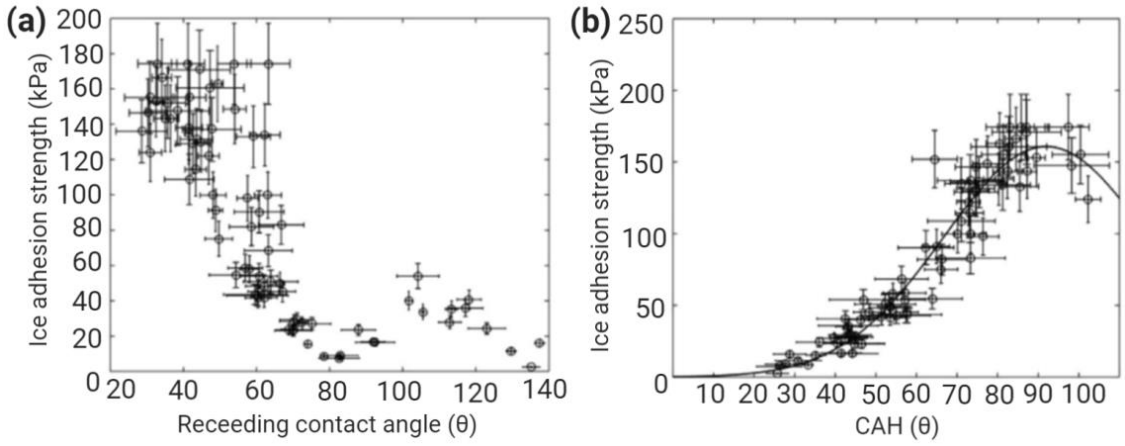


Figure 2.6: Ice adhesion strength as a function of (a) θ_{rec} (b) CAH [10].

Golovin et al. plotted the ice adhesion strength as a function of $1 + \cos\theta_{rec}$ in figure 2.7a. The plotting narrates: (1) in contradiction with Mueler assumption, the measured ice adhesion strength did not closely correlate with the theoretical $1 + \cos(\theta_{rec})$, and the specific Vytaflex 40 coating consisting of 15 wt% cod liver oil showed $\theta_{rec} = 12^o$, whereas ice adhesion was 27 ± 10 kPa; (2) that the theoretical $1 + \cos(\theta_{rec})$ only worked on high shear modulus elastomers (i. e. $I^* < 1.05$), as shown in figure 2.7b and the elastomers without interfacial slippage (without the inclusion of lubricating oil) [71].

A mixed-mode failure of the ice cubes has been reported, i.e. when the shear force is applied to remove the ice cubes, the ice does not move away completely and up to 25% of the ice still adheres to the substrate area [55]. It is assumed that the reduction of receding contact angles increases the probability of the mixed-mode failures: either the coatings are distorted after multiple tests or the coatings initially have low receding contact angles [55].

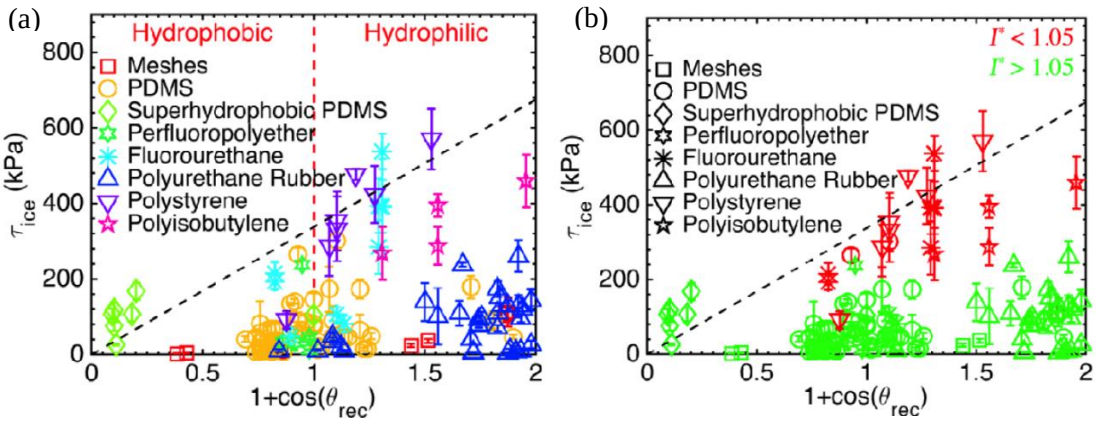


Figure 2.7: Ice adhesion strength as a function of (a) $1 + \cos\theta_{rec}$ and (b) I^* [71].

Limitations of hydrophobic surfaces in icephobic applications

For decades, since the inception of icephobicity studies, the idea behind the use of superhydrophobic materials as icephobic materials are widely debated as the superhydrophobic surface offers a minimized contact with the water droplet and a weak ice bond may be formed [72]. This hypothesis is critically questioned in certain cases: (1) water condenses on surfaces and forms a layer of small fine ice particles i.e. micro frost formation [21], (2) when the temperature is lowered, the receding water contact angles are dramatically decreased [47], and (3) the challenge of retaining superhydrophobic performance under persistent harsh applications [7, 24, 73-75]. Under low humidity conditions, the superhydrophobic materials show excellent icephobic behaviours, even at a temperature of -20 ^{o}C~-30 ^{o}C [7, 74, 76]. However, under high humidity conditions, the capillary condensation of water may attach to the surface texture/asperity and the wetting model may change to the Wenzel configuration from the Cassie-Baxter configuration [77, 78]. Thus, the direct deployment of superhydrophobic materials/surfaces for icephobic purposes is not a perfect solution [69, 79-82].

A superhydrophobic surface is characterised by its spatially uniform intrinsic interfacial energies, and the frost may be formed on the surface indiscriminately. Due to the substantial contact with the surface, the formed ice is likely to create a stronger bond than that on smoother surfaces, which could potentially compromise the hydrophobic capabilities [83, 84] and an increased amount of energy may be required to break the adhesion between the highly complex topographical features [19, 24, 83]. Such kinds of frost formation can be delayed by controlling the nucleation rate of the condensing droplets and restricting the anchoring of the water droplets on the top surface or in a void valley i.e. a weak or Cassie Ice [48].

2.2.2 Influence of surface roughness on icephobicity

Surface roughness or asperities plays a detrimental role in icephobicity studies and the roughness can be categorized into three types: (i) superhydrophobic roughness range of 50 nm - 100 μm [7, 74, 75, 85] (referred as rough surface or higher roughness), (ii) surfaces to avoid ice anchoring of roughness range <100 nm [76, 86, 87] (referred as smooth surfaces or lower roughness), and (iii) surfaces to annihilate the ice nucleation of roughness range <10 nm [8, 29, 86] (referred as ultra-smooth or ultra-fine surfaces). The annihilation of ice nucleation over surfaces is further explained in the latter part of this chapter. Saito et al. [88] found that the reduction in ice adhesion strength is possible with the high levels of roughness as it increases the number of air pockets presented between the interfacial ice-substrate contacts. However, surface roughness also increases the number of possible anchoring sites, which may lead to higher adhesion strengths in some instances [10]. Thus, this indicates that the surface roughness plays a crucial role in ice

adhesion and changing the surface topography or the restructuring of surfaces may be key in reducing the ice adhesion strength [70, 89].

Susoff et al. [70] studied superhydrophobic plates by immersing the plates in a vessel full of water and found that the force required to peel off the ice was multiple times higher than that of the pristine plate tipped in the water vessel following a similar procedure. Thus, they concluded that even if the surface behaves superhydrophobic, the ice adhesion significantly depends on surface roughness or the structure of the surface. Additionally, surface roughness along with other parameters strongly depends on the effective surface area of the sample (i.e. the mean interfacial area) [70].

Zou et al. [90] in their experimental results showed that water contact angles from as-received aluminium (AR Al) to sandblasted aluminium (SB Al) changed from 83^{o} to 37^{o}, respectively. The results predicted the Wenzel Model and indicated that the hydrophilic properties of a surface can be enhanced by the change in surface roughness. Interestingly, higher water contact angles were determined on fluorinated-carbon (FC) film-coated samples due to the enhanced high surface energy imparted by the fluorine molecules and could be predicted by a Cassie-Baxter model. A slight improvement in water contact angles was also noticed in the case of silicone-doped hydrocarbon coated samples. Generally, the fluorination of samples results in higher water contact angles, but the results did not show a reduction in ice shear strengths, shown in figure 2.8a [90]. The results also suggested that the ice adhesion strength on the sandblasted samples jumped 1.5-1.9 times as that of the as-received samples due to the increased surface roughness (root-mean-square), shown in figure 2.8b. In comparison to the non-fluorinated substrates, the ice adhesion is lowered by 1.4 and 1.9 times for the FC film deposited SB

and AR samples, respectively [90]. Furthermore, Janjua et al. [10] concluded that with an increase in contact angle hysteresis, ice adhesion decreases and this trend is valid when the CAH is higher than that of 92^{o} and the higher CAH is coupled with a high surface roughness.

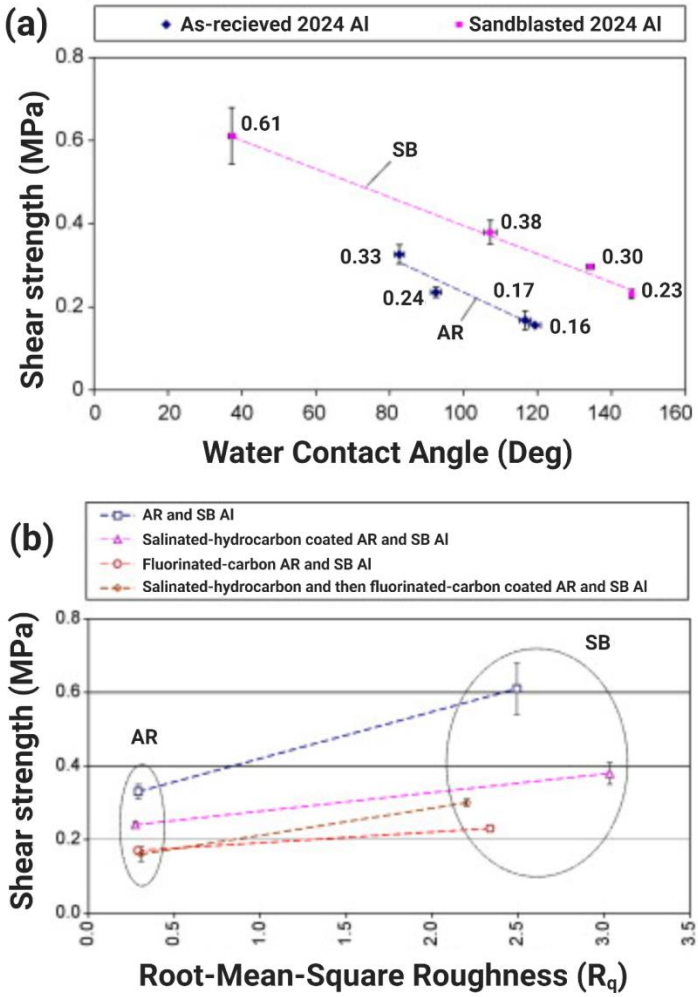


Figure 2.8: Ice adhesion strength vs. (a) water contact angles and (b) root-mean-square (adapted from reference [90]).

Hao et al. [27] showed that by controlled nucleation and effective heat transfer, the freezing process on the rough surfaces can be delayed and such results require the surface roughness to be in a controlled pattern, and the void or the interval of a pattern should be

smaller in size than the critical ice nuclei. Following the procedure, a pre-superhydrophobic surface with controlled surface textures can have superhydrophobic capabilities, together with efficient ice removal and anti-icing capabilities [91]. Poulikakos and co-workers [8, 79] prepared nanometre-scale roughness grooves on hydrophilic surfaces and interestingly showed a longer droplet freezing delay. The magnitude of the freezing delays was at least one order higher than a traditional superhydrophobic surface with low wettability and larger surface roughness.

Chen et al. [28] reported that a liquid-fused coating surface showed rough morphology with R_a of 0.536 nm when in the air and when the coating was submerged in the water, the surface became smoother with R_a of 0.264 nm. The results indicate that a liquid-like layer was formed when the coating was submerged, and this thin layer would induce icephobicity by minimising the interfacial contact area of the formed ice. For smoother surfaces, the results indicated one order of magnitude reduction in ice adhesion and for rougher surfaces, a three-fold increase in the magnitude of ice adhesion strength was reported in comparison to the pristine substrates at similar conditions [28]. To further understand the role of surface roughness, the type of formed ice also matters when considering the icephobicity. For example, the impact ice forms a hard bond with the textured surfaces, while the bulk-formed glaze ice demonstrated a lower ice adhesion strength [92, 93]. The impact ice are normally formed by the fast incoming supercooled droplets, like during icing fog or rain conditions and these micro-droplets penetrate into the void valley or textures of the rough surfaces or pores and anchor with the solid surface [83, 94]. According to another study, a layer of PTFE was applied on rough

coatings and the ice adhesion on bulk-formed ice was reduced. However, no significant reduction of ice adhesion was observed on impact glaze ice [95].

Interfacial mechanisms such as electrostatic interaction, hydrogen bonding, and van der Waals forces could also be responsible for the ice adhesion and mechanical interlocking of ice on the surface [79, 96, 97]. Ice adhesion is significantly reduced on materials/surfaces with a lower surface energy surface [69, 98]. The science behind their impressive icephobic performance is the weaker molecular interaction between the coating surface and the water/ice interfaces [99, 100]. Another factor influenced by the surface energy is droplet freezing delay, and it is reported that the droplet freezing delay can be altered or controlled by a pre-defined surface roughness. The ice nucleation starts with the formation of crystallites, which can be achieved in either homogeneous or heterogeneous ice nucleation. In homogenous nucleation, the crystallites are formed by thermal fluctuations and larger nuclei are only formed after overcoming the free energy barriers among the surrounding liquid. Whereas, in heterogeneous nucleation, crystallites are formed with the help of heterogeneous ice seeds, such as on a solid surface (roughness asperities) [101, 102], dust, impurities or other ice crystals as they reduce the activation energy [27].

Jung et al. [8, 103, 104] reported that one order of magnitude longer freezing delay was observed with a surface having higher wettability and nano-scale roughness. The results suggested that the surface roughness had a strong influence on ice nucleation and its growth. In the experiments, they used samples having different surface roughness values, e.g. from a few nanometers to several micrometres. Smoother samples showed a remarkable freezing delay and the droplets were in an unfreeze condition for a 150 times

longer than the other samples [8]. This significant delay in freezing can be attributed to the low roughness values or roughness values comparable to the radius/size of the critical ice nucleus [76]. The samples having similar surface roughness but variable surface energies showed a strong dependence on surface energy and the surface having lower surface energy demonstrated a longer freezing delay. The theory of classical heterogeneous ice nucleation states that surface roughness and wettability (hydrophobicity) are two main factors that decide the freezing probability, i.e. the rate of critical nuclei generation in the droplet [87]. They further studied the dependence of freezing delay on surface roughness and assumed that the freezing delay rose with lower surface roughness and a longer freezing delay was expected on surfaces with lower surface energy [76].

In terms of thermodynamics for homogeneous ice nucleation of a supercooled water droplet on a solid surface, the free energy barrier ΔG is higher than that of heterogeneous nucleation [87]. The theory suggests that the critical size r_c must be reached for the formation of stable ice nuclei at a given temperature and can be calculated using equation 2.8 [87].

$$r_c = {2.\gamma_{IW}}/{\Delta G_{f,v}} \tag{2.8}$$

Where $\Delta G_{f,v}$ is volumetric free energies between water-ice interfaces per unit volume and γ_{IW} is interfacial water-ice energy. At the temperature of -25 ^{o}C, the critical size of ice nuclei was determined experimentally at $r_c \approx 1.7$ nm. These results suggest that the radius of curvature of roughness should be close to the critical size of ice nuclei to suppress the icing effects and prevent the formation of stable ice nuclei as the critical size

favours homogenous ice nucleation. Thus, the classical theory identifies a strong bearing of roughness radius of curvature on the freezing delay mechanism [29].

Therefore, it is reasonable to assume that the maximisation of the free energy barrier for the development of ice embryo (lower surface energy) and the minimisation of effective interfacial contact area (smoother or lower surface roughness) of the super-cooled droplet will significantly increase the icing/freezing delay. However, the formation of ice nuclei is not a simple function of surface roughness [29]. Thus, effective strategies need to be identified and deployed. One such strategy could be the application of nano-structuring and the idea had been debated in anti-icing coatings. It was reported that the nanostructured substrates with 0.17 nm – 173 nm RMS roughness demonstrated a remarkable freezing delay, i.e. three-order increase in magnitude and suggested that the values of curvature should be less than ten times the critical radius to mitigate the icing nucleation/formation [29].

The interface between the ice/water and the superhydrophobic surfaces with low ice adhesion strength is dominated by van der Waal's forces [105] and the mechanical adhesion decreases with the increase of water contact angles [106-108]. The adhesion strength, in this case, can be calculated using equation 2.9 [105],

$$\tau_a = \frac{U}{6\pi D^3} \tag{2.9}$$

Where the thickness of depletion layers is denoted by *D* (normally in the range of 0.1-1 nm) and Hamaker constant, *U*, bearing value 10~19 J. Typically, the adhesion strength of ice reduces and *D* increases with the increase of water contact angles. The fluoro based POSS/PEMA surface will have a depletion layer thickness in the order of 1 nm and the highest intrinsic hydrophobicity values are measured on these surfaces [40].

2.2.3 Mechanism of ice breakage on elastomers

For a “soft” or rubbery coating, the shear stress piles up at the interface, instead of building evenly across the coating. This mismatch in strain under stress due to a large moduli difference in soft elastomers and ice surfaces result in a path for easy release of ice [96]. According to the mechanism of hydrodynamic lubrication, the viscosity to the thickness ratio of the aqueous film is directly proportional to ice adhesion strength [109]. The mechanism of ice slippage also includes the contribution of the relative stiffness of the coating materials to the ice adhesion, while also considering the effect of surface energy and roughness to minimise the adhesion. In these rubbery coatings, the thickness plays an important role as larger vertical displacements on thicker coatings lead to concentrated stress at the line or frontier plane, instead of a plane [3], as shown in figure 2.9.

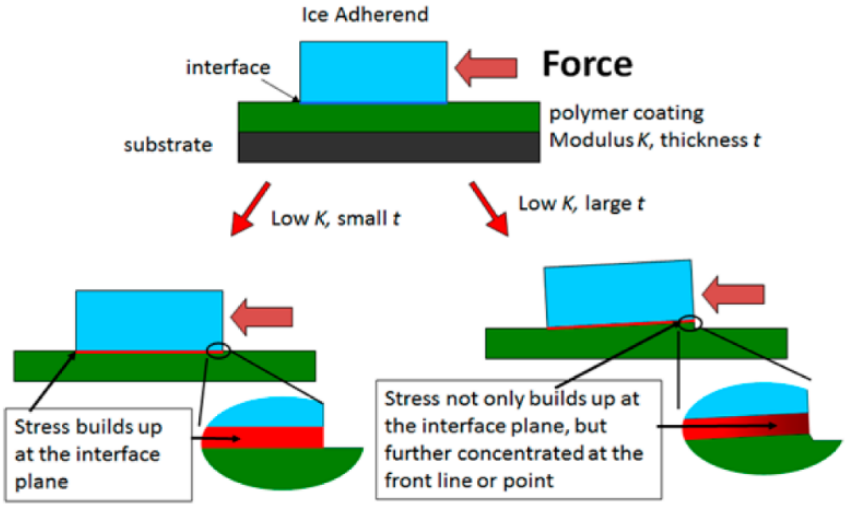


Figure 2.9: Interfacial cavitation process [3].

Golovin et al. [71] showed that the interfacial slippage can be achieved in different elastomeric coatings by altering the crosslink density, irrespective of their material chemistry. They also concluded that the work of adhesion is also not valid in the case of

elastomeric coatings as the ice slips before achieving the required work to break the adhesion.

Viscoelastic nature can demonstrate both liquid- and solid-like properties, and these properties are found in elastomers. Viscoelastic attributes of the elastomeric coatings can be tuned in distinct ways [71]. Firstly, it could be achieved by modifying the physical stiffness of elastomers via the alteration of polymeric crosslink density. Secondly, by changing the non-slip boundary condition through the addition of polymeric uncross-linked chain [110]. The first condition can be achieved by inducing a process called interfacial cavitation [111]. This process develops macroscopic cavities to cleave the ice/surface interface apart and predict the required shear stress. To shear a hard solid formation from a soft surface such as an ice-coating interface, then the stress is given by:

$$\tau = Y(W_p G/t)^{1/2} \tag{2.10}$$

Where *Wp* is the practical work of adhesion, *Y* is an experimental constant, *t* is the thickness of the coating, and *G* is the shear modulus [112]. To alter the physical stiffness, equation 2.11 can be used.

$$G = RT\rho^{CL} \tag{2.11}$$

Assuming isotropy, *R* is the universal gas constant and ρ^{CL} is cross-link density. The conservation of momentum in solid-solid contact articulates that at the interface, there is no slip and the velocity is zero. However, in the cases of soft or elastomeric surfaces, the polymeric chains are considerably mobile and produce slip conditions or non-zero velocity at the interface, and these kinds of behaviours are reported for rubbers [111], adhesives [110], and polymer melts [113]. The behaviour is coined by the term,

interfacial cavitation or slippage and this slippage can be achieved via shear stress τ at the surface as mentioned in equation 2.12:

$$\tau = Gfa/KT \ \ or \ \tau \propto G \tag{2.12}$$

Where *k* is the Boltzmann's constant, *T* is the temperature, *a* is the segmental length to detach the single chain and *f* is the force needed [114, 115]. It is clear from the equation that the interfacial slippage can be enabled in polymeric chains by systematically designing the coatings to enhance icephobic performance for different elastomeric coatings by tailoring ρ^{CL} and embedding miscibility [71].

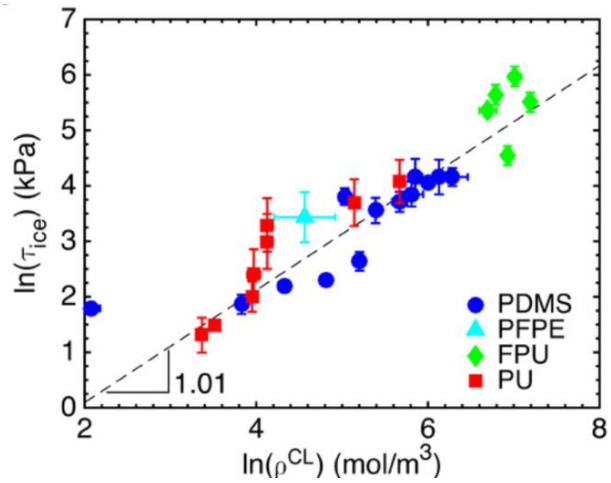


Figure 2.10: Cross-link density vs. ice adhesion strength [71].

According to the Griffith fracture criterion at the coating-ice interface, the square root of the composite modulus (E^*) is directly proportional to fracture stress (τ_f) [116] and it can be expressed as,

$$\tau_f \sim (E^*)^{1/2} \tag{2.13}$$

To demonstrate the practicality of the concept, Golovin et al. [71] fabricated samples with controlled properties: lower cross-link density, the addition of oil (to induce

slippage), and deployed PDMS and PU as polymer matrices as they can firmly lock lubricants inside the matrices and have shown thermodynamic stability over the period of 9 months under harsh conditions [78, 117]. These lubricant/liquid infused polymer coatings reduce the contact angle hysteresis as water and liquid minimize the impinging contact area and reduce the anchoring of ice i.e. induce icephobicity [118]. In the experiments, the lower unaltered PDMS coating has ice adhesion of 150 kPa, whereby altering to lower cross-link density results in 5 fold decrease in ice adhesion to 33 kPa i.e. without the use of any texture, fluorination or lubricating layers [71]. Their experimental results are plotted in figure 2.10.

The results are in good correlation with the cross-link density and the measured strength of ice adhesion. Two important concepts could also be drawn: (1) extremely low ice adhesion strength can be obtained by using low cross-link density polymers and (2) the interfacial slippage can be deployed on low cross-link density surface to further lower down the ice adhesion strength [71].

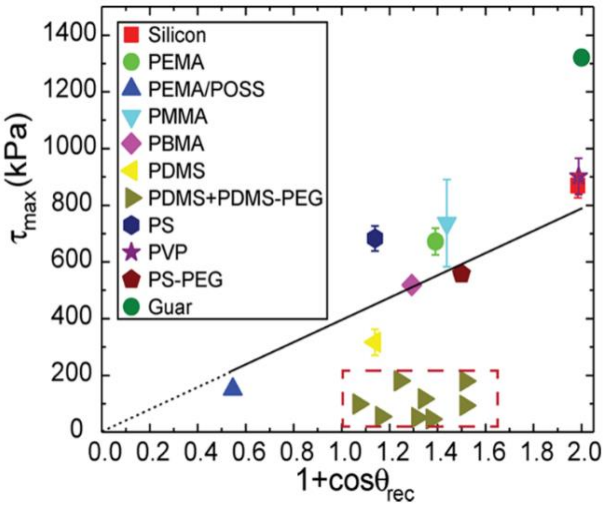


Figure 2.11: PDMS+PDMS-PEG coatings practical work of adhesion [40].

Chen et al. [40] formulated similar coatings having low cross-link density and enabling the interfacial slippage capability. The coatings were PDMS+PDMS-PEG (ethylene glycol) based and the PDMS-PEG contents varied from 1 to 5 wt%. The coatings showed a remarkable icephobic performance as shown in figure 2.11 [40], but it did not correlate with the work of adhesion as indicated by Mueler et al. [55].

2.3 Effects of environmental conditions on ice nucleation and hydrophobicity

Ice nucleation depends on a variety of factors, including atmospheric conditions and the ice may form differently in certain environments. The nature of ice nucleation or the precipitation process in natural environments includes frost formation, fog icing, in-cloud icing, snow, and freezing rain (wintry mix) [119, 120] etc. and this diversity of icing phenomenon results in unique ice accretion formations, which could be dependent on a range of temperatures, wind conditions and the level of humidity [121].

The lower temperatures increase the viscosity of super-cooled droplets and the probability of a droplet bouncing is shrunk due to the increased contact time [122]. Furthermore, during supersaturation or high-humidity conditions, the bouncing effect of super-cooled droplets is ineffective or minimised due to saturation and enhanced contact time, and this promotes non-bouncing Wenzel droplets [80, 86, 123, 124]. Yeong et al. [125] demonstrated the humidity effects on rolling and WCAs measured on polyurethane/organoclay nanocomposites, which were exposed to thermally homogenous cycles. They concluded that the rolling off angles increased by a factor of 2 when the humidity (RH) levels were changed from 20% to 80%. A sudden loss of WCAs was reported during warming and cooling cycles and they concluded that the condensation is the primary factor in the loss of superhydrophobicity as shown in figure 2.12 [125].

Momen et al. [12] reported similar results and confirmed that the condensation and/or micro-frost formation nullify the superhydrophobic effect under high humidity conditions, and the transformation from Cassie-Baxter to Wenzel configuration takes place. In terms of de-icing, the formed saturated ice is more complicated and difficult to de-ice [12, 126] and may have formed in the localised microstructure during unsaturated conditions, owing to the changes in latent heat of crystallization [127].

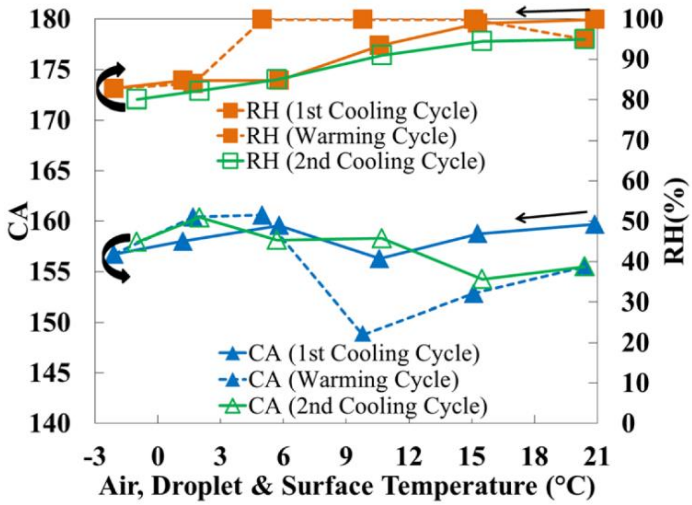


Figure 2.12: A comparison of WCAs in terms of ambient temperatures and humidity [125].

Although the majority of work is focused on the effect of humidity on superhydrophobic surfaces, few researchers adopted new techniques to combat the humidity. Sun et al. [123] embedded a hydrophilic membrane together with freezing ice depressants in a superhydrophobic material matrix to prevent micro-condensation under saturated conditions. The use of freezing ice depressants prevented the ice accumulation on the surface and overall, the surface behaved in a superhydrophobic manner. However, the use of freezing ice depressants may preclude a wide range of icephobic applications [123].

Another approach is infusing a lubricant in a polymeric matrix, or better known as SLIPS. Kim et al. [24] demonstrated a 60% reduction in ice accumulation over the lubricant-infused polypyrrole-coated aluminium coatings as compared to that of the superhydrophobic aluminium and hierarchical polypyrrole-coated aluminium coatings. Ozbay et al. [78] incorporated hydrophobic and hydrophilic lubricants into the polypropylene matrix and reported the hydrophilic lubricant filled surfaces to be more effective at −2 °C and 56−83% relative humidity. Introducing a stable lubricant interface on superhydrophobic surfaces makes the droplet motion slower due to viscous dissipation [128]. However, the physical infusion of liquid raises the questions of the lubricant retention or stability in the long run under high-speed droplet impact and/or under varied atmospheric conditions [24, 129].

2.4 Design strategies of icephobic surfaces/coatings

Various fabrication methods of icephobic surfaces have been reported and they can be categorised into three types, involving coating development, surface treatment, and surface modification.

2.4.1 Superhydrophobicity

The application of nanocomposite coatings is a practical way to achieve superhydrophobicity via the incorporation of nanostructured fillers into various coating matrices. The incorporation satisfies the desirable material properties required to render the surface superhydrophobic such as roughness asperities and altering the surface energy etc. An important aspect of using nanocomposites is to retain the pristine properties of the matrix materials and to enhance a specific material performance with the involvement of nano-fillers. Seyfi et al. [130] demonstrated water contact angles of 161^{o} and a sliding

angle of 3^{o} by depositing 0.6 wt% of hydrophobic nanoparticles in a polyurethane matrix. In terms of icephobic properties, Cao et al. [21] synthesised acrylic polymer by free radical polymerization of glycidyl methacrylate, butyl methacrylate, and polystyrene in toluene under the initiation of azobisisobutyronitrile (AIBN), followed by the precipitation of resulting acrylic polymer in hexane. The results indicated no ice accretion occurred on the material surface after repetitive tests in similar conditions [21] as specified by Mishchenko et al. [7].

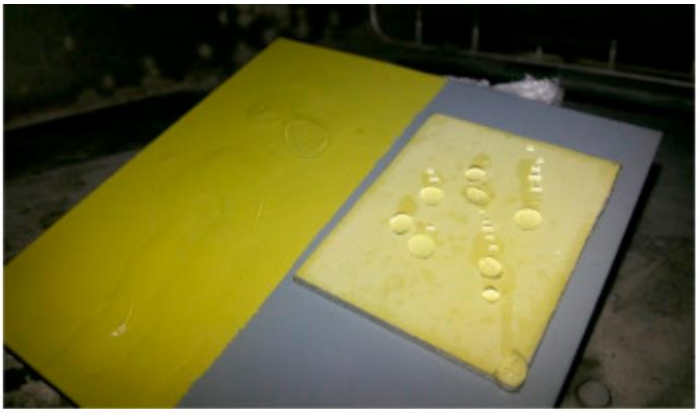


Figure 2.13: Droplets sliding on pristine polymer (left sample) and nanoparticles mixed polymer (right sample) [131].

Liu et al. [132] demonstrated icephobicity as well as superhydrophobic performance on fluoroalkyl silane lubricated nano silicon oxide deposited surfaces. An icing delay of 289 seconds was demonstrated after the deposition of fluoroalkyl silane-based self-assembled monolayers (SAMs). A two-fold decrease in ice adhesion strength was also observed in comparison to that of pristine substrates. Hancer et al. [131] mixed the polysilicon (silsesquioxane) matrix with 12 nm SiO_2 nanoparticles, and the nanoparticles were rendered hydrophobic by the chemical modification using a self-assembled monolayer of perfluoro-decyl trichlorosilane (PFCS). They reported near theoretical

superhydrophobicity of 178^{o} at 3 wt% nanoparticle content and surface roughness value of 43 nm [131]. These coatings demonstrated promising anti-icing performance and droplet sliding angle was measured at 30^{o} degrees tilted at -20 ^{o}C, and the droplets slide off without undergoing the freezing process as shown in figure 2.13. Similar results were observed even after the coating underwent 500 abrasion cycles [131].

2.4.2 Infusion of lubricating liquids

A number of studies used polyurethane and polydimethylsiloxane as matrix materials and introduced various elasticity conditions i.e. altering the cross-link density of polymers by varying the composition of binder and the polymer contents. Golovin et al. [71] mainly studied the use of polyurethane coatings and altered the cross-link density and infused the polymers with natural oils. They also conducted icephobic tests on all the coatings, including lubricated polymers and found the coatings were extremely durable. The coatings demonstrated promising icephobicity even after 100 icing and heating cycles and 5000 abrasion cycles. They reported sustained icephobicity under sub-zero temperatures at -30 ^{o}C as well [71]. Kim et al. [24] fabricated nanostructured Slippery Liquid-Infused Porous Surfaces (SLIPS) using aluminium as a base substrate. They deposited highly textured polypyrrole layers on as-received aluminium substrates utilizing electrodeposition. The coatings were then fluorinated and a lubricant was infiltrated into the pores of the coatings using a heat treatment method [24]. They reported the ice adhesion reduction factor of 87 and a reduced ice adhesion to 15.6 kPa. Interestingly, they demonstrated similar results even under high humidity conditions and at the temperature of -10 ^{o}C, which was very impressive considering the high humidity

environments. The results may suggest a reduction in micro-condensation due to smoother morphology [24].

Wang et al. [133] mixed polyurethane with a varying amount of hydrophilic pendant group i.e. dimethylolpropionic acid (DMPA). They tested the coatings with/without the inclusion of DMPA and demonstrated that the ice adhesion reduced with the increase of DMPA content in the polymer matrix. A 30-fold reduction in ice adhesion strength was observed as compared to that of the pristine substrate. The coatings demonstrated the capability to maintain the icephobic properties even after 30 de-icing cycles down to -55 ^{o}C and could also be applied to a variety of substrate materials [133]. Liu et al. [134] developed sandwich-like multilayers of polyurethane sponges with a layer-by-layer deposition of silver nanoparticles and polydopamine (PDA) films. They demonstrated promising anti-icing properties down to -15 ^{o}C and a remarkable droplet freezing delay of 10,000 seconds as compared to just 117 seconds on the pristine substrates.

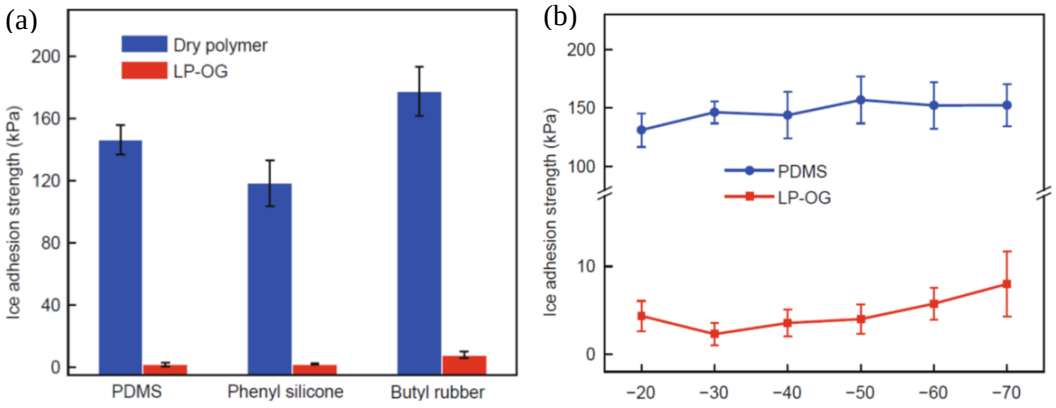


Figure 2.14: Comparison of ice adhesion strength in terms of (a) materials and (b) sub-zero temperatures [135].

Wang et al. [135] reported organogel (OG) infused polymers coatings and OG was added by swelling the LP (liquid paraffin) in cross-linked polymer networks. The polymer

networks used were polydimethylsiloxane, phenyl silicone, and butyl rubber. The ice adhesion strength on the OG-polymer coatings was reduced remarkably by 85 times as compared to that of the dry polymeric coatings. The coatings also retained their icephobic performance down to -70 ^{o}C, shown in Figure 2.14. Interestingly, no considerable change in the microstructure of coatings was reported, i.e. before and after the addition of OG and a similar result was obtained in terms of roughness asperities [135].

2.4.3 Lower surface roughness

Controlling roughness asperities to a level of nano-level to annihilate the ice nucleation before it grows heterogeneously is a sensible strategy for icephobic materials. To control the roughness asperities, samples with nano-size structures such as honey-comb, pillars, and brick pattern etc. had been produced to study surface superhydrophobicity and ice freezing delay. Mishchenko et al. [7] used highly ordered and nano-sized structures bearing high aspect-ratio on various substrates by the Bosch process (reactive ion etching) to create hydrophilic, hydrophobic and superhydrophobic surfaces. The hydrophilic surface was as-received aluminium plates, the hydrophobic surfaces were silane-functionalised smooth silicon wafers, and the superhydrophobic surfaces were nano-structured and silane-functionalised silicon wafers. Ice formed on the hydrophilic surfaces in few seconds, while the hydrophobic surfaces showed an approximate 1-minute delay in icing at -10 ^{o}C. Furthermore, the nanostructured superhydrophobic surfaces showed no ice accretion over a period of approximately 30 minutes, and similar results were obtained at the temperature range of -25 ^{o}C to -35 ^{o}C as shown in figure 2.15 [7].

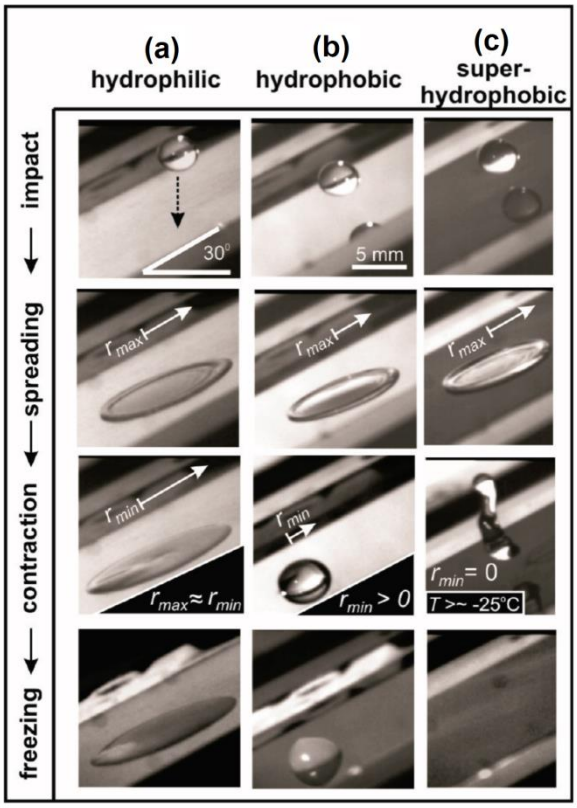


Figure 2.15: Behaviour of water droplet impingement on (a) hydrophilic, (b) hydrophobic, and (c) super-hydrophobic surfaces (adapted from reference [7]).

Eberle et al. [29] fabricated various hydrophilic and hydrophobic surfaces with different nano-scaled roughness from 0.17 nm ~ 176 nm (RMS), while some surfaces were in plain grain structure and some were in hierarchical type. Various nano-scaled roughness was achieved by polishing aluminium with silicon oxide nanoparticles, followed by an etching process, using cryogenic ICP (inductively coupled plasma). Furthermore, the hierarchical structure was achieved using photolithography [29]. The surfaces were rendered hydrophobic by depositing a PFCS monolayer on top of the etched or lithographed surfaces. It was demonstrated that the nano-pits in surfaces greatly reduced the ice nucleation rate and resisted a heterogonous ice growth. The samples also exhibited high freezing

delays and a remarkable icing delay of approximately 25 hours was observed on ultrafine ($R_a \approx 0.17$ nm) hydrophobic surface with hierarchical structures. These freezing delays are one of the longest reported in anti-icing research to date [29].

2.4.4 Passive coatings for hybrid ice protection

Developing an anti-icing passive system that perfectly repels the ice is currently not sufficient for long-term protection against ice. It seems to be more practical if ice protection is combined with both active and passive ice protection solutions [23], which may require active energy supplies [136, 137]. For example, the incorporation of functionalised and pristine graphene have been utilised to heat the surface for ice protection [45, 65, 66]. Wang et al. [23] developed a new superhydrophobic coating by spraying dispersion consisting of graphene nanoribbons that were functionalised by a perfluoro-dodecylate agent as shown in figure 2.16.

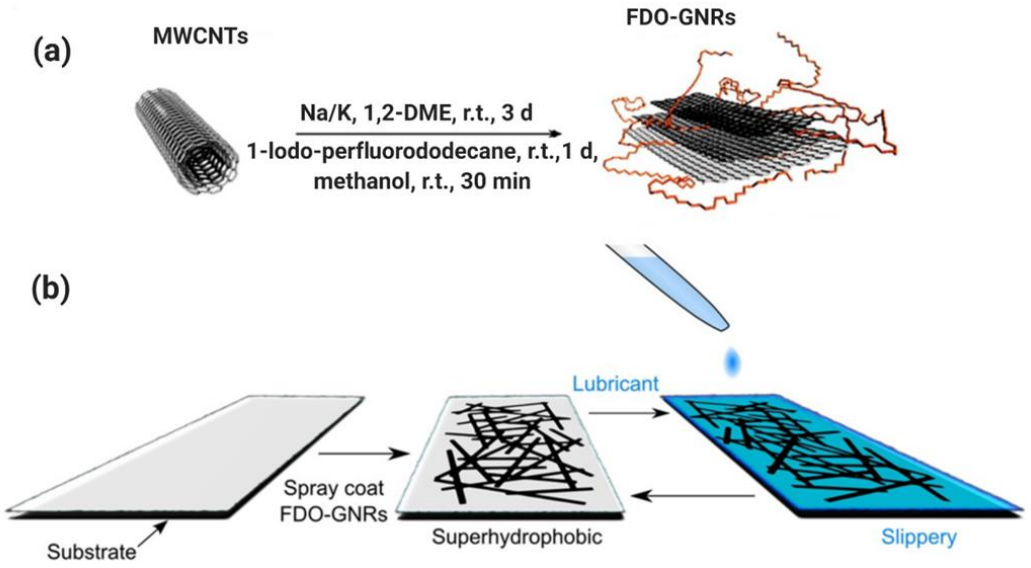


Figure 2.16: Fabrication method of (a) functionalised graphene and (b) anti-icing coating (adapted from reference [23]).

The sheet resistance of the coating was measured at ~320 $\Omega \cdot sq^{-1}$ and a water contact angle of 161°. The coating had the capability to provide both passive ice protection and active ice protection (auxiliary heating) in severe environmental conditions. The coating demonstrated anti-icing performance down to -14 ^{o}C and the capability of active ice protection was tested by applying 12 V potential at -32 ^{o}C. The coating took 40 seconds to de-ice the formed ice blocks [23]. Similar tests are also conducted on coatings without the lubricating liquid at -32 ^{o}C and the coating took 90 seconds to de-ice the attached ice block at a higher voltage of ~40 volts [23]. Thus, the tests demonstrate the significance of lubricating liquid in icephobic coatings.

2.5 Evaluation methods of ice adhesion strength

A fundamental initiation based on fracture mechanics to determine ice adhesion strength and its characteristics were developed by Lockington and Andrews [138, 139]. Ice adhesion strength can be calculated based on the interfacial interaction and mode of ice detachment from the surface. Since then, many new custom methods have been introduced and the fundamental attributes affecting ice adhesion have been studied. However, significant inconsistency exists in the reported values measured by different methodologies.

The majority of the de-icing tests consists of mechanical tests (such as push method) [140-142], shear method (such as shear lap joint test) [143-145], centrifuge rotating test [10, 146, 147], and tensile method [148-150]. One of the most widely used methods to measure ice adhesion strength is the horizontal/vertical push (HPM) method owing to its simplistic and economical design. The ice adhesion strength measured on the push method is greatly affected by the contact location of a force probe and the stress

distribution may not be completely uniform [1, 151]. The centrifugal method (CAT) on the other hand is the most repeated ice adhesion test and is ideal for larger facilities. However, the method is complicated to set and unable to produce stress-strain curves [1, 151]. In comparison, the strain rates obtained using tensile tests are in the range of 10^{-5}–10^{-3} s^{-1}, whereas, strain rates obtained using centrifuge methods are in order of 10^{-6} s^{-1}. This gives the idea that the centrifuge method has good accuracy over ice adhesion tests [152].

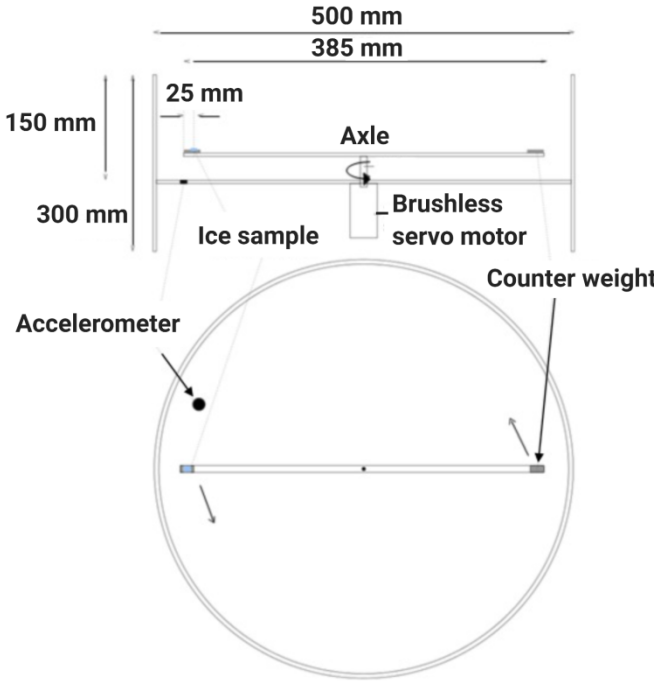


Figure 2.17: Typical setup of ice adhesion centrifuge setup (adapted from reference [10]).

Some approaches use moulds to grow the ice over the substrate using gravity and some methods are based on the spray of super-cooled water inside the centrifugal apparatus to mimic atmospheric conditions such as freezing rain (applicable on power lines) or super-cooled droplet impinging (applicable on aeroplanes) [55]. In actuality, the sample attached with a block of glaze ice was mounted on a rotor and spun

at increasing velocity. When the adhesion strength of ice on the surface was overcome by the centrifugal force originated by the rotation, the ice detached at a certain speed of rotation. These variables were recorded and the shear strength to detach the ice was calculated as the adhesion strength between the ice and the specific surface [10]. A typical setup of a centrifuge apparatus is shown in figure 2.17.

The ice adhesion strength measured using the force transducer method was reported by Jellinek et al. around three decades ago [153] and now this method is widely used by many researchers [54, 154-160]. It consists of a simple arrangement i.e. water columns freeze on the test substrates and force is applied via a force transducer to detach the formed ice. A typical arrangement is shown in figure 2.18.

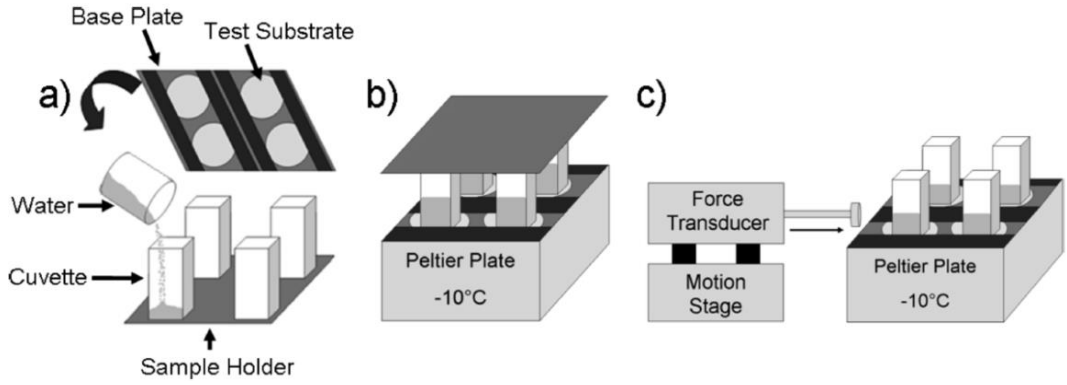


Figure 2.18: Force transducer ice removal method [55].

Firstly, the empty columns are placed on the sample holder and the calculated volume of water is poured in the columns. Then the test substrate is mounted on the base plate and the arrangement is put upside-down on a Peltier plate to freeze the water on the test substrates. The test substrate is measured by attaching a thermocouple near to sample area on the base plate [55].

The ice adhesion strength is calculated by dividing the cross-sectional area of solid-water interaction with the maximum force measured at the time of ice detachment. Apart from custom-built equipment, commercially available equipment named dynamic mechanical analyzer can also be deployed to measure ice adhesion strength as shown in figure 2.19. This process is relatively similar to the one specified above and it uses a probe to remove the ice cylinder grown at -15 ^{o}C in an environmental chamber and calculated the peak removal force [3]. This system is also capable of rapidly changing the temperatures.

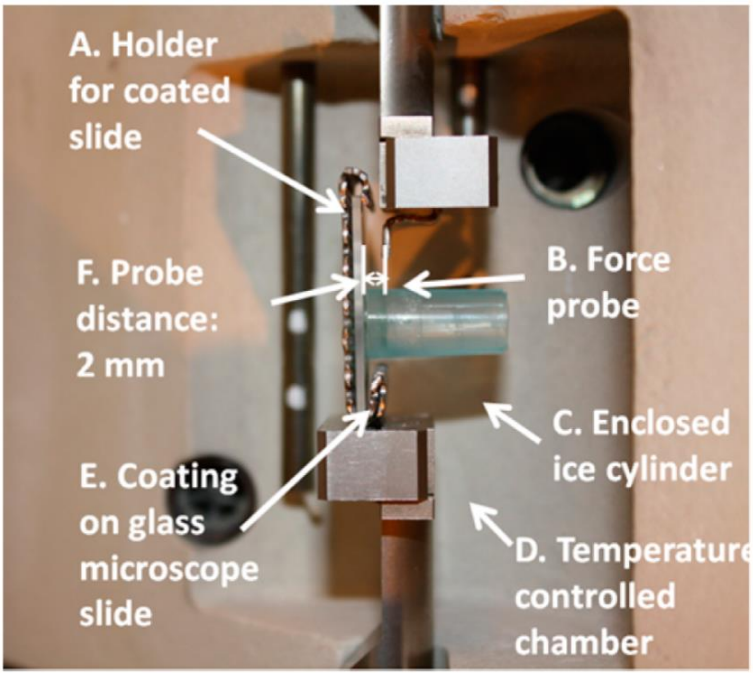


Figure 2.19: Typical arrangement of DMA probe ice adhesion test [3].

The zero cone method (a variant of shear lap joint tests) is one of the least used methods in literature owing to its complex bulky setup and the need for a sophisticated mould. The apparatus consists of an outer cylindrical mould and an inner pin to hold the sample as shown in figure 2.20. The pin is fixed via a bottom notch to the cylindrical mould and an annular gap is kept within the mould. The coating is applied to the pin. The gap is filled

with deionized water and the test block is kept in the icing chamber or freezer overnight at -25 ^{o}C [70]. A thermocouple is also attached at bottom of the pin to measure any temperature gradient across the sample. The test temperature is -14 ^{o}C and the cylindrical mould is mounted on a tensile test machine.

The non-existence of a standardised icephobicity evaluation method means that each research group publishes their own measured data and comparability of data is difficult due to variation in icing sample preparation, measured magnitude, applied force and the interfacial contact areas. For example in de-icing tests, the ice adhesion measured on existing de-icing methods varies by several orders of magnitude [1] and stress distributions across the interface area are not uniform and are uneven [31]. Additionally, from a fracture mechanics point of view, different shear and peel stresses are exerted on crack tips and the crack formation and propagation entirely depends on the load case and orientation [32].

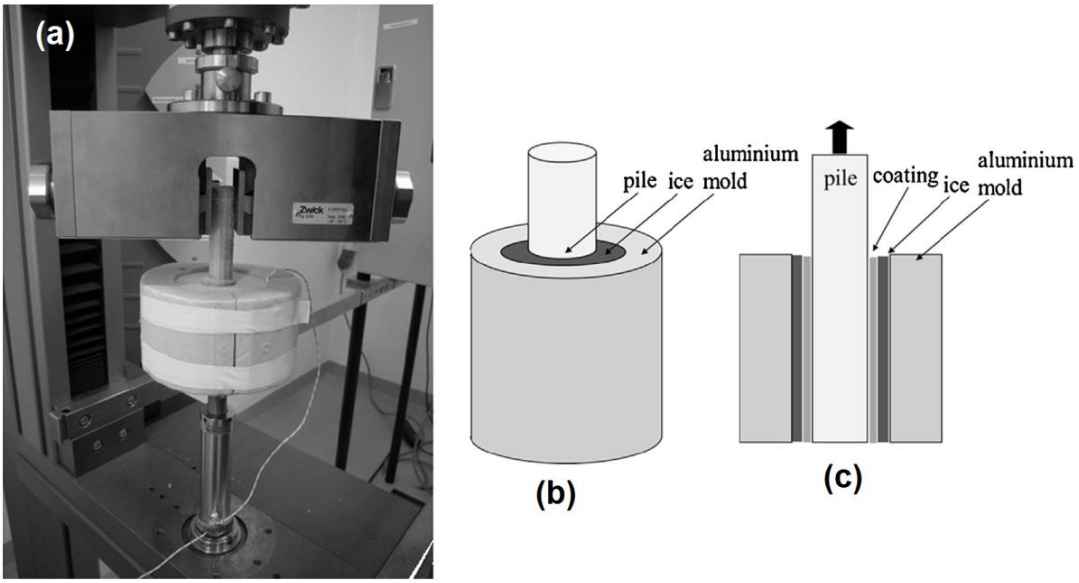


Figure 2.20: Shear lap joint method: (a) test conditions, (b) 3D representation, and (c) section view of the ice mould [70].

As shear stress is strain rate dependent, the comparison of results just by their ice adhesion strength is not appropriate and it is more reasonable to compare or put forward a factor with respect to the reference of pristine materials. It will give an idea of how many times the formulated material reduced the ice adhesion strength in comparison to as-received or bare materials and this factor is called as Adhesion Reduction Factor (ARF) [70]. For example, if an icephobic coating on aluminium [10, 51, 67, 90] is to be tested in terms of ice adhesion strength then the ratio of ice adhesion strength of pristine aluminium (τ_{Alu}) to ice adhesion strength of coatings-based aluminium ($\tau_{coating}$) gives the ARF [70] as:

$$\mathrm{ARF} = \frac{\tau_{Alu}}{\tau_{coating}} \tag{2.14}$$

Thus, from equation 2.14, a higher factor of ARF means the coated surface has low adhesion strength [152]. Janjua et al. [10] in their paper, showed a correlation of contact angle hysteresis (CAH) with ARF. After successive cycles of their testing, they indicated that CAH increases with the decrease of ARF. In order to evaluate the post-experiment performance of the coatings, Zaid et al. fitted ARF as an exponential decay after N cycles as,

$$\mathrm{ARF(N)} = \mathrm{ARF(1)}(e^{-N\propto} + C) \tag{2.15}$$

Where *C* represents the retained icephobic performance after *N* cycles and $\propto$ is the coating deterioration rate. Thus, if *N* tends to infinity, then the targeted coating's adhesion reduction factor is $\mathrm{ARF}\,(1).\,C$ and this emphasizes the long term surface and/or chemical finish damages to the substrate icephobicity on which the coating is deposited [10].

2.6 Challenges

From the review in this chapter, there are a few key challenges for the R&D of icephobic coatings. Firstly, the use of hydrophobicity to achieve icephobicity is a highly contested strategy and it is widely studied. A certain surface roughness leads to enhanced water repellency due to increased trapping of air in the surface void valley, helping the water droplets in their transition composite state to resist wetting on a surface and encouraging an early roll-off (reduced roll-off water contact angles) [161]. It is favourable to initiate the ice nucleation in a hypothetically Cassie-Baxter state and a weaker bond may be formed due to the reduced possibility of ice anchoring and a minimised contact with the surface which discourages the rapid heat transfer [162]. However, under certain environmental conditions, the water droplets could transform into the Wenzel state by either the condensation of moisture (i.e. high humidity or supersaturated conditions) [163] or by the relative motion of incoming water droplets (i.e. kinetic energy) [164]. These conditions may result in a substantial contact with the surface and an increased amount of energy may be required to break a mechanically interlocked ice formed around the surface asperities [165]. Additionally, the inability to retain high water contact angles in sub-zero temperature also poses a performance challenge for hydrophobicity-induced icephobicity applications [47]. These performance challenges could reduce the effect of hydrophobicity on icephobicity and if a layer of ice is formed on a hydrophobic surface, then the surface-induced icephobicity could be made redundant.

Secondly, there is a broader consensus on the role of surface roughness in delaying the ice formation and ice nucleation can be annihilated or immensely delayed by deploying surface roughness patterned close to or smaller than the critical ice nuclei size [166, 167].

Another advantage of these smoother surfaces is that the surfaces are durable as compared to that of rougher surfaces and a reliable icephobic performance could be expected as the surface is not reliant on certain surface roughness to induce hydrophobicity which could be damaged during ice shearing processes [168]. However, with lower surface roughness, the interfacial contact of ice is significantly enhanced as compared to hydrophobic surfaces, and the material chemistry and properties play an important part [169]. In other words, the ice adhesion could be sufficiently reduced by minimising the ice anchoring points but a synergetic effect of either low surface energy or a softer interface is required to induce a low ice adhesion. For example, remarkable freezing delays are expected on smoother, functionalised surfaces as it lowers the free energy barrier and favours a homogeneous ice nucleation [170]. On the other hand, the ice adhesion could be considerably enhanced if a surface has high surface energy or unfavourable conditions (surface impurities) that may promote the ice/surface interface bonding mechanisms [38]. Additionally, there is a challenge to retain a smoother morphology under harsh environmental conditions, such as during water impinging, which can significantly distort the microstructural structure and impart possible ice anchoring points (surface anomalies).

Thirdly, polymeric surfaces and coatings, including the use of liquid infused surfaces (SLIPS), have been a popular choice of researchers for passive ice protection and many reports have indicated a lower ice adhesion strength on polymeric coatings and surfaces [171, 172]. Lower modulus polymer coatings pave way for the easy release of developed ice (de-icing), due to mismatch in strain under stress due to a large moduli difference and the infusion of lubricating liquids or functionalisation with low surface energy chemicals

reduces the probability of heterogeneous ice nucleation (anti-icing). However, limited studies have been conducted on the durability of these coatings and surfaces, liquid replenishment within the material matrix, and the material ability to maintain icephobic performance after significant microstructural damage. Furthermore, most studies conducted icing/de-icing cycles or mechanical tests such as abrasion resistance or indentations etc. [173, 174] which may not meet the requirements of key application areas for icephobic coatings in aerospace and wind energy. Wind turbine blades and leading-edge undergo severe water/ice crystals droplet impingement/erosion and the resilience of icephobic coatings could be better evaluated using water/particles suspension erosion tests [175]. The idea of durability enhancement or the mechanical reinforcement of polymeric coatings is rarely examined, which could aid in the development of erosion-resistant icephobic coatings. The reinforcements could also provide the necessary durability required to maintain the liquid replenishment within the polymeric matrix.

Furthermore, the requirements to induce anti-icing and de-icing performance are not coherent and require balanced tradeoffs to develop a complete icephobic material. For example, the anti-icing capability is mainly imparted either by a minimised interfacial contact to mitigate the heat transfer and encourage a droplet slide-off or by introducing/incorporating freezing depressants to discourage/resist the ice nucleation. First of all, the mitigated heat transfer and early droplet slide-off work on a reduced interfacial contact, whereas, the reduction of super-cooling point by the freezing depressants requires an enhanced liquid/solid interaction. Another reason is the reduced interfacial contact for anti-icing performance is mainly materialised by a combination of

hieratical/lower surface roughness and/or low surface energy surface, which in turn, could encourage the micro-water condensation conditions and may result in enhanced ice anchoring on the surface (increased shearing force to de-ice).

Lastly, the meaningful strategies for the R&D of icephobic coatings may include the investigation of smoother morphology, lubricating liquid/hydrophobic functionalisation, incorporation of nano- and micro-particles, and the utilization of polymeric coatings with lower elastic modulus. Once a low adhesion polymer or composite is pre-selected, further examinations may be carried to enhance the durability and resilience of the coatings against the erosion impact, ensuring the continued icephobic performance. Apart from the material research and development challenges, the non-existence of a standardised icephobic evaluation method also poses another complication, especially in terms of comparability of relevant data. The ice adhesion data may vary with the change of icing sample preparation, measured magnitude, applied force, and interfacial contact areas [151], however, the data could be simplified, by adopting a uniform approach in multiple test setups [31]. For example, if interfacial contact areas and icing sample preparation are kept the same, then the preliminary comparative results could be used to colligate different icephobicity evaluation methods.

In summary, a comparative study of different established de-icing and anti-icing was conducted to understand the material-dependent responses and to quantify the effect of surface characteristics in de-icing and anti-icing evaluation. The comparative study will be instrumental to identify appropriate methods for de-icing and anti-icing evaluation. The fundamental studies were further extended to understand the systematic

influence/intrinsic dependence of ice anchoring and ice adhesion on surface characteristics. The PU matrices were selected based on the fundamental studies and their icephobic performance, and the fillers were incorporated to improve the mechanical response to rigorous impinging impacts. Lastly, a biomimetic coating design was proposed to promote promising icephobicity even after a substantial surface damage.

Chapter 3

Methodologies

A total of six different variants of polyurethane (PU) coatings, including a thermoplastic PU, were examined in this work. A polydimethylsiloxane (PDMS) coating and two metallic substrates were also investigated along with the PU coatings. The metallic substrates were prepared using grinding and chemically-induced polishing methods, and all the polymeric coatings were coated on the aluminium substrates. The polymeric coatings were formulated using a series of preceding steps including magnetic stirring and ultrasonic dispersion, and the coatings were deposited either using spin coating, dip coating, or brush method, followed by the oven drying/curing/post-heat treatment processes. The surface/particle functionalisation was carried using a chemical vapour deposition method. The developed metallic substrates and polymeric coatings were characterised using scanning electron microscopy (SEM), optical 2D and 3D profile measurement, thickness evaluation, and shore hardness measurement for the polymeric coatings. The developed samples were also subjected to static and dynamic surface wettability measurement on a goniometer, and the wetting behaviour was observed via the in-situ water condensation technique using an environmental SEM. The icephobic performance of the developed samples was evaluated using both anti-icing and de-icing methods. The anti-icing capability of the developed samples was evaluated using water droplet freezing delay, static and dynamic anti-icing performance, in-situ icing observation, and icing wind tunnel tests. The de-icing methods include centrifugal, normal tensile, horizontal push, and electro-thermal methods. A majority of these

icephobicity tests were conducted on custom-built equipment setups and in-house in the university, with the exception of icing wind tunnel evaluation, normal tensile and horizontal push de-icing methods. The durability of developed coatings was investigated using water (+SiC particles) impinging erosion tests and a further evaluation of the liquid retention capability of liquid-infused coatings via an overnight water immersion technique. Finally, the icephobic performance was reevaluated on the impinged/immersed coatings to ascertain the continued icephobic capabilities of the developed coatings. The material types and coatings are summarised in table 3.1. Error bars were calculated based on a standard deviation of three measured values.

3.1 Substrates and raw materials

Two-part thermoset polyurethanes namely: Vytaflex 40A (PU-1); Smooth-Cast Semi-Rigid Series 61D (PU-2); Smooth-Cast 320 70D (PU-3); Smooth-Cast ONYX 80D (PU-4); PMC-790 (PU-5) were procured from Smooth-on (USA), and thermoplastic polyurethane matrix Estane 54610 (TPU) in form of pellets was provided by Lubrizol (USA). Polydimethylsiloxane (PDMS) R-2180 was purchased from NuSil Technology, USA. Hexagonal Boron Nitride nanoparticles with a size of 70 nm (hBN NPs) were obtained from Lower Friction (Canada). Hydrophobic functionalized silicon dioxide nanoparticles AEROSIL R 9200 ($nSiO_2$) were purchased from Evonik UK.

Kevlar Aramid pulp, Twaron ® 5011 (Kevlar fibres, 125 µm average length), was kindly provided by Teijin Aramid GmBH (Germany). Carbiso Mil 100µ (milled carbon fibres, 80-100 µm average length) was obtained from Easy composites (UK). Reduced graphene nanoplatelets, CamGraph G3 (GR, lateral size of ~400 nm and flake thickness of ~3 nm), were purchased from FGV Cambridge Nanosystems (UK). Nanodiamonds powder (ND,

spherical size ≤100 nm) was procured from Jichang Metal processing Ltd. (China). Silicon carbide particles (SC224 600 mesh) for the water impinging erosion test were supplied by Simba Materials (UK). Triton X-100 was purchased from Sigma-Aldrich.

1H,1H,2H,2H-Perfluorooctyltriethoxysilane (POTS) was procured from Fluorochem Ltd UK. Micro-polishing cloth and colloidal silica suspension were procured from Struers and MetPrep respectively. N, N-Dimethylformamide (DMF), ethanol, and xylene were supplied by Sigma-Aldrich UK. The metallic plates, SS 303 and aluminium 2024, were procured from Smith Metal Centres Ltd, UK. All materials were used as received.

3.2 Preparation of metallic surfaces

Stainless steel 303 (SS 303) and aluminium 2024 (Al 2024) plates measuring 50 mm x 20 mm x 3 mm and 50 mm x 20 mm x 1 mm respectively were used. All aluminium and stainless steel plates were washed with ethanol and deionized water three times and then dried using compressed air, prior to testing and further treatment.

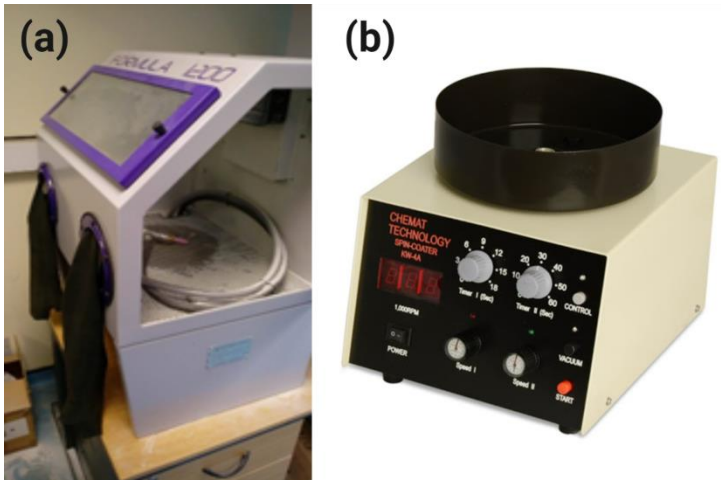


Figure 3.1: (a) Guyson F1200 Sandblaster and (b) Chemat spin-coater KW-4A.

Table 3.1: List of the prepared metallic samples and their surface treatments.

Sample types	Sample codes	Surfaces	Surface treatment	Description
Aluminium substrates (Al)	Al-AR	Al2024	-	As-received
	Al-SB		Sandblasted	With 180-220 µm alumina particles
	Al-fSB		Sandblasted	POTS Functionalised
	Al-S1		Grinded	Grinded (with 320 grit)
	Al-S2		Polished	With 1 µm polishing cloth
	Al-S3		Polished	With 0.25 µm Silica particles
Stainless steel substrates (SS)	SS-AR	SS 303	-	As-received
	SS-SB		Sandblasted	With 180-220 µm alumina particles
	SS-fSB		Sandblasted	POTS Functionalised
	SS-S1		Grinded	Grinded (with 320 grit)
	SS-S2		Polished	With 1 µm polishing cloth
	SS-S3		Polished	With 0.25 µm Silica particles

The metallic plates were smoothened using grinding and polishing with a series of steps employing sandpapers having grits sizes of (i) 220 and 320, (ii) 400, 600 and 1 µm polishing cloths, and (iii) 0.25 µm (chemically induced) polishing cloths using Metprep colloidal silica suspension particles for samples (i) Al-S1/SS-S1, (ii) Al-S2/SS-S2 and (iii) Al-S3/SS-S3, respectively. Al-SB/SS-SB samples were roughened in a Guyson F1200 sandblaster system, shown in figure 3.1a, with Guyson 180-220 µm alumina particles. All metallic samples are listed in table 3.1.

3.3 Preparation of pure polymeric coatings

All polymeric coatings were applied on the aluminium substrates and the substrates were sandblasted to enhance the coating adhesion, in a Guyson F1200 sandblaster with 180-220 µm alumina particles. The substrates were then washed with ethanol and deionized water thrice and dried using compressed air before the coating application.

PU-1, PU-2, PU-3, PU-4 and PU-5 resins were prepared using magnetic stirring at Part A : Part B weight ratios of 100 : 100, 100 : 93, 100 : 90, 100 : 83 and 200 : 100 respectively. IKA® C-MG HS7 hotplate was for magnetic stirring. Then the resins were brush coated on the sandblasted aluminium substrates. PU-1 coatings were cured in memmert GmbH WF110 oven, at room temperature (RT) for 16 hours and post-treated at 65 ^{o}C for 4 hours. PU-2 and PU-3 coatings were cured at 30 ^{o}C for 5 hours and post-treated at 65 ^{o}C for 4 hours. PU-4 coatings were cured 65 ^{o}C for 5 hours and post-treated at 121 ^{o}C for 4 hours. PU-5 coatings were cured at 25 ^{o}C for 48 hours and post-treated at 65 ^{o}C for 4 hours. The TPU coatings were developed by dissolving 1 gram of TPU pellets in 1.5 ml of DMF and the coatings were applied using the dip-coating method. For PDMS coatings, magnetic stirring was used to mix 1 gram of PDMS Part A and Part B (1:1) in 3 ml xylene for 3 hours. All the developed pure polymeric coatings are detailed in table 3.2.

3.4 Nanocomposite coatings

3.4.1 Hydrophobic coatings

For hydrophobic coatings (TPU-5/5f/10/40/60/80), 2 grams of TPU pellets were dissolved in 3 ml of DMF on a magnetic stirrer at 60 ^{o}C. TPU/hBNs coatings with 5/10/40/60/80 wt% of hBN NPs were dispersed in 1/1.5/3.0/4.0/5.0 ml DMF using ultrasonic mixing for one hour, respectively. The ultrasonic mixing was carried using

Cole-Parmer 08895-46 ultrasonic bath. Magnetic stirring was then used to mix the solution in a single vial for 60 minutes, followed by 30 minutes of ultrasonic mixing. All TPU/hBNs coatings were fabricated using the dip-coating method. The resultant coatings were dried in the oven at 80 ^{o}C for 4 hours and followed by a further treatment at 150 ^{o}C for 8 hours. The composition of the coatings is mentioned in table 3.2.

Table 3.2: List of pure polymeric and functional coatings and their compositions.

Sample types	Sample codes	Substrates	Coatings / filler	Description
Pristine polymeric coatings (PU/TPU/PDMS)	PU-1	Al2024	Thermoset PU variants	Pristine
	PU-2			
	PU-3			
	PU-4			
	PU-5			
	TPU		Thermoplastic PU	
	PDMS		PDMS	
Thermoplastic polyurethane nanocomposite coatings (TPU-hBN)	TPU-5	Al2024	Nanocomposite	hBN (5 wt%)
	TPU-f5			POTS Functionalised hBN (5 wt%)
	TPU-10			hBN (10 wt%)
	TPU-40			hBN (40 wt%)
	TPU-60			hBN (60 wt%)
	TPU-80			hBN (80 wt%)
Superhydrophobic coatings (PDMS-nSiO_2)	SHS-5	Al2024	Nanocomposite	nSiO_2 (5 wt%)
	SHS-10			nSiO_2 (10 wt%)
	SHS-20			nSiO_2 (20 wt%)
	SHS-40			nSiO_2 (40 wt%)

3.4.2 Superhydrophobic coatings

For superhydrophobic coatings (SHS-5/10/20/40), magnetic stirring was used to mix 1 gram of PDMS Part A and Part B in 1 ml xylene for 3 hours and ultrasonically dispersing 5/10/20/40 wt% of nano-SiO_2 in 2.5/3.0/3.5/4.0 ml of xylene, respectively. The formed

nanoparticle dispersions were then mixed with the PDMS solution using magnetic stirring for one hour, followed by 30 minutes of ultrasonic mixing. The coatings are further detailed in table 3.2.

Chemat Technology spin-coater kW-4A, shown in figure 3.1b, was used to apply the PDMS/ $nSiO_2$ coatings on the aluminium samples at a rotation speed of 1500 RPM for one minute and the coatings were dried and cured at 60 ^{o}C for 60 minutes, and then 150 ^{o}C for 150 minutes.

3.4.3 Nanodiamond incorporated polyurethane coatings

The nanodiamond incorporated polyurethane coatings were fabricated using the PU-5 solution and the solution was magnetically stirred at a Part A : Part B ratio of 200 : 100 by weight. Nanodiamond powders were introduced (as determined using the required weight percentages) and mixed in the resin solution during the stirring. The incorporated PU resins were then ultrasonically mixed for a further 30 minutes, and brush coated on the sandblasted aluminium substrates. All nanodiamond incorporated polyurethane coatings were cured at 25 ^{o}C for 48 hours and post-treated at 65 ^{o}C for 4 hours. The composition of nanocomposite-reinforced coatings is mentioned in table 3.3.

3.4.4 Graphene incorporated polyurethane coatings

A PU-5 solution was used to incorporate graphene powder mesh and the powder (required weight percentage) was incorporated during the magnetically stirring process. PU-5 was magnetically stirred at a Part A : Part B ratio of 200 : 100 by weight. The incorporated solution was then ultrasonically mixed for a further 30 minutes, and brush coated on the sandblasted aluminium substrates. All graphene incorporated polyurethane coatings were cured at 25 ^{o}C for 48 hours and post-treated at 65 ^{o}C for 4 hours.

Table 3.3: The reinforced/liquid-infused PU coatings and their compositions.

Sample types	Sample codes	Substrates	Surface treatment / coating / filler	Description
PU coatings with carbon fibre (PU-CF)	PU-CF-0.5	Sandblasted Al2024	Fibre-reinforced PU-5	Carbon fibre (0.5 wt%)
	PU-CF-1			Carbon fibre (1 wt%)
	PU-CF-3			Carbon fibre (3 wt%)
	PU-CF-5			Carbon fibre (5 wt%)
	PU-CF-20			Carbon fibre (20 wt%)
PU coatings with Kevlar fibres (PU-KV)	PU-KV-0.5	Sandblasted Al2024	Fibre-reinforced PU-5	Kevlar fibre (0.5 wt%)
	PU-KV-1			Kevlar fibre (1 wt%)
	PU-KV-3			Kevlar fibre (3 wt%)
	PU-KV-5			Kevlar fibre (5 wt%)
	PU-KV-20			Kevlar fibre (20 wt%)
PU coatings with nanodiamond (PU-ND)	PU-ND-0.5	Sandblasted Al2024	Nanocomposite PU-5	Nanodiamond (0.5 wt%)
	PU-ND-1			Nanodiamond (1 wt%)
	PU-ND-3			Nanodiamond (3 wt%)
	PU-ND-5			Nanodiamond (5 wt%)
	PU-ND-20			Nanodiamond (20 wt%)
	PU-ND-40			Nanodiamond (40 wt%)
PU coatings with graphene (PU-GR)	PU-GR-0.5	Sandblasted Al2024	Nanocomposite PU-5	Graphene (0.5 wt%)
	PU-GR-1			Graphene (1 wt%)
	PU-GR-3			Graphene (3 wt%)
	PU-GR-5			Graphene (5 wt%)
Liquid infused PU coatings (PU-gly)	PU-gly-20	Sandblasted Al2024	Liquid-infused PU-5	Glycerol (20 wt%)
Liquid infused fibre-reinforced coatings (PU-CF-gly/GIFRP)	PU-20CF-20gly (GIFRP)	Sandblasted Al2024	Hybrid PU-5	Carbon fibre (20 wt%) and glycerol (20 wt%)

3.5 Fibre-reinforced composite coatings

Carbon and Kevlar fibres were used to fabricated fibre-reinforce PU composite coatings and the fibres were mixed in desirable weight percentages. PU-5 solutions were magnetically stirred in two separate vials at a Part A : Part B ratio of 200 : 100 by weight. The fibres were introduced during the stirring stage and the solutions were then ultrasonically mixed for a further 30 minutes, and brush coated on the sandblasted aluminium substrates. All fibre-reinforced polyurethane composite coatings were cured at 25 ^{o}C for 48 hours and post-treated at 65 ^{o}C for 4 hours.

3.6 Liquid-infused coatings

Liquid-infused PU coatings were fabricated by the inclusion of glycerol, in desired weight percentages, in PU-5 resin solutions. Liquid-infused fibre-reinforced coatings were also produced via the incorporation of carbon fibres and the infusion of glycerol in PU-5 coatings. Both the liquid and fibres were introduced during the magnetically stirring of PU-5 coating at Part A : Part B ratio of 200 : 100 by weight. The infused/hybrid PU resins were then ultrasonically mixed for further 30 minutes for the uniform distribution of glycerol droplets across the polyurethane matrix, and then, brush coated on the sandblasted aluminium substrates. The liquid-infused PU coatings were cured at 25 ^{o}C for 48 hours. The samples were not post-heat treated, as the post-heat treatment at higher temperatures could have an impact on the glycerol retention within the polyurethane matrix.

3.7 Surface/particle functonalisation

The hydrophobic functionalisation of hBN NPs (TPU-f5) was performed in a solution containing 400 mg of hBN NPs in 400 ml ethanol and the solution was ultrasonically

mixed for 1 hour. 3 ml of POTS were added to the solution and the hBN NPs were heat-treated at 80 ^{o}C for 120 under reflux. The functionalised nanoparticles in the resultant solution were separated using centrifugal equipment, shown in figure 3.2a. The functionalised hBN NPs were then washed several times with ethanol and water. The NPs were left overnight to dry in an oven at 100 ^{o}C. The dry functionalised hBN NPs were used to incorporate TPU coatings, mentioned as TPU-fBN coatings. The functional coatings are listed in table 3.2.



Figure 3.2: (a) The HERMILE labortechnik Z 200 A and (b) Sauter TI test stand with the Sauter HBA durometer.

The aluminium and stainless steel samples were roughened using the Guyson F1200 sandblaster system using Guyson 180-220 µm alumina particles and the metallic substrates were then washed with ethanol and deionized water thrice and dried using compressed air before the hydrophobic functionalisation. The samples were grafted by self-assembled monolayers of POTS using the chemical vapour deposition (CVD) method in a sealed vessel with 0.3 mL POTS at 180 °C for 3 hours. The functionalised

substrates are mentioned as Al-fSB/SS-fSB substrates. The functional surfaces are further described in table 3.1.

3.8 Surface characterisation

3.8.1 Scanning electron microscopy

An FEI Quanta 650 ESEM (environmental scanning electron microscope), shown in figure 3.3, was used to acquire microstructural images and morphological changes on the eroded coatings. The coatings were sprayed with a gold or platinum layer (~5 nm) to enhance imaging and reduce beam damage to the coating. Gold or platinum layers were sprayed using Polaron SC7640 vacuum sputter equipment. The sputtered coatings along with substrates were mounted using epoxy resin with studs placed on the sample stage. The SEM images were generated using a low-vacuum secondary electron (LFD) detector at a pressure of 75 kPa and a high voltage of 10 kV. The working distance was kept at 8 mm. Several HD images were captured to compare the observed materials at various comparable magnifications.

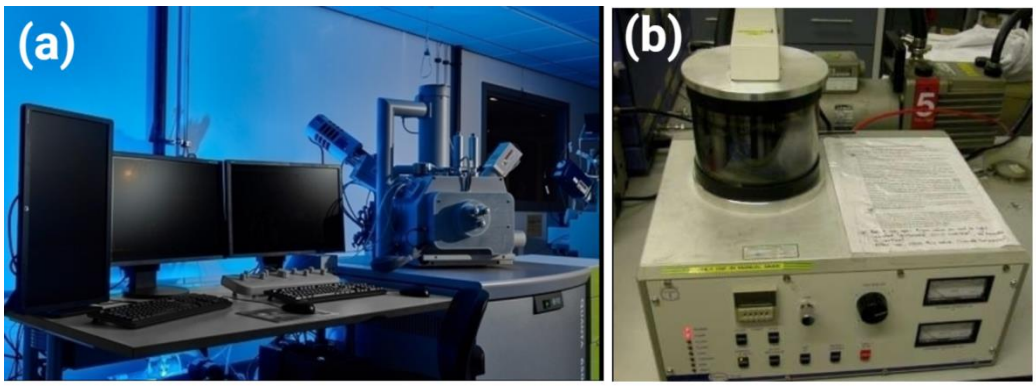


Figure 3.3: (a) The FEI Quanta 650 ESEM system and (b) Polaron SC7640 vacuum sputter equipment.

3.8.2 Surface roughness measurement and 3D profilometry

A Zeta-20 non-contact optical profiler, using a 50x magnification lens and at a working distance of 1 mm, was used to evaluate the surface roughness (R_a) and generate 3D profiles. The equipment and schematic diagram are shown in figure 3.4. The system is powered by ZDot™ technology, which simultaneously collects high-resolution 3D data over a continuously changing segmental distance from the surface. Therefore, the system generates 3D profiles by combining the optical data captured during the segmental steps. The surface profile data collected by the system was also extracted and were recreated via Matlab to generate further images to indicate true morphological changes on the surface.

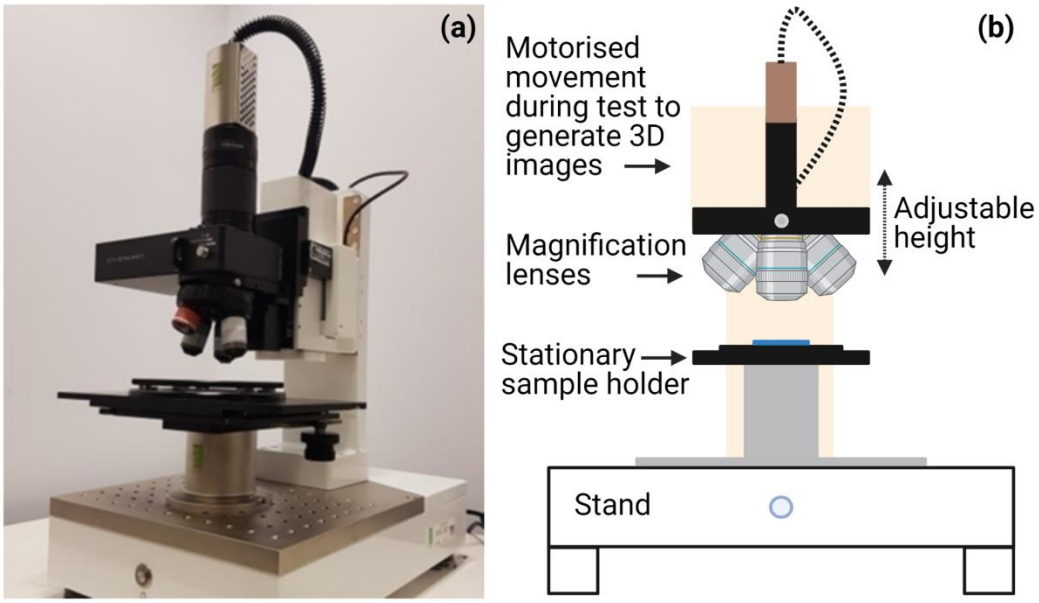


Figure 3.4: (a) A Zeta-20 non-contact optical profiler and (b) schematic diagram of the same equipment.

The roughness values reported were the average of a minimum of 30 measurements, and R_a was measured over a line stretching across the observed surface. An area of 2.5 x 3.5 mm was observed with each reading. The surface examination was carried out in a dark

room to mitigate any influence of additional unwanted illuminance on the surface. The detailed account of surface roughness measured on all the examined surfaces are provided in Appendix A.

3.8.3 Thickness measurement

The coating thickness was measured using Mahr GmBH Marcator 1075R digital indicator. The indicator is capable of measuring one micrometre to 20 millimetre thick coatings. For developed coatings, the substrates were measured before and after the coatings were applied. The difference in the results is the coating thickness and the average coating thickness is around 400 microns.

3.9 Evaluation of hydrophobicity

Water contact angles (WCAs) were measured using FTÅ200 goniometer, shown in figure 3.5 and the sessile drop technique was used to process the signals and generate images. The goniometer has a dedicated syringe attached to a motorised controller and the volume capacity and the type of syringe were pre-specified in the software before the analysis. The dispensing of water was controlled by the motorised moment and a 5 µl water droplet was analysed. The sessile drop technique was employed for the analysis of WCAs. The system was kept at room temperature conditions and the temperature was monitored for the consistency and repeatability of results. In this project, the same equipment was used to measure static and dynamic WCAs.

In static-type measurements, a control volume of de-ionised water was dispensed and the image was generated using the goniometer. Using the sessile drop technique, water contact angle measurements was recorded. In dynamic-type measurements, a control volume of de-ionised water was dispensed and the tip of the syringe was immersed in the

water droplet. Software analysis was changed to dispense in drop method (a type of sessile drop technique).

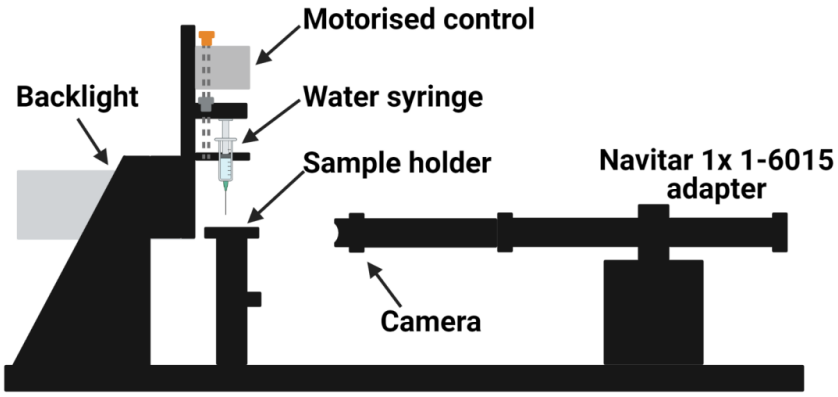


Figure 3.5: The FTÅ200 goniometer.

There are two types of dynamic type measurements i.e. advancing water contact angles and receding water contact angles. The difference between advancing and receding water contact angles is called water contact hysteresis (CAH). The rate of water dispensation/retraction was set at 1 μl/s and it was ensured that there were no air bubbles in the syringe. For advancing water contact angles, the angle of the water droplet towards the surface (wetting) was measured in iterations with respect to the changing base area (wet surface area). Similarly, for receding water contact angles, the angle of the water shearing (de-wetting) was measured in iterations with respect to the changing base area. Once the data were stored, the dynamic WCAs were only recorded when the base area was changing periodically and the CAH was calculated after the dynamic WCAs were measured.

In-situ water condensation observation

In-situ water condensation observation was carried in an FEI Quanta 650 ESEM (environmental scanning electron microscope). The system has the capability to adjust

water vapour pressure within the test chamber to simulate high-humidity conditions. The in-situ water condensation in this work was carried at 97%-100% relative humidity and the sample was examined using a gaseous secondary electron detector (GSED) detector at a chamber pressure of 0.3-0.7 kPa. It is imperative to mention that the coatings were not sputtered with gold or platinum layers for these tests as it may alter the surface characteristics of the surface, such as surface energy or wettability. The samples were exposed to high-humidity conditions for a certain period of time and the water vapours were allowed to condense on the surface. The HD SEM images were captured once a certain microstructural water condensation was achieved.

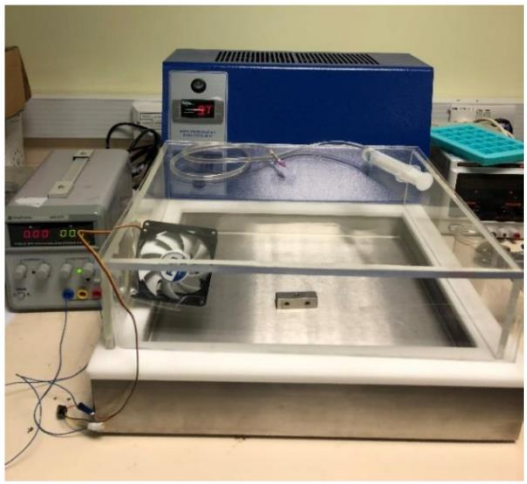


Figure 3.6: The Peltier cooling plate used for the majority of the anti-icing tests.

3.10 Anti-icing methods

All the anti-icing tests were conducted in a custom-built chamber located on RZ Medizintechnik GmbH Peltier cooling plate, shown in figure 3.6. The temperature around the testing area was monitored using an open K-type thermocouple which was placed near the samples during the tests. In all the tests, a fan, circulating the airflow at ~3.8 m/s (or ~32 CFM), was operational to ensure temperature consistency in the chamber.

3.10.1 Water droplet freezing delay test

The ambient temperature was set at -11 ^{o}C for water droplet freezing delays tests. The surface temperature was monitored using a high-temperature type K surface probe and maintained at -10 ^{o}C. The measurement method is described in detail elsewhere [132] and is depicted in figure 3.7. A controlled volume, 5 µl, was dispensed using a syringe pump on ten different spots of the samples and an average of the freezing delays was calculated.

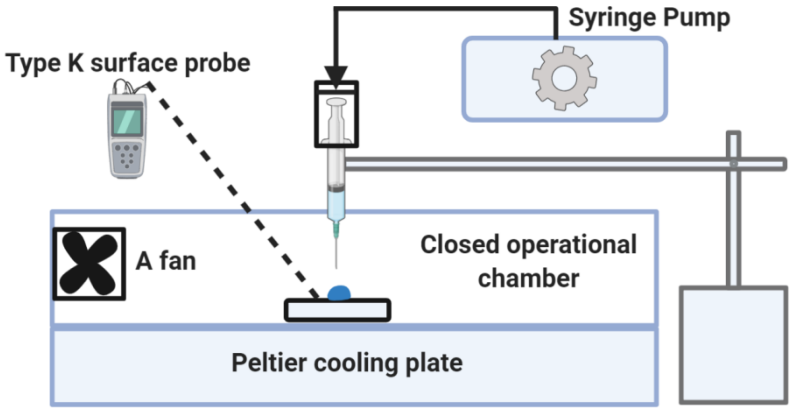


Figure 3.7: The water droplet icing delay test setup (created using biorender.com).

3.10.2 Static anti-icing tests

The samples were placed at 45^{o} angle against a metal stand and facing nebulized humid vapours. The nebulized humid vapours were generated using Omron Ultrasonic Nebulizer NE-U17. A total of 20 ± 2 ml of humid vapours were fed into the system to encourage condensation/frosting and simulate stormy icing conditions, as shown in figure 3.8. The water vapours were maintained throughout the tests and the volume was monitored. The surface temperature of -10 ^{o}C was maintained throughout the tests (and measured through an open K-type thermocouple). The test duration was one hour and the weight of frost accumulated was measured. Each test was repeated three times and an average was calculated. The surface was pictured via a high definition camera thrice

during the ice accumulation process to understand the ice nucleation over the different surfaces.

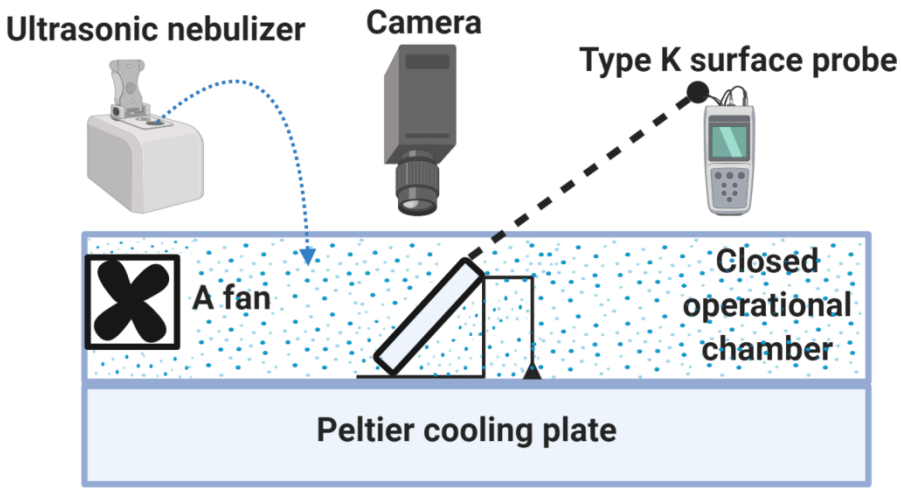


Figure 3.8: A depiction of static anti-icing test setup (created using biorender.com).

3.10.3 Dynamic anti-icing tests

The dynamic anti-icing tests employ a similar setup to that of static anti-icing tests, but instead of the stationary stand, the setup hosts a dynamic rotor, shown in figure 3.9a. The custom-built metal rotor with 6 seats for samples was used for rotary tests, shown in figure 3.9b. The samples were fastened by means of a screw and the rotor was spun at 30 rpm in similar humid conditions as static anti-icing tests. To ensure repeatability and to expose the coated surface only, the backside or metallic side of the samples were covered by peel-able tape and the tape was peeled after the tests. The ice accumulation was measured after an hour of test and an average of three tests was calculated. The samples were also pictured after the tests and a sample test is visualised in Appendix A.

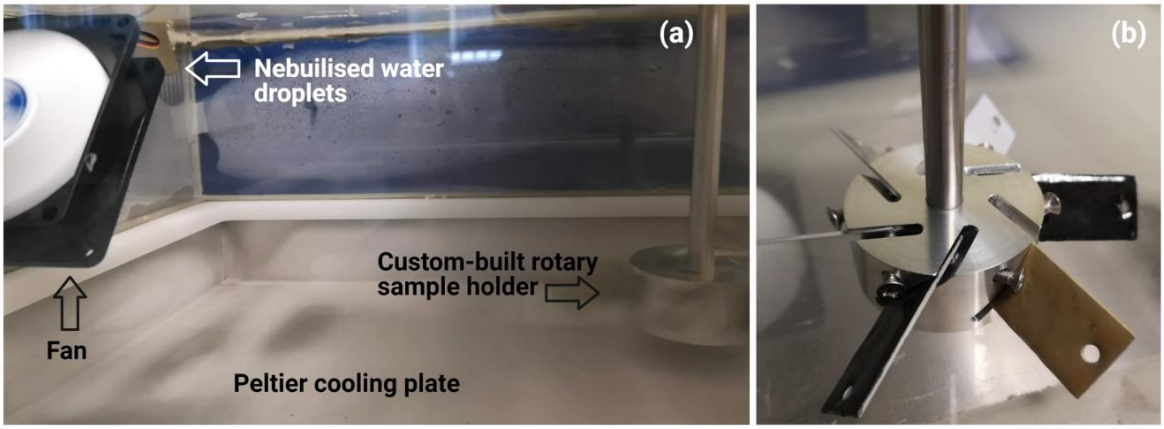


Figure 3.9: (a) The setup of dynamic anti-icing tests and (b) the custom-built 6-seater metal rotor.

3.10.4 Anti-icing test after an overnight water immersion

The technique was deployed to understand the retention and influence of liquid-infused coatings on anti-icing performance. The technique involved submerging the samples in distilled water for 24 hours and the static and dynamic anti-icing tests were repeated on liquid-infused coatings. Furthermore, anti-icing tests were again repeated on water-immersed coatings after 24 hours of first testing to ascertain the obtained results. In total, there were two tests conducted in 48 hours. The tests were carried along the dry coatings to compare the liquid-infused coatings in similar environment and conditions.

3.10.5 In-situ icing and de-icing observation

An FEI Quanta 650 ESEM (environmental scanning electron microscope) with controlled humidity and temperature was used to perform in-situ icing observations. In the in-situ icing study, the chamber humidity was raised above 90% RH to wet the surface and the temperature was dropped to sub-zero temperature (down to -5 ^{o}C) using a Peltier cooling plate to allow the ice growth over the surface. The water-cooled Peltier cooling stage is shown in figure 3.10. Once the ice is grown on the surface, the ice was carefully retracted

via a controlled change in temperature and humidity. The ice retracting patterns were recorded. The system is capable of generating micro-level SEM images for the icing study, and the ice retracting behaviour on the surface was analysed.

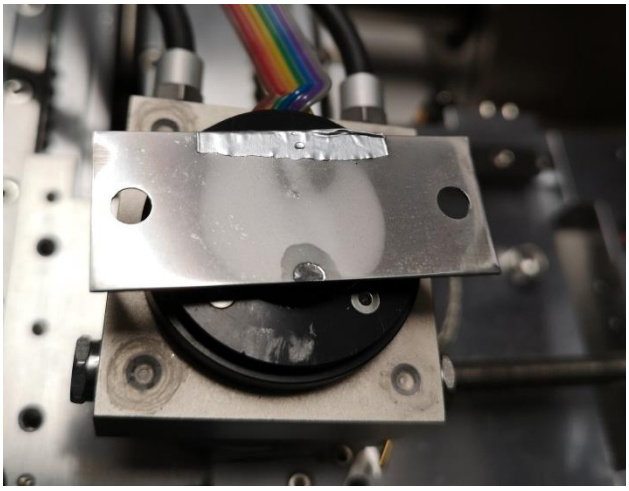


Figure 3.10: The Peltier cooling plate used in the in-situ icing observations.

3.11 De-icing methods

3.11.1 Centrifugal method (CAT)

The centrifugal de-icing tests were conducted in two separate equipment i.e. environmental chamber to mimic environmental icing conditions and centrifuge systems to provide centrifugal shear force to remove the ice formed. Design Environmental ALPHA 1550-40H equipment was used to mimic icing conditions, shown in figure 3.11. All the sample tests were conducted at a temperature of -10 ^{o}C.

The centrifuge system consists of a stainless steel (SS) cylindrical drum of depth 300 mm and diameter 500 mm, shown in figure 3.12c. The carbon-reinforced fibre spinning arm, of thickness 3 mm, width 20 mm and radius of 192.5 mm is attached to a MOOG G403-2053A servo motor. The servo motor can attain a rotational speed of 4500 rad/min and

was accelerated and decelerated at 33 rad/min/sec and 200 rad/min/sec, respectively. The ice was grown over the sample by means of silicon moulds having 3.1 ml of de-ionised water. The moulds were then flipped upside down and kept against gravity for overnight freezing at -10 ^{o}C, depicted in figure 3.12a.



Figure 3.11: The design environmental chamber.

Once the ice was formed, the sample was mounted on the spinning arm and a counter-weight mimicking similar weight (sample, substrate, water, and mould) was attached, depicted in figure 3.12b. The counterweight was pivotal to avoid vibrational forces that could be generated due to the unbalanced centrifugal forces. Together with the spinning arm, an accelerometer was attached to measure the acceleration of the spinning arm at the time of detachment of an ice block. A delicate approach was employed when samples are

being mounted to avoid introducing a mechanical history in the formed ice. Gloves were worn so that heat exchange between sample and human heat was minimal and sufficient time is allocated (5-6 minutes) once the chamber was closed after mounting of sample to attain constant and uniform temperature for testing.

The centrifugal shearing force *F* (N) is determined from Eq. (3.1):

$$F = mr\omega^2 \tag{3.1}$$

where ω (rad/s) is the rotational speed at the point of ice removal, *r* (m) is the rotor length, and *m* (kg) is the mass of ice. The ice (shear) adhesion strength τ_{ice} can then be calculated as

$$\tau_{ice} = {}^{F}/_{A} \tag{3.2}$$

where *A* (m^2) is the substrate/ice contact area.

The centrifugal method to evaluate the ice adhesion strength in this work has previously been applied by many researchers [10, 67, 152] and a recent publication indicated its compatibility with the other widely used methods such as the horizontal force transducer method [31]. However, for a dynamic test such as the centrifugal method, there is always a risk of inherent motion or shake during the sample mounting procedures [176], and it was rectified in this study by developing multiple rods that could be directly used for ice accretion on the samples and then mounted on the testing rig with minimal impact on the ice bonding.

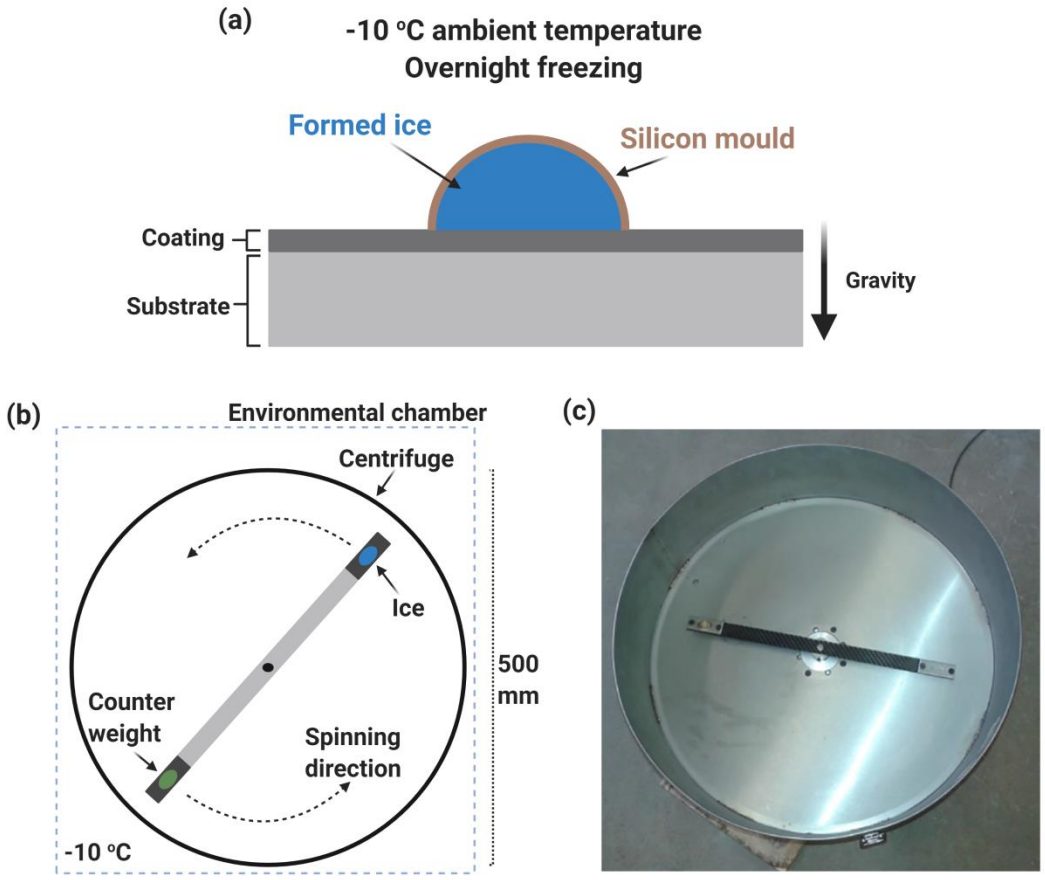


Figure 3.12: (a) Ice formation on a sample surface, (b) the details of the centrifugal testing method, and (c) the actual picture of the centrifuge (adapted from reference [177]) (figure created using biorender.com).

3.11.2 Horizontal push method (HPM)

Ice shear strength was measured using a horizontal push method, in collaboration with the University of British Columbia, in a custom-built setup at the surface temperature of -10 ^{o}C, shown in figure 3.13. More details on the custom-built setup are detailed were reported previously [71].

A square-shaped mould of volume 5.48 cm^3 was used to formed ice on a closed-loop water-cooled Peltier plate. The height of the force probe in HPM was kept at a minimal distance from the surface to eliminate the discrepancies in the adhesion measurements. The adhesion strength was measured employing a digital force gauge, pushed at 100 µm/s and the force gauge had a capacity of measuring up to 500 N at a resolution of 0.1N.

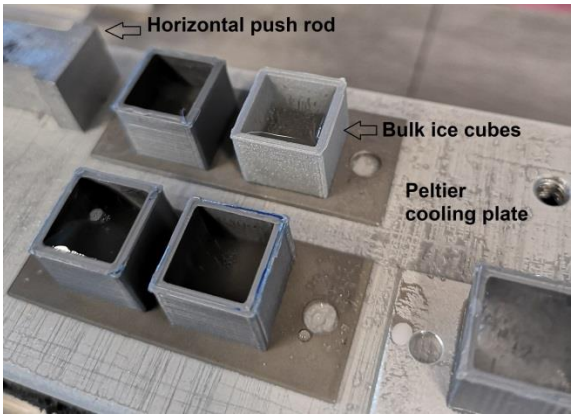


Figure 3.13: A focused image of the horizontal push method, together with ice samples.

3.11.3 Normal tensile (NTM)

Unlike the centrifugal and push methods which are based on shear strength (Mode II fracture), the tensile de-icing method measured the normal adhesion strength (Mode I fracture). However, due to the application of transverse motion on one side of the bulk ice, the shear-based de-icing methods often produce a combination of Mode I and Mode II fracture [151, 178]. The normal adhesion force on the tensile method was measured via a custom-made ice mould in a lab, based at the University of British Columbia and the equipment is visualised in figure 3.14a. The system was connected to a force gauge and was pulled using the threads connected on the opposite ends of the ice mould, shown in figure 3.14b.

The shape and geometry of the ice mould were optimised to achieve a uniform stress distribution across the contact area. More details on the tensile method and its construction were reported previously [179]. A digital force gauge of a similar configuration as that of HPM was used. The surface temperature was maintained at -10 ^{o}C during the ice formation and throughout the testing duration.

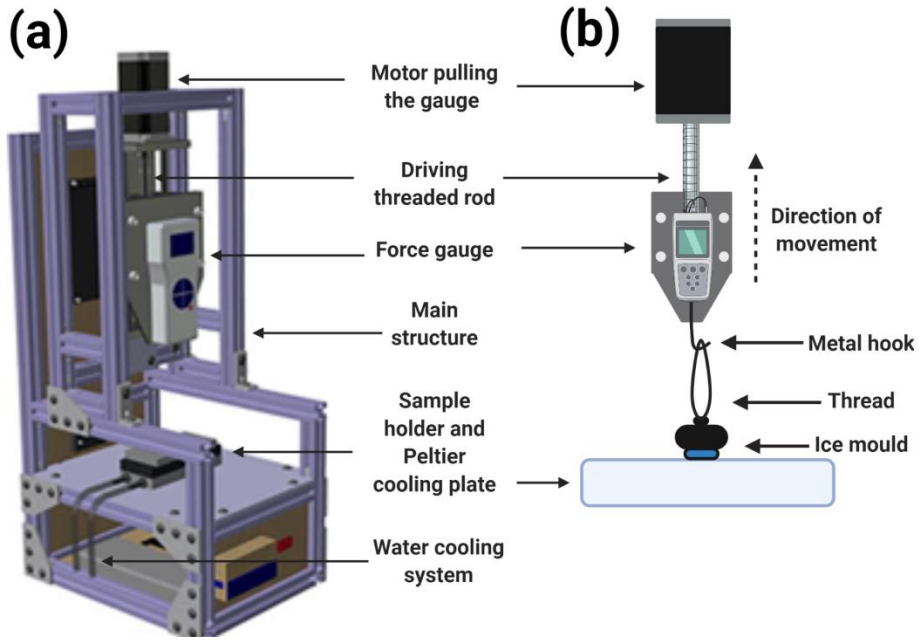


Figure 3.14: (a) the normal tensile de-icing method (adapted from reference [179]) and (b) the schematic principle of the tensile method.

3.11.4 Electro-thermal de-icing evaluation

For electro-thermal de-icing tests, the bulk ice was formed over the surface using silicone moulds against gravity and the ice was formed overnight. The electro-thermal de-icing evaluation was carried out by the introduction of heating at ice/surface interfaces, and no external mechanical forces were introduced during the ice melting process and the ice was allowed to detach under the gravitational pull, as depicted in figure 3.15. It is important to mention that the samples were held perpendicularly and a shear force could

be generated at the ice/solid interfaces under the influence of gravity. Thus, the electro-thermal de-icing method is different from other de-icing methods used in this study which mainly utilise external mechanical forces to de-ice. The electro-thermal de-icing was conducted in a custom-built de-icing rig, constituting a sandwiched heating element that was connected to a 12 V, 0.3 A power source to heat the sample. The samples were mounted on the rig and were allowed to cool down to -10 ^{o}C. The test was initiated at a time when the surface temperature reached -10 ^{o}C. The de-icing method is described in detail in previous work [180]. The temperature was monitored using a rod thermostat which was inserted in the rig, located between the heating element and the sample. In all the tests, a fan was operational to ensure temperature consistency in the chamber.

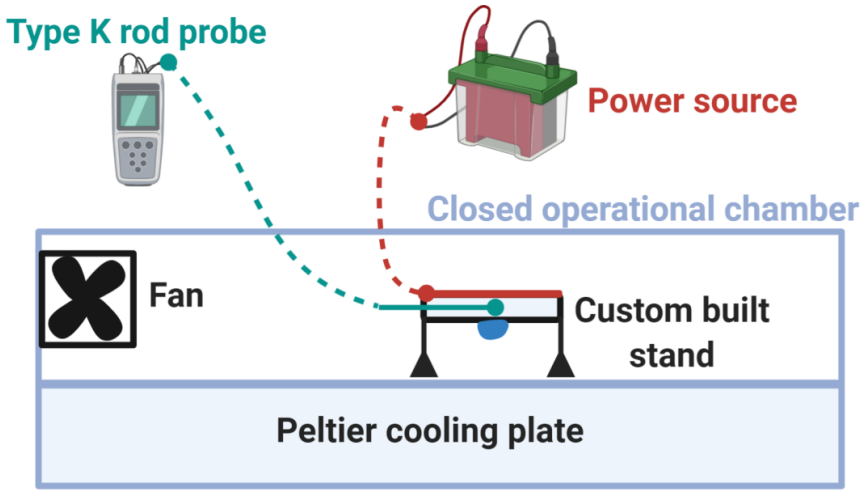


Figure 3.15: The electro-thermal de-icing test setup.

3.12 Surface durability

3.12.1 Shore hardness tests

Shore hardness was measured using a SAUTER durometer having Shore hardness A and D scales, shown in figure 3.2b. The durometer was attached to SAUTER test stands TI-

AO and TI-D for Shore hardness A and D scales, respectively. The hardness reported was an average penetration (Shore) value based on 10 separate measurement.

3.12.2 Water impinging erosion tests (WIETs)

To evaluate the coating durability, erosion tests from the impingement of silicon carbide aqueous suspension were carried out. The silicon carbide suspension was prepared using 1 wt% silicon carbide microparticles and 0.1 wt% of Triton X-100. The suspension was then magnetically stirred for 4 hours. During the impinging test, the suspension was pressurized through a PNR ultrasonic atomiser nozzle (MAD 0331 B1BB) using compressed gas and the micro-droplets impinged onto the coating specimen, as depicted in figure 3.16. The system was maintained at a liquid flow rate of 1.2 mL/s, a distance between the nozzle and the specimen of 4 cm, and a duration of 90 minutes. The surface morphology, surface roughness and ice adhesion strength of the coatings were measured before and after the erosion tests.

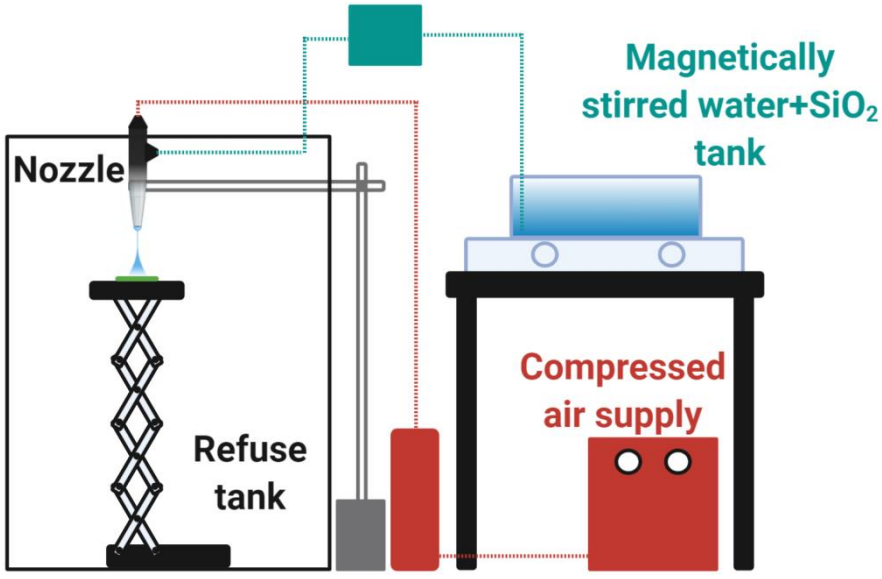


Figure 3.16: A depiction of water impinging erosion test setup (created using biorender.com).

Chapter 4

Variations of response with surface characteristics in icephobicity evaluation methods

4.1 Introduction

Multiple aspects of ice-related problems were widely studied but ice adhesion (de-icing) or a delay in ice formation (anti-icing) remain the primary indicators in passive icephobic studies. Over the last 90 years, dissimilar ice forming techniques and different de-icing and anti-icing evaluation methods were used to evaluate the icephobic performance. The majority of de-icing tests consist of mechanical tests (such as push method) [140-142], shear methods (such as shear lap joint test) [143-145], centrifuge rotating tests [10, 146, 147], and tensile methods [148-150]. The anti-icing tests consist of water droplet freezing delays [181, 182] and anti-frost performance [83, 183]. Despite the passive icephobicity studies existing for decades, there is no standardised method to measure icephobic performance. The lack of a standardised icephobicity evaluation method means that each research group publishes their own measured data and the comparability of data is difficult due to the variation in icing sample preparation, measured magnitude, applied force and the interfacial contact areas. Interlaboratory examinations have been initiated in the last few years [31, 184], and reviews on existing evaluation techniques are reported [1, 151, 185]. However, the influence of surface characteristics has not been studied.

Thus, there is a need to initially examine the variation in response of popular icephobicity evaluation methods and subsequently, understand the role of surface characteristics and interfacial mechanisms for both icephobic strategies. These results can prompt further understanding on the influence of surface characteristics, which may involve a systematic alteration in surface characteristics.

In this chapter, an interlaboratory comparative study of three de-icing methods was conducted and the results were compared with anti-icing test methods. The influence of surface characteristics in icephobicity evaluation methods was investigated. Firstly, ice adhesion strength was measured with three established de-icing methods, ensuring the same interfacial contact area (3.1 cm^2) for all the tests. Secondly, the effect of heat conduction on ice detachment was examined via a hybrid de-icing method, without introducing an external mechanical force and experiencing the gravitational pull. Thirdly, anti-icing capabilities were evaluated using water droplet freezing delays and static ice accumulation studies. The preliminary water droplet freezing delay and ice accumulation results were plotted alongside the ice adhesion results measured using the CAT method to observe if the surface characteristics have a similar quantifiable impact on anti-icing evaluation methods as compared to those of the de-icing methods. For the first time, the de-icing and anti-icing results using established testing methods were compared and the variation in response of each method to surface roughness and/or wettability was investigated. The methods were also debated in terms of fracture mechanics at ice/solid interfaces, thermodynamics, and the influence of surface wettability. The conclusions could help to offer crucial pre-selection information of popular icephobicity evaluation methods and their variation in response with surface characteristics.

4.2 Response variation with surface characteristics in different de-icing methods

4.2.1 Comparative analysis of de-icing methods

The ice adhesion measurements acquired using the HPM, the CAT, and the NTM are illustrated in figure 4.1a, 4.1b, and 4.1c, respectively. The results obtained on the CAT and the HPM methods suggest a linear relationship of ice adhesion strength with surface roughness. All the methods were sensitive to surface roughness, but the CAT method showed greater sensitivity. For example, on aluminium substrates, ~12 fold increase in ice adhesion was observed from Al-SB to Al-S3 samples using the CAT method, whereas, ~2 fold increase was observed on the HPM method. The metallic samples examined in this chapter were roughened, as-received, and smoothed substrates and are detailed in table 3.1. The microscopically rough surface not only provides large cavities for possible ice anchoring points and substantial mechanical interlocking but also extends the contact area of the ice, thus the true interfacial contact area is enlarged. Similarly, the smoothening of surfaces reduces the number of cavities and subsequently, the overall true interfacial area is shrunk and the mechanical interlocking is minimised. Thus, the interfacial area and mechanical interlocking of ice could be used to explain the higher ice adhesion on the microscopically rough surface.

The CAT and the NTM demonstrated a greater sensitivity among the studied samples. For example, the dotted-square in figure 4.1a, 4.1b, and 4.1c show that the polymeric nanocomposite samples indicated a higher ice adhesion as compared to the metallic samples at similar surface roughness using the CAT and NTM methods. The composition of polymeric nanocomposite coatings examined in this chapter is detailed in table 3.2. A ~2 fold increase in magnitude was observed between the polymeric and metallic samples

on both the CAT and NTM methods, compared to ~1.2 fold increase using the HPM method. The adhesive ice failure was reported on the majority of the tested samples in all three de-icing methods, whereas the ice on rougher surfaces, especially on sandblasted samples, might have been detached cohesively. Thus, the definitive comparisons drawn in this section, in terms of ice detachment magnitudes, were only based on the adhesion failures.

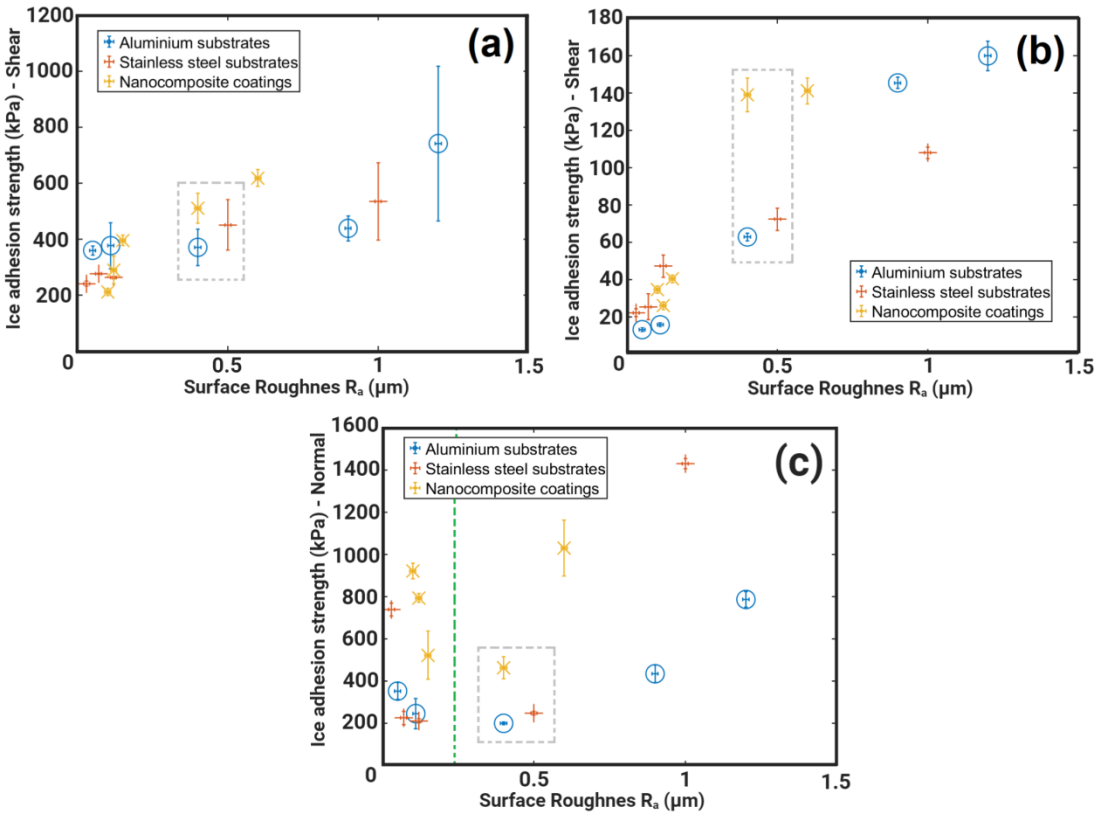


Figure 4.1: Ice adhesion strength vs. surface roughness using (a) the horizontal push method, (b) the centrifugal method, and (c) the tensile method. The dotted square indicates samples with similar surface roughness and the dotted line indicates a change (an increase) in ice adhesion strengths below a certain surface roughness range.

Some observations can be drawn on the ice adhesion results measured with the NTM setup. Firstly, the magnitude of ice adhesion measured on the NTM setup is in the range of 200-1500 kPa, as compared to 200-800 kPa and 10-160 kPa using the HPM and CAT methods, respectively. The comparison of the ice adhesion strength does not necessarily suggest a direct relationship between the studied de-icing methods, but the differences in magnitude measured by different de-icing methods could be reflected in figure 4.1. A direct comparison of ice adhesion magnitude may not be suitable as the NTM measures the ice fracture in Mode I fracture (tensile detachment), whereas the shear methods detach the ice in a combination of Mode I and Mode II fracture (shear and tensile detachment).

Secondly, ice adhesion measured using the NTM method demonstrated a non-linear relationship with surface roughness, rather a non-monotonic curvilinear relationship. Surprisingly, a higher ice adhesion strength was recorded on the smoother samples using the NTM method, whereas, the ice adhesion strength on similar samples decreased with the lower surface roughness using the CAT and HPM methods. This observation suggests that there are other influencing factors in the NTM methods, and the results are further debated in terms of surface wettability in the next section.

4.2.2 Correlation of contact angle hysteresis on ice adhesion

The previous section indicated a strong sensitivity of the de-icing methods on surface roughness and the lower surface roughness resulted in reduced ice adhesion strength on most samples. However, a higher ice adhesion was obtained on the smoothed samples in the NTM test. To understand ice adhesion behaviour with the NTM method, the ice adhesion results were plotted in a single figure with contact angle hysteresis (CAH)

values as shown in figures 4.2a, 4.2b and 4.2c. Two conclusions can be drawn from figure 4.2. Firstly, the CAH demonstrated inverse proportionality with ice adhesion strength on the SS samples. Similar correlations of ice adhesion strength with CAH were also observed on the aluminium samples and TPU-BN coatings, and the figures are given in Appendix A. It is imperative to mention that the ice adhesion, obtained using the CAT and the NTM methods did not correlate with CAH values completely. The CAHs correlated with surface roughness (R_a) below 0.5 µm on the studied surfaces and the receding water contact angles also followed a similar trend, shown in Appendix A. The correlation of CAHs on ice adhesion in a certain range suggests a dominant role of surface wettability, whereas the mechanical interlocking forces may add up on surfaces roughness above 0.5 µm due to a higher interfacial contact with the surface.

The surface roughness (R_a) of <0.5 µm is not a rigid value to evaluate the relationship of CAHs with surface roughness as the data is limited to reach a conclusion; it is rather an indication of a probable change in ice fracture mechanics. Bishoy et al. [186] indicated a modest dependence of ice adhesion strength in the surface roughness (RMS) at <0.5 µm and reported a several-fold increase in adhesion strength with a larger surface roughness (1-5 µm). This critical surface roughness (<0.5 µm) might be linked to the detailed microstructures. Similar observations were also reported in other relevant works [70, 187]. Thus, the ice adhesion obtained on a surface with the roughness below the critical range could be explained by CAHs, whereas the rapid increase in ice adhesion beyond the critical range may be attributed to the mechanical forces generated in the enhanced interfacial contact area.

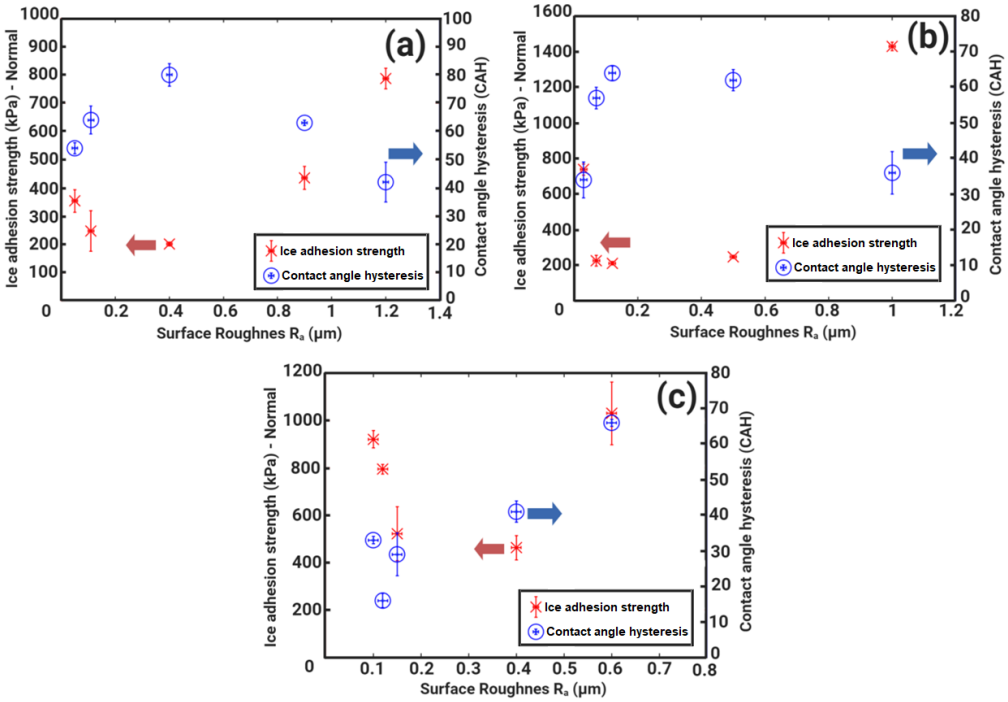


Figure 4.2: Ice adhesion strength and CAH vs. surface roughness on the (a) aluminium substrates, (b) SS substrates, and (c) TPU-BN coatings obtained using the NTM method. The red arrows indicate the ice adhesion strength data points and the blue arrows indicate the contact angle hysteresis data points.

Secondly, the ice adhesion correlated 'inversely' with CAHs on tensile ice adhesion strength, contrary to many studies that suggest a direct relationship using shear ice adhesion methods [188, 189]. However, the tensile ice adhesion demonstrated a partial correlation with receding water contact angles over a certain range of surface roughness, with an exception of sandblasted samples, as shown in Appendix A. It is imperative to mention that the ice adhesion increased systemically with an increase of surface roughness in the shear-based de-icing methods, whereas in the normal-based tensile method, the ice adhesion decreased with an increase in surface roughness at first and then the adhesion strength increased over a certain range of higher surface roughness. The

roughening of surfaces may result in a change of spatial parameter (e.g. auto-correlation length), which links to the spacing of surface features. Davis et al. [190] reported similar findings on an air-pressurised tensile system and indicated that the ice adhesion correlated directly with the spatial parameter, rather than a partial correlation with the arithmetic roughness.

The relationship of tensile ice adhesion with CAHs could be further explained in terms of the interfacial contact area and the subsequent change in surface wettability. Typically, the water contact angles are an indicator of surface tension exerted by the substrate and an enhancement of the angles indicate a decreased chemical affinity with the substrate (considering the polar component only) [53, 154]. Furthermore, the work required breaking the ice interface or work of adhesion on a tensile system is the product of the interfacial contact area and surface free energy [185]. Additionally, the CAHs are an indicative measurement for surface free energy, and Gao et al. [191] explained CAHs from the perspective of the kinematics of a metastable droplet. They reported the CAHs values as a reflection of the activation energy and the CAHs can be quantitatively expressed in terms of changes in interfacial free energy. However, this assumption is only valid for liquids on a perfectly smooth surface and may differ from a frozen liquid as a solid adhesive. Thus, the smoothing of samples may alter the probability and/or intensity of surface wetting, which are heavily influenced by the surface energy. The relationship between the $F(x)$ (force required to break an ice/surface interface) and the work of adhesion W_a (the practical work calculated based on surface wettability) is not straightforward but they are intrinsically linked to one another [192].

4.2.3 Ice adhesion strength of POTS coated surfaces

The idea of measuring ice adhesion on samples having similar surface roughness but varying surface wettability was explored to understand the influence of the POTS coated surfaces on the studied de-icing methods. Figure 4.3a shows the ice adhesion measured on the aluminium samples before and after the hydrophobic-functionalisation. An increase in CAHs after the functionalisation of the metallic surfaces could be attributed to a higher interfacial contact and the surfaces are expected to be wetted in a Wenzel (or mixed with Cassie-Baxter) regime [193]. The results obtained on the aluminium samples indicate a reduction in ice adhesion across the de-icing methods. The ice adhesion obtained on the SS samples and TPU-BN coatings is summarised in figure 4.3b and 4.3c, respectively. The TPU-BN coatings were incorporated with either pristine hBNs particles or POTS functionalised hBNs particles for comparison purposes.

The results confirmed that the NTM method demonstrated a greater sensitivity to the surface functionalisation as compared to other de-icing methods and indicated a significant reduction in ice adhesion strength after surface functionalisation. A dominant role of surface wettability (CAHs) on normal ice adhesion strength could be reflected in figure 4.3. The HPM method was relatively insensitive to the change to the POTS coated surfaces and surprisingly, the ice adhesion increased after the surface functionalisation of hBNs nanoparticles incorporated in TPU-5 coatings. The tests indicated a clear dominance of mechanical forces over the influence of wetting behaviours in the cases of the HPM and the CAT methods, and these methods might have only evaluated the mechanical adhesion of ice. The dominancy of mechanical forces might come from the stress concentrations that could have been generated due to the uneven distribution of

shear and peeling forces as depicted in figure 4.4a. This may form the rationale behind the significant reduction in ice adhesion after hydrophobic functionalisation using the NTM method (as the mechanical interlocking of ice would have much less effect on perpendicular pull-up forces), whereas, the mechanical forces-dominant systems, such as the CAT and the HPM methods, were less sensitive to wettability.

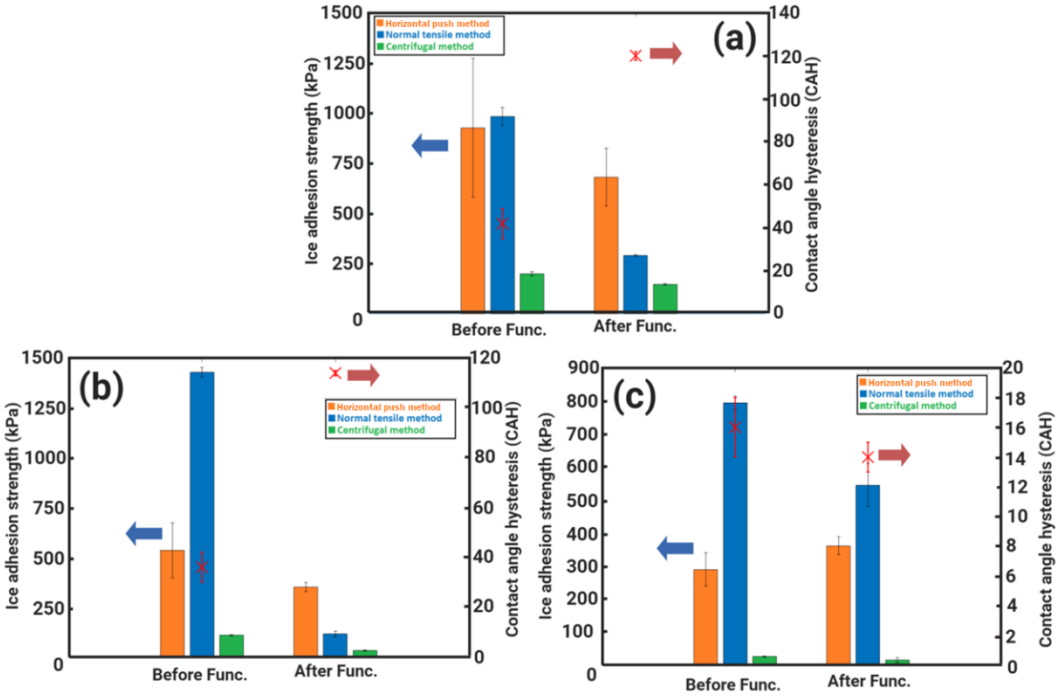


Figure 4.3: Ice adhesion before and after the surface functionalisation of (a) the SS-SB samples (b) Al-SB samples, and (c) TPU-5 coatings (Before Func.: incorporated with pristine hBNs, After Func.: incorporated with POTS functionalised hBNs). The red arrows indicate the contact angle hysteresis data points and the blue arrows indicate the ice adhesion strength data points.

4.2.4 Effect of heat conduction on ice detachment

Several researchers have also examined the use of active support in combination with a passive system to aid the de-icing process [194, 195]. The idea is also an active field of

research in aerospace and wind energy industries as the energy-saving alternatives to current energy-intensive de-icing methods. In this section, the studied samples, which demonstrated considerable sensitivity to surface roughness and/or wettability using the mechanical de-icing methods, were examined to understand the influence of heating potential at the ice/surface interfacial contact area under the gravitational pull, but without the influence of a detaching external mechanical shear/normal force. Theoretically, a shear force could be generated at the ice/surface interfaces by gravity as the sample was held perpendicularly to the surface. Preliminary tests were conducted to investigate if the surface characteristics of the samples have any impact on the duration of heating in ice melt tests. It is imperative to mention that the substrates' or coatings' thermal and electrical conductance might influence the test readings. The coating thickness in the case of the polymeric coatings may also produce a thermal gradient across the coating types. Thus, the tests were purely indicative and direct comparisons could not be drawn to compare the heating de-icing mechanism to passive de-icing methods.

Schaaf et al. [196] conducted various tensile ice adhesion measurements on samples having different surface roughness and the interfacial contact area was heated with an induction heating method. They indicated that the smoother surfaces needed a less debonding energy under a similar tension loading at a temperature of –6 ^{o}C. In this chapter, the constant heating potential was supplied at ice-surface interfaces via heat conduction through the heating plate, shown in figure 3.16 and ambient temperature was controlled throughout the tests. The heating potential was continued until the ice cube dropped under the influence of gravity and no external additional force was exerted on

the ice cube. The heating time (time to detach the ice cube), alongside ice adhesion measured on the centrifugal method, on the SS samples is shown in figure 4.4a. The results obtained on the aluminium samples and TPU-hBN coatings are summarised in figure 4.4b and 4.4c, respectively. These figures indicate a partial correlation of the heating time with surface roughness (R_a) below 0.5 µm. Furthermore, the time to detach the ice cube on all the studied samples was in the range of 530-700 seconds.

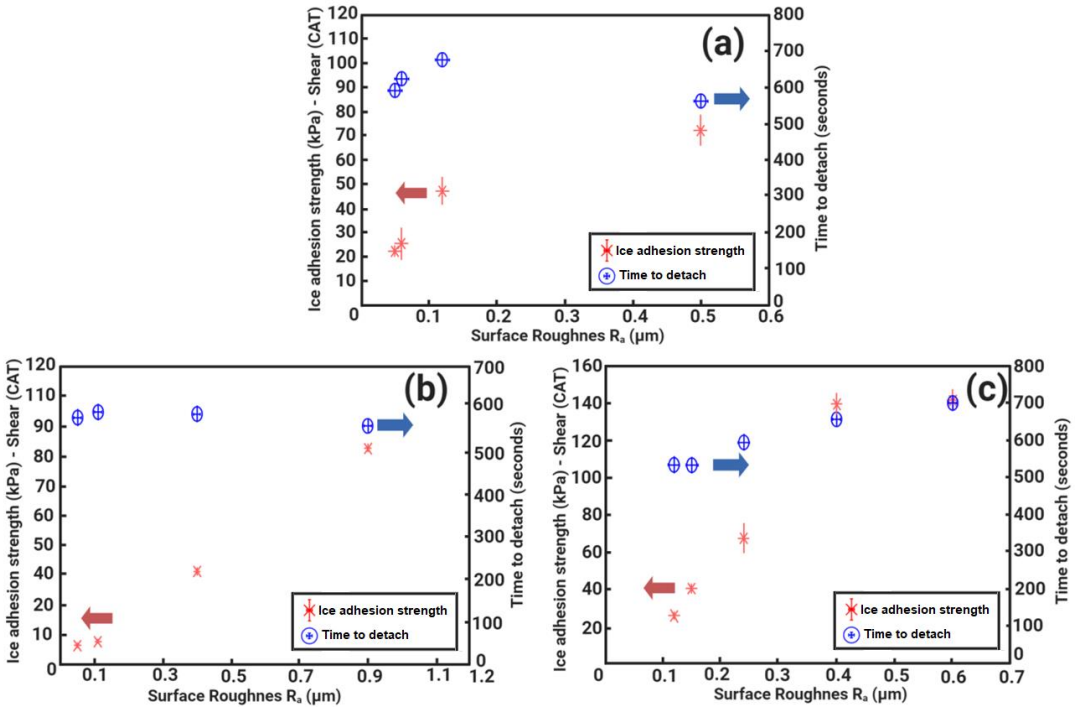


Figure 4.4: Ice heating melt tests on (a) the SS substrates, (b) the aluminium substrates, and (c) TPU-BN coatings. The red arrows indicate the ice adhesion strength data points and the blue arrows indicate the time to detach data points.

4.3 Response variation with surface characteristics in different anti-icing evaluation techniques

In this section, the anti-icing methods, droplet freezing delays and frost accumulations, were compared on all the studied samples and are plotted alongside the ice adhesion measured using the CAT method. The idea was to identify: (1) a correlation, but a direct comparison may not be suitable as the freezing mechanism and ice nucleation does not entirely impact the de-icing mechanisms; and (2) to evaluate the effect of surface characteristics on anti-icing examinations. Thus, the preliminary tests were conducted to observe if the surface characteristics, which demonstrated considerable variation in response in the de-icing methods, have a similar quantifiable impact on the anti-icing evaluation methods.

4.3.1 Water droplet freezing delays

The freezing mechanism of a water droplet on a cooled surface can be described in 5 steps: supercooling, nucleation, decalescence, freezing, and solidification/tempering of the ice structure [197]. Jung et al. [198] reported the start of nucleation occurring at gas/liquid interfaces, contrary to popular reference at liquid/solid interfaces. The crystallisation occurs in two stages: originating from the gas/liquid interfaces and leading to the liquid/solid interface, and then from the liquid/solid interfaces to the entirety of droplet. Thus, the solid/liquid interfaces could play a leading role, especially in terms of droplet/surface thermodynamics and the ice nucleation/crystallisation mechanisms.

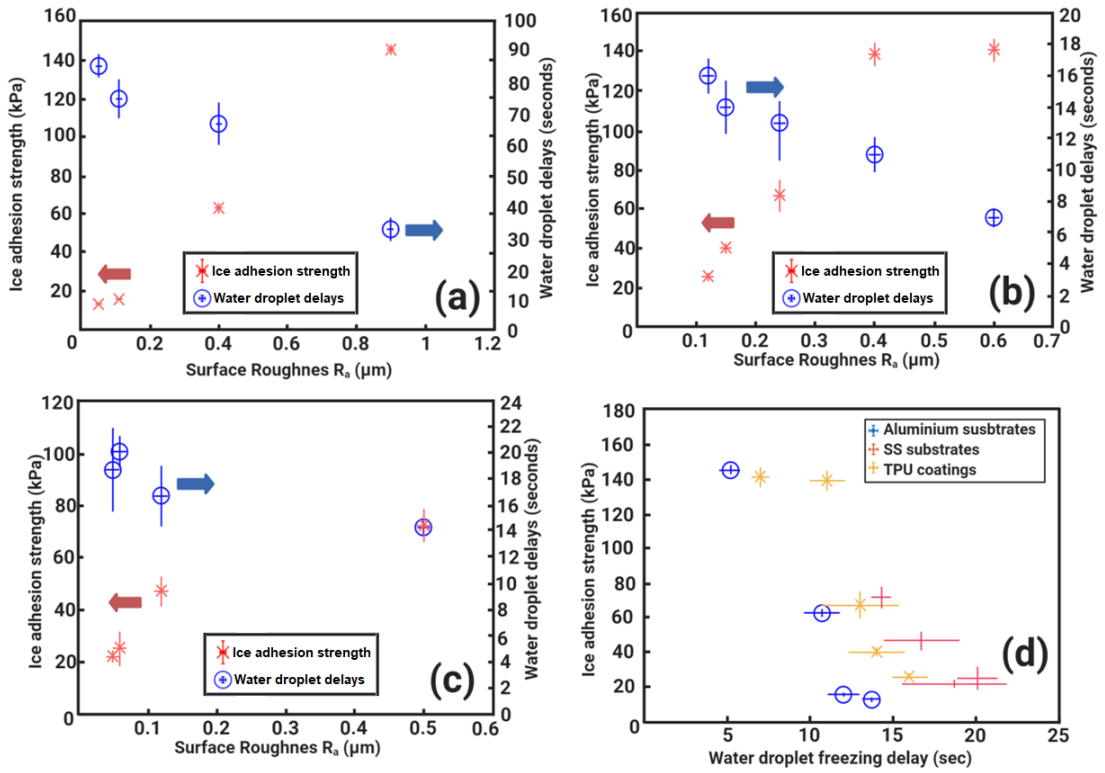


Figure 4.5: Droplet freezing delays tests on the (a) aluminium substrates, (b) TPU-BN coatings, and (c) stainless steel substrates. The red arrows indicate the ice adhesion strength data points and the blue arrows indicate the water droplet freezing data points. (d) The droplet freezing delays are plotted against the ice adhesion values, measured using the CAT method.

The water droplet icing delays measured on the aluminium samples are illustrated in figure 4.5a. The icing delays on the TPU-hBN coatings and SS samples are summarised in figure 4.5b and 4.5c, respectively. It is clear from the figures that the droplets took more time to freeze on the smoothened surfaces (metallic and polymeric surfaces alike). On average, a ~2 fold increase in freezing delays was observed on the smoothed metallic samples as compared to that on the as-received metallic samples. A similar increase in freezing delays was also observed on the TPU-hBN coatings. Generally, the surface

functionalisation on the metallic substrates and TPU-f5 coatings also yielded a ~2 fold increase on average in freezing delays as compared to that of the non-functionalised metallic substrates and TPU-5 coatings. The freezing delay results are listed in Appendix B. Thus, the application of low surface energy chemicals on the surfaces and the smoothening of the samples resulted in similar water droplet icing delays. Overall, the duration of freezing delays was nearly halved on the aluminium samples as compared to that of the SS samples and TPU-hBN coatings and the water droplet freezing delays demonstrated a direct correlation with ice adhesion, shown in figure 4.5d.

4.3.2 Frost accumulation

In this section, the static frost accumulation test was conducted on all studied samples to observe a correlation between the de-icing and anti-icing test methods. It is imperative to mention that a correlation among the icephobicity methods is purely indicative and a direct comparison could not be drawn as the methods use different techniques to evaluate the icephobic performance. The static frost accumulation results on the aluminium samples are plotted; together with the ice adhesion measured using the CAT method in figure 4.6a.

Firstly, the ice accumulations were insensitive to the variation in surface roughness under high humid conditions and frost of similar magnitude was accumulated on all the aluminium samples. A similar pattern of ice accumulation was also observed on the SS samples, shown in figure 4.6b. However, the accumulated frost varied in the case of the TPU-BN coatings. Overall, the frost accumulation slightly increased with an increase in surface roughness of the TPU-hBN coatings, however, no clear correlation with the ice adhesion was observed as shown in figure 4.6c.

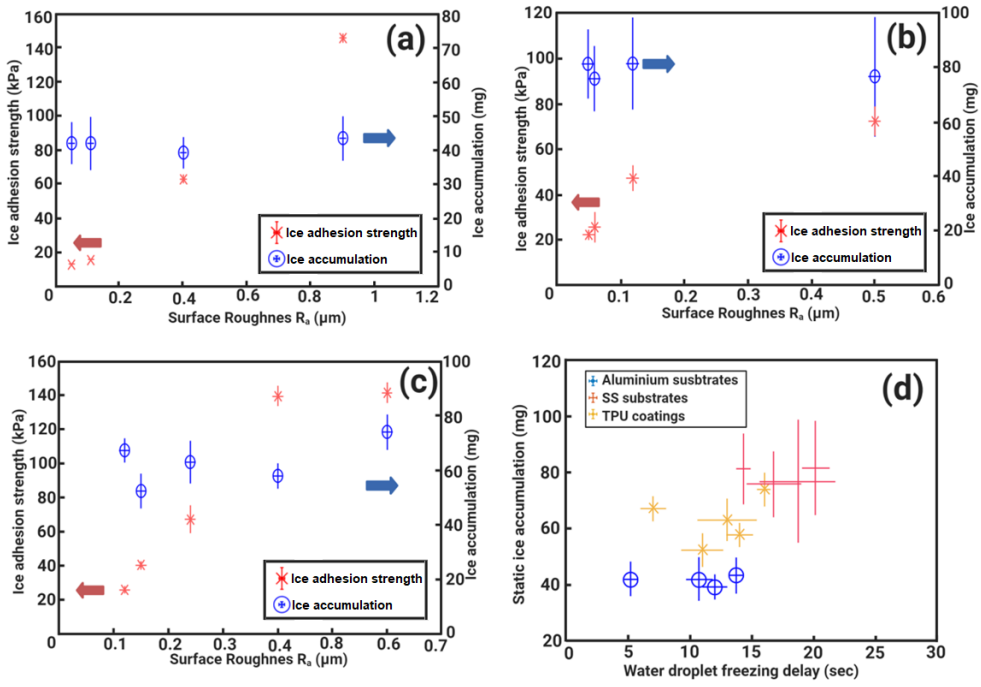


Figure 4.6: Static ice accumulation tests on the (a) aluminium samples, (b) stainless steel, and (c) TPU-BN coatings. The red arrows indicate the ice adhesion strength data points and the blue arrows indicate the ice accumulation data points. (d) The static ice accumulations are plotted against the water droplet delays.

Secondly, the SS samples and TPU-hBN coatings accumulated nearly ~2-fold more frost on average as compared to the aluminium samples. Thus, the ice accumulations could be dependent on individual material chemistry as the magnitude of frost accumulation changed with a change in material. A similar increase in water droplet freezing time was also observed, shown in figure 4.6d, highlighting the possible effect of surface chemistry on the droplet delays and ice accumulations.

The Images of the frost densification process on the SS samples are shown in figure 4.7. Figure 4.7a clearly indicates that the frost densification mechanism was different among the SS samples. The frost nucleation clusters were mostly interlinked and densified on

SS-AR samples, while a number of frost nucleation clusters on SS-S3 samples were isolated and disconnected. These frost accumulation observations on the samples with varied surface characteristics slowly diminished with time and further frost accumulations are shown in figures 4.7b and 4.7c. Rahman et al. [199] also indicated a ~24% decrease in frost density on the micro-grooved surfaces with narrow depth and smallest width of pillars.

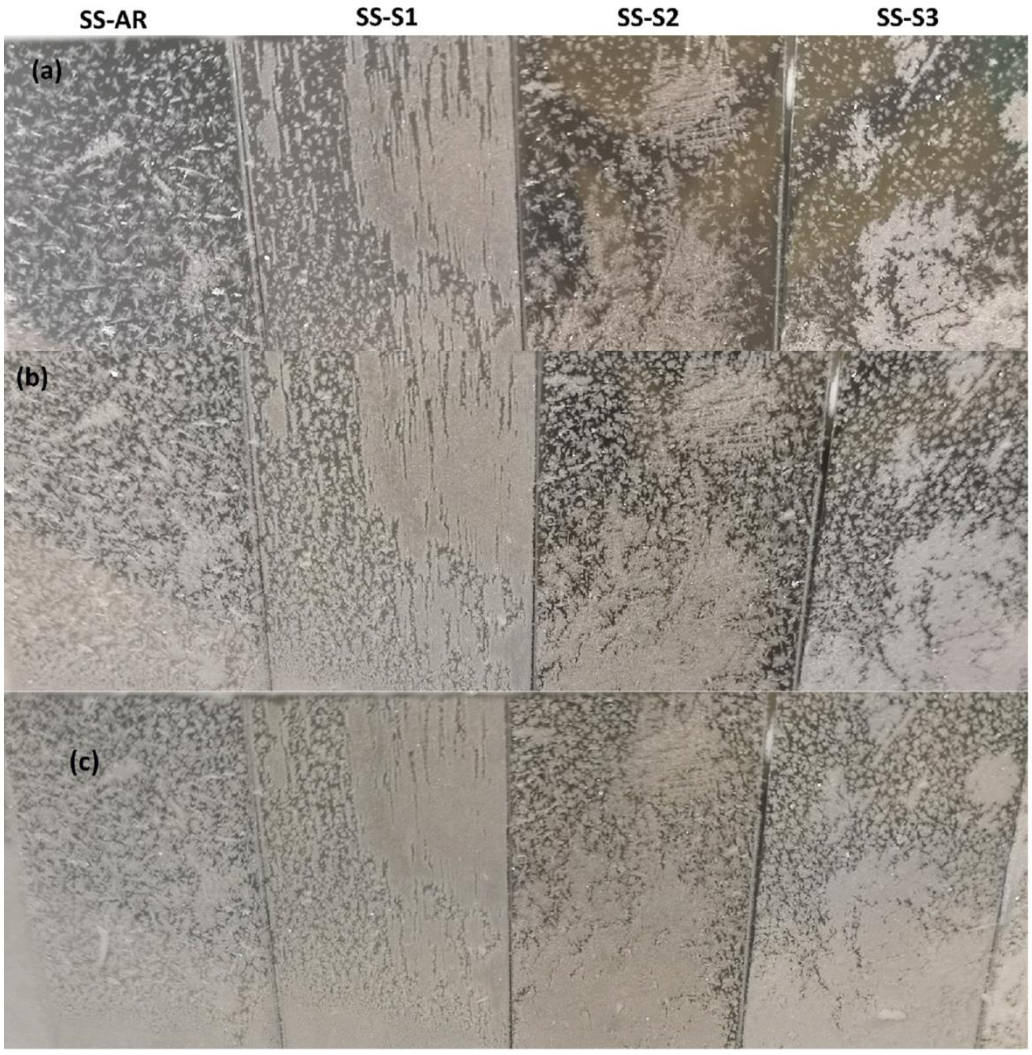


Figure 4.7: Frost densification on the SS substrates after (a) 10, (b) 20 and (c) 30 minutes.

4.4 Comparative analysis of different icephobicity evaluation methods

The results obtained on anti-icing and de-icing methods in this study indicated a considerable variation in icephobicity evaluation measurements and suggested some meaningful correlations with surface characteristics. For example, the shear-based de-icing and water droplet freezing delay methods indicated a linear relationship of ice adhesion strength with surface roughness, whereas, the normal-based and electro-thermal de-icing methods showed a partial relationship with surface roughness. Similarly, surface wettability demonstrated a direct relationship with the normal-based de-icing and frost accumulation methods and a partial relationship with the shear-based methods. In this section, the results obtained on anti-icing and de-icing methods are thoroughly debated to understand the key factors affecting the icephobicity evaluation measurements.

Firstly, the intrinsic shear strength or the nominal adhesional force per unit area measured with de-icing methods is dependent on the true interfacial contact area and can be calculated by dividing the shear/normal force by the interfacial ice contact area. However, the loading on an interfacial contact area may not be uniformly distributed using different de-icing evaluation methods and could jeopardize the accuracy of ice adhesion measurements. For example, an increase of 1.5 fold ice adhesion strength was reported on the push method as compared to that of the centrifugal method, with an uncertainty of 36% on an aluminium substrate at a temperature of -10 ^{o}C [31].

The interfacial stress can be categorised into two distinctive types: the outward force or the peeling stress and the shear stress along with the interface. The centrifugal and push methods develop peeling stress at the edges of the ice sample whereas the rest of the interfacial contact area is mainly dominated by the shear stresses [200, 201] as shown in

figure 4.8, thus inducing a fracture in a combination of Mode I and Mode II failures. The stress concentration at the edges of ice/surface interfaces is severe in the case of the push methods as compared to the centrifugal methods, shown in figure 4.8c and 4.8d. The FEA analysis on the push method indicated strong stress concentrations at the interface and the edges [32, 202]. However, stress concentrations at the interfaces alone do not provide a plausible explanation for the higher magnitude of ice adhesion strength measured on HPM methods. To the best of the authors' knowledge, researchers have so far not considered the effect of aerodynamic drag on ice adhesion strength using CAT methods in a laboratory setup. The drag on the ice sample while spinning in a centrifuge, depicted in figure 4.8b, may explain the lowered ice adhesion strength measured using CAT methods, as it may aid an early release of ice. On the contrary, in an NTM method, a uniform distribution of shear stresses might be approached on a tensile method [179] as the tensile method mainly involves the normal or tensile stresses, the mechanism is illustrated in figure 4.8e.

In the case of microscopically rough surfaces, the chances of cohesive fracture are high due to the mechanical interlocking of ice on the surface asperities and the probability of a pure adhesional fracture is lowered [185]. Ice may rupture in two forms: an adhesive (mode I) or a cohesive (mode II) fracture. The fracture of ice depends on the magnitude of the applied load, the rate of loading, testing temperatures, and the type of ice formed/accumulated [203]. In addition to a change in fracture mechanism, the presence of liquid-like layers (LLL) at the ice/surface interface may further complicate the adhesive release of ice. LLL is known to aid the easy removal of ice by inducing a slippery behaviour at the ice/solid interface [204], however, the ice adhesion was mainly

evaluated under a shear based method. Goertz et al. [205] experimentally measured the adhesive response of LLL on the ice surfaces using a normal force mechanism and they formed a bulk ice cube on a Peltier cooling system (similar to the system used in this study). They reported that at the temperature -10 ^{o}C, the thickness and adhesive force were maximised, however, the values of both properties decreased with further decreasing temperature (down to -30 ^{o}C). Thus, there is a possibility of the LLL layers (the viscous and meniscus forces) working as an adhesive between the ice/solid interfaces, leading to an enhanced ice adhesion under a normal force mechanism, in addition to the increased affinity with wettability or increased interfacial contact due to a higher spatial parameter over a range of higher surface roughnesses [190].

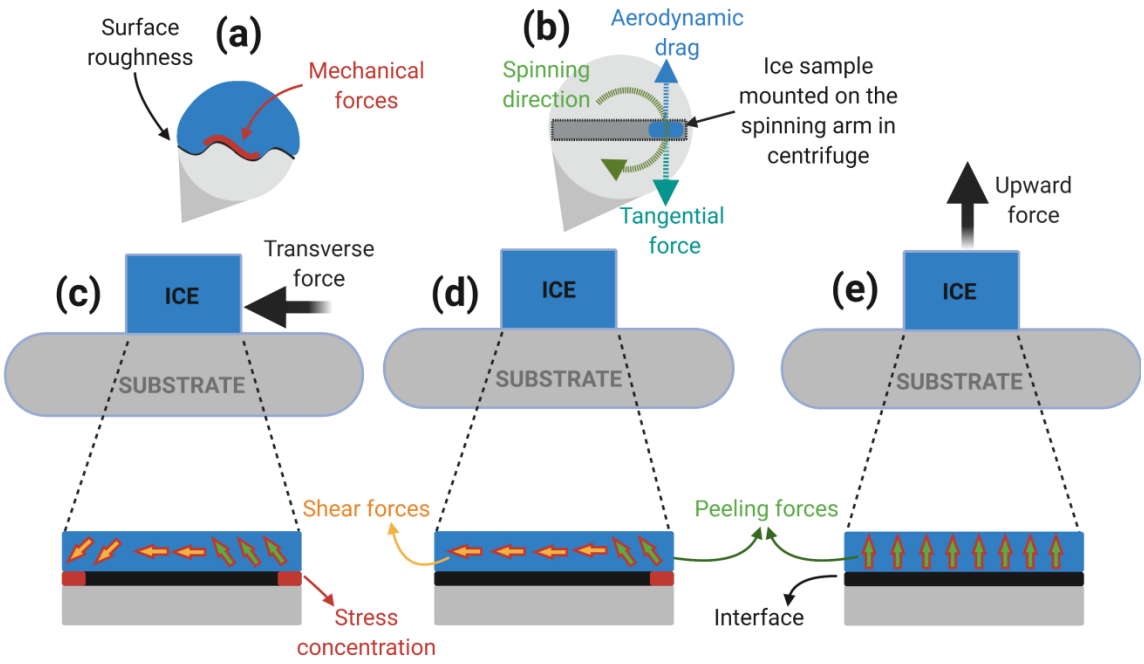


Figure 4.8: (a) The mechanical forces around the surface asperities. (b) The forces acting on the ice rotating in a centrifuge. The mechanism and force schematics of de-icing methods: (c) horizontal push method, (d) centrifugal method, (e) normal tensile method. (The figure was drawn using biorender.com).

The ice shearing methods such as the CAT and the HPM methods produce a combination of shear and peeling forces, whereas, the NTM method predominantly generates the normal forces. A recent study indicated the ice adhesion compatibility between the HPM and the CAT methods [31]. However, the studies conducted by Schulz et al. [32] on the push method demonstrate irregular stress distributions at the ice/surface interfaces. Their FEA model suggested strong peeling forces and stress concentrations at the edges of ice bulk and uneven stress forces across the contact area, as depicted in figure 4.8a. Whereas, the interfacial stress on centrifugal methods were evenly distributed and could reach near-constant values provided the substrate was an ideal rigid surface [32]. They also suggested that the influence of shear stresses were higher than the peel stresses under the FEA model assumptions, thus, indicating the mechanical forces-centric nature of the shear methods.

Thus, to conclude in terms of the de-icing evaluation method, an ideal de-icing evaluation test would involve a singular force that must promote the adhesional fracture. However, the complete isolation of de-icing forces is not realistic. Instead, the methods may involve a loading case where several stress components exist but one dominates. The NTM method is one of the analytically straightforward stress states and offers a dominant component of normal forces. However, the NTM method is likely to induce a cohesive failure, is influenced by the surface wettability, and subsequently, the possible influence of LLL layers. Furthermore, the selection of a shear method would be practical for de-icing evaluation as the shear forces are useful for mimicking forces present in applications requiring de-icing. For example, if the ice is removed by aerodynamic force alone, then the largest stress component for such a loading would be in shear [178]. In

terms of shear methods, the HPM method is simple and cost-effective. However, the transverse shear method is not designed to create uniform stress at the interface and a constant force on one side may not create a single uniform force at the interface. The method may also induce strong stress concentrations in the interface region, and produce uneven and/or ununiformed distribution of interfacial shear forces [151]. The HPM and NTM methods may also not be suitable for impact or sprayed de-icing evaluation. The use of the CAT method makes a better case for de-icing methods as they are appropriately sensitive to both the mechanical and wetting conditions. The CAT is also the most repeatable ice adhesion test, has a higher probability of adhesive failure, and is ideal for large components and different types of ice formations, such as spray, accumulated, and bulk formations [1, 151]. Furthermore, Work et al. [1] indicated an average variation of 14.7%, 18.7%, and 24.1% for CAT, HPM, and NTM on aluminium samples, respectively. Thus, the CAT method offers a small variation in results as compared to that of HPM and NTM methods. The CAT method also offers a dominant component of shear forces than the peeling forces and the shear stress are almost constant in the interface [32]. However, it is imperative to mention that the CAT method is complicated to evaluate the relationship of strain rate and adhesion strength, is expensive to set, and the influence of aerodynamic drag and vibrational forces is yet unknown [1].

Secondly, in terms of the electro-thermal heating method, the variation in heating time could be explained by the total initial ice adhesion force F and the force on ice/surface interface may have changed due to surface characteristics. The residual adhesion force F_o can be calculated as [206]:

$$F_o = (F - F_m).K \qquad (5.1)$$

whereas F_m is the deducted ice adhesion at the melting part and K is the modification coefficient. The value of K is dependent on the surface material, surface morphology, ice uniformity and the adhesion state. Assuming no losses, the heat energy Q at the interfacial area can be mathematically calculated as [206]:

$$Q = \frac{U^2}{R} t \tag{5.2}$$

whereas t is the heating time, R is the resistance value of the heating material, and U is the power supply voltage. R and U were constant in the ice heating melt tests conducted in this study, thus $Q \propto t$ can be assumed.

The results of ice heating melt tests could be explained using equation 5.1 and 5.2. The results seem to indicate a correlation over a certain range of surface roughness, which could be explained using the modification coefficient K as the coefficient is dependent on surface morphology, whereas, the heat energy required melting the ice interface could be approximated using the heating time. Thus, the heating period required to detach the ice could be up to 530 seconds, whereas, further delay (up to 700 seconds) in the separation of ice bulk might come from the influence of surface characteristics.

Thirdly, the water droplet freezing delay results could be explained in terms of heat transfer and ice nucleation mechanisms [91]. The heat transfer from the droplet to a cold substrate or the rate of heat loss, $\frac{dQ}{dt}$, can be calculated as [207-209]:

$$\frac{dQ}{dt} = \lambda_i \frac{A_h + A_o}{2} \frac{T_1 - T_2}{h} \tag{5.3}$$

where h is the height of the ice layer, T_1 and T_2 are the interfacial temperatures at water/ice and ice/substrate interfaces, respectively. A_h and A_o are the interfacial area at water/ice and ice/substrate interfaces, respectively, and λ_i is the heat conductivity of ice. The interfacial contact area at the ice/substrate interface A_o can be calculated as [207]:

$$A_o = r\pi a^2 \tag{5.4}$$

where r is the roughness factor and a is the radius of the interfacing circle between ice and the cold substrate.

Ice nucleation of a water droplet on a surface can be further explained using the classical theory of nucleation. The free energy barrier for heterogeneous ice nucleation ΔG_c can be described using the interfacial correlation factor $f(m,x)$ and compared with a free energy barrier of homogeneous ice nucleation ΔG_c^{homo} as [91]:

$$\Delta G_c = \Delta G_c^{homo}.f(m,x), \qquad \Delta G_c^{homo} = \frac{16\pi\gamma_{IW}^3}{3(\Delta G_v)^2} \tag{5.5}$$

where ΔG_v is the volumetric free energy between the liquid and the ice and γ_{IW} is the interfacial ice-water tension. The interfacial correlation factor, $f(m,x)$ can be calculated as [91, 210]:

$$f(m,x) = \frac{1}{2} + \frac{1}{2}\left(\frac{1-mx}{w}\right) + \frac{x^3}{2}\left[2 - 3\left(\frac{x-m}{w}\right) + \left(\frac{x-m}{w}\right)^3\right] + \frac{3mx^2}{2}\left(\frac{x-m}{w} - 1\right) \tag{5.6}$$

Where $x = {}^{r}/_{r_c}$, $m = \cos\theta$, and $w = (1 + x^2 - 2xm)^{1/2}$. r_c is the critical nucleus radius and θ is the ice embryo contact angle in supercooled water on the nucleating particle of radius r. x is a parameter that changes with surface roughness.

Hence, surface roughness plays an important role in both the heat transfer and ice nucleation mechanisms. Equations 5.3 and 5.4 dictate the direct influence of surface roughness factor r to the rate of heat loss, $\frac{dQ}{dt}$. Equations 5.5 and 5.6 show that surface roughness close to a critical radius of ice nuclei x influences the interfacial correlation factor, $f(m,x)$. A decrease in surface roughness may also decrease the free energy barrier of heterogeneous ice nucleation ΔG_c and could result in significant droplet freezing delays. The samples in this study also experienced increased freezing delays with lower surface roughness, thus, this change could be attributed to the decreased free energy barrier of water droplets and/or the reduced rate of heat loss.

Fourthly, the frost formation and frost accumulation can be described using the rate of frost densification and the rate of frost thickness, respectively [211]. The rate of frost densification or the change of frost density over time is the total mass influx of water vapours diffusing on the surface and subsequently, phase transforming to frost crystals. Whereas, the frost thickening mechanism depends on the rate at which water vapours freeze on frost crystallisations and subsequently, the frost layers multiply over ice layers. In other words, the initial frost crystallisation can be quantified using the frost densification mechanism and further frost accumulation on the initial crystallised frost using the frost thickening mechanism [211]. Thus, the frost growth, during both stages (frost densification and layering), is dependent on surface characteristics that could influence the initial droplet distribution during the condensation process [199].

The observations of frost densification on the SS substrates, shown in figure 4.7, highlight the unique frost densification processes for different surface roughness and the phenomenon could lead to a weakened bond of ice/frost on a smoother interface. This

means that the less densified ice/frost at the ice/surface interfaces may pave the way for easy release of ice, which could be the case for lower ice adhesion on the smoothed samples in this study. The ice density was not calculated in this chapter but based on preliminary results, surface roughness could play an influential part in the surface frost densification process and the ice/surface interfaces might be weakened and encouraged to an early fracture.

Lastly, to conclude, the results obtained on anti-icing and de-icing methods indicated an intrinsic role of surface characteristics, whereas the degree of variation in response is driven by interfacial mechanisms, specific to the icephobicity evaluation method. Surface roughness seems to play a pivotal role in the response at different measuring conditions, indicating either a direct or partial relationship with all the methods studied in this chapter. Notably, the results obtained on tensile-based de-icing methods correlated directly with CAHs, demonstrating the intrinsic relationship with surface wettability.

4.5 Summary

An interlaboratory experimental investigation was conducted in this chapter to compare the de-icing evaluations methods. The results obtained using anti-icing methods were also examined. The study focused on the influence of surface characteristics involving popular anti-icing and de-icing methods and to identify and understand the underlying interfacial mechanisms or factors that cause the variation in response.

In terms of the mechanical de-icing methods, the ice adhesion obtained on shear-based methods suggests a linear relationship between ice adhesion strength and surface roughness, whereas the tensile (normal) method indicated an inverse curvilinear relationship with contact angle hysteresis. Furthermore, the electro-thermal and normal-

based de-icing evaluation suggested a partial correlation over a specified range of surface roughness. The tensile forces are majorly dominant forces on normal-based methods which have the direct dependency on wettability (product of area and surface energy), whereas, the mechanical forces in horizontal push methods may create the stress concentrations. The influence of mechanical forces was also confirmed during the hybrid heating de-icing method. In terms of anti-icing methods, the obtained results suggested a longer water droplet freezing delay and a reduced rate of frost densification on the smoothed samples, whereas the rate of frost thickness did not differ significantly.

To conclude, the results obtained in this study indicate the CAT method make a better case for de-icing methods as they are appropriately sensitive to both the mechanical and wetting conditions. Furthermore, this chapter highlighted significant discrepancies among the icephobicity evaluation methods, but at the same time, several correlations based on surface characteristics were identified and quantified. These correlations could be further exploited to understand the material-dependent behaviours of the icephobicity evaluation methods and the variations in response with the surface characteristics investigated in this chapter offered the crucial information on pre-selection of testing regimes to accurately measure the performance of icephobic materials.

Chapter 5

Influence of surface characteristics on ice adhesion and ice anchoring

5.1 Introduction

Surface characteristics, such as surface roughness or wettability, play a crucial role in imparting icephobicity. For example, the idea of deploying superhydrophobicity-induced icephobicity has been widely studied [8, 18, 19, 212] and superhydrophobicity on a solid surface is the synergetic result of low surface energy and rough asperities [26, 63, 213, 214]. However, in some studies, the introduction of rougher asperities on the surface (which renders the surface superhydrophobicity) [215, 216] leads to a higher number of possible ice anchoring points and the anchored ice would require higher stress to break the ice on the surface with complex topographical features [19, 24]. On the other hand, surface texturing or patterning has also been argued for achieving promising anti-icing performance (e.g. droplet freezing delays, etc.) [8, 76]. However, these extraordinary improvements in anti-icing performance did not directly contribute to de-icing (shear removal of ice) abilities in most of the previously-conducted studies in literature and it would be interesting to study the systematic dependence of surface roughness on de-icing abilities.

Surface roughness, one way or another, seems to play an influential role in imparting icephobicity and it is essential to study the direct effects of surface roughness, while

keeping other parameters such as surface wettability or interfacial cavitation unchanged. Furthermore, many studies hypothesise the formation of micro-frost under high humidity conditions on superhydrophobic surfaces [12, 21, 22, 125, 126, 217], which could lead to increased number of hydrogen bonds (water-solid) [22, 186-188]. Thus, it would be worthwhile to examine the surfaces with different surface roughness and wettability conditions at a micro-scale. These observations will provide essential information on how water wets the microstructural surface and subsequently, how ice is formed. These in-situ water condensation and icing studies could validate the micro-frost formation and provide the crucial understanding related to ice retraction mechanism, which is often linked to maintaining high receding water contact angles [23, 47].

In the first part of this chapter, samples with different surface roughness were prepared and the effects of surface roughness on ice adhesion strength were studied. The correlations with other surface characteristics such as surface wettability and interfacial cavitation were also examined. In the second part, in light of these experimental results and assumptions, in-situ water condensation and icing observations were also carried out to acquire the direct evidence of ice anchoring over surface roughness asperities of the examined coatings/surfaces under high humidity conditions. These studies aim to identify the vital link of surface roughness on ice adhesion strength and to validate the hypothesis of ice anchoring in rough asperities, including on superhydrophobic surfaces.

5.2 Microstructural analysis of the surfaces and coatings

A variation in surface roughness was introduced using grinding, polishing or sandblasting of the metallic substrates and via incorporation of nanoparticles in the polyurethane matrix.

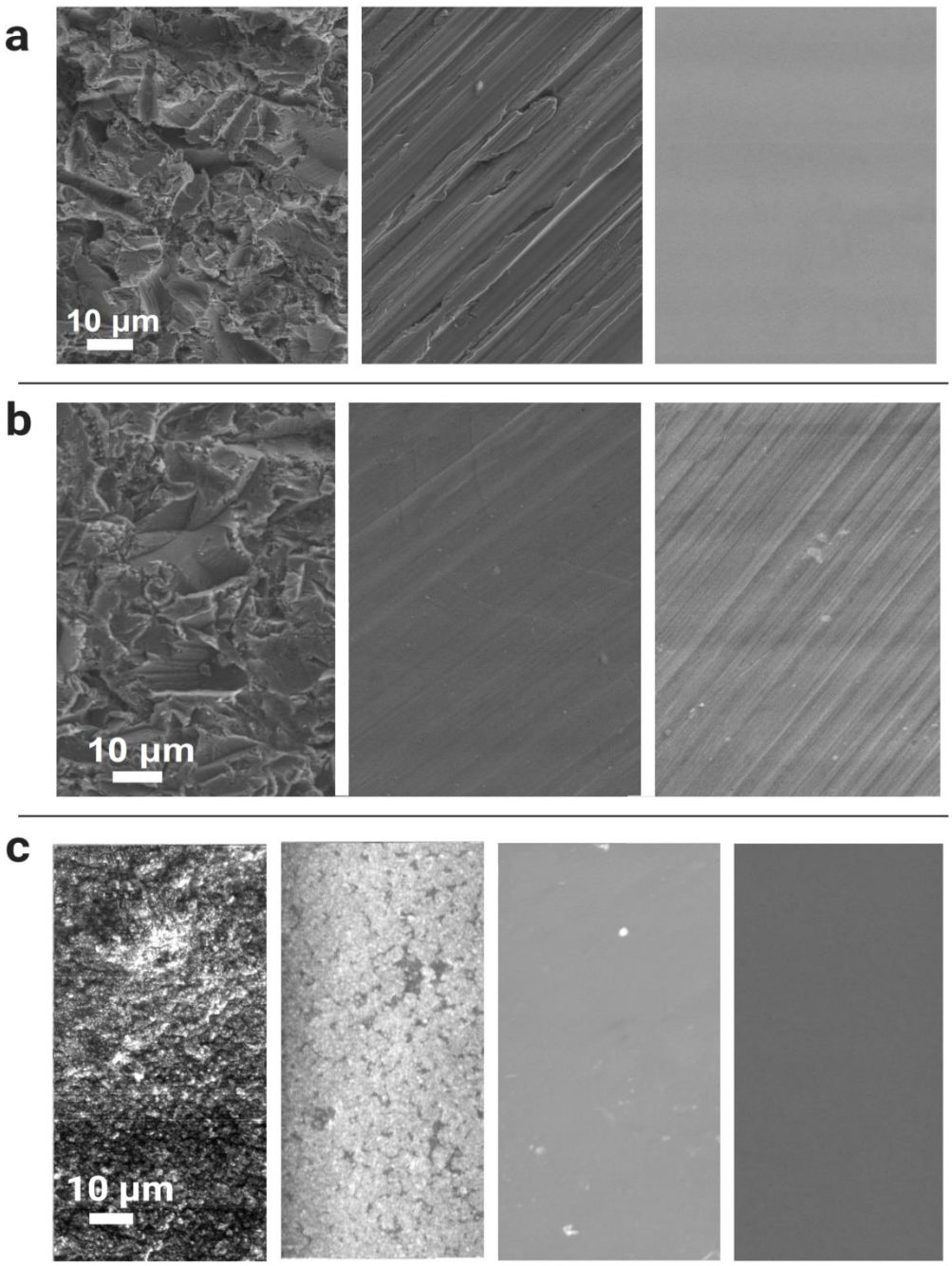


Figure 5.1: The microstructure of (a) aluminium, (b) stainless steel, and (c) TPU-BN samples, from the roughest sample on the left side to the smoothest sample on the right. The as-received metallic samples were roughened using sandblasting and smoothened using grinding and polishing. The TPU coatings were roughened by increasing the nanoparticle concentration in the coating matrixes. All images have the same scale bar.

The surface roughness (R_a) of sandblasted SS-SB samples was 1 ± 0.02 µm and was brought down to 0.03 ± 0.01 µm on the chemically-smoothened SS-S3 samples. The composition of the metallic samples discussed in this section was detailed in table 3.1. The microstructural structures of SS-SB, SS-AR, and SS-S3 (from right to left) are shown in figure 5.1a. Similarly, surface roughness (R_a) was reduced from 1.2 ± 0.02 µm on Al-SB samples to 0.05 ± 0.01 µm on Al-S3 samples and from 0.6 ± 0.01 µm on TPU-80BN to 0.01 ± 0.01 µm on TPU-5BN coatings.

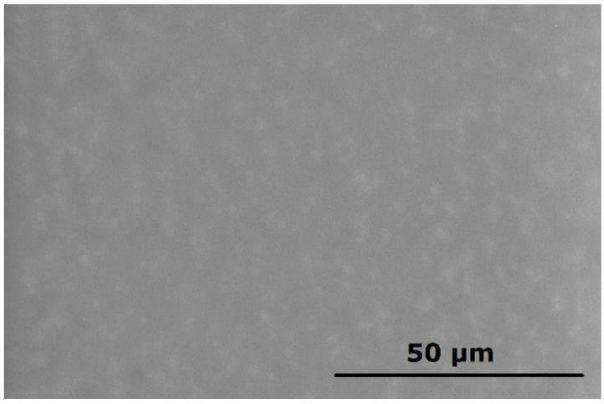


Figure 5.2: Microstructural image of PDMS coatings.

The microstructural images of the aluminium substrates (Al-SB, Al-AR, and Al-S3 from right to left) and TPU-hBN coatings (TPU-5, TPU-10, TPU-40, and TPU-80 from right to left) are shown in figure 5.1b and 5.1c, respectively. The pure polymeric coatings discussed in this chapter are PU-1, PU-2, PU-3, PU-4, and PDMS polymers and their respective surface roughness (R_a) was measured as 0.08 ± 0.01 0.6 ± 0.01 µm, 0.9 ± 0.02 µm, 0.2 ± 0.01 µm, and 0.23 ± 0.01 µm. . The composition of the pure polymeric and superhydrophobic coatings discussed in this section was detailed in table 3.2. Overall, the pure PU coatings have relatively smoother morphology, compared to that of as-received

metallic coatings but they possess different surface roughness and shore hardness values. The microstructural of PDMS coatings is shown in figure 5.2.

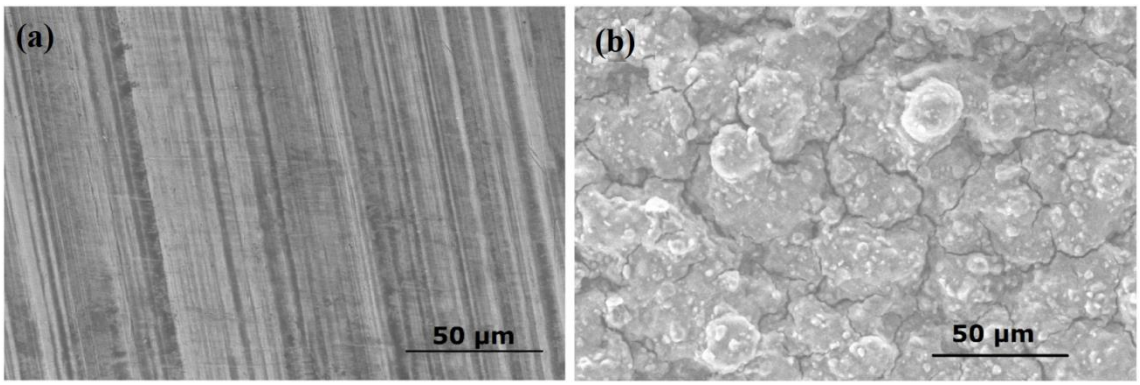


Figure 5.3: SEM images of (a) Al-AR substrates and (b) SHS-40 coatings.

The microstructural morphology of Al-AR substrates and SHS-40 coatings are shown in figure 5.3a and 5.3b, respectively. The surface roughness of PDMS coatings was R_a ~0.23 ± 0.01 µm as compared to that of Al-AR substrates R_a ~0.9± 0.01 µm and SHS-40 coatings R_a ~2± 0.03 µm.

5.3 Influence of surface roughness and wettability on ice adhesion

In this section, a series of hydrophilic metallic substrates and hydrophilic, hydrophobic, and superhydrophobic polymeric coatings were investigated. The coatings/substrates were carefully fabricated to control the surface roughness and the ice adhesion strengths using centrifugal test were performed on these surfaces.

5.3.1 Stainless steel surfaces

Ice adhesion strengths on stainless steel (SS) surfaces are shown in figure 5.4. Firstly, the ice adhesion strengths were in correlation with surface roughness and the lowest ice adhesion strength was recorded on SS-S3 samples at 22.2 ± 2 kPa. 33-fold reduction in surface roughness (from SS-SB to SS-S3) resulted in a 3-fold reduction in ice adhesion

strength (i.e. adhesion reduction factor, ARF). However, no significant reduction in ice adhesion strength was observed on SS-S2 and SS-S3, i.e. 25.4 ± 7 and 22.2 ± 2 kPa respectively.

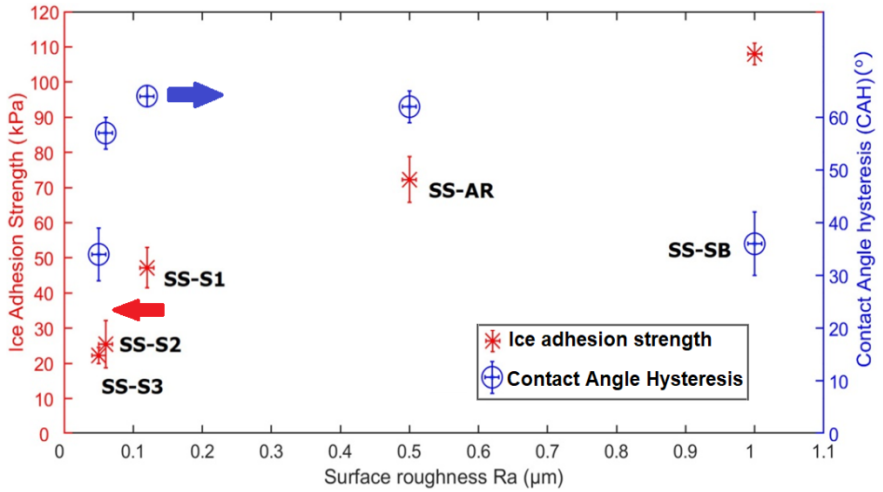


Figure 5.4: Ice adhesion strength on the stainless steel substrates with different surface roughnesses. The red arrows indicate the ice adhesion strength data points and the blue arrows indicate the contact angle hysteresis data points.

Reports from the literature [212, 218] indicated a proportionality of ice adhesion with the contact angle hysteresis (CAH) but such results were not observed on our SS substrates except for SS-S2 and SS-S3 samples.

5.3.2 Aluminium surfaces

A notable reduction in ice adhesion strength was observed on the aluminium substrates in comparison to the SS substrates, as shown in figure 5.5. It is imperative to mention that the surface roughness of Al substrates was reduced 24 times (from Al-SB to Al-S3) as compared to a 33-fold roughness reduction on the SS substrates. Ice adhesion strength was reduced from 145.5 ± 3 kPa on Al-AR samples to 13.1 ± 1 kPa on Al-S3 samples i.e.

91% reduction and an adhesion reduction factor of 11. The decrease in ice adhesion strength observed on the metallic samples was achieved by altering one surface parameter: surface roughness.

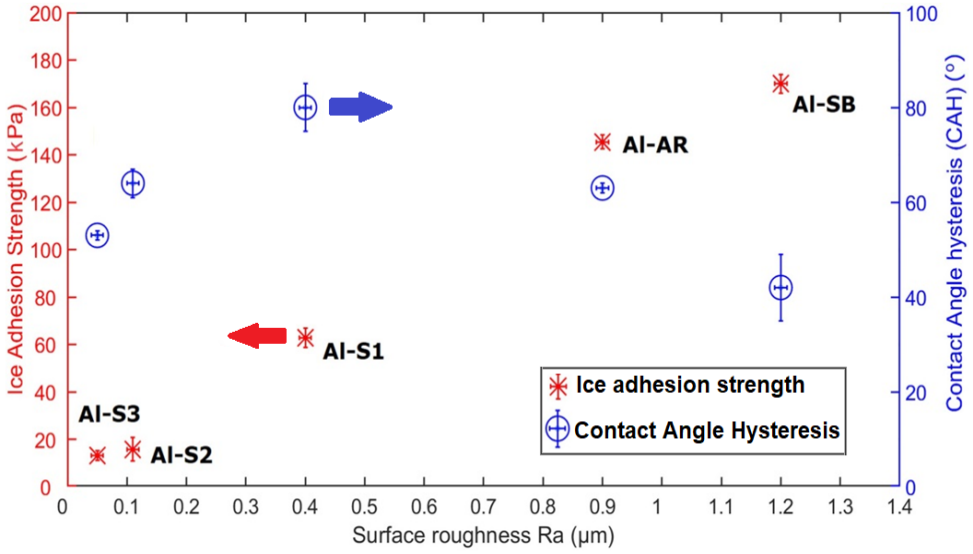


Figure 5.5: Ice adhesion strength on the aluminium substrates with different surface roughnesses. The red arrows indicate the ice adhesion strength data points and the blue arrows indicate the contact angle hysteresis data points.

In comparison with the SS substrates, a similar pattern of ice adhesion strength dependence on surface roughness is noticed on Al substrates. Ice adhesion strength correlated well with the reduction in surface roughness when above 100 nm. Smoothening of the substrates with a roughness of less than 100 nm i.e. Al-S2 and Al-S3 (and SS- S2 and SS-S3 in section 5.3.1) did not produce a marked change in ice adhesion strength. Interestingly, for the metal substrates, the CAH values are demonstrating some correlation with ice adhesion strength until surface roughness reaches ~0.5 µm and loses the correlation when the surface roughness is higher than 0.5 µm. However, the value of 0.5 µm is not a rigid figure and the assumption is made based on the available results.

Another considerable observation is that Al-S2 and Al-AR have similar CAHs but the ice adhesion strength varied by ~89% (reduction).

5.3.3 Polymeric coatings

Pure polymeric coatings

The polymeric coatings showed a drastic change in ice adhesion strength with surface roughness and CAHs, and a similar pattern of ice adhesion strength dependence on surface roughness (in comparison with other coatings) was observed on polymeric coatings i.e. PDMS, PU-1, PU-2, PU-3, and PU-4 coatings, as indicated in figure 5.6. Although the wettability of the studied coatings might differ, the basic composition of PU-based coatings was assumed to be the same.

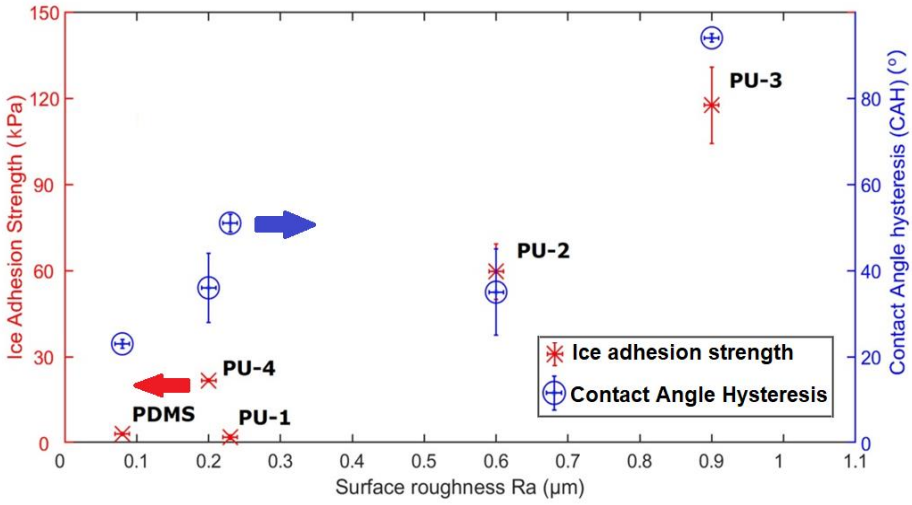


Figure 5.6: Ice adhesion strength on the pure polymeric surfaces with different surface roughnesses. The red arrows indicate the ice adhesion strength data points and the blue arrows indicate the contact angle hysteresis data points.

The highest ice adhesion was measured on PU-3 coatings at 117.6 ± 13.3 kPa and the lowest was 2 ± 0.8 kPa on PU-1 coatings. Interestingly, the PDMS and PU-1 coatings had

hydrophobic and hydrophilic polymeric matrices respectively, but their ice adhesion strength did not vary considerably. This development highlights the intrinsic effect of surface roughness over ice adhesion strength regardless of the influence of wettability. In terms of CAH relevance for the pristine polymeric coatings, ice adhesion strength did not correlate with CAH as their roughnesses were lower than 0.5 µm.

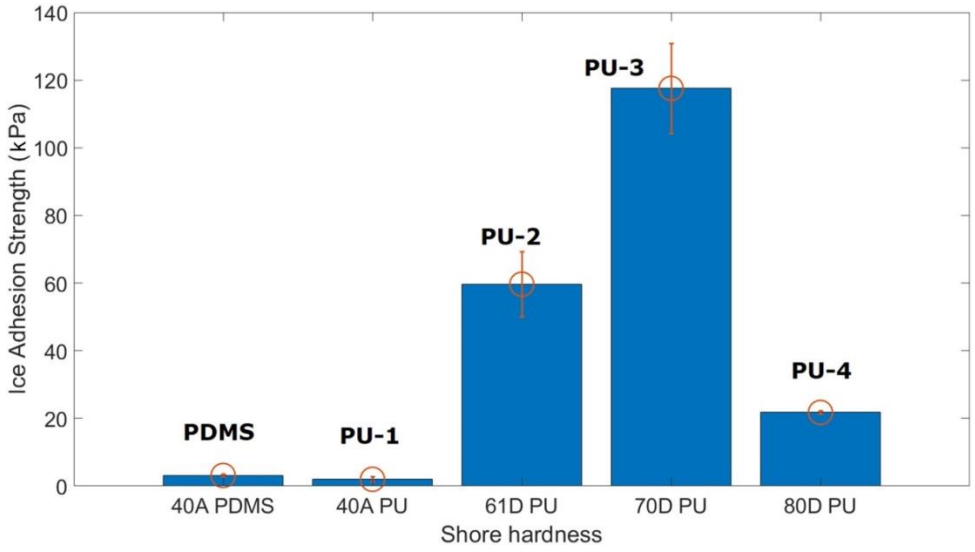


Figure 5.7: Ice adhesion strength on the pure polymeric surfaces with a different shore hardness.

Another engaging observation is the dependence of hardness of the polymeric coatings on ice adhesion as shown in figure 5.7. It was reported that ice adhesion strength decreasing with the decreasing polymer cross-link density, which corresponds to a reduction of mechanical properties of the polymers. It is a phenomenon known as interfacial cavitation [3, 71]. As the ice forms, it would be worth looking into the formation of ice over different polymers having different hardness. From figure 5.7, it is suggested that the ice adhesion strength on the polymeric surfaces increased as the shore hardness is increased at first. However, the ice adhesion strength is quite low on PU-4 coatings with a shore hardness of 80D. Considering PU-4 is the hardest among the developed polymers,

the hardness of the polymer could be a secondary factor for ice adhesion strength as PU-4 has lower surface roughness as compared to PU-2 and PU-3 coatings.

TPU nanocomposite coatings

The surface roughness of TPU-hBN coatings was controlled using the incorporation of nanoparticles in the TPU matrix. A higher amount of nanoparticles reflected a high change in surface roughness. Again, the ice adhesion strength correlated with surface roughness as indicated in figure 5.8.

Interestingly, the ice adhesion strength dropped drastically from TPU-60 to TPU-5 samples. However, it remained unchanged on TPU-60 and TPU-80 samples, despite the change in CAHs. In all the cases, the effect of surface roughness was instrumental on ice adhesion strength and could not be neglected. Ice adhesion strength on TPU-80 coatings decreased from 141.22 ± 7 kPa to 25.9 ± 2 kPa on TPU-5 coatings, i.e. a 5-fold reduction.

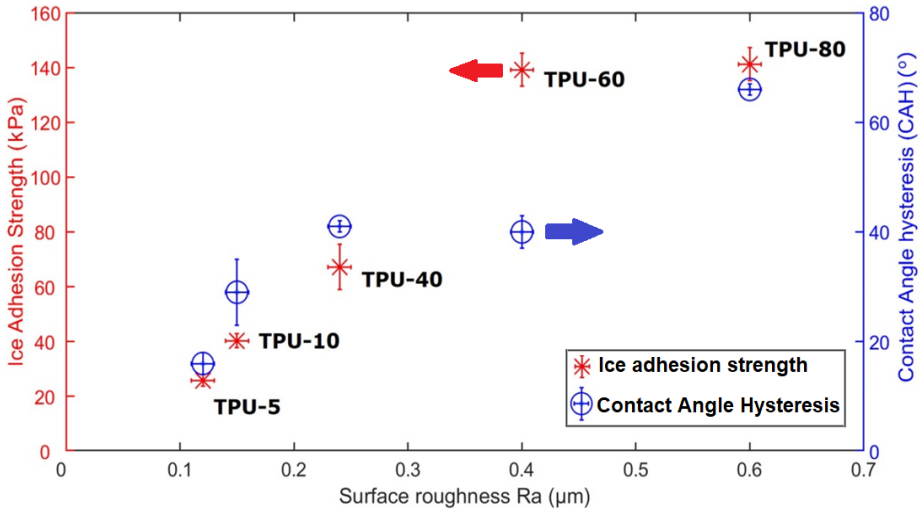


Figure 5.8: Ice adhesion strength on the TPU nanocomposite coatings with different surface roughnesses. The red arrows indicate the ice adhesion strength data points and the blue arrows indicate the contact angle hysteresis data points.

Superhydrophobic coatings

In the previous section, the dependence of ice adhesion strength on surface roughness regardless of the surface wettability was demonstrated. In this section, the effect of the hydrophobicity and superhydrophobicity (with the same material composition) is studied, as shown in figure 5.9. SHS-5 was a hydrophobic coating and ice adhesion on this coating was measured to be 5.4 ± 2 kPa. SHS-10/SHS-20/SHS-40 were superhydrophobic coatings and their ice adhesion strengths increased as the concentration of SiO_2 nanoparticles in the polymer matrix were increased.

Five key points can be drawn from these results. Firstly, when the wettability of PDMS-nSiO_2 coatings was tuned from hydrophobic to superhydrophobic, there was a slight increase in ice adhesion strength. This could be the result of either the hardening of nanocomposite coatings driving the ice adhesion strength up, or the number of anchoring points for the ice increasing. Secondly, the ice adhesion strengths on SHS-10 and SHS-20 tend to remain in the same range, which gives the idea that the superhydrophobicity-induced icephobicity was imparted to the coatings. Superhydrophobicity-induced icephobicity is icephobicity achieved using a minimal contact with surface asperities, this could results in the reduced influence of surface properties during ice formation (heterogeneous ice nucleation) and may disrupt the heat exchange between ice and the surface leading to weakly bonded ice (discouragement of solidification frontier formation). Thirdly, the surface roughness becomes a dominant factor in SHS-40 coatings and the ice anchoring (mechanical interlocking of ice) was mostly likely to happen. Fourthly, the surface roughness played a dominate role on hydrophobic and

hydrophilic coatings/substrates alike. Lastly, CAH showed no direct relationship to ice adhesion strength for PDMS-nSiO_2 coatings.

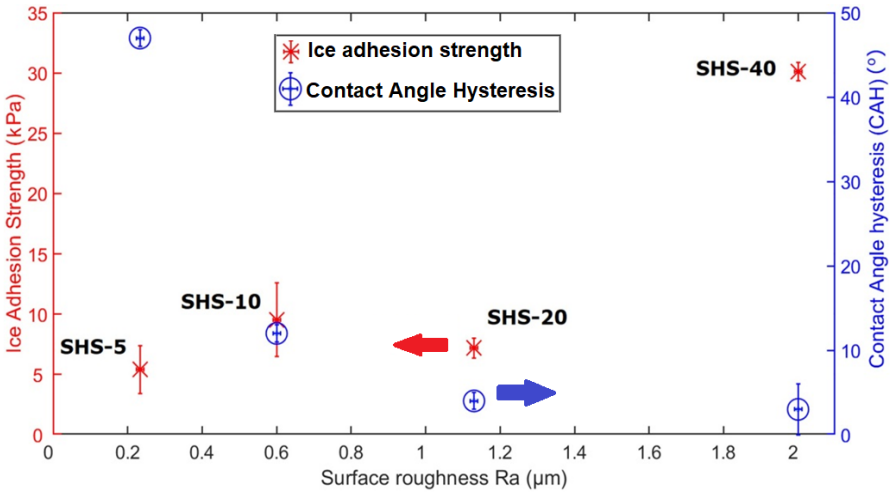


Figure 5.9: Ice adhesion strength on variable surface roughness of superhydrophobic coatings. The red arrows indicate the ice adhesion strength data points and the blue arrows indicate the contact angle hysteresis data points.

5.3.4 An overview of the influence of surface roughness on ice adhesion strength

Ice adhesion strength versus variable surface roughness discussed in section 5.3.3 is summarized in figure 5.10. Overall, the ice adhesion strength tends to decrease with the reduction in surface roughness values. Ice adhesion strength above 160 kPa could not be determined due to the equipment limitation. However, there is sufficient evidence in the available literature of increased ice adhesion strength beyond 160 kPa with an increase in surface roughness. Momen et al. [12] reported ice adhesion strengths of 220 kPa and 270 kPa at R_a values of 5 µm and 8 µm respectively, using a similar centrifugal method. Another study involving blade de-icing under centrifugal influence reported a 250% increase in ice adhesion strength, i.e. ~200 kPa to ~670 kPa on samples with a surface

roughness R_a of 0.65 µm to 2.67 µm, respectively [219]. Hassan et al. [89] found a linear correlation on samples having a surface roughness R_a of 0.47 to 1.65 µm and ice adhesion strength of 142 kPa to 2279 kPa.

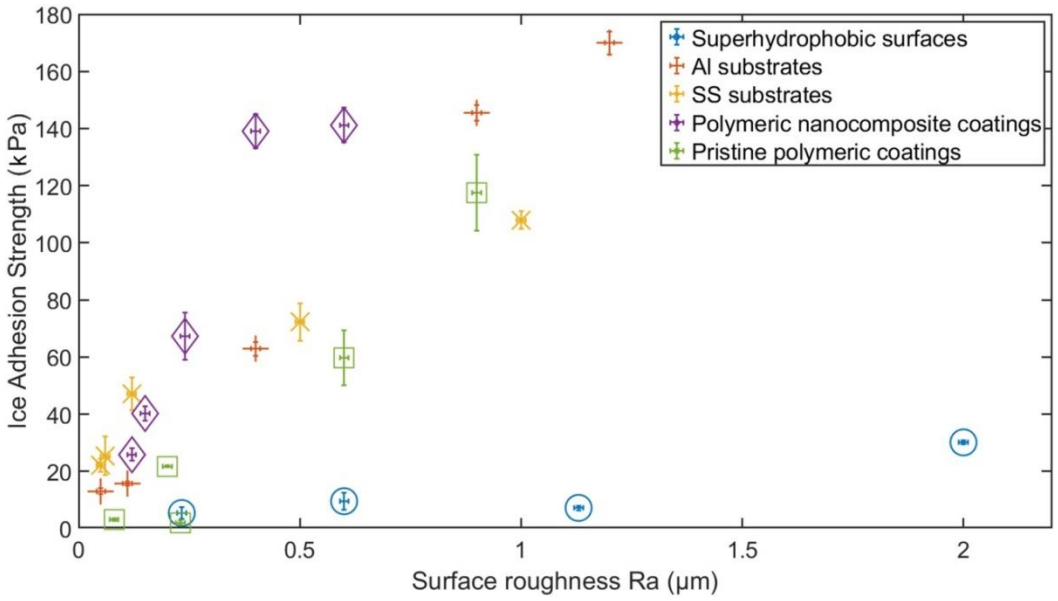


Figure 5.10: Overview of ice adhesion strength versus variable surface roughnesses.

The lowest surface roughness in figure 5.10 corresponds to SS-S3 substrates. However, PU-1 coatings have the lowest ice adhesion strength among the studied surfaces. This signifies the collective or synergetic effect of surface properties such as wettability or interfacial cavitation that affect icephobic performance. The ice adhesion strength test was conducted based on bulk ice accretion (glaze ice) and it would be worthwhile to look into different methods such as impact ice (in-cloud ice) and hard rime ice (precipitated ice). A recent study suggested that higher ice adhesion strength may occur in these methods [220].

The data in figure 5.10 can also be categorized into two groups: one is hydrophobic and hydrophilic coatings, and the other is superhydrophobicity-induced icephobic coatings.

Although ice adhesion strength on both coating groups correlates with surface roughness, superhydrophobic coatings tend to be rougher in comparison to other coatings, maintain promising icephobic performance in high roughness ranges, and showed no correlation with CAHs. This can be justified as superhydrophobicity-induced icephobicity, and is mainly achieved by reducing the cross-sectional area of water contact. Thus, the effect of surface roughness is minimal but evident.

5.4 Effect of hydrophobic-functionalised surfaces on ice adhesion strength

The influence of surface roughness on ice adhesion strength was so far justified. However, the influence of hydrophobic-functionalisation of surface having a similar surface roughness was not explicitly checked. Al-fSB/SS-fSB and TPU-f5 were functionalised using 1H,1H,2H,2H-Perfluorooctyltriethoxysilane (POTS) via chemical vapour deposition and nanoparticle functionalisation, respectively. The substrates/coatings were developed with similar surface roughness (± 0.05 µm) and identical samples were used for water contact angle measurement and ice adhesion strength tests (three samples each) to avoid the degradation of POTS layers due to hydrolysis [221].

The ice adhesion strength results indicated that the POTS-functionalised surfaces aided the easy removal of ice and resulted in lower shear strength, compared to that of the non-functionalised surfaces as indicated in figure 5.11. It is imperative to mention that the hydrophobic-functionalisation rendered the surface hydrophobic but no significant change in the water receding angles was observed. These results are in conflict with other studies [10, 19, 52, 55] which indicated the influential and direct proportional role of receding angles on ice adhesion strength. Zou et al. [90] reported the reduction of ice

adhesion strength on functionalised surfaces having similar surface roughness and the adhesion nearly doubled on sandblasted aluminium substrates as compared to that of pristine aluminium substrates. This study correlated well with our results. The application of the low surface energy treatment resulted in an average decrease of 47% in ice adhesion strength across the tested surfaces.

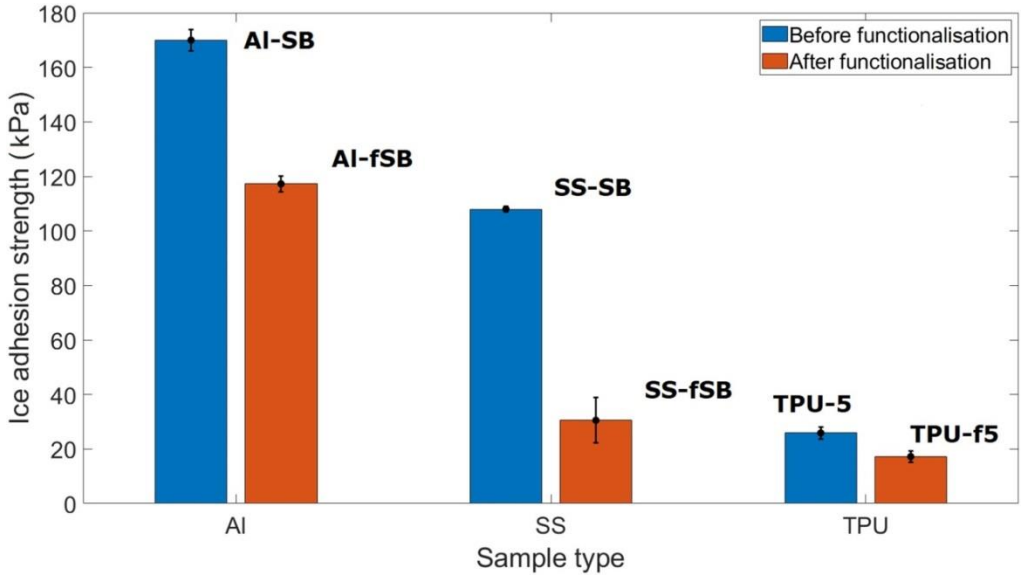


Figure 5.11: Ice adhesion strength: application of low surface energy chemical.

5.5 In-situ icing observation and ice anchoring on different topographical surfaces

5.5.1 In-situ wetting behaviour

The Al-AR substrates, PDMS and SHS-40 coatings were exposed to high humidity levels (90-100% RH) and temperatures were dropped to a range of 1 ^{o}C to 4 ^{o}C to carry out in situ water condensation in a low vacuum chamber. The top and side views of micro-level water condensation formed on AR-Al samples during in situ water condensation are shown in figure 5.12a and 5.12b. It was observed that water condensed on the aluminium

substrates randomly. The condensed water droplets were uniformly distributed but the droplet size varied throughout the observed surface.

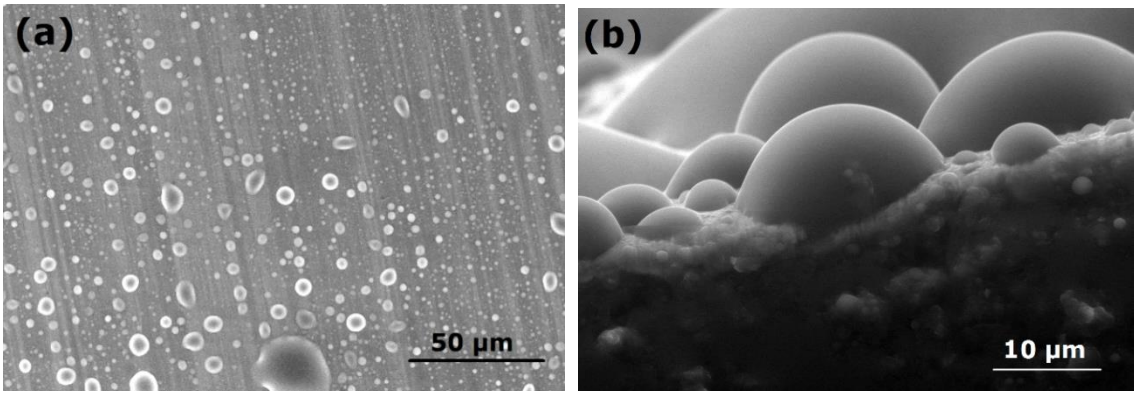


Figure 5.12: In-situ water condensation on Al-AR substrates at 3 ^{o}C and 97% humidity (a) Top view and (b) side view.

The pattern of in-situ water condensation on the superhydrophobic SHS coatings was interesting and the surface morphology is shown in figure 5.13a. It is clear in figure 5.13b and 4.13c that micro-condensation on the superhydrophobic surfaces is evident under high humidity conditions and three main points could be drawn based on the analysis. Firstly, the SHS coatings had a rougher surface consisting of the void valley (a number of material voids) along the surface and the in-situ water condensation results confirmed that the water condensation commenced along the rough asperities of the coatings. Thus, it can be assumed that the surface can only be entirely wetted when the condensed droplets form a uniform water layer on the rough surfaces, i.e. wetting the void valley first, and the entire surface. Ice grown from these condensed droplets will require an extra shearing force (higher ice adhesion strength) as the formed ice will be interlocked in the rough asperities.

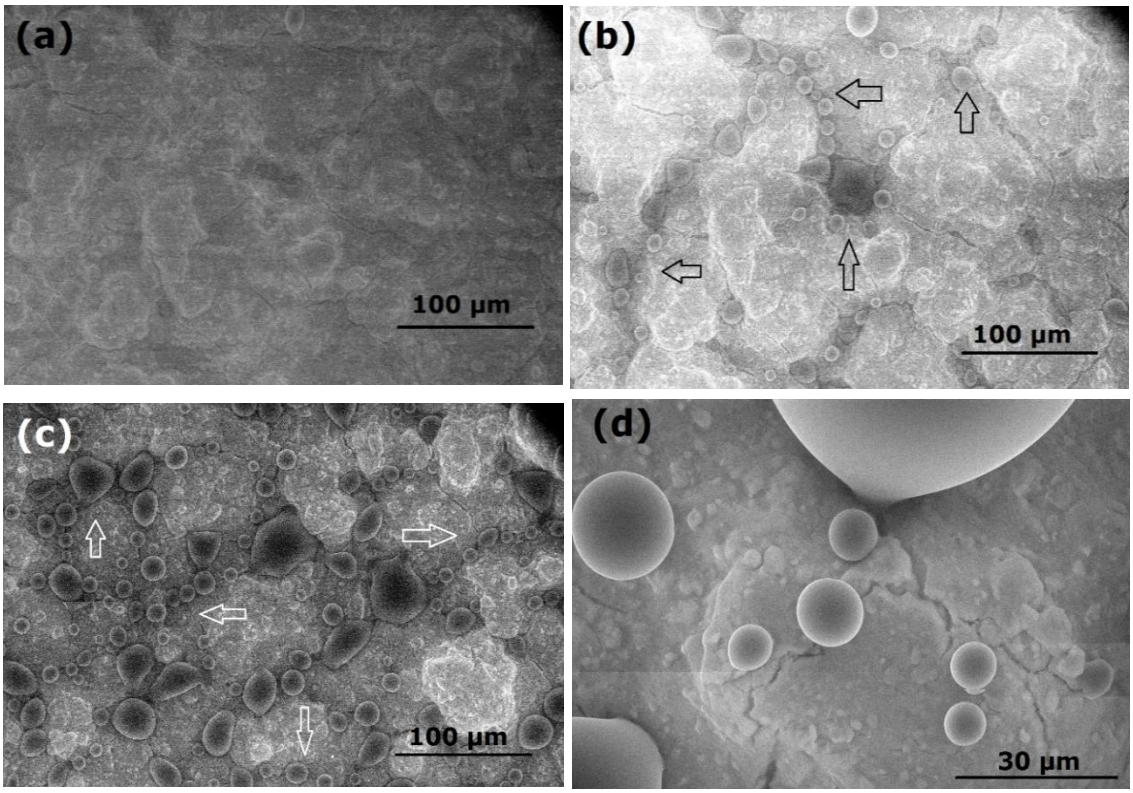


Figure 5.13: In-situ condensation on the SHS-20 coatings at 4 ^{o}C and 98% humidity (a) at start and after (b) 10 seconds, and (c) 20 seconds. (d) A magnified image at 100% humidity conditions. The arrows point to the water condensation along the surface voids.

Secondly, the incorporation of hydrophobic silicon oxide nanoparticles induced the formation of material voids over the surface, and the voids are prominent over the entire surface morphology. The examination of in-situ water condensation on these surfaces reveals that the initiation of micro condensation of water started in the voids as indicated (arrows) in figure 5.13c and 5.13c. It can be assumed that the cracks act as nucleation seeds for the micro-condensation of water [24] and the micro-condensation could compromise/nullify the superhydrophobic ability of the material after formation of a thin layer of ice [21, 28].

Thirdly, the SHS coating surface demonstrated superhydrophobic performance at the micro-level as shown in figure 5.13d and relatively large suspended water droplets in a much more spherical shape in comparison to Al-AR substrates as shown in figure 5.12a. The superhydrophobic ability of the material was also validated under high humidity conditions and in low vacuum (pressure) conditions at the microscale.

In-situ water condensation was also attempted on pure hydrophobic PDMS coatings but no condensation was formed on these coatings under 100% humidity conditions. It is imperative to mention that the top view was adopted to validate in-situ water condensation and a thin layer of water might have formed on PDMS coatings which were not measured or observed due to equipment limitations and/or the transparent nature of the polymer coating.

5.5.2 In-situ ice growth and retracting behaviors

Based on the discussion above, the phenomenon of in-situ water condensation on a rougher surface was thoroughly explained. Furthermore, it would be interesting to observe the visualization of the ice anchoring process. In this section, in-situ icing observation was conducted on Al-AR, Al-S3, SS-AR, SS-S3, SHS-40, and TPU-10BN surfaces. The surfaces were carefully selected to consider the effect of surface roughness. The ice was nucleated at high humidity conditions (90-98% RH) under low-pressure on a cold Peltier stage (-8 ^{o}C to -3 ^{o}C). During cooling, the in-situ ice may have formed at different temperatures as the examined surfaces may possess different thermal gradients. A similar technique was also employed in other studies, and in-situ ice growth (growth of water droplets in the void valley) was confirmed on superhydrophobic surfaces [222-224]. The above mentioned conditions also induced capillary action of water droplets

among the surface grooves and the ice would form in and around the surface rough asperities. The formed in-situ ice was retracted at higher temperatures (above the freezing temperature on the top surface) and lower humidity levels (60-80% RH) to ensure controlled receding of the ice.

The as-received metallic surfaces

The ice retraction process on Al-AR substrates is depicted in figure 5.14 (a-f). Figure 5.14a illustrates the direction of the retraction and figure 5.14b shows the weakening of the ice and fragmentation of the ice into smaller sections. The retracted ice is indicated in figure 5.14c, 5.14d, 5.14e, and 5.14f, and ice anchoring is evident throughout the ice retraction process (yellow and green circles indicated in the figure 5.14). As the retraction process continues in figure 5.14c, the ice starts to break into segments and shows early signs of the anchored ice. The anchoring of ice is observed in figure 5.14d even after the 80 seconds of the ice retraction process. Finally, the initial anchored ice is fully retracted (figure 5.14e), and the ice anchoring is maintained in the second layer of block ice.

The ice anchoring mechanism is fully validated in figure 5.14f when the second layer of ice anchoring is completely detached from the main ice block and the second layer of ice continues to remain anchored on the surface as indicated (circled) in figure 5.14f. It is imperative to mention that the micro-sized ice in the surface rough grooves provides several potential anchoring points of the ice to strongly adhere to the surface and the ice adhesion strength would be significantly higher. Similar behaviour was observed on SS-AR substrates, but the ice anchoring was less severe compared to that of Al-AR substrates, owing to the difference in material composition as well as the surface roughness.

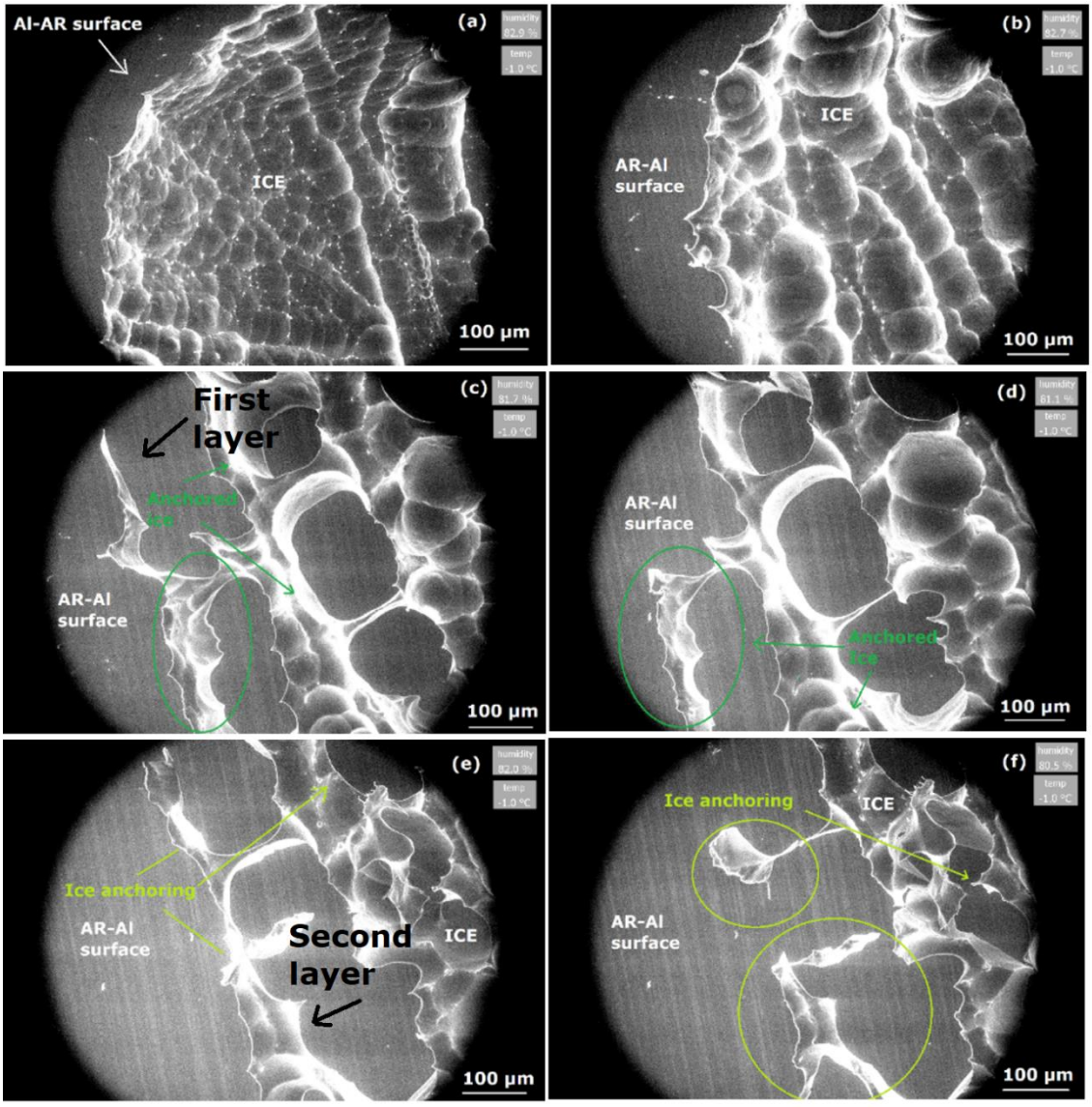


Figure 5.14: In-situ icing retraction on Al-AR samples after (a) 0, (b) 20, (c) 60, (d) 80, (e) 140, and (f) 160 seconds. The anchored ice is indicated by circles and the ice anchoring points/process during the ice retraction are denoted by arrows. The ice retraction starts in sub-figures (a) and (b), the first layer of anchored ice is shown in sub-figures (c) and (d), and the second layer of ice anchoring and the anchored ice are indicated in sub-figures (e) and (f), respectively.

The smoothened metallic surfaces

In comparison to the as-received metallic substrates, SS-S3 substrates were deployed for the in-situ icing study and the ice was formed uniformly throughout the observed surface. Interestingly, there is no ice anchoring present on the smoothened substrates as evidenced in figure 5.15.

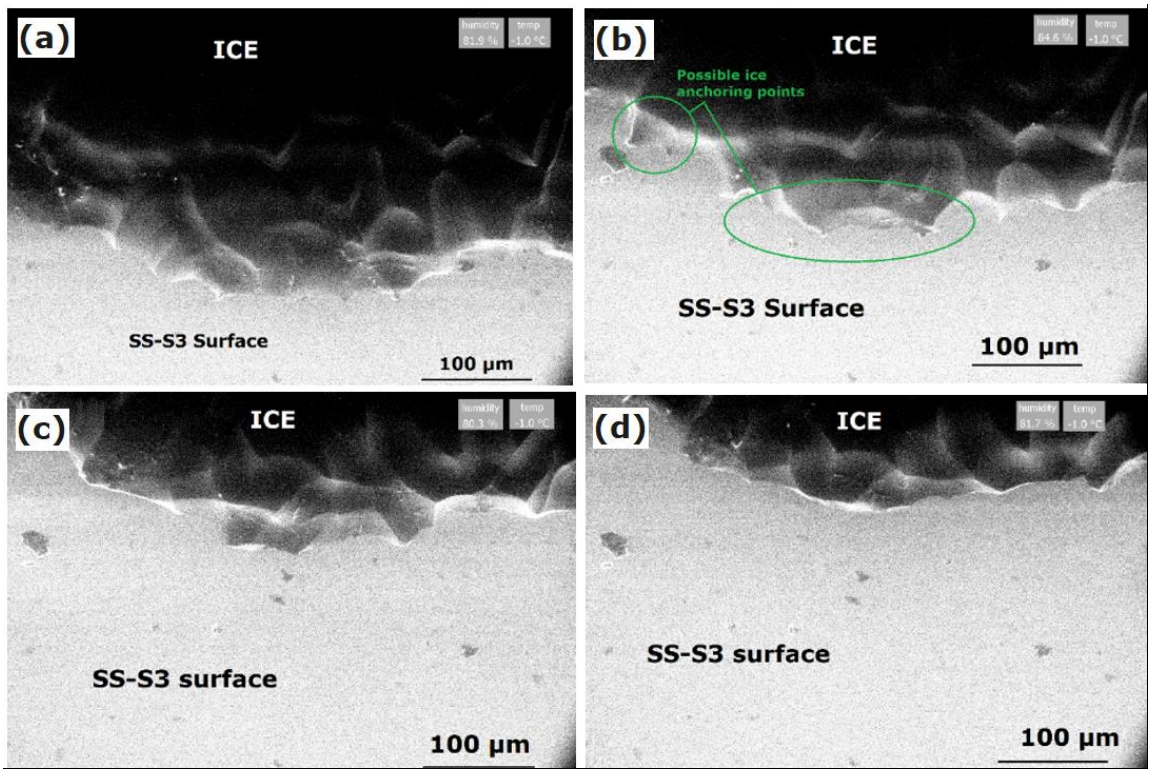


Figure 5.15: In-situ icing retraction on SS-S3 samples after (a) 0, (b) 40, (c) 60, and (d) 80 seconds. The circles in sub-figure (b) indicate the possible ice anchoring points during the ice retraction process.

Uniform formation of ice can be observed in figure 5.15a, and the possible ice anchoring points/sites are identified in figure 5.15b. In figure 5.15c, the ice retracts and does not anchor as previously noted on the as-received metallic substrates. The formed ice continues to retract without anchoring as indicated in figure 5.15d. These are promising

results as they visualise the effect of surface roughness and highlight its importance on ice adhesion strength, which indicates a similar correlation. These studies validate the effect of water micro-condensation on ice adhesion strength and subsequently on icephobic performance.

Superhydrophobic surfaces

SHS-40 coatings had a superhydrophobic surface and the ice anchoring mechanism was evident, as shown in figure 5.16 (green circles). The ice anchoring could also be validated from ice adhesion strength as its ice adhesion strength rose 5.4 times as compared to the SHS-5 surface.

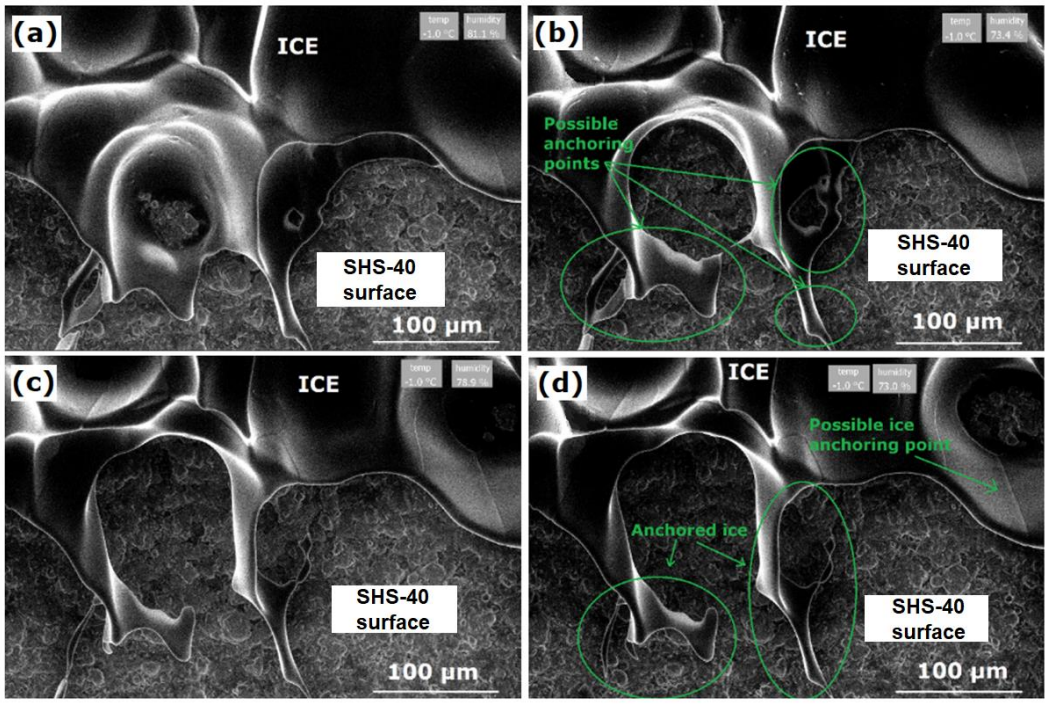


Figure 5.16: In-situ icing retraction on SHS-40 samples after (a) 0, (b) 40, (c) 60, and (d) 80 seconds.

The size of the anchor was considerably large in size (10-30 µm) and was comparable to that of Al-AR substrates, discussed in section 5.5.2. Preliminary results suggest that the

superhydrophobicity of the surface neither had a mitigating effect on the level of anchoring nor prevented the ice anchoring to occur. Figure 5.16a shows the developed ice before the ice retraction process and the possible ice anchoring points during the ice restriction process are marked in figure 5.16b.

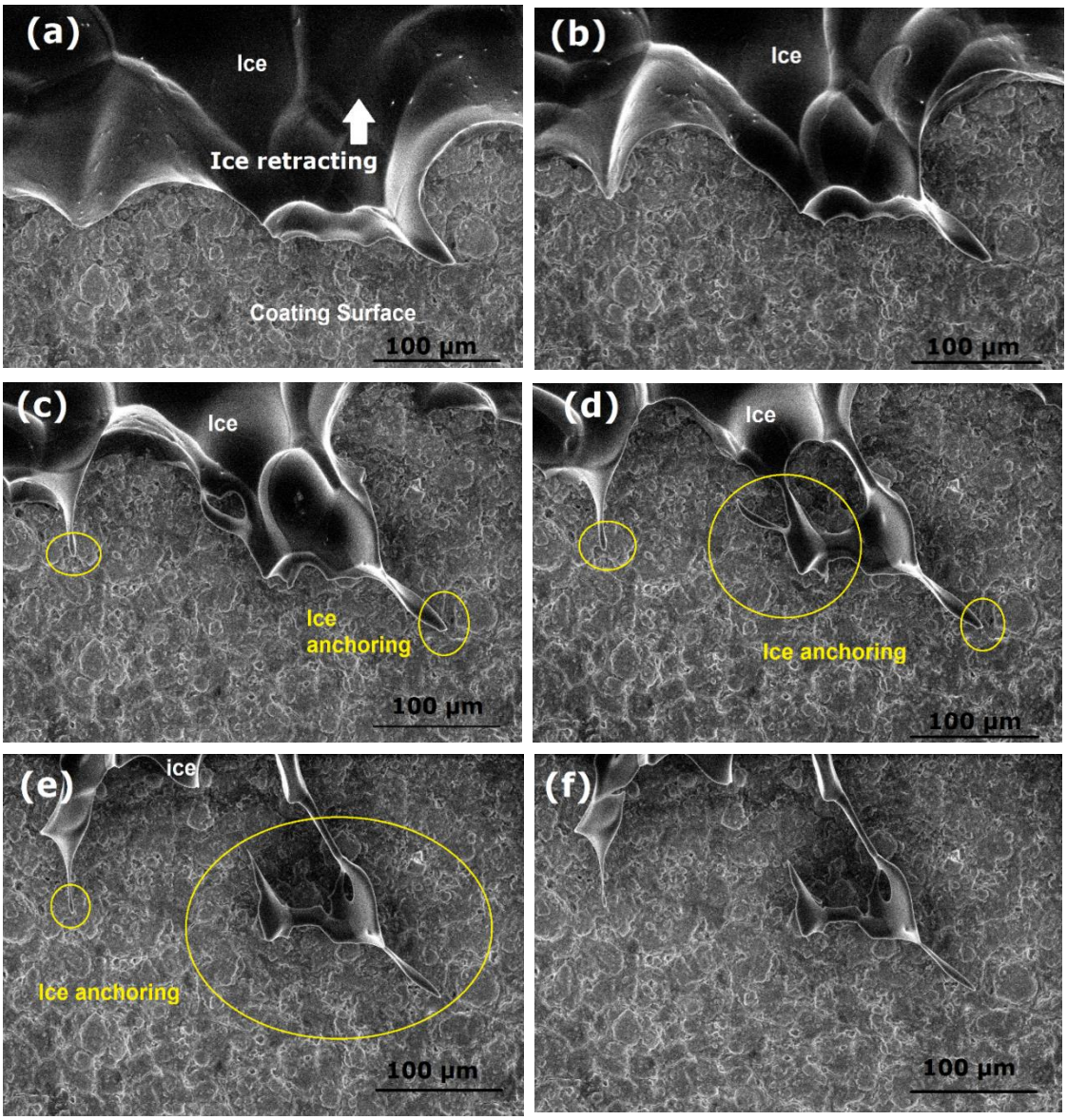


Figure 5.17: Ice anchoring mechanism on SHS-20 samples after (a) 3, (b) 6, (c) 9, (d) 12, (e) 15 and (f) 18 seconds.

This could be the main reason that superhydrophobic surface loses superhydrophobicity/icephobicity as either the water condensates in the void valleys under high humidity conditions and forms thin layer of ice [21, 28], or the shearing of this anchored ice distorts the rougher asperities on the surface. The superhydrophobicity could be mitigated as it is reliant on rough asperities [91, 131]. In either case, the superhydrophobic performance of a coating surface could be nullified which has a domino effect on superhydrophobicity-induced icephobic performance. The developed ice remains even after 80 seconds of ice retraction process as observed in figure 5.16c, and the ice maintained the anchor as observed in figure 5.16d (green circles).

Further tests on the SHS coatings were carried to ascertain the preliminary data, shown in figure 5.17. The ice retraction process this time was accelerated to identify any changes on ice anchoring process using similar SHS coatings. The ice formation over the superhydrophobic surface is still observed in figure 5.17a, although the surface exhibited superhydrophobic behaviour at micro-scale. During the retracting process, which is intrinsically a shearing process [56, 96], some ice stuck or anchored in the rough asperities at the highlighted area of the coating surface as indicated in figure 5.17c-d. This is the first physical and direct visual representation of the ice anchoring process. Through the process, the entire grown ice was retracted but the anchoring of ice over the surface was rigid and stubborn as shown in figure 5.17e-f.

TPU nanocomposite coatings

The ice retraction process on the TPU-10BN surface demonstrated a different ice retraction mechanism, as shown in figure 5.18. In figure 5.18a, instead of retracting outward towards the edge of the coating (as observed on other coatings/surfaces), the ice

simply started the melting at the accretion positions. In figure 5.18b, the ice was melting in fragmented sections and smaller patches of ice were anchored on the surface as indicated. These patches of ice became more visible in figure 5.18c, and these patches stayed on the observed surface even after the big blocks of ice were completely melted (figure 5.18d). These results depict the intense and stubborn ice anchoring mechanism. In comparison to the ice adhesion strength results, TPU-10BN did not show higher ice adhesion strength which would signify the effect of interfacial cavitation, and the ice detaches due to the soft nature of the polymer matrix.

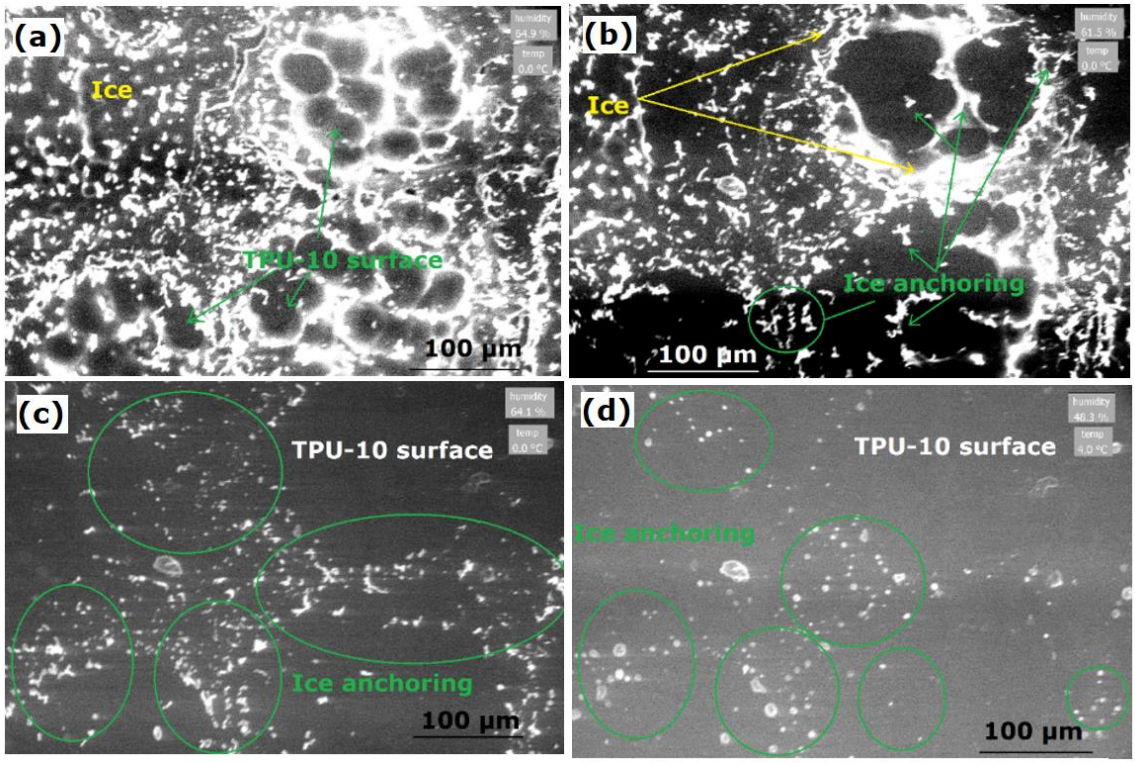


Figure 5.18: In-situ icing retraction on TPU-10BN samples after (a) 0, (b) 40, (c) 60, and (d) 80 seconds.

Furthermore, as the concentration of hBN particles increased in the TPU-BN nanocomposites, the ice adhesion strength of these nanocomposites nearly equated to that

measured on the SS-AR substrates. Thus, it could be assumed that the inter-facial cavitation became less effective with the hardening of the polymer. A possible explanation for this significant increase in ice adhesion strength is the severity of ice anchoring observed on TPU-BN nanocomposites, which would lead to a stronger ice bond on the surface.

5.6 Mechanism of heterogeneous formation of ice

Ice adhesion strength is dependent on various factors including surface variables, purity of water, and the growth of ice over surfaces (heterogeneous or heterogeneous-homogenous mixed formation of ice) [85, 127]). Previous studies (static type tests) suggested that heterogeneous nucleation is accelerated if the interfacial correlation factor $f(m, R')$ is altered by increasing the effective area of contact or by changing the wettability of the surfaces. The interfacial correlation factor (i.e. the probability of ice nucleation) is defined through two parameters, m and R' [225]. m is defined as,

$$\mathrm{m} = {(\gamma_{\mathrm{sf}} - \gamma_{\mathrm{sc}})}/{\gamma_{\mathrm{cf}}} \approx \cos\theta^0 \ (-1 \leq \mathrm{m} \leq 1) \qquad (4.1)$$

where γ_{cf}, γ_{sc} and γ_{sf} are the interfacial energies between the crystal phase and the fluid phase, the substrate and the crystal phase, and the substrate and the fluid phase respectively, and θ^0 is the contact angle of the ice nucleus on the substrate. R' is defined as

$$\mathrm{R}' = {\mathrm{R}}/{\mathrm{R_c}} \qquad (4.2)$$

where R is the radius of a flattened surface and R_c are the critical radius of the nuclei on the surface (at a specified temperature and nucleation condition). When $R \geq R_c \, sin\theta^0$,

the contact angle (where θ^0 is the contact angle of the ice nucleus on the substrate) remains unchanged on the surface and when $R < R_c\ sin\theta^0$, the contact angle grows at a rate of $sin^{-1}\left({}^{R}/_{R_c}\right)$ as it is limited due to geometric restriction of the surface [225].

Thus the interfacial correlation factor is dependent on the ratio of the radius of a surface to the critical radius of the surface (R'), and on the synergetic effect of the wettability of the surface and interfacial free energies (water/ice-surface) (m). It is assumed that the introduction of low surface energy without changing surface roughness will not significantly prevent ice nucleation. Furthermore, our results also indicated that the surface roughness is a more dominating factor than the effective area and the wettability.

It is reported that ice nucleation can be annihilated or significantly delayed by deploying surface with roughness close to or smaller than critical ice nuclei size (1.2 nm – 2 nm under supercooling) [29, 76]. The rate of ice nucleation over the surface depends on homogenous and heterogeneous nucleation barriers [30, 226]. It is important to control or minimize the heterogeneous nucleation rate, which is mainly influenced by foreign particles present in the water and on the surface, interfacial energies among the surface, and interaction of the liquid/solid and surface geometries. By favouring the homogenous nucleation, the need to control effective contact area as required by superhydrophobicity-induced icephobicity methods [225] could be eliminated. Previous studies have indicated the surface roughness (R_a) of less than 100 nm [76, 86, 87] is instrumental to induce anchor-free ice nucleation over the surfaces and the annihilation of ice nucleation may be possible on surfaces with roughness less than 10 nm [8, 29].

5.7 Summary

The effects of rough asperities on ice anchoring were long speculated in icephobicity studies but no direct validation was reported. In this chapter, the systematic reduction of ice adhesion strength was demonstrated with the decrease of surface roughness regardless of surface wettability, including on a range of surfaces. On metallic surfaces, ice adhesion strength was reduced dramatically by lowering the surface roughness, without any surface coating and functionalisation. For aluminium specimens, surface roughness was reduced by 24-fold which resulted in an 11-fold or ~91% reduction in ice adhesion strength. Moreover, the studied PDMS and PU coatings are hydrophobic and hydrophilic, respectively. However, their ice adhesion strengths did not change considerably. On the contrary, low surface energy treatment on the surface showed a direct reduction of ice adhesion strength.

Furthermore, the ice anchoring mechanism on surface voids was validated in the present work via in-situ icing observations, and it was shown that surface roughness directly contributed to ice anchoring. On the Nano-SiO_2/PDMS coatings, the water formed along the rough asperities and surface cracks of the coatings which imparted ice anchoring and acted as seeds for heterogeneous ice nucleation. Strong visual evidence of the ice anchoring mechanism over surfaces has been obtained on these coatings. The results further indicated that the ice did not anchor on smoothened metallic surfaces but anchored on the as-received metallic surfaces and polymeric coatings.

The results obtained in this chapter demonstrate the synergetic effect of surface roughness and surface energy/interfacial cavitation on ice adhesion strength (in line with the interfacial correlation factor), and the fact that the ice is likely to anchor on rough

asperities. Interestingly, the CAHs of all the studied surfaces (except pristine polymeric and superhydrophobic coatings) were strongly correlated with ice adhesion strength below a surface roughness of R_a 0.4 µm.

Chapter 6

Development of durable reinforced polyurethane coatings

6.1 Introduction

Polymeric surfaces and coatings have been a popular choice for passive ice protection and many reports have indicated low ice adhesion strength on polymeric coatings and surfaces [17, 227]. It was established in Chapters 4 and 5 that the surface characteristics play a crucial role in imparting icephobic performance and low ice adhesion could be achieved by a synergetic effect of low surface roughness and low surface energy or via interfacial cavitation. The smoother and softer polymer could pave way for the easy release of ice, whereas, the icephobic performance is not dependent on a certain range of surface roughness. Polymeric coatings, such as polydimethylsiloxane (PDMS) and polyurethane (PU), could be the major candidates in the development of icephobic coatings [141, 228, 229]. However, limited efforts have been paid to the durability of the coatings and their capability to maintain icephobic performance after erosion impact. The key application areas of icephobic coatings are in aerospace and wind energy, both of which involve rigorous water droplet erosion. The leading edge of aircraft often suffers ice crystals impingement in sub-zero temperatures and/or rain droplets erosion. Wind turbine blades may undergo severe water droplet impingement as well and coating erosion resistance under the working conditions is also critical. Therefore, the designed icephobic coatings need to resist such surface erosion damage (morphological and/or topographical) that may deteriorate the icephobic performance.

Most studies have either conducted icing/de-icing cycles [10, 230-232], chemical stability [71, 180, 233], and/or durability evaluation using mechanical methods (such as abrasion resistance, indentations, scratch tests, and sandblasting etc.) [140, 149, 233-235]. Wu et al. [236] tested their sol-gel coatings by nanoindentation, pencil-scratch resistance, and weight loss rate under different sandblasting conditions, indicating that the measured ice adhesion strength was maintained below 70 kPa after mechanically endured durability tests. Beemar et al. [237] reported an ice adhesion strength at around 6 kPa, even after 1000 abrasion cycles on a PDMS gel surface. Zhuo et al. [238] measured an increase in ice adhesion strength from 12 kPa to 20 kPa after 800 abrasion cycles on a PDMS coating. Liu et al. [239] carried out an impinging study on a PDMS nanocomposite coating using a silicon carbide suspension at 37 m/s velocity and a liquid flow rate of 72 mL/min, but did not re-evaluate the ice adhesion strength after the impinging erosion. Furthermore, the research interest to explore the inclusion of hard materials in a soft polymer matrix is overwhelming, and many studies have been conducted to investigate the mechanical properties of composites reinforced with fibrous and/or nano inclusions [140, 149, 233-235]. These reinforcing techniques could be explored to improve the mechanical properties and durability of icephobic coatings, especially under the erosion impacts.

In this chapter, polyurethane-based low ice adhesion coatings were formulated and reinforced with nanoparticles and micro-fibres. Polyurethane is a relatively durable material, as compared to other studied icephobic candidate materials and offers a smoother morphology and the material flexibility needed for anchor-free de-icing performance. The main aim of this study was to explore an effective approach to enhance

the durability of PU-based icephobic coatings. The incorporation of micro-fibres and nanoparticles in this work was driven by the need to enhance durability in surface icephobicity under erosion impact, even after non-ignorable material damage. Water impinging tests using silicon carbide (SiC) particle suspension were used to simulate the water droplet erosion. It was suggested that the inclusion of fibres was more beneficial in this context than the nanoparticles. The addition of fibres helps to distribute the droplet impact energy more widely across the polyurethane matrix and helps to reduce the stress concentration points on the coating surface by minimising crack initiation during the incubation period. Thus, less ice anchoring on the surface would be formed, leading to easier ice removal and maintaining the desirable icephobic performance even after the erosion impacts.

6.2 Microstructural characterisation of the reinforced coatings

As the material suffers erosion attack, the impinged surface may generate some ice anchoring points which would increase ice adhesion strength. The changes in the surface morphology on all the coatings as a result of the impingement are discussed in this section. The surface roughness were also measured and listed in Appendix B.

6.2.1 Pure PU-5 coatings

The microstructural images of the pristine PU coatings and their surface after Water impingement erosion tests (WIETs) are shown in figure 6.1a. The PU coating studied in this chapter (PU-5) was a pre-selection of low ice adhesion type and the complete list of examined PU variants are mentioned in table 3.2. It is evident that the surface morphology had been significantly altered and the surface was much rougher after WIETs. The impinging water droplets and SiC particles created cavities on the surface as

shown in figure 6.1. The surface roughness (R_a) also drastically increased from 0.08 µm to 0.45 µm on the PU coatings after WIETs. The pure PU coating was also studied over a larger area and the 3D profile of an impinged PU coating is provided in Appendix A. The figure shows a valley where the cavities are ~25-80 µm deep, making them easy to induce mechanical interlocking of ice. The initial water condensation and subsequent ice formation had been observed in the surface cavities as discussed in Chapter 5.

6.2.2 Nanocomposite coatings

The surface morphology of PU-ND-3 coatings (figure 6.1b), has also changed considerably after WIETs. The reinforced-PU nanocomposite coatings used in this chapter and their reinforcement information are detailed in table 3.3. The coatings are titled as PU-XX-YY, whereas XX is the filler type and YY is the weight percentage. The surface morphology of PU-GR-3 after WIETs is shown in figure 6.1c. The PU-GR-3 and PU-ND-3 coatings had surface roughnesses (R_a) of 0.1 µm and 0.07 µm respectively before WIETs, and a clear increase in surface roughness to 0.21 µm was observed on both nanocomposite coatings after WIETs.

Notably, the change in surface roughness was much lower than that observed on the pure PU coatings, indicating that the incorporation of fillers resisted the erosion attack on the nanocomposite surfaces. A mixture of cracks and cavities were formed after WIETs on the surface of PU-ND-3 coating, instead of the cavities observed on the pure PU coatings in figure 6.1b.

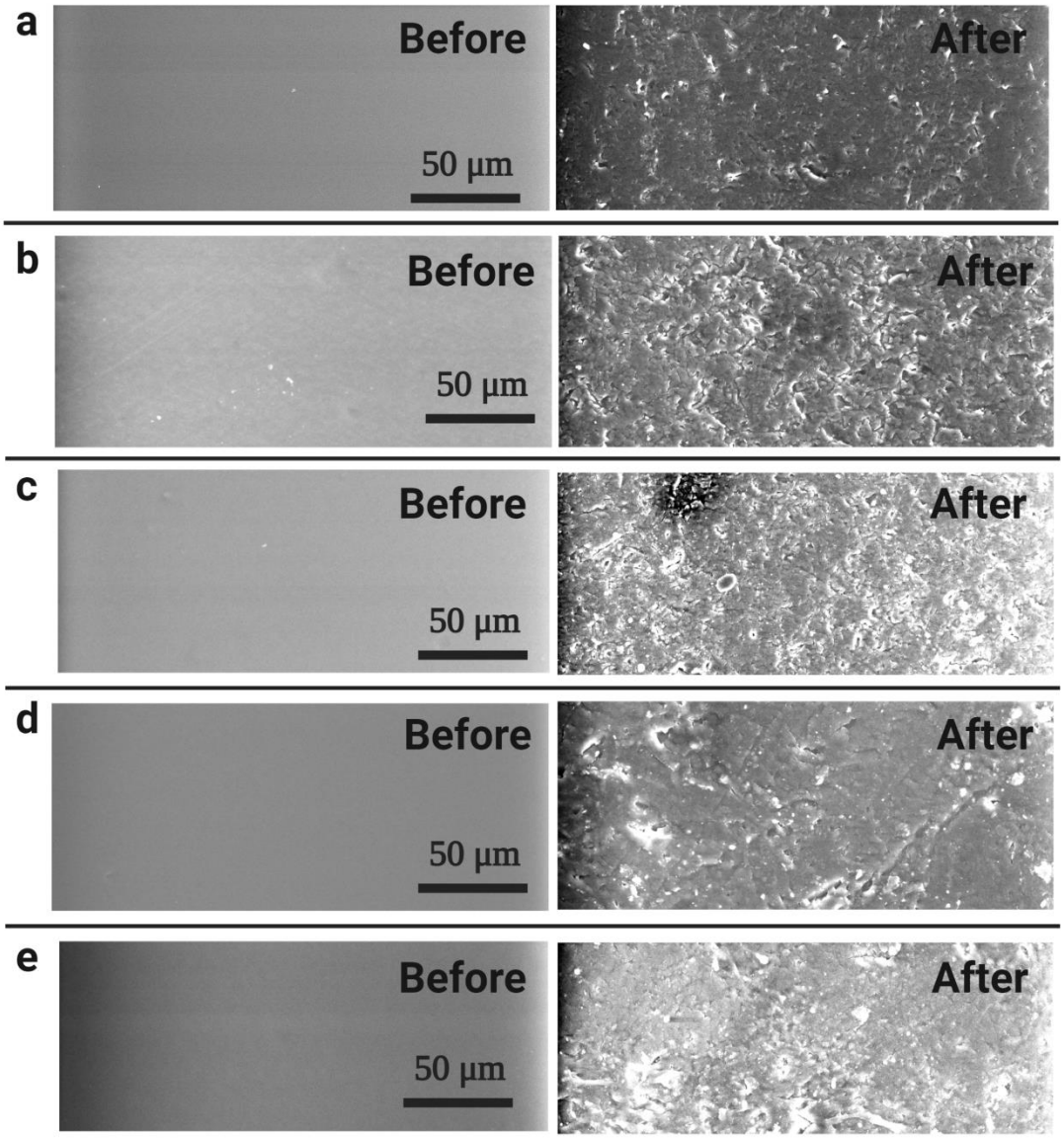


Figure 6.1: Microstructural images of before and after WIETs on the (a) pure PU, (b) PU-ND-3, (c) PU-GR-3, (d) PU-KV-3, and (e) PU-CF-3 coatings. All images have the same scale bar.

The 3D surface profiles of PU-ND-3 and PU-GR-3 are provided in Appendix A. The depth of cavities is considerably reduced on both nanocomposite coatings as compared to the pure PU coatings, and the cavities are up to 25 µm deep.

6.2.3 Fibre-reinforced composite coatings

The microstructural image of PU-KV-3 coatings after WIETs is shown in figure 6.1d. The fibre-reinforced PU coatings used in this chapter and their reinforcement information are detailed in table 3.3. The coatings are titled as PU-XX-YY, whereas XX is the filler type and YY is the weight percentage. A similar image after WIETs on PU-CF-3 coatings is shown in figure 6.1e. Surface roughness (R_a) changed from 0.07 µm on PU-CF-3 coatings to 0.27 µm and from 0.10 µm on PU-KV-3 coatings to 0.25 µm after WIETs. Both impinged fibre-reinforced coatings indicated a larger increase in surface roughness as compared to the impinged nanocomposite coatings. A closer inspection of surfaces of both fibre-reinforced coatings suggests that a significant portion of polymeric surface was largely intact and the fibres were effective to restrain crack initiation, significantly reducing the number of surface cavities.

The material damage around the fibres in the composite coatings is shown in figure 6.3c and 6.3d. The 3D profile of impinged PU-KV-3 surface, provided in Appendix A, indicates the surface damage incurred after the erosion tests. The 3D profile of impinged PU-CF-3 coatings is provided in Appendix A. The cavities on both fibrous coatings appear to be ~40-70 µm in depth.

6.3 Effect of incorporated fillers on coating hardness

Polymeric coatings with low elastic modulus are likely to induce a lower ice adhesion strength [3, 71] and from literature, the incorporation of Kevlar fibres, carbon fibres, nanodiamonds [240-242], and graphene [243] often indicated a significant increase in mechanical properties, e.g. shore hardness and material stiffness, of the polymeric matrix. Thus, it is important to evaluate the coating hardness and understand the degree of

change in hardness with different fillers. Shore hardness values could be used as representative values for elastic modulus [244] and the representative values are equivalent to elastic modulus measured via other typical methods [245]. In this section, Shore hardness of the filled-PU coatings were measured and were compared to that of pure PU coatings. The pure PU coatings exhibited a Shore hardness of 40D, and the incorporation of fillers increased the hardness, especially for PU-KV-5, where 24 points increase was observed to 64D. The incorporation of fillers in PU-GR and PU-CF coatings led to an enhancement of the hardness. However, the increase in hardness was relatively insensitive to the amount of filler as shown in figure 6.2. In the PU-KV and PU-ND coatings, a notable increase in the hardness was observed with increasing filler content. Generally, the inclusion of fillers increased the hardness of the polymeric coatings by 12~62%.

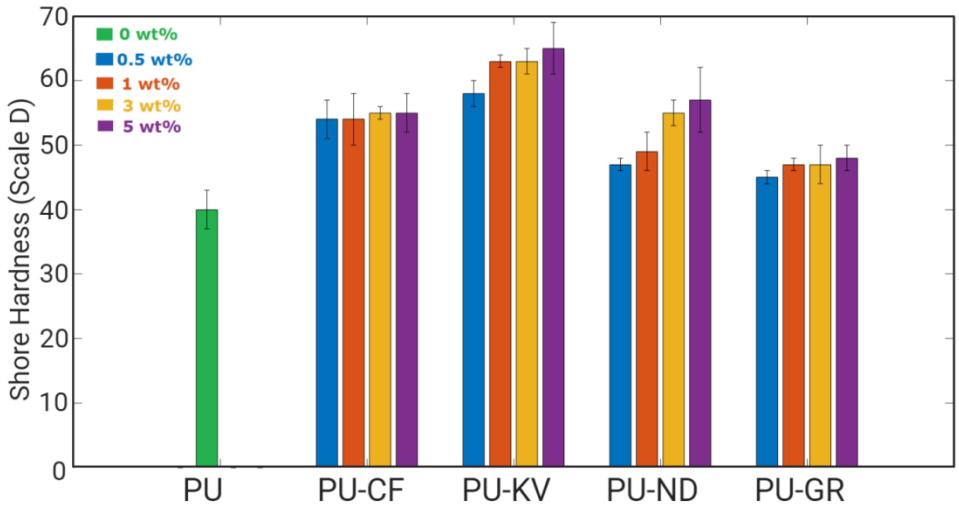


Figure 6.2: Effect of fillers on the Shore D hardness of polymer coatings.

6.4 Inclusion of high weight percentages of fillers

In section 6.2, the coatings incorporated with 3 wt% fibres demonstrated more promising results in terms of maintaining icephobic performance than the equivalent loading of

nanoparticles. In this section, coatings with higher filler contents were prepared to explore the possibility of enhancing the durability of the polyurethane matrix. This could further reduce the number of ice anchoring points and help to maintain low ice adhesion strength.

6.4.1 PU nanocomposite coatings

The incorporation of nanodiamonds in PU coatings was limited to a maximum of 40 wt%. Further incorporation was difficult to process as the formulated solutions were highly viscous, thus, not suitable for the brush application. The composition of highly filled nanocomposite coatings as compared to that of other nanocomposite coatings is detailed in table 3.3.

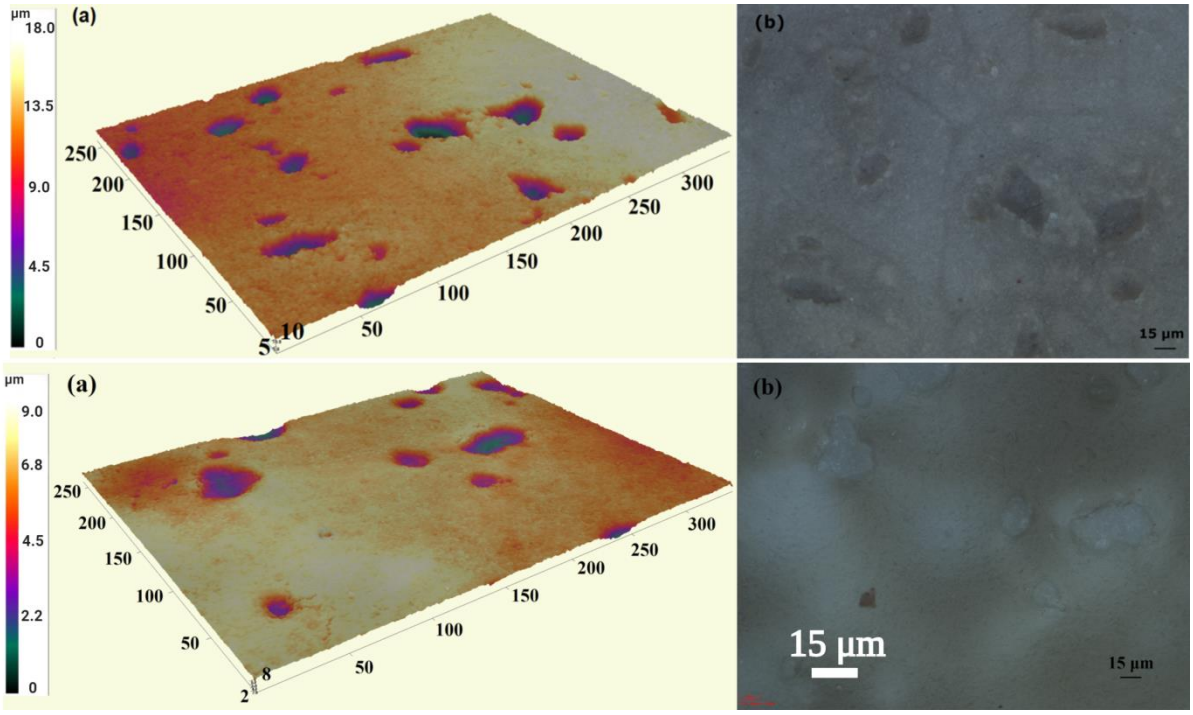


Figure 6.3: (a) 3D profile and (b) 2D image of PU-ND-40 coatings and (c) 3D profile and (d) 2D image of PU-KV-20 coatings after WIETs.

The surface roughness (R_a) changed from 0.21 µm to 0.24 ± 0.03 µm (slight increase) on PU-ND-20 and from 0.21 µm to 0.17 ± 0.02 µm (slight decrease) on PU-ND-40 before and after WIETs. Overall, the surface roughness after WIETs decreased with a higher concentration of nanodiamonds. The surface morphology of PU-ND-40 coating after WIETs and the surface cavities generated are shown in figure 6.3a and 6.3b, and the cavities appears to have a depth of around 13 µm, whereas those on PU-ND-3 surface as ~25 µm deep (the 3D profile is provided in Appendix A).

The morphological changes on PU-ND-3 and PU-ND-20 surfaces are shown in figure 6.1b and 6.4a, respectively. It is clear that the morphological damage on the surface was further reduced with a higher concentration of nanodiamonds and the number of cavities was considerably reduced. Figure 6.4a indicates that the cavities on PU-ND-20 surface, which could be ice anchoring sites, were reduced in both the numbers and the depth when compared to those on PU-ND-3 coatings, as shown in figure 6.1b.

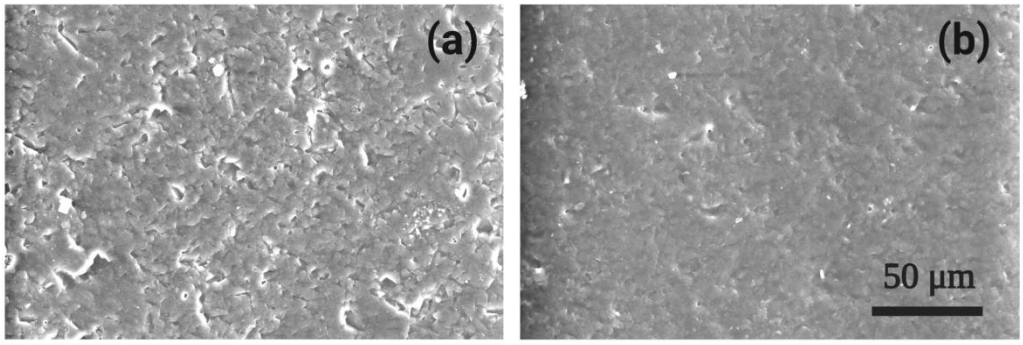


Figure 6.4: Microstructural images of (a) PU-ND-20 and (b) PU-KV-20 coatings after WIETs.

6.4.2 Fibrous PU coatings

A maximum of 20 wt% of Kevlar and carbon fibres were incorporated in the PU matrix, and the microstructural images of both fibre-reinforced coatings after the erosion damage

are shown in figure 6.5a and 6.5b, respectively. The composition of highly filled fibre-reinforced coatings as compared to that of other fibrous coatings is detailed in table 3.3. Both coatings demonstrated promising durability during WIETs and the surface roughness did not change significantly compared to that on as-prepared surfaces. The surface roughness (R_a) on PU-CF-20 coatings changed from 0.12 µm to 0.15 µm after WIETs, and from 0.12 µm to 0.22 µm on PU-KV-20 coatings. The 20 wt% fibre-reinforced coatings demonstrated the lowest increase in surface roughness after WIETs across all the studied coatings. The depth of cavities on PU-KV-20 coatings was in the range of ~2-7 µm, nearly halved in magnitude compared to those on PU-ND-40 coatings.

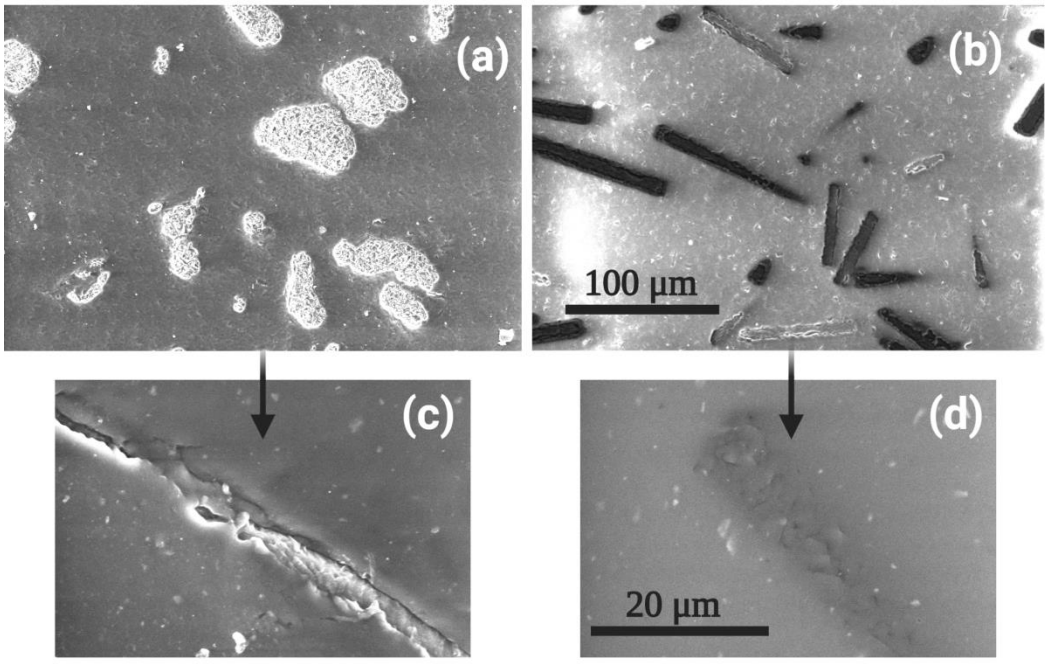


Figure 6.5: (a) PU-KV-20 and (b) PU-CF-20 coatings after WIETs (same scale bar). Possible material damage around the incorporated (c) Kevlar and (d) carbon fibres (same scale bar).

The number of cavities was also reduced on the 20 wt% fibre-reinforced coatings as compared to those on the 3 wt% fibre-reinforced coatings. A comparison between PU-KV-3 and PU-KV-20 coatings is shown in figure 6.1d and 6.4b. The high filling of fibres in polyurethane coatings was in favour of resisting the microstructural damage caused by the erosion. Less number of surface cavities was observed on the 20 wt% fibre-reinforced coatings, and the depth of the cavities was also reduced. In terms of fibres, carbon fibres in this study were more effective in resisting the morphological changes when compared to Kevlar fibres, as shown in figure 6.5a and 6.5b. Figure 6.5 also indicates an obvious size reduction of the cavities on PU-CF-20 coatings and the size of cavities is significantly reduced (around 10 μm).

6.5 Impact of water erosion tests on ice adhesion strength

Many researchers have used cyclic de-icing tests to evaluate the icephobic performance of the coatings [10, 230-232] and abrasion tests to evaluate the durability of icephobic coatings [140, 149, 233-235]. However, the impingement test is more representative of realistic application conditions to evaluate the coating durability when considering the potential applications in aerospace and wind turbine. The ice adhesion strengths, before and after WIETs, on specific coatings are shown in figure 6.6d. Generally, the coating hardness had a direct effect on ice adhesion strength.

6.5.1 Evaluation of as-prepared coatings

The ice adhesion strengths on all the as-prepared samples were less than 7 kPa, except for PU-KV-0.5, PU-KV-20, and PU-GR-5 coatings, as indicated in figure 6.6b. Higher ice adhesion strengths on PU-KV-20 and PU-GR-5 are thought to be due to the changes in morphology resulted from the higher filler concentrations. PU-KV-0.5 is an exception

and its relatively high ice adhesion strength may be mainly attributed to surface defects formed during the coating preparation, which is evidenced by the higher surface roughness as listed in Appendix B. A direct relation of ice adhesion strength with shore hardness is drawn in figure 6.6a. For example, the incorporation of 20 wt% of Kevlar fibres in the PU matrix leads to an increase in shore hardness to 78D and a 4-fold in ice adhesion strength was measured. The incorporation of fillers could alter the surface characteristics and influence the ice formation process, as observed in the PU-KV-0.5 coatings. Generally, the ice adhesion strength increased with the incorporation of fillers, but they were mostly kept under 10 kPa before WIETs.

6.5.2 Post-impingement tests

The ice adhesion of the pristine and impinged PU coatings is 2.6 kPa and 83.1 kPa respectively, indicating an approximately 32-fold increase after the erosion. Compared to the values of the pure PU coatings, the ice adhesion strength of PU-GR-3 coatings after WIETs was nearly halved. Similar results were also observed on PU-ND-3 coatings for which the ice adhesion strength changed from 2.7 kPa to 45.4 kPa after WIETs. This value of PU-KV-3 coatings changed from 5.1 kPa to 16.1 kPa after WIETs; while on PU-CF-3, it increased from 5.6 kPa to 16.8 kPa.

Overall, the ice adhesion increased by approximate 3 folds on the 3wt% fibrous PU coatings after WIETs. The incorporation of high filling of nanodiamonds (higher than 3 wt%) resulted in reduced ice adhesion as compared to that of PU-ND-3 coatings. The ice adhesion strength on PU-ND-20 coatings decreased from 39.9 kPa to 28.9 kPa on PU-ND-40 coatings. The increase in ice adhesion on PU-KV-20 and PU-CF-20 coatings after WIETs was 1.4 fold and 2-fold, respectively. Compared to the pure PU coatings, a ~10-

fold reduction in ice adhesion strength after WIETs was obtained on the PU-CF-20 coatings, whereas it was a ~5-fold reduction on the PU-KV-20 coatings.

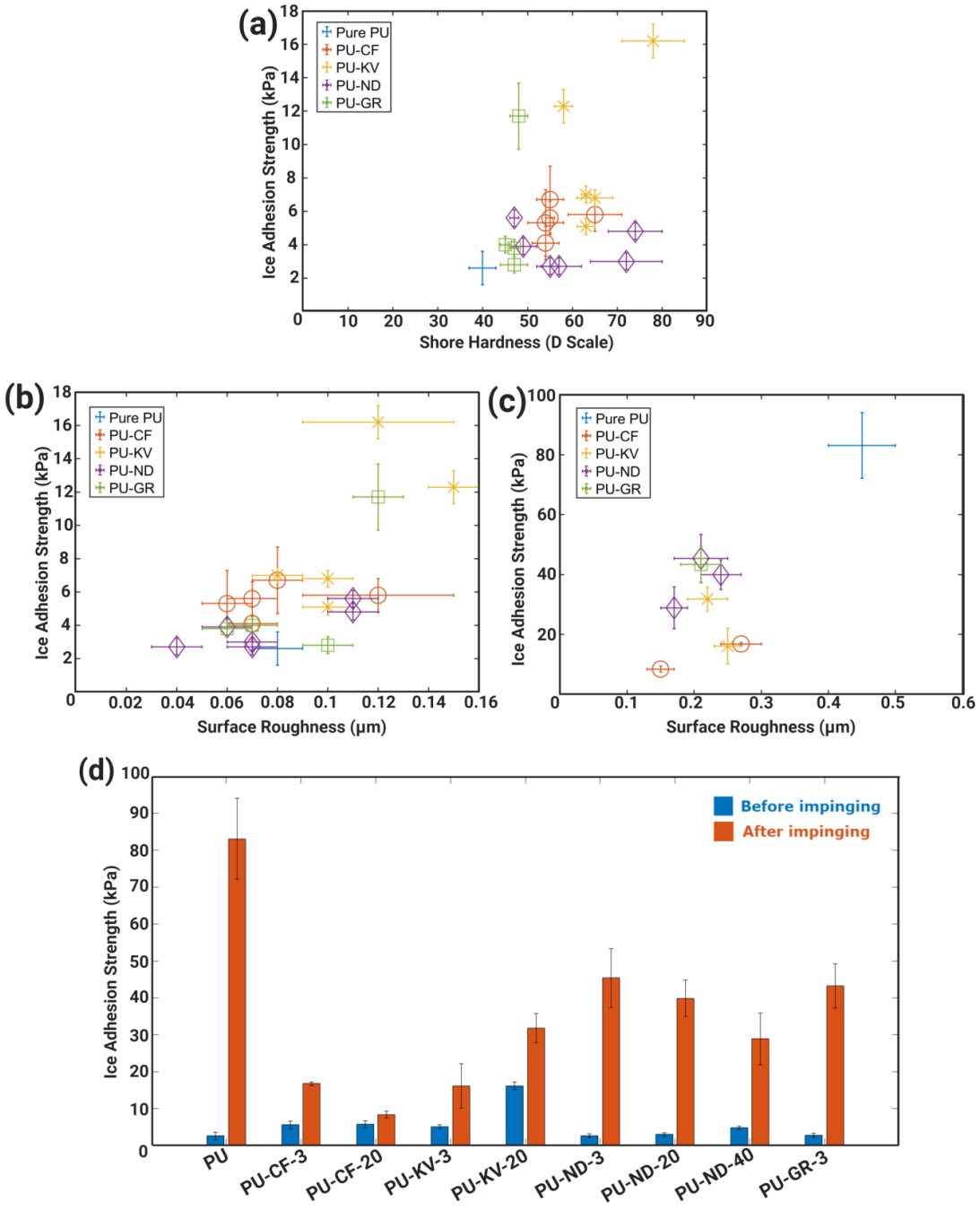


Figure 6.6: Ice adhesion strength in comparison to (a) Shore D hardness values, surface roughness (b) before and (c) after WIETs. (d) Ice adhesion strength before and after WIETs.

The incorporation of fillers was effective in resisting the formation of larger and/or deeper cavities, as shown in figure 6.1, and the possible ice anchoring was either reduced or weakened. These specific changes in ice adhesion strength indicate that the post-impingement icephobic performance was intrinsically dependent on the filler contents and structures. Fibres are likely to induce less ice anchoring points and fewer microstructural changes after WIETs. The ability of ice to anchor on the surface is highly reliant on the surface roughness, and the post-impingement ice adhesion is plotted against the impinged surface roughness in figure 6.6c. It is evident that the fibre-reinforced surfaces minimised the surface crack propagation and there were fewer anchoring points available, thus facilitating the removal of ice. The figure also highlights the dominating role of surface roughness and no apparent correlation with the relation to shore hardness values is observed. Fundamentally, the inclusion of fillers results in improved durability of the PU coatings. In terms of icephobic performance, it is impressive that PU-CF-20 coatings still maintains the ice adhesion strength below 10 kPa after the silicon carbide suspension impinging erosion, and only a 1.4 fold increase in ice adhesion strength is observed, which is a significant improvement as compared to that on the pure PU coatings.

6.6 Durability enhancement mechanisms

The enhanced durability of the polymeric coatings could be explained in two distant mechanisms: surface characteristics and erosion resistance. Firstly, polymeric coatings with low elastic modulus are often linked to induce a low ice adhesion strength [3, 71]. The Shore hardness in this work indicated an enhanced hardness after the incorporation of fillers, which suggests an increase in the elastic modulus [244]. Thus, the results

obtained in this chapter support the need to lower down the elastic modulus of polymers to induce a low ice adhesion as indicated in figure 6.6a. However, the ice shear mechanism is a complex phenomenon and as the material suffers the erosion attack, the surface morphology randomly deteriorates in a way that could influence the icephobic performance of the coatings. The effect of hardness on de-icing performance becomes more apparent with the deterioration of the coatings, shown in figure 6.6c. The incorporated coatings demonstrated enhanced resistance to erosion attacks and the durability of the coating is subsequently enhanced. Although the enhancement of hardness resulted in a slightly increased ice adhesion, the reinforcement of coatings enhances the durability of the coatings, to maintain low ice adhesion strength after the erosion impacts.

The coatings studied in this chapter were reinforced with different nanoparticles and fibres and the fibres seem to be more beneficial in terms of coating durability. Moreover, in terms of fibre incorporations, carbon fibres seem to be more beneficial as compared to that of Kevlar fibres. For example at 20 wt% fibres loading, the Kevlar-reinforced coatings suffered higher damage, evidenced by the deeper and wider cavities as compared to those on carbon fibres reinforced coatings. The damage on PU-KV-20 coatings could be explained by the fibre interface bonding and the fibre aspect ratio. Firstly, In terms of fibre interfacial bonding with the polymeric matrix, carbon fibres demonstrated higher interfacial strength than Kevlar fibres, as reflected from the eroded coating surface: the carbon fibre was still tightly packed in the polyurethane matrix, whereas the Kevlar fibre was exposed after the erosion impact (figure 6.5c and 6.5d). Secondly, the interfacial bonding of fibres is closely related to the toughening

mechanisms, such as fracture energy and fracture toughness, and the work of fracture would be greatly increased due to covalent bonding between the matrix and fibres [246]. Lastly, the mechanical properties were demonstrated to be strongly dependent on the aspect ratio of the reinforcing fibres, and the aspect ratio of the carbon fibres (~14) used in this work is much higher than that of Kevlar fibres (~3). It is believed that filler with a higher aspect ratio would provide greater resistance against erosion impact [247].

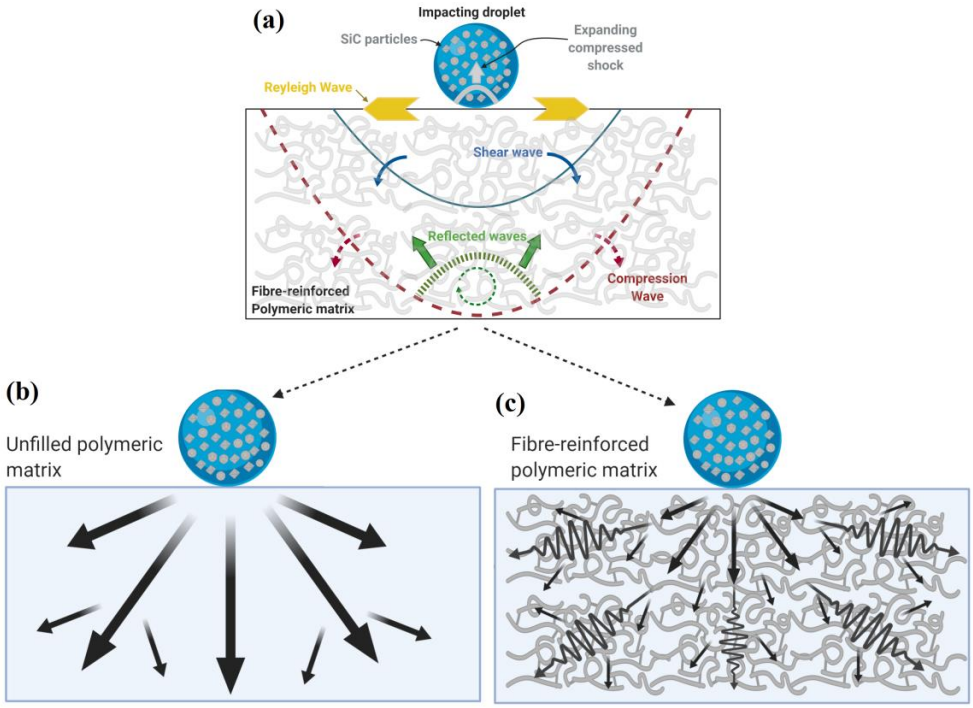


Figure 6.7: (a) Stress waves generated after the impact of a water droplet/sand particles (The mechanism is adapted from [249]) and the stress waves on (b) a pristine polymer and (c) a fibre-reinforced polymer (figure created using biorender.com).

Secondly, the erosion of material induces cracks on the surface. The crack initiation and propagation can be described as a combination of four mechanisms: (1) direct removal of material or deformation caused by the direct high-speed impact; (2) propagation of stress waves across the material; (3) fatigue incurred by the surface with repetitive droplet

impinging; (4) the inability of material to elastically recover (progression into plastic deformation region) before the next impact event [248]. The erosion resistance depends on how the material behaves at the impact zone and how stress waves generated at the impact zone are propagated to the rest of the solid target. These stress waves consist of three multidirectional waves as illustrated in figure 6.7a [249]. The velocities at which these waves propagate depend on the material density, Poisson's ratio and elastic modulus of the target. Microstructural discontinuities also result in enhanced stress waves due to stress concentrations on the surface, and the material may experience structural failure if the stress waves exceed the dynamic fracture strength of the target material [250].

Erosion resistance of the polyurethane coatings, thus, could be imparted by carefully selecting and incorporating fillers in the matrix in order to distribute the stress waves effectively. However, it is imperative to understand the causes that initiate the erosion deterioration in the coatings and which material properties could be linked to erosion initiation. Erosion initiation in wind turbine blades has been widely debated and surface fatigue was identified as a key failure mechanism [251-253]. The fatigue of the coating during erosion can be explained using two mechanisms. Firstly, water impinging is a form of repetitive loading and the fractures are often observed after the spot has been struck by several impacts [254]. In this work, the impingement test consists of a mixture of water with hard SiC particles, and the particles could inflict a higher scratch and cause more damage upon impact as compared to water droplets, as illustrated in figure 6.7b. The depletion and deterioration of the surfaces caused by impinging particles were also observed in figure 6.1, 6.3, and 6.5. Secondly, the fractures caused by erosion could lead

to a fatigue failure [255]. However, Alder et al. [256] indicated that fatigue may play a secondary role. They found that the topological changes in the surface or crack initiations during the incubation period are the main factors that accelerate the erosion rate. Thus, erosion resistance could be imparted in the polymeric coatings by deploying materials and/or incorporation of fillers that limits crack initiation and propagation, and preventing the generation of stress concentration points which may accelerates the erosion rate [257]. These cracks may also prompt the possible formation of ice anchoring points, resulting in the mechanical interlocking of ice on the surface. Thus, preventing the crack initiations on the surfaces has clear advantages for maintaining icephobic performance.

High erosion resistance in elastomers is linked to their viscoelastic behaviour and low modulus prevents the pressure buildup, thus avoiding the stress concentrations across the surface, making them a better candidate for heavy rain impact erosions [254]. However, elastomers frequently fail underneath the surface under repetitive loads, while the surface remains intact. The erosion process on the fibre-reinforced elastomeric coatings could be explained by two modes. Firstly, the local resin removal may result in the exposure of fibres to the erosive environment. Secondly, there could be a breakage of fibres as a result of direct impingement and cracks may start to form around and perpendicular to the fibre length as shown in figures 6.5c and 6.5d. Erosion impact on unfilled thermoset polymers induces breakage and massive chunking of resin due to their brittle behaviour. A massive increase in surface roughness was observed on the unfilled PU coatings in this study, as illustrated in figure 6.1a. Instead, the incorporation of fibres in the resins results in chipping and fracture of fibres instead of polymeric fractures, and the composite's ability to withstand repetitive impact loads is greatly enhanced. The degree of surface

cracks can be greatly reduced on the coating surface after the incorporation of fibres. Fibres also hold the polymeric structure in place and provide a discontinuous path for shock transmission through the material as compared to the pure polymeric resin, as simulated in figure 6.7c.

To conclude, the fibre structures in elastomeric coatings effectively distribute the water droplet/sand energy across the composite structures without significant damage to the polyurethane matrix. The inclusion of fibres is also known to prevent crack initiations, making them the ideal candidate for icephobic applications, particularly since cracks serve as possible ice anchoring points. Specifically, carbon fibre reinforced coatings are promising candidates for icephobic applications as they have superior fatigue resistance as compared to Kevlar fibre filled composites [258]. Our experiments confirmed that the carbon fibre reinforced coatings had better erosion resistance and the surface cavities were much smaller on Kevlar fibre-reinforced coatings. Carbon fibre reinforced elastomeric coatings have all four characteristics for ideal durable icephobic coatings: higher erosion resistance, inhibition of surface cracks, ability to resist the plastic deformation, and stiff fibres to withstand against the significant structural loading conditions.

6.7 Summary

A new approach was developed to enhance the durability of low ice adhesion polyurethane coatings in this chapter. The incorporation of micro-fibres and nanoparticles in the coating matrix was driven by the need for enhancing durability in surface icephobicity under erosion impact. Ice adhesion strength after erosion was maintained to a low level with the incorporation of the fillers as compared to the pure PU coatings.

It was found that the fibre reinforcement was more effective in restricting the surface damage as compared to the addition of nanofillers. The ice adhesion strengths on the pristine and impinged PU coatings were 2.6 kPa and 83.1 kPa, respectively. As a comparison, the ice adhesion strength of the PU coatings with 20 wt% carbon fibres slightly increased from 5.6 kPa to 8.4 kPa, essentially keeping the adhesion below 10 kPa even after the erosion, and a ~10-fold reduction in ice adhesion strength was achieved as compared to that of the pure PU coatings. This distinction could be explained by better interfacial bonding and a higher aspect ratio of the carbon fibres in the PU matrix.

The significantly improved icephobic durability of the carbon fibre-reinforced PU coatings could be attributed to the reduced number and shallowed surface cavities. The number/size of surface cavities formed during water erosion, which could act as possible ice anchoring points, were minimised with the incorporation of the fillers. The inclusion of fibres helps to distribute the droplet/sand impact energy more widely which could reduce the stress concentration in the coatings by minimizing crack initiation during the incubation period. The methodology proposed in this work can also be used for the durability enhancement of other polymeric coatings, especially the coatings designed for high-impingement conditions or erosive environments.

Chapter 7

Development of bio-inspired durable ultra-low ice adhesion coatings

7.1 Introduction

Over the last few decades, passive de-icing has been a growing research topic and it has been suggested that inspiration could come from nature to develop a bio-inspired design to mitigate/resist ice formation (anti-icing) and/or to remove the formed ice easily (de-icing). Several bionic ideas inspired by mussels [259], and frog skin [260] were put to test to aid icephobicity and promising results were reported. Biomimetic designs were also inspired by fish proteins, such as the use of anti-freezing proteins (AFPs) to reduce the supercooling point and to delay the ice nucleation process over the surfaces. Two typical approaches were used: directly grafting AFPs on functionalised surfaces [16, 261], and mimicking the ice depressing effect of AFPs using the direct infusion of cryoprotectants on low-surface energy functionalised surfaces [262, 263]. The direct role of AFPs on ice nucleation or ice adhesion is questionable as hydrophobicity-induced icephobicity [141, 162, 229] and solid/liquid interfaces [16, 261] play an influential part.

Apart from bio-inspired concepts, slippery liquid-infused coatings/surfaces have gained significant popularity among the research community [148, 172]. The fabrication of slippery surfaces can be achieved by either a physical infusion of liquids in the polymeric matrix or by impregnating the surface asperities. In both cases, the infused liquid works

to weaken the ice/surface interface, by either delaying the ice formation or by forming more loosely bonded ice on the surface. The formation of loosely anchored ice on the surface could be attributed to the reduction in the number of available surface cavities since these are levelled due to liquid impregnation; this may hinder the anchoring of ice in the surface asperities. Furthermore, the use of a smoother morphology has already been explored in chapter 5 and 6 to create low ice adhesion surfaces.

The use of AFPs-inspired coatings or liquid infused coatings poses performance challenges such as coating durability and liquid retention inside a material matrix. For example, several studies indicated the depletion of infused liquid after cyclic de-icing tests or mechanical durability tests [264-267]. Thus, there is a need for an effective material system or mechanism that could work to provide the necessary durability, help with liquid replenishment, and maintain a soft and smooth surface to induce interfacial cavitation/anchor-free ice [3, 267].

In nature, cetacean skin is characterised by a number of microscopic qualities such as smoothness, the lack of hair follicles, and lipid-infused surfaces, which emits oil to improve hydrodynamics. On top of these qualities, the skin consists of keratins, collagen and elastin fibres that work to provide mechanical strength and elasticity to the skin. These fibres make the skin more adaptable to repetitive loads (without undergoing a plastic deformation). The concept of fibre reinforcement, mimicking collagen fibres, could also be used for icephobic surfaces to improve their structural and mechanical response, in continuation of the work conducted in chapter 6. Furthermore, a microscopically smooth surface could be beneficial for anchor-free ice nucleation, and if a weaker or reduced number of ice anchors do occur, then the softer or flexible material

could induce interfacial cavitation to pave the easy path for ice to release. These concepts were examined in detail in Chapter 4. Additionally, the concept of lipid droplets, hosted in cetacean skin, can be further mimicked, such as the infusion of a liquid in the flexible material matrix and the selection of liquid can be specifically made to reduce the supercooling point, like chionophiles which emit a cryoprotectant to depress the ice nucleation. Hence, the idea of combining an infused ice-depressing liquid in a reinforced polymer composite could significantly weaken or even inhibit the ice/solid interfaces, whereas the reinforcements could provide necessary durability to maintain the icephobic performance.

In this chapter, the proposed design concept is inspired by the anatomy of cetacean skin and the coatings mimicked the structure of the skin. A polyurethane (PU) matrix was used to produce a smooth and soft surface, with the matrix infused by a cryoprotectant, glycerol, to reduce the supercooling point and provide a flexible surface. Carbon fibres were incorporated, along with the infused liquid, to provide strength and mimicking collagen fibres in the skin. The icephobic performance of formulated glycerol-infused fibre-reinforced icephobic (GIFRP) coatings was evaluated using established de-icing and custom-built anti-icing tests, and the tests were repeated after silicon carbide-based water suspension erosion and overnight water immersion, respectively, to determine the longevity of the coatings.

7.2 Bio-inspired coating structure design

Cetacean skin is an elastic material [268] and consists of three layers: the epidermis (top exposed layer), dermis (intermediate thick layer), and endodermis (blubber) [269]. However, the typical distinction between the dermis and epidermis is not as noticeable in

cetacean skin. The typical anatomy of cetacean skin is shown in figure 7.1a. All three layers of the skin consist primarily of collagen and elastin fibres surrounded by the keratins scleroproteins [270]. Most of the skin's mechanical structure, strength, and stiffness comes from collagen fibres and keratins, and the elastin fibres, as the name suggests, provide elasticity and extensibility to the skin [268]. Keratins are insoluble, chemically unreactive fibrous macromolecules and they create very tough disulfide cross-linkages across the epidermis [270]. The proposed GIFRP coatings involve two different types of biomimicry: one aspect to mimic cetacean skin and another to mimic chionophiles.

In the proposed coating design, carbon fibres were incorporated in the PU matrix to resemble collagen fibres interwoven in elastin fibres and keratins. The composition of the proposed coating was detailed in table 3.3. In cetacean skin, elastin fibres and keratins are typically interwoven or arranged in a branching pattern in a collagen fibre matrix as shown in figure 7.1a, to prevent tearing and limit dispensability. The elastomeric matrix is interlinked by stretchable chains (resembling elastin fibres), which could provide the necessary elasticity, and are connected by strong chemical bonds (for example, vulcanisation) [271]. The collagen fibres have high tensile strength (500-1000 kg/cm^2, higher than steel) [272] and the carbon fibres also possess high tensile strength values (35140-35560 kg/cm^2). In other words, the skin is a composite where strong collagen fibres are embedded in a tough elastic elastin fibre matrix that provides the necessary structural strength. Collagen breaks into small segments under load and the fibres disperse the energy along the length of the fibre and prevent the stress from concentrating in one area or transmitting to another fibre segment [271].

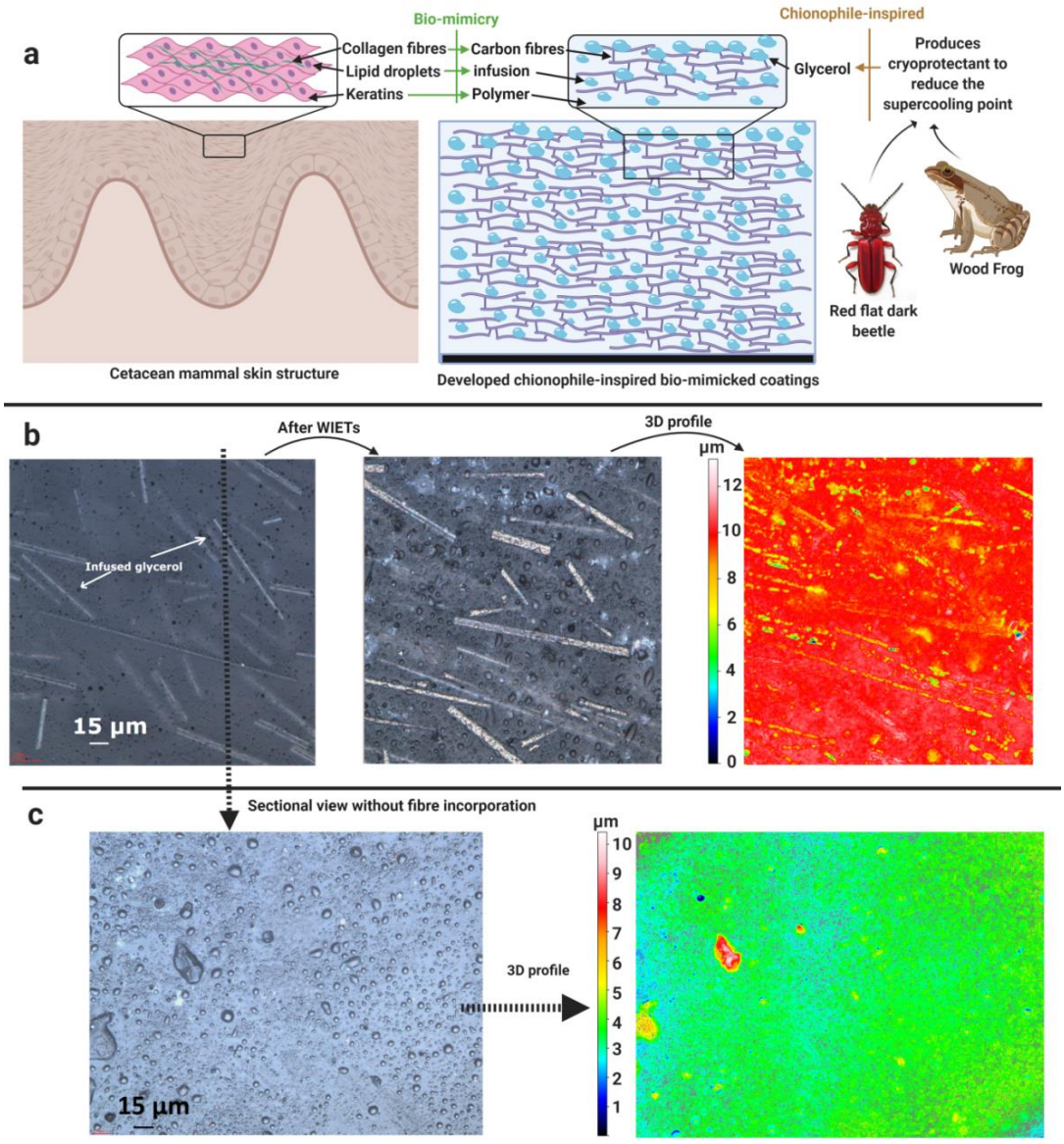


Figure 7.1: (a) The microstructural design of the developed coatings, mimicked by the anatomy of a cetacean mammal skin and inspired by the cryoprotective properties of wood frog and red flat dark beetles, (b) the microstructural image of GIFRP coatings and the same coating after the erosion tests, including a 3D picture, and (c) the sectional view of PU-20gly coatings (after it is cut) and their 3D profile (created using Biorender.com). Interestingly, fibre-reinforced polymeric coatings also exhibit similar behaviour under load, dispersing the energy along the fibre length and fibre-breakage under the erosion

impacts [273]. The impacts on the polymeric matrix results in the chipping and fracture of fibres instead of material fractures, thus, the composite's ability to withstand repetitive impact loads is greatly enhanced.

The top exposed layer of the cetacean skin epidermis provides an elastic and relatively smooth surface. This kind of skin completely lacks hair follicles which would otherwise increase drag in the water. Another important epidermal relationship for the cetacean lies in the variable elasticity of the skin itself which could be attributed to the high ratio of elastin fibres in the dermis [270]. Smoother surface or lower elastic modulus in elastomeric coatings could be utilised for easy release of ice [3, 267], whereas the lack of surface anomalies, like the absence of hair follicles in cetacean skin, means that ice is hard to anchor or discouraged towards heterogeneous ice nucleation.

Interestingly, the cetacean skin structure also hosts phospholipid-rich cornified layers in the form of lipid droplets [274]. The presence of these lipid droplets in cetacean skin improves hydrodynamics by continually exuding oil droplets which help to lubricate the skin allowing the water to pass more smoothly. Similar to the diffusion of oil droplets in cetacean skin, the proposed GIFRP coating will host a number of glycerol droplets as shown in figure 7.1a and these droplets could be slowly diffused on the surface to impart and maintain icephobicity. Glycerol is categorized as a cryoprotectant and is known to repress the freezing point of water and enhance supercooling [275]. Thus, the presence of glycerol on the surface may weaken the ice/surface interfaces, which could reduce ice adhesion strength. The inclusion of glycerol is inspired by chionophiles such as the wood frog and red flat dark beetles that use polyhydric alcohols to prevent extracellular ice formations by colligative action of cryoprotectants and regulate the freeze concentration

of cells from reaching an injurious level [276]. For example, the beetles produce antifreeze glycolipids and proteins and lower the supercooling point. They go into diapause and inhibit the ice nucleation by producing multimolar concentration glycerol that protects them from freezing [277]. The presence of glycerol on the proposed surface is intended to repress the ice nucleation as glycerol forms stronger hydrogen bonds with water molecules and works to disrupt the ice crystal lattice formation by competing with water-to-water hydrogen bonding unless the temperature is significantly lowered [278]. The presence of glycerol to impart icephobicity is ensured by a uniform distribution of glycerol pockets in the coating matrix and the slow diffusion of glycerol on the surface.

To summarise, carbon fibres were incorporated in a PU matrix to mimic cetacean skin's anatomy and the infusion of glycerol was inspired by chionophiles as illustrated in figure 7.1a. The fibre-reinforced polymers impart overall durability and the infusion of glycerol is intended to create super-cooling conditions that may inhibit/resist ice nucleation and may work to form weaker ice/solid interfaces.

7.3 Microstructure analysis

The microstructural image of GIFRP coatings is illustrated in figure 7.1b. The composition of liquid-infused and fibre-reinforced coatings was detailed in table 3.3. The observation of figure 7.1b indicates that the uniformity of carbon fibres throughout the polymeric matrix and the glycerol pockets are in sizes of 0.1-2 μm. The incorporated fibres in the elastomeric matrix resemble the arrangement of collagen fibres interwoven in the cetacean skin. Additionally, the presence of glycerol pockets resembles that of lipid-rich droplets in the cetacean skin, which may act as a reservoir to ensure a layer of glycerol on the surface, whereas a continued presence of glycerol on the surface may

induce a chionophilic response. To understand the uniformity of the glycerol pockets in PU-20gly coatings, free-standing layers of similar thickness (4 mm) were fabricated. These layers were then bifurcated using a sharp blade and the glycerol infusion through the coating thickness was observed via a scanning electron microscope (SEM) system. The sectional view of PU-20gly coatings is shown in figure 7.1c. The figure clearly indicates that the glycerol was uniformly distributed and the coating's capability to retain the liquid inside the polyurethane matrix. The sectional uniformity of glycerol pockets distribution observed on PU-20gly coatings could be assumed for GIFRP coatings as there was no disparity in coating application methods. The microstructural images of other polymeric coatings and as-received aluminium substrates (Al2024), which were also used for a comparative purpose, are also provided in Appendix A.

The surface roughness (R_a) on pure PU coating (PU-5) was measured at 0.08 ± 0.01 µm. The composition of pure PU-5 coatings was detailed in table 3.3. The inclusion of glycerol generated liquid pockets in the polyurethane matrix and the surface roughness changed to 3.2 ± 0.07 µm. The surface roughness on PU-20gly coatings, excluding the glycerol pockets, was measured at 0.14 ± 0.05 µm and including glycerol pockets at 3.2 ± 0.07 µm. The surface roughness (R_a) of 0.12 ± 0.03 µm was measured on PU-CF20 coatings and 0.22 ± 0.04 µm on GIFRP coatings. The surface roughness (R_a) of 0.9 ± 0.01 µm was measured on the aluminium substrates, a higher magnitude of surface roughness as compared to all the polymeric samples used in this chapter.

Surface changes after erosion

The surface morphology of the developed coatings is shown in figure 7.1 and can be explained in two distinctive properties: the change in surface roughness and the glycerol

retention after water impinging erosion tests (WIETs). Firstly, the surface roughness (R_a) on pure PU coatings changed from 0.08 ± 0.01 µm to 0.45 ± 0.05 µm after WIETs and from 0.14 ± 0.05 µm to 0.7 ± 0.1 µm on PU-20gly coatings. As compared to pure PU coatings, the change in surface roughness (R_a) after erosion attack was greatly reduced on the fibre-reinforced coatings, indicating the incorporation of fibres mitigated the erosion impact. The microstructural images of GIFRP coatings and the same coating after the erosion tests are shown in figure 7.1b. The surface roughness of PU-20CF coatings changed from 0.12 ± 0.03 µm to 0.15 ± 0.02 µm after WIETs. Whereas on bio-inspired GIFRP coatings, the surface roughness increased from 0.22 ± 0.04 µm to 0.32 ± 0.04 µm after WIETs. It is imperative to mention that the infused liquid seems to have been retained on GIFRP coatings after the erosion tests, observed in figure 7.1b. The coatings could have either exposed the infused glycerol after the erosion or furnished it via a slow-releasing mechanism.

7.4 Evaluation of Shore hardness

Shore hardness measurement conducted on the coatings showed that the hardness on pure PU coatings decreased from 40D to 33D after the inclusion of glycerol, whereas on fibre-reinforced coatings, it decreased from 65D to 54D. Thus, the hardness of the coatings decreased with the liquid infusion and the hardness values obtained on the fibre-reinforced coatings are higher than those of pure PU or PU-20gly coatings.

7.5 Icephobic performance of fibre-reinforced liquid infused coatings

7.5.1 Evaluation of static anti-icing properties

Water droplet freezing delays

The static water droplet icing delay was measured on all the studied polymeric coatings including on the aluminium substrates and the results are summarised in figure 7.2a. Distilled water droplets froze in ~7 seconds on the aluminium substrates, whereas the droplets took 44~49 seconds to freeze on pure PU and PU-20CF coatings. The freezing time was significantly delayed on PU-20gly and GIFRP coatings to ~364-372 seconds and the inclusion of glycerol resulted in a ~659% increase in water droplet icing delays as compared to that of pure PU coatings. The incorporation of fibres enhanced the water droplet freezing delay time by ~11% in the case of pure PU coatings and ~2% in the case of the glycerol infused PU coatings.

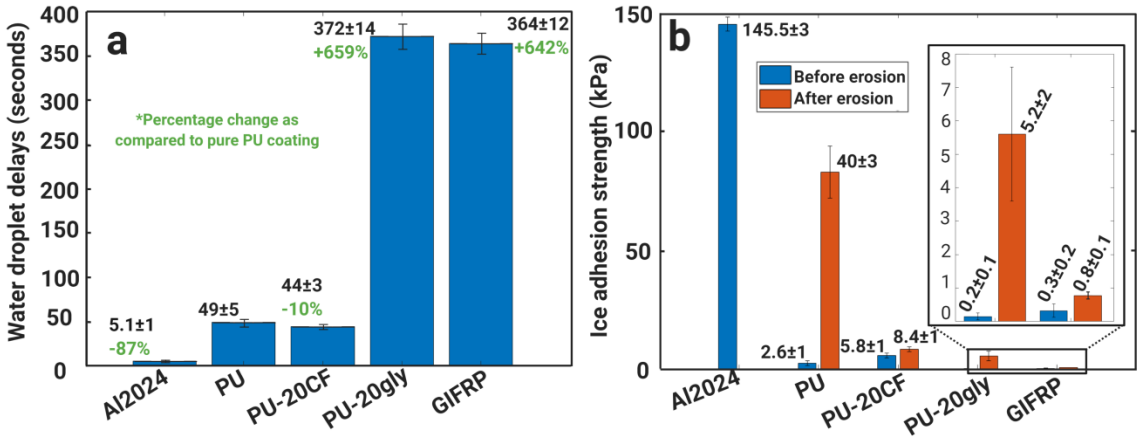


Figure 7.2: (a) Water droplet icing delay and (b) de-icing results before and after the erosion tests on developed and the aluminium samples.

Furthermore, it is imperative to mention that the water droplet icing delay of the eroded samples could be assumed based on the conclusions reached in Chapter 4, where the droplet icing delay correlated with surface roughness values. Thus, a similar water droplet delay on eroded GIFRP coatings is expected as the surface deterioration is significantly restricted using the fibrous biotic design, as detailed in section 7.3.1.

Static frost accumulations

Static frost accumulation tests were also conducted on the polyurethane coatings with and without the inclusion of glycerol. In comparison to the aluminium substrates, PU and PU-20CF coatings demonstrated lower frost accumulation. Both polymeric coatings accumulated ~35-36 mg of frost as compared to 76 mg on the aluminium substrates. Surprisingly, the glycerol infused coatings weighed heavier after the anti-icing tests as compared to the dry PU coatings and resulted in similar frost weight accumulations as the aluminium substrates. The visual inspection of GIFRP coatings in figure 7.3a suggests that the frost accumulation was more like condensate accumulation and the coatings accumulated negligible frost during the test duration. . The increased mass could be justified due to the hygroscopic nature of glyercol, which collected condensated water, mainly during the frost accumulation tests. figure 7.3a also shows accumulated frost on the exposed metal side, signifying the ice depressing role of the fabricated coatings. The glycerol infused polyurethane coatings demonstrated promising anti-icing performance in the static anti-icing tests and the coatings were successful in resisting the frost accumulation/ice nucleation on the coating surface.

7.5.2 Dynamic frost formation

Dynamic anti-icing tests were performed via a custom-made rotatable apparatus at the rotational speeds of 30 rpm and 300 rpm. The speeds of rotatable sample holder were selected to simulate near-static and dynamic conditions and to minimise the effect of enhanced air circulation on frost accumulation. The major difference between the static and dynamic anti-icing tests was the relative movement of samples.

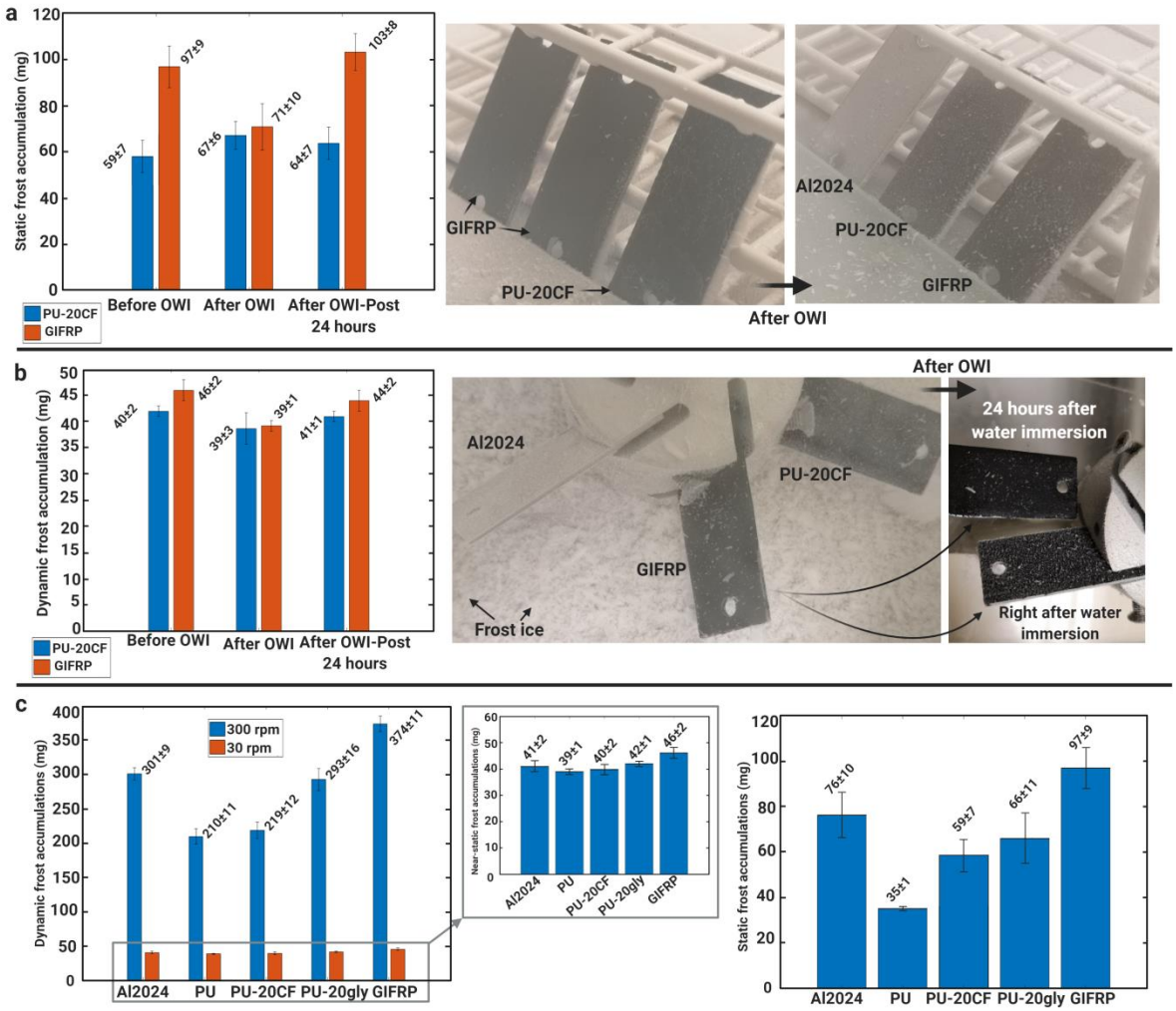


Figure 7.3: (a) The accumulative data on static frost accumulation before and after 24 hours of the overnight water impression tests (experimental details are provided at the end), together with the photos of samples during the tests, (b) the dynamic frost accumulation measurements at 30 rpm speeds and the relevant pictures of samples before and after the overnight water immersion, (c) the distinctions drawn between the dynamic frost accumulations tests at two rotational speeds and a comparison is made with static frost accumulations tests.

In the static test, the samples were placed stationary; whereas in the dynamic test, the samples were mounted on a rotatable sample holder. The results of dynamic frost

accumulation tests on the metallic and polyurethane coatings are summarised in figure 7.3b. On average, the dynamic anti-icing tests generated ~565% more frost at 300 rpm as compared to the tests conducted at 30 rpm. The enhanced frost accumulation could be due to higher air circulation in the chamber as the rotation might have influenced the airflow and resulted in higher accumulations. The frost accumulations did not change significantly on the surfaces at 30 rpm, however, correlated with the results obtained at 300 rpm as shown in figure 7.3c. At 300 rpm speed, similar magnitudes of frost formation of ~210 mg and ~219 mg were observed on PU and PU-20CF coatings, respectively. The metallic substrates accumulated ~301 mg of frost at a similar speed. Once again, the glycerol-infused polyurethane coatings were significantly heavier as compared to that of pure PU coatings and ~293 mg and ~374 mg of frost/condensate were accumulated on PU-20gly and GIFRP coatings, respectively.

The visual inspection of the glycerol-infused coatings indicated a similar observation as the static anti-icing tests and the coatings resisted the frost accumulation and accumulated condensate instead. The coatings after the dynamic tests are shown in figure 7.3b. The frost formation was evident on the aluminium substrates and PU-20CF coatings, whereas negligible frost formation was observed on GIFRP coatings. Larger chunks of frost lie on the surface of GIFRP coatings and these frost chunks might have come from the frost collected by the fan in the chamber. Similar larger chunks of frost ice are also indicated on the icing plate shown in figure 7.3b which might have sprinkled due to the centrifugal action of fan blades. The results, in correlation with the static anti-icing tests, suggest that skin-inspired GIFRP coatings were effective in resisting the frost formation/ice nucleation on the surfaces and were mostly kept ice-free for the duration of the test as

compared to the dry polyurethane coatings and metallic substrates. Furthermore, the anti-icing performance of the eroded samples could be assumed based on the conclusions reached in Chapter 4, where the frost formation did not demonstrate a direct link with surface roughness. Thus, considering the material composition is unchanged and the continued presence of glycerol layers is ensured, a similar frost formation mechanism reported on pristine GIFRP coatings in this section could be assumed for the eroded GIFRP coatings.

7.5.3 Effect of overnight water immersion on frost formation

The initial results on GIFRP coatings suggested a promising anti-icing performance, both in terms of the static and dynamic anti-icing tests. The GIFRP coatings were immersed in distilled water for 24 hours and the static and dynamic anti-icing tests were repeated on the coatings. Overnight immersion of the glycerol-infused coatings in water could have an effect on the retention of glycerol in the polyurethane matrix and anti-icing performance might be hampered. Repeated test results are illustrated in figure 7.3a (static tests) and figure 7.3b (dynamic tests). The static frost accumulation tests on water-immersed PU-20CF and GIFRP coatings resulted in a similar magnitude of frost, indicating the effect of glycerol on anti-icing performance was nullified after the overnight water immersion. A similar outcome was observed on the dynamic anti-icing tests as well. The nullified anti-icing performance of water immersed GIFRP coatings as compared to that of PU-20CF coatings is shown in figure 7.3a. The figure indicated no difference in frost accumulations on the glycerol-infused coating as compared to the dry coatings. To ascertain the obtained results, the anti-icing tests were again repeated after 24 hours of initial overnight water immersion. The anti-icing performance of GIFRP

coatings was restored and the coatings again started to resist the frost accumulation. The 24-hours post-water immersion surface of GIFRP is shown in figure 7.3b. These tests suggest that the GIFRP coatings may possess the capability to self-heal or the coatings could release the infused liquid slowly to maintain icephobic performance. In either case, the coatings regained the icephobic performance after 24 hours of the overnight water immersion tests and a similar overnight water immersion response on the eroded GIFRP coatings could also be assumed as there is no apparent change in material composition, based on the conclusions reached in Chapter 4. It is imperative to mention that both tests were conducted at intervals of 24 hours each and durability studies with time can be studied in the future.

7.5.4 Impact of erosion on de-icing properties

Ice adhesion strength tests were conducted on all the studied polyurethane coatings and as-received aluminium substrates. Ice adhesion results before and after WIETs are summarized in figure 7.2b. The ice adhesion on the aluminium substrates was ~145 kPa and ~2.6 kPa on pure PU coatings, a ~56-fold reduction in ice adhesion on pure PU surfaces. The incorporation of 20 wt% carbon fibres in the polyurethane matrix increased the ice adhesion by ~2 fold to 5.8 kPa as compared to that of pure PU coatings. The infusion of glycerol in pure PU and PU fibre-reinforced coatings resulted in ice adhesion of 0.15 kPa and 0.32 kPa, respectively. Pure PU coatings exacerbated the ice adhesion after the erosion tests to 83.1 kPa, a ~32 fold increase. Similarly, ice adhesion on PU-20gly coatings increased by ~37 fold after the erosion tests. This steep increase in ice adhesion might be the result of a greater number of possible ice anchoring points (surface

cavities) generated by the impinging particles as indicated by the increase of the surface roughness of the samples.

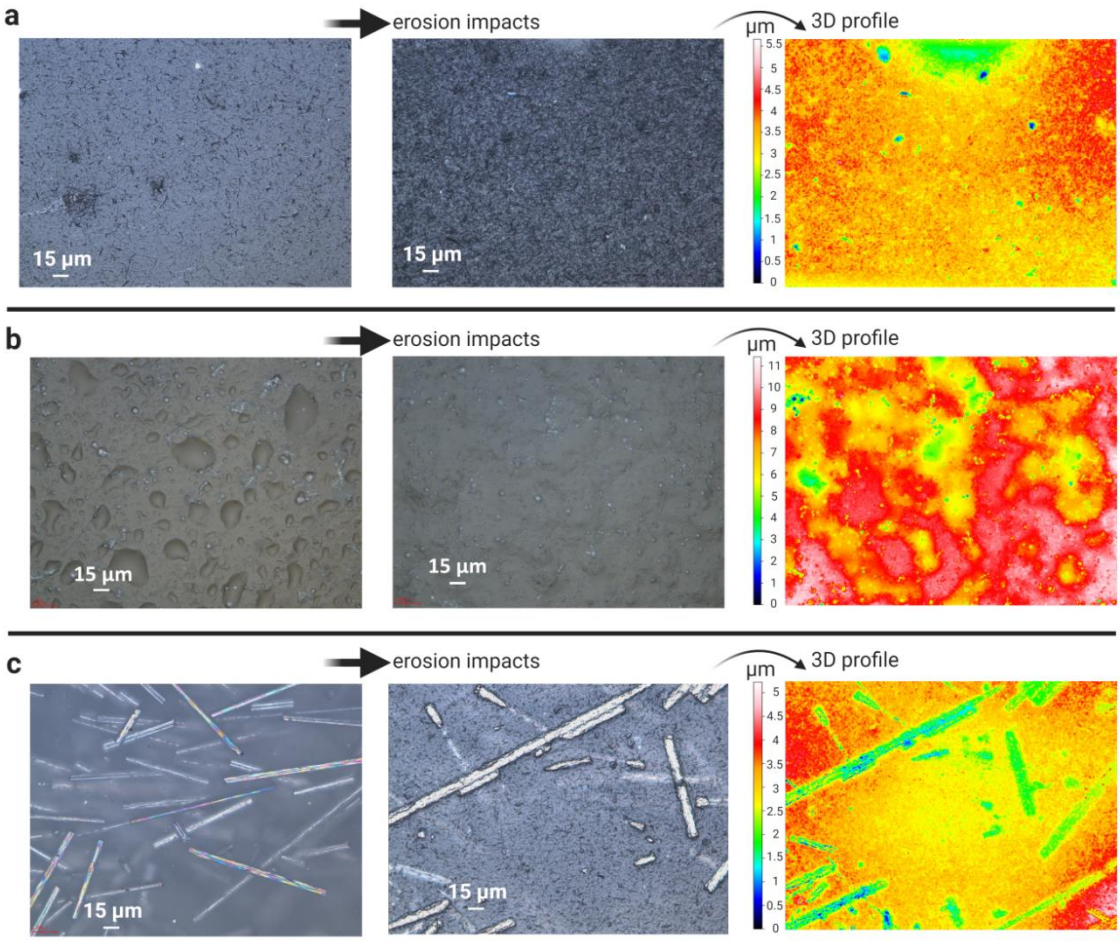


Figure 7.4: Microstructural images of pure PU (a), PU-20gly (b), and (c) PU-20CF coatings and the same coatings after the erosion tests, together with the 3D profiles. All images have the same scale bar.

The incorporation of carbon fibres was successful in restricting the morphological damages caused by the impacting droplets/sand particles on the surfaces as indicated in figure 7.4 and could be supported by figure 7.5. Figure 7.5a and 7.5b indicate the surfaces detoriated throughout the impinging process and the cavities or chipping of coatings are evident. However, in figure 7.5c, the deteriation seems to be concentrated around the

incorporated fibres and the fibres are likely taking the damage. The ice adhesion of PU-20CF coatings increased by a mere ~1.5 fold after the erosion tests, as compared to a ~32-fold increase on pure PU coatings. The impinged PU-20gly coatings indicated a higher change in surface roughness as compared to that of PU and PU-20CF coatings, however, resulted in lower ice adhesion. This reduction on PU-20gly coatings gives the idea that glycerol was still suppressing the stronger interaction between the ice and the surface even after the erosion tests.

The results obtained on GIFRP coatings were most promising and the ice adhesion increased from 0.22 kPa to 0.77 kPa after the erosion tests. These values are one of the lowest ice adhesion strength reported in literature after the coatings have been damaged and a comparative table is listed in table 7.1. to compare the ice adhesion strength and durability evaluation of the recent icephobic coatings from literature. A material is believed to be icephobic if the material maintains ice adhesion below 10 kPa and ice adhesion on the hybrid GIFRP coatings was kept below 1 kPa after the erosion tests.

7.6 Bio-inspired coating durability and liquid retention mechanisms

The impinging droplets/sand particles create multiple stress waves on the impact zone and these stress waves consist of three multidirectional waves as discussed in chapter 6 and was depicted in figure 6.7a [249]. . These stress waves are detrimental to the durability of the coatings and may impart voids in the material, especially on the surface, if the stress waves exceed the dynamic fracture strength of the target material [250]. The effect of these waves are often connected with the fatigue properties as the material experience repetitive loads and the fractures caused by the erosion may lead to a

Table 7.1: A comparison of ice adhesion strength and durability of the recent icephobic coatings.

Coating/Material	**Filler incorporation / coating treatment**	**Icephobicity evaluation method**	**Ice adhesion strength, as produced (kPa)**	**Durability analysis**	**Ice adhesion strength after durability evaluation (kPa)**	**References**
GIFRP coatings	Carbon Fiber and Glycerol	Centrifugal method	0.32 ± 0.2	Water+SiC particle impinging erosion	0.77 ± 0.1	Current work
Superhydrophobic silicone rubber surfaces	Micro compression molding (μCM)	Centrifugal method	93 ± 1.2	7 icing/de-icing cycles	126 ± 1.1*	[141]
		Push method	90 ± 1.3		85 ± 0.9*	
	Atmospheric pressure plasma (APP)	Centrifugal method	42 ± 2.2		91 ± 0.9*	
		Push method	32 ± 2.6		45 ± 1.8*	
PDMS gels	Increased concentration of t-PDMS	Push method	5.2 ± 0.4	100 icing/de-icing cycles	~5*	[237]
				1000 abrasion cycles	~7.2*	
Low cross-linked PU (CB coating)	Interfacial slippage enabled 15wt% Safflower oil	Push method	~4 ± 3	100 icing cycles Thermal cycling	9 ± 2*	[267]

				5000 abrasion cycles		
PDMS modified superhydrophobic surface (SOIP)	Infused with silicon oil	Push method	22 ± 5	15 icing/de-icing cycles	81*	[279]
				4 months of environmental exposure	55 ± 13	
Porous anodic aluminium oxide (oil+350 oil)	Infused with silicon oil	Centrifugal method	8 ± 0.8	5 icing/de-icing cycles	17 ± 3*	[280]
Slide-ring cross-linked PDMS (SP-10%)	Crosslinking of PDMS	Vertical push method	13 ± 1.3	20 icing/de-icing cycles	~12*	[238]
				800 abrasion cycles	~22*	
PDMS-urea coatings (PDU300)	Dynamic crosslinkers (tuning the hydrogen bonds)	Vertical push method	38.3 ± 0.5	20 icing/de-icing cycles	~50*	[149]
PDMS based sandwich-like sponges (10:10)	Crosslinking of PDMS	Vertical push method	0.9	25 icing/de-icing cycles	~1*	[281]
Organogel (OG) coating	Swelling cross-linked PDMS networks with liquid paraffin (LP)	Push method	1.7 ± 1.2	35 icing/de-icing cycles	~8*	[135]
				100 days of	~9*	

				exposure		
PDMS embedded silicone oil surfaces	Infused with silica aerogel	Push method	~5	20 icing/de-icing cycles	<20*	[282]

*After the final cycle

fatigue failure [255]. However, Alder et al. [256] indicated that fatigue plays a secondary role, and concluded that the topological changes (microstructural discontinuities) or stress concentrations on the cracks during the incubation period are the main factors that accelerate the erosion rate. Thus, minimising the surface damage is the key in achieving the lasting icephobic performance, as it will mitigate the erosion rate, as well as provide minimal number of possible ice anchoring points. In chapter 6, the impingement test consists of a mixture of water with hard SiC particles, and the particles could inflict a higher damage as compared to that of water droplets. The results conducted in this work indicate that the crack initiations to be a lead factor as the reinforced-fibre composites demonstrated fewer surface anomalies after the erosion tests. The incorporation of fibres in the matrices results in better loading transfer and the increase of coating toughness. Thus, the capability of composite to withstand repetitive impact loads is greatly enhanced.

Additionally, high erosion resistance on elastomers, like the one used in this work, is linked to their viscoelastic behaviour and low modulus enables elastomers to dissipate the impact energy and prevents the pressure buildup, thus avoiding the stress concentrations across the surface [254]. Likewise, a low modulus elastomer could also provide a path for easy release of ice (low ice adhesion) due to a mismatch in strain under stress and large moduli difference between soft and ice surfaces [3, 267]. On the other hand, the fibre structure in the polyurethane matrix could effectively withstand the impacting energy by distributing the kinetic energy of water droplet/sand particles across the discontinuous fibre structure without causing any significant damage as depicted in figure 4a. In the structure of skin, the response of the discontinuous collagen fibrils to an external loading

could effectively prompt stress redistribution and prevent the stress concentration in one area, leading to substantial energy dissipation [271]. The fibre-reinforced coatings studied in this thesis were incorporated with milled carbon fibres, instead of typical long fibres to produce an isotropic response to the impacting particles and also providing a discontinuous path for impacting energies. However, the introduction of milled carbon fibres came with a trade-off of using lower aspect ratio (length/depth) of the fibres and higher aspect ratios are indicated to have greater fatigue resistance [247]. Generally, the erosion process on fibre-reinforced elastomeric composite seems to take place in two modes [273]. Firstly, the local resin removal results in exposure of fibres to the erosive environment, as shown in the 3D profile in figure 7.4c. Secondly, a possible breakage of fibres as a result of direct impingement (as a result of plastic deformation) and the cracks start to form around the fibre interface.

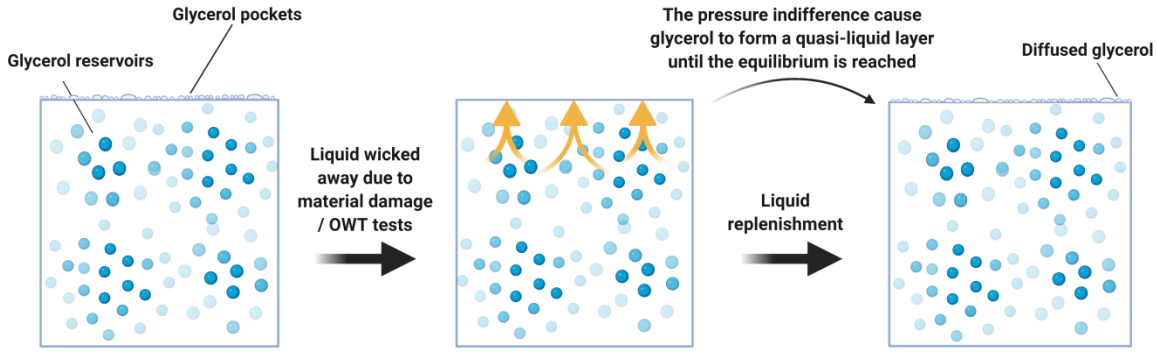


Figure 7.5 Liquid replenishment process on GIFRP coatings via diffusion after the glycerol pockets were wicked away (created using Biorender.com).

Another important aspect is the liquid retention in the polyurethane matrix. Most of the slippery or liquid infused coatings are faced with existential problems such as poor durability and depletion of infused liquid over time or due to material damage. With each

frosting/defrosting cycle, a portion of the lubricant was lost either via wicking away or evaporation [7, 96, 103, 283]. The inclusion of glycerol could also be used to resemble the lipid droplets in a cetacean skin type, providing a flexible liquid-like interface that may act as a squeezable temporary refuge to store the elastic potential energy until the load is transferred to the collagen fibres and/or the tissues to dissipate the energy [284]. The glycerol forms a quasi-liquid layer on the surface and when the surfaces are impacted using the erosion technique or the glycerol is wicked away, the coating squeezes glycerol on the surface via capillary wicking to maintain a quasi-liquid layer until equilibrium is reached as shown in figure 4b. The diffusion of glycerol may not be affected by the erosion damage as the glycerol reservoirs are uniformly distributed across the coating matrix. The long-term stability and resilience of infused liquid coatings are further associated with low viscosity liquids and using a working liquid with different surface tension than that of interacting liquids [285, 286]. Glycerol satisfies both conditions and the viscosity is likely to decrease with sub-zero temperatures [287]. However, the studies concerning the stability of infused liquids are limited to fluorinated, silicon, and minerals oils [286, 288]. Sun et al. [260] conducted a similar study, like the one debated in this work, using propylene glycol and reported promising stability of the infused liquid over a variety of anti-icing analysis. The design of GIRRP coatings enables the effective retention of the infused liquid within the fibrous structure. This strategy offers an alternative promising design as compared to other liquid-infused surfaces, which use either porous or textured impregnated surfaces to ensure the stability of the infused liquid, rather than reinforcing the matrix materials. It is imperative to mention that some degree of dissolution is inevitable as glycerol is highly miscible with water, however, the

solubility of glycerol could be considered in other beneficial factors. Firstly, the solubility of glycerol during the crystallisation process creates a misfit between the water molecules, which results in ice not being strongly adhered to the polyurethane surface. The presence of glycerol in the water droplets also works to disrupt the ice crystal lattice formation by forming stronger hydrogen bonds with water molecules and competing against the water-water hydrogen bonding [278], which could be the case for the anti-icing results, when mainly the condensate was accumulated on the surface (resisting frosting) and the surface was majorly frost-free. Secondly, the glycerol-water miscibility was investigated at a range of salinities and temperature levels [289], which offers a promising potential of icephobic performance for offshore and aerospace applications. Additionally, the infusion of glycerol also does not pose any environmental challenges as the infused liquid is a natural alcohol and is not as toxic as many fluorinated infusions studied in the literature [24, 98, 290].

The synergetic effect of ice depression induced by the infusion of glycerol and structural strength properties and crack inhibition capabilities provided by the incorporation of carbon fibres in the polyurethane matrix imparted continued icephobic performance after the erosion impacts. A layer of infused glycerol (in form of liquid pockets) was present on the surface even after the severe erosion damages and the incorporation of fibres could be the reason behind the retention of infused liquid in the polyurethane matrix.

7.7 Summary

The development of erosion-resistant glycerol-infused fibre-reinforced polyurethane (GIFRP) coatings was carried out by mimicking the surface structure of the cetacean skin. On the other hand, the supercooling point was reduced with the infusion of glycerol,

inspired by chionophiles such as wood frog and red flat dark beetles. The main aspirations behind the coating design were to address the performance challenges of liquid-infused icephobic coatings, such as coating durability, the depletion of infused or impregnated liquid, and the inability to maintain a smoother morphology after material/surface damage.

An effective and sustained presence of glycerol was instrumental to the surface being virtually ice/frost-free for the duration of static and dynamic anti-icing tests. The infusion of glycerol assisted by delaying water droplet freezing time to ~364-372 seconds, a 659% increase in freezing delays as compared to that of aluminium substrates. At the same time, the adaptation of the fibrous structure in the coatings helped in two distinctive ways. Firstly, the fibre network was efficient in retaining the infused liquid inside the polyurethane matrix after surface damages and the replenishment was possible due to the diffusion of infused liquid. Secondly, the restriction of surface damage caused the ice adhesion to reduce to 0.77 kPa on the GIFRP coatings, as compared to that of 83.1 kPa on pure PU coatings after the erosion tests. Thus, the synthesised bio-inspired coatings not only reduced the ice adhesion magnitude by ~107 fold after the erosion tests but also maintained the ice adhesion strength less than 1 kPa.

Chapter 8

Conclusions and Future Work

8.1 Conclusions

The purpose of this dissertation was to research and develop new types of polyurethane icephobic materials and composite coatings for potential applications in the aerospace and wind energy industries. It was essential to review studies to interpret the true definition of icephobic materials and surfaces (Chapter 2). A total of six different variants of polyurethane (PU) coatings, including a thermoplastic PU, were examined in this thesis. Furthermore, a polydimethylsiloxane (PDMS) coating and two metallic substrates were also investigated along with the PU coatings. In-situ characterisation, hydrophobic and icephobic evaluations, and durability analysis were conducted on the developed coatings/substrates using standard and custom-built equipment (Chapter 3).

Two main strategies were identified to induce icephobicity and were investigated in this thesis. At first, fundamental studies relating to surface icephobicity and icephobicity evaluation methods were carried out (Chapter 4 and 5), then the two strategies, which were experimental in nature, were realised to ascertain the fundamental studies and to induce enhanced icephobic performance needed to produce durable icephobic surfaces (Chapter 6 and 7). The experimental work was thoroughly planned to offer a balanced

research output on the fundamental aspects of icephobicity studies and to impart the acquired knowledge for the fabrication and investigation of novel durable icephobic materials/surfaces.

A comparison of the de-icing and anti-icing evaluation methods was conducted in Chapter 4 and their variation in response to surface characteristics was investigated. The mechanical de-icing methods include centrifugal, push and tensile methods. The centrifugal and the horizontal push (shear) methods suggested a linear relationship of ice adhesion strength with surface roughness, whereas the tensile (normal) method indicated an inverse curvilinear relationship with contact angle hysteresis. A partial correlation of contact angle hysteresis on the shear-based methods was also indicated over a specified range of surface roughness. Further attempts were also made on 1H,1H,2H,2H-perfluorooctyltriethoxysilane coated surfaces and the ice adhesion indicated a clear reduction on the normal de-icing method, whereas, the shear-based methods did not show a considerable change in ice adhesion, highlighting their mechanical forces-centric response. Apart from ice adhesion evaluation methods, water droplet freezing delay suggested a direct correlation with surface roughness and higher freezing delays were recorded on smoother surfaces. Static frost accumulation did not demonstrate a considerable change in magnitude. However, visual examination suggested a reduction in ice densification on the smoothened surfaces, indicating a weakened bond between the ice/solid interfaces, paving the way for easy fracture of ice or lower ice adhesion. Lastly, a further evaluation was conducted using a hybrid de-icing method, to verify the roles of surface characteristics on ice removal involving heating, which demonstrated a partial

correlation of energy consumption with the ice adhesion strength over a specified range of surface roughness. The results in this chapter provide crucial information on the variation of response concerning surface characteristics and offer material-dependent correlations of the popular anti-icing and de-icing methods. The conclusions could be applied to define an appropriate testing method for the evaluation of icephobic surface and coatings.

The roles of surface roughness on icephobicity including ice adhesion strength have been long debated in icephobicity studies. However, the direct/systematic influence of surface roughness on ice adhesion strength while keeping other surface characteristics such as surface wettability and interfacial cavitation unchanged are seldom reported. In Chapter 5, systematic reduction of ice adhesion strength with the decrease in surface roughness regardless of the surface wettability was demonstrated across all the studied material types, i.e. metallic surfaces and polymeric coatings with different surface wettability. In-situ icing observation studies indicated that the ice did not anchor on smooth metallic surfaces and polymeric coatings but anchored on rough surfaces including superhydrophobic coatings. The effect of surface wettability was argued against the ice adhesion strength based on our results and similar ice adhesion strength was found on materials having different wettability (i.e. hydrophilic and hydrophobic coatings, and surfaces having different contact angle hysteresis). On the contrary, the introduction of low surface energy chemicals (via deposition and/or functionalisation) on the surface having similar surface roughness showed a direct reduction of ice adhesion strength. These results indicated the surface roughness is vital in achieving icephobic performance,

however, the ultra-low ice adhesion strength could be achieved by the synergetic effect of low surface roughness and low interfacial cavitation (in line with the interfacial correlation factor).

Icephobic performance of low-ice adhesion polymeric coatings has been studied intensively for passive ice protection. However, limited efforts were conducted to identify strategies for enhancing the durability of the coatings to maintain low ice adhesion after erosion impact. In Chapter 6, several polyurethane-based nanocomposite and fibre-reinforced coatings were developed and investigated to understand the deteriorating behaviour of the coatings under rigorous impinging erosion tests and the subsequent impact on ice adhesion. The inclusion of fillers resulted in up to 38 points increase in Shore hardness relative to the pristine PU coatings. The ice adhesion strengths on 3 wt% nanoparticle-reinforced coatings after the erosion tests were nearly halved, whereas, a 5-fold reduction was observed on 3 wt% fibre-reinforced coatings compared to that of the pure PU coatings. The results indicated that the incorporation of fillers was effective in reducing the ice anchoring points, and that, after the impingement, the icephobic performance was retained by either lowering surface roughness or by minimizing surface deterioration. Fibres took a more effective role in limiting crack initiation and resisting crack propagation. The ice adhesion strength of the coatings increased from 5.6 kPa to 8.4 kPa with 20 wt% carbon fibres incorporated PU coatings, essentially keeping the adhesion below 10 kPa even after rigorous impinging tests and a ~10-fold reduction in ice adhesion strength as compared to the pure PU coatings. The

incorporation of the fibres led to enhanced durability and retention of excellent icephobic performance via a mechanism that is adaptable to other polymeric coatings.

Liquid-infused polymeric surfaces have demonstrated promising icephobicity. However, the capability to maintain the icephobic performance after material damage has been a challenge, both in terms of conserving a smoother surface and replenishment of infused liquid. Cetacean skin possesses a microscopically smooth texture in the form of cells lubricated with lipid proteins and consists of structural fibres that ensure durability. With reference to the structure of cetacean skin, glycerol infused fibre-reinforced polyurethane coatings (GIFRP) was proposed in Chapter 7. Instead of hosting the lipid proteins, the coatings were infused with glycerol, a known cryoprotectant to induce the supercooling of water, a strategy inspired by wood frogs and red flat dark beetles to prevent freezing. The inclusion of glycerol delayed water droplet freezing duration by 659%, while negligible frost accumulated on the fabricated coatings during anti-icing tests. The reinforcement of fibres was effective and the surface damage was reduced by a factor of 4, compared to the pure polyurethane coatings under erosion impact. The incorporation of fibres has proven to be beneficial for infused-liquid replenishment and the slow-releasing capabilities of GIFRP coatings. Minimised surface deterioration and the continued presence of glycerol on GIFRP coatings demonstrated a small increase in ice adhesion from 0.22 kPa to 0.77 kPa after the erosion tests, one of the lowest values reported in literature after substantial surface damage. The concept inspired by cetacean skin and the cryoprotective features of chionophiles was instrumental in keeping the ice adhesion under 1 kPa after erosion impact.

8.2 Future Work

The scope of this PhD project ranged from the understanding of fundamental aspects of icephobicity, the fabrication and examination of low adhesion durable coatings, and the variation of response of icephobicity evaluation methods. Thus, several specific fields were identified to carry out work in the future, for further advancement of icephobicity science.

Firstly, in addition to the surfaces studied in this work, there is room for further improvement in reducing the surface roughness, close to the ice nuclei radii. These ultra-low surface roughnesses could be achieved via a structured lithographed surface or etching process and would be useful to understand the true dependence of surface roughness on ice adhesion, possibly identifying a range of surface roughnesses where the ice adhesion strength is the lowest. The results could also be helpful to derive a theoretical correlation between the surface roughness and ice adhesion strength. This correlation can be further studied in regards to the synergetic effect of surface roughness with surface energy and/or interfacial cavitation, possibly reaching a point where the surface characteristics maximise the icephobic performance. The studies can be further expanded to include the use of more superhydrophobic surfaces to ascertain the findings. Additionally, the results obtained in this thesis indicated an influential role of metal composition on ice adhesion. Thus, further studies are recommended on the metallurgical studies and their impact on ice adhesion strength. These studies could be useful to impart inherently icephobic performance directly in the structural metals. For example, the use of a hardened alloy with the inherent icephobic capability will allow the surface to be less

affected by the external impinging particles, maintaining a smoother surface, and be inherently icephobic to induce lasting performance. Furthermore, the effect of material's thermal conductivity on ice adhesion strength is largely unknown and it could of interest as the ice adhesion strength is highly influenced by the interfacial ice bonding mechanisms. This relationship becomes especially important in the case of ice formations on a Peltier plate, where thermal gradient may delay the ice nucleation procedure which could introduce mechanical history to the ice samples and possibly changing the ice type and its properties.

Secondly, in terms of de-icing methods, there is still a lack of clear understanding of why and how the ice fails in an adhesive or cohesive manner. The influence of ice properties, surface characteristics, and the peeling and shearing forces at ice/surface interfaces on these failures are yet to be known. In this regard, finite element analysis (FEA) simulations could be carried to analyse the fractural behaviour of ice on the de-icing methods, which is still scarcely used in icephobicity studies. An investigation on the rationale behind the considerable increase in ice adhesion strength after a certain surface roughness range will significantly help in identifying the mechanical forces-centric behaviour of the de-icing evaluation methods. Additionally, a conflicting correlation of CAHs in shear-based and normal-based de-icing systems and the role of the liquid-like layers on the tensile method need further examination. Furthermore, there is a need to investigate the role and influence of aerodynamic drag on samples spinning at high rotational speeds in a centrifuge. In terms of the electro-thermal heating de-icing method, it would be interesting to study the synergetic effect of localised heating and ice shearing

forces. For example, combining the centrifugal method with an electro-thermal heating bed, that could introduce shearing de-icing forces and localised heating at the same time. However, this test could only be applicable for systems that do not employ a Peltier cooling plate or in other words, do not induce freezing by means of a surface but in ambient temperatures. In terms of anti-icing test techniques, a detailed study on the possible influence of material chemistry/composition on frost accumulation is recommended. These studies can be further examined using FEA simulations and would certainly help to understand the influence of surface characteristics on ice nucleating and frost accumulation mechanisms. Furthermore, the static and dynamic anti-icing methods could be further improved to meet the atmospheric icing conditions mentioned in CS-25 certification specifications for a large plane in an attempt to meet and simulate the realistic atmospheric icing conditions.

Thirdly, in addition to the silicon carbide-water solution impinging studied in this thesis, the remit of water impinging methods can further be expanded to high-speed erosion and icing wind tunnel evaluations to better evaluate the conditions in aerospace and wind energy applications, coupled with an investigation on material loss after the durability analysis, which may answer crucial questions on the sustainability of the coatings in a longer run. A further fortification of polymeric coatings is recommended, by surface functionalisation of fibres to enhance the interface bonding of the composite coatings and/or by hybridisation with another type of fibres and/or nanoparticles. Furthermore, the filler incorporations could be carefully selected to maximise the surface durability,

possibly with thermally or electrically conductive fillers to impart electro-thermal capabilities to the composite coatings which could be used to aid the easy release of ice.

Lastly, regarding the liquid retention within the coating matrix, there is a lack of widespread liquid retention evaluations and the absence of reliable techniques to measure liquid retention is a hurdle for meaningful development of liquid-infused composite coatings. Thus, there is a need to invent discover new approaches and new mechanisms to better evaluate the liquid retention capability of both impregnated surfaces and infused coatings in a longer run, including an examination of dissolution of coatings over time due to capillary wicking of the infused liquid. Furthermore, the challenges involving the physical infusion of liquid in coatings could also be addressed by introducing a chemically-bonded infused liquid, such as the concept of 'soaked' coatings. There is also a need to carry out a further investigation on the effect of overnight immersion tests on coatings' icephobic performance with time, in addition to 24 hours intervals studied in this thesis. Additionally, there is a need to improve the diffusion mechanism for both impregnated surface and infused coatings, which could ensure a continued presence of the liquid to depress the ice nucleation process, especially in the event of wetting or liquid wicking conditions. Lastly, in terms of polymeric coatings, there is a need to evaluate the performance of materials at sub-zero temperatures (down to -60 ^{o}C) to identify any change in icephobic performance.

References

[1] A. Work, Y. Lian, A critical review of the measurement of ice adhesion to solid substrates, Progress in Aerospace Sciences, 98 (2018) 1-26.

[2] M.S. Park, Aircraft De-Icing System Using Thermal Conductive Fibers, (2015) 276. source: https://commons.erau.edu/edt/276.

[3] C. Wang, T. Fuller, W. Zhang, K.J. Wynne, Thickness dependence of ice removal stress for a polydimethylsiloxane nanocomposite: Sylgard 184, Langmuir, 30 (2014) 12819-12826.

[4] L. Battisti, Ice Prevention Systems (IPS), in: Wind Turbines in Cold Climates, Springer, (2015) 251-324.

[5] V.C. Gungor, D. Sahin, T. Kocak, S. Ergut, C. Buccella, C. Cecati, G.P. Hancke, A Survey on Smart Grid Potential Applications and Communication Requirements, IEEE Transactions on Industrial Informatics, 9 (2013) 28-42.

[6] M.P. Trzaskos, A. Klein-Paste, Effect of temperature and prewetting for ice penetration with sodium formate, Transportation research record, 2674 (2020) 140-150.

[7] L. Mishchenko, B. Hatton, V. Bahadur, J.A. Taylor, T. Krupenkin, J. Aizenberg, Design of Ice-free Nanostructured Surfaces Based on Repulsion of Impacting Water Droplets, ACS Nano, 4 (2010) 7699-7707.

[8] S. Jung, M. Dorrestijn, D. Raps, A. Das, C.M. Megaridis, D. Poulikakos, Are superhydrophobic surfaces best for icephobicity?, Langmuir, 27 (2011) 3059-3066.

[9] S.G. Cober, G.A. Isaac, J.W. Strapp, Characterizations of aircraft icing environments that include supercooled large drops, Journal of Applied Meteorology, 40 (2001) 1984-2002.

[10] Z.A. Janjua, B. Turnbull, K.-L. Choy, C. Pandis, J. Liu, X. Hou, K.-S. Choi, Performance and durability tests of smart icephobic coatings to reduce ice adhesion, Applied Surface Science, 407 (2017) 555-564.

[11] J.B. Boreyko, C.P. Collier, Delayed frost growth on jumping-drop superhydrophobic surfaces, ACS nano, 7 (2013) 1618-1627.

[12] G. Momen, R. Jafari, M. Farzaneh, Ice repellency behaviour of superhydrophobic surfaces: Effects of atmospheric icing conditions and surface roughness, Applied Surface Science, 349 (2015) 211-218.

[13] Y.H. Yeong, A. Milionis, E. Loth, J. Sokhey, Self-lubricating icephobic elastomer coating (SLIC) for ultralow ice adhesion with enhanced durability, Cold Regions Science and Technology, 148 (2018) 29-37.

[14] F. Arianpour, S. Farhadi, M. Farzaneh, Effect of heterogeneity on hydro/ice-phobic properties of alkylsilane/fluoro-alkylsilane-based coatings on Al substrates, Journal of Coatings Technology and Research, 14 (2017) 267-275.

[15] X. Li, G. Wang, B. Zhan, S. Li, Z. Han, Y. Liu, A Novel Icephobic Strategy: The Fabrication of Biomimetic Coupling Micropatterns of Superwetting Surface, Advanced Materials Interfaces, 6 (2019) 1900864.

[16] Y. Gwak, J.-i. Park, M. Kim, H.S. Kim, M.J. Kwon, S.J. Oh, Y.-P. Kim, E. Jin, Creating Anti-icing Surfaces via the Direct Immobilization of Antifreeze Proteins on Aluminum, Scientific Reports, 5 (2015) 12019.

[17] W. Cui, T.A. Pakkanen, Fabrication of transparent icephobic surfaces with self-reparability: Effect of structuring and thickness of the lubricant-elastomer layer, Applied Surface Science, 504 (2020) 144061.

[18] Y. Wang, J. Xue, Q. Wang, Q. Chen, J. Ding, Verification of icephobic/anti-icing properties of a superhydrophobic surface, ACS applied materials & interfaces, 5 (2013) 3370-3381.

[19] M. Nosonovsky, V. Hejazi, Why superhydrophobic surfaces are not always icephobic, ACS nano, 6 (2012) 8488-8491.

[20] Y. Shen, H. Tao, S. Chen, L. Zhu, T. Wang, J. Tao, Icephobic/anti-icing potential of superhydrophobic Ti6Al4V surfaces with hierarchical textures, RSC Advances, 5 (2015) 1666-1672.

[21] A.J. Meuler, G.H. McKinley, R.E. Cohen, Exploiting topographical texture to impart icephobicity, ACS nano, 4 (2010) 7048-7052.

[22] Y. Wang, M. Li, T. Lv, Q. Wang, Q. Chen, J. Ding, Influence of different chemical modifications on the icephobic properties of superhydrophobic surfaces in a condensate environment, Journal of Materials Chemistry A, 3 (2015) 4967-4975.

[23] T. Wang, Y. Zheng, A.-R.O. Raji, Y. Li, W.K. Sikkema, J.M. Tour, Passive anti-icing and active deicing films, ACS applied materials & interfaces, 8 (2016) 14169-14173.

[24] P. Kim, T.-S. Wong, J. Alvarenga, M.J. Kreder, W.E. Adorno-Martinez, J. Aizenberg, Liquid-infused nanostructured surfaces with extreme anti-ice and anti-frost performance, ACS nano, 6 (2012) 6569-6577.

[25] J.G. Smith, C.J. Wohl, R.E. Kreeger, J. Palacios, T. Knuth, Surface Chemical Functionality Effect Upon Ice Adhesion Shear Strength, in: 8th AIAA Atmospheric and Space Environments Conference, (2016) 3444.

[26] Z. Yoshimitsu, A. Nakajima, T. Watanabe, K. Hashimoto, Effects of surface structure on the hydrophobicity and sliding behavior of water droplets, Langmuir, 18 (2002) 5818-5822.

[27] S. Ozbay, H.Y. Erbil, Ice accretion by spraying supercooled droplets is not dependent on wettability and surface free energy of substrates, Colloids and Surfaces A: Physicochemical and Engineering Aspects, 504 (2016) 210-218.

[28] J. Chen, Z. Luo, Q. Fan, J. Lv, J. Wang, Anti-Ice Coating Inspired by Ice Skating, Small, 10 (2014) 4693-4699.

[29] P. Eberle, M.K. Tiwari, T. Maitra, D. Poulikakos, Rational nanostructuring of surfaces for extraordinary icephobicity, Nanoscale, 6 (2014) 4874-4881.

[30] X. Liu, Interfacial effect of molecules on nucleation kinetics, The Journal of Physical Chemistry B, 105 (2001) 11550-11558.

[31] S. Rønneberg, Y. Zhuo, C. Laforte, J. He, Z. Zhang, Interlaboratory Study of Ice Adhesion Using Different Techniques, Coatings, 9 (2019) 678.

[32] M. Schulz, M. Sinapius, Evaluation of Different Ice Adhesion Tests for Mechanical Deicing Systems, SAE International, (2015) 2135.

[33] G. Croce, E. De Candido, W.G. Habashi, J. Munzar, M.S. Aubé, G.S. Baruzzi, C. Aliaga, FENSAP-ICE: Analytical model for spatial and temporal evolution of in-flight icing roughness, Journal of Aircraft, 47 (2010) 1283-1289.

[34] W.L. Golding, In-flight icing and how airlines are coping, Journal of Aviation/Aerospace Education & Research, 13 (2004) 5.

[35] O. Yirtici, S. Ozgen, I.H. Tuncer, Predictions of ice formations on wind turbine blades and power production losses due to icing, Wind Energy, 22 (2019) 945-958.

[36] M. Etemaddar, M.O.L. Hansen, T. Moan, Wind turbine aerodynamic response under atmospheric icing conditions, Wind Energy, 17 (2014) 241-265.

[37] Q. Su, S. Chang, Y. Zhao, H. Zheng, C. Dang, A review of loop heat pipes for aircraft anti-icing applications, Applied Thermal Engineering, 130 (2018) 528-540.

[38] C. Wei, B. Jin, Q. Zhang, X. Zhan, F. Chen, Anti-icing performance of super-wetting surfaces from icing-resistance to ice-phobic aspects: Robust hydrophobic or slippery surfaces, Journal of Alloys and Compounds, 765 (2018) 721-730.

[39] Y. Zhuo, F. Wang, S. Xiao, J. He, Z. Zhang, One-Step Fabrication of Bioinspired Lubricant-Regenerable Icephobic Slippery Liquid-Infused Porous Surfaces, ACS Omega, 3 (2018) 10139-10144.

[40] D. Chen, M.D. Gelenter, M. Hong, R.E. Cohen, G.H. McKinley, Icephobic Surfaces Induced by Interfacial Nonfrozen Water, ACS Applied Materials & Interfaces, 9 (2017) 4202-4214.

[41] L. Zheng, R. Shafack, B. Walker, K. Chan, The impact of high humidity on the ice-phobicity of copper-based superhydrophobic surfaces, Nanomaterials and Nanotechnology, 7 (2017) 1847980417707174.

[42] J. Dong, Z. Yao, T. Yang, L. Jiang, C. Shen, Control of superhydrophilic and superhydrophobic graphene interface, Scientific reports, 3 (2013) 1733.

[43] D. Quéré, Rough ideas on wetting, Physica A: Statistical Mechanics and its Applications, 313 (2002) 32-46.

[44] G. McHale, N. Shirtcliffe, M. Newton, Contact-angle hysteresis on super-hydrophobic surfaces, Langmuir, 20 (2004) 10146-10149.

[45] A. Marmur, Soft contact: measurement and interpretation of contact angles, Soft Matter, 2 (2006) 12-17.

[46] M. Nosonovsky, Multiscale roughness and stability of superhydrophobic biomimetic interfaces, Langmuir, 23 (2007) 3157-3161.

[47] R. Karmouch, G.G. Ross, Experimental study on the evolution of contact angles with temperature near the freezing point, The Journal of Physical Chemistry C, 114 (2010) 4063-4066.

[48] K.K. Varanasi, M. Hsu, N. Bhate, W. Yang, T. Deng, Spatial control in the heterogeneous nucleation of water, Applied Physics Letters, 95 (2009) 094101.

[49] T. Deng, K.K. Varanasi, M. Hsu, N. Bhate, C. Keimel, J. Stein, M. Blohm, Nonwetting of impinging droplets on textured surfaces, Applied Physics Letters, 94 (2009) 133109.

[50] D. Richard, C. Clanet, D. Quéré, Surface phenomena: Contact time of a bouncing drop, Nature, 417 (2002) 811-811.

[51] K.K. Lau, J. Bico, K.B. Teo, M. Chhowalla, G.A. Amaratunga, W.I. Milne, G.H. McKinley, K.K. Gleason, Superhydrophobic carbon nanotube forests, Nano letters, 3 (2003) 1701-1705.

[52] S. Kulinich, M. Farzaneh, How wetting hysteresis influences ice adhesion strength on superhydrophobic surfaces, Langmuir, 25 (2009) 8854-8856.

[53] A. Dotan, H. Dodiuk, C. Laforte, S. Kenig, The Relationship between Water Wetting and Ice Adhesion, Journal of Adhesion Science and Technology, 23 (2009) 1907-1915.

[54] V. Petrenko, S. Peng, Reduction of ice adhesion to metal by using self-assembling monolayers (SAMs), Canadian Journal of Physics, 81 (2003) 387-393.

[55] A.J. Meuler, J.D. Smith, K.K. Varanasi, J.M. Mabry, G.H. McKinley, R.E. Cohen, Relationships between water wettability and ice adhesion, ACS applied materials & interfaces, 2 (2010) 3100-3110.

[56] L. Gao, T.J. McCarthy, Wetting 101°, Langmuir, 25 (2009) 14105-14115.

[57] C. Furmidge, Studies at phase interfaces. I. The sliding of liquid drops on solid surfaces and a theory for spray retention, Journal of colloid science, 17 (1962) 309-324.

[58] T. Young, III. An essay on the cohesion of fluids, Philosophical transactions of the royal society of London, 95 (1805) 65-87.

[59] A. Dupre, Theorie mecanique de la Chaleur, Chapter IX, Actions moleculaires (suite), Paris: Gauthier-Villars, (1869).

[60] A.V. Pocius, Adhesion and adhesives technology: an introduction, Carl Hanser Verlag GmbH Co KG, 2012.

[61] L. Gao, T.J. McCarthy, Teflon is hydrophilic. Comments on definitions of hydrophobic, shear versus tensile hydrophobicity, and wettability characterization, Langmuir, 24 (2008) 9183-9188.

[62] K.L. Mittal, Adhesion measurement of thim films, thick films and bulk coatings, in: Symposium: Headquarters ASTM, ASTM, 1978.

[63] A. Cassie, S. Baxter, Wettability of porous surfaces, Transactions of the Faraday society, 40 (1944) 546-551.

[64] R.N. Wenzel, Resistance of solid surfaces to wetting by water, Industrial & Engineering Chemistry, 28 (1936) 988-994.

[65] C. Della Volpe, M. Brugnara, D. Maniglio, S. Siboni, T. Wangdu, About the possibility of experimentally measuring an equilibrium contact angle and its theoretical and practical, Contact Angle Wettabil. Adhes., 4 (2006) 79.

[66] C. Della Volpe, D. Maniglio, S. Siboni, M. Morra, An experimental procedure to obtain the equilibrium contact angle from the Wilhelmy method, Oil & gas science and technology, 56 (2001) 9-22.

[67] S. Kulinich, M. Farzaneh, Ice adhesion on super-hydrophobic surfaces, Applied Surface Science, 255 (2009) 8153-8157.

[68] A. Tuteja, W. Choi, M. Ma, J.M. Mabry, S.A. Mazzella, G.C. Rutledge, G.H. McKinley, R.E. Cohen, Designing superoleophobic surfaces, Science, 318 (2007) 1618-1622.

[69] T. Bharathidasan, S.V. Kumar, M. Bobji, R. Chakradhar, B.J. Basu, Effect of wettability and surface roughness on ice-adhesion strength of hydrophilic, hydrophobic and superhydrophobic surfaces, Applied surface science, 314 (2014) 241-250.

[70] M. Susoff, K. Siegmann, C. Pfaffenroth, M. Hirayama, Evaluation of icephobic coatings—Screening of different coatings and influence of roughness, Applied Surface Science, 282 (2013) 870-879.

[71] K. Golovin, S.P. Kobaku, D.H. Lee, E.T. DiLoreto, J.M. Mabry, A. Tuteja, Designing durable icephobic surfaces, Science advances, 2 (2016) e1501496.

[72] G. Fang, A. Amirfazli, Understanding the anti-icing behavior of superhydrophobic surfaces, Surface Innovations, 2 (2014) 94-102.

[73] X. Yao, Y. Song, L. Jiang, Applications of bio-inspired special wettable surfaces, Advanced Materials, 23 (2011) 719-734.

[74] P. Tourkine, M. Le Merrer, D. Quéré, Delayed freezing on water repellent materials, Langmuir, 25 (2009) 7214-7216.

[75] V. Bahadur, L. Mishchenko, B. Hatton, J.A. Taylor, J. Aizenberg, T. Krupenkin, Predictive model for ice formation on superhydrophobic surfaces, Langmuir, 27 (2011) 14143-14150.

[76] L. Cao, A.K. Jones, V.K. Sikka, J. Wu, D. Gao, Anti-icing superhydrophobic coatings, Langmuir, 25 (2009) 12444-12448.

[77] A. Kirillova, L. Ionov, I.V. Roisman, A. Synytska, Hybrid Hairy Janus Particles for Anti-Icing and De-Icing Surfaces: Synergism of Properties and Effects, Chem. Mater, 28 (2016) 6995-7005.

[78] S. Ozbay, C. Yuceel, H.Y. Erbil, Improved icephobic properties on surfaces with a hydrophilic lubricating liquid, ACS applied materials & interfaces, 7 (2015) 22067-22077.

[79] T.M. Schutzius, S. Jung, T. Maitra, P. Eberle, C. Antonini, C. Stamatopoulos, D. Poulikakos, Physics of icing and rational design of surfaces with extraordinary icephobicity, Langmuir, 31 (2014) 4807-4821.

[80] M. He, H. Li, J. Wang, Y. Song, Superhydrophobic surface at low surface temperature, Applied Physics Letters, 98 (2011) 093118.

[81] L. Oberli, D. Caruso, C. Hall, M. Fabretto, P.J. Murphy, D. Evans, Condensation and freezing of droplets on superhydrophobic surfaces, Advances in colloid and interface science, 210 (2014) 47-57.

[82] H. Wang, G. He, Q. Tian, Effects of nano-fluorocarbon coating on icing, Applied surface science, 258 (2012) 7219-7224.

[83] K.K. Varanasi, T. Deng, J.D. Smith, M. Hsu, N. Bhate, Frost formation and ice adhesion on superhydrophobic surfaces, Applied Physics Letters, 97 (2010) 234102.

[84] K.A. Wier, T.J. McCarthy, Condensation on ultrahydrophobic surfaces and its effect on droplet mobility: ultrahydrophobic surfaces are not always water repellant, Langmuir, 22 (2006) 2433-2436.

[85] A. Alizadeh, M. Yamada, R. Li, W. Shang, S. Otta, S. Zhong, L. Ge, A. Dhinojwala, K.R. Conway, V. Bahadur, Dynamics of ice nucleation on water repellent surfaces, Langmuir, 28 (2012) 3180-3186.

[86] G. Heydari, E. Thormann, M. Järn, E. Tyrode, P.M. Claesson, Hydrophobic surfaces: topography effects on wetting by supercooled water and freezing delay, The Journal of Physical Chemistry C, 117 (2013) 21752-21762.

[87] N. Fletcher, Size effect in heterogeneous nucleation, The Journal of chemical physics, 29 (1958) 572-576.

[88] H. Saito, K. Takai, G. Yamauchi, Water- and ice-repellent coatings, Surface Coatings International, 80 (1997) 168-171.

[89] M. Hassan, H. Lee, S. Lim, The variation of ice adhesion strength with substrate surface roughness, Measurement Science and Technology, 21 (2010) 075701.

[90] M. Zou, S. Beckford, R. Wei, C. Ellis, G. Hatton, M. Miller, Effects of surface roughness and energy on ice adhesion strength, Applied Surface Science, 257 (2011) 3786-3792.

[91] P. Hao, C. Lv, X. Zhang, Freezing of sessile water droplets on surfaces with various roughness and wettability, Applied physics letters, 104 (2014) 161609.

[92] S. Farhadi, M. Farzaneh, S. Kulinich, Anti-icing performance of superhydrophobic surfaces, Applied Surface Science, 257 (2011) 6264-6269.

[93] C. Laforte, J.-L. Laforte, Deicing strains and stresses of iced substrates, Journal of Adhesion Science and Technology, 26 (2012) 603-620.

[94] G. Fortin, J. Perron, Ice adhesion models to predict shear stress at shedding, Journal of adhesion science and technology, 26 (2012) 523-553.

[95] L. Makkonen, Ice adhesion—theory, measurements and countermeasures, Journal of Adhesion Science and Technology, 26 (2012) 413-445.

[96] B. Liu, K. Zhang, C. Tao, Y. Zhao, X. Li, K. Zhu, X. Yuan, Strategies for anti-icing: low surface energy or liquid-infused?, RSC Advances, 6 (2016) 70251-70260.

[97] R. Fillion, A. Riahi, A. Edrisy, A review of icing prevention in photovoltaic devices by surface engineering, Renewable and Sustainable Energy Reviews, 32 (2014) 797-809.

[98] H.A. Stone, Ice-phobic surfaces that are wet, ACS nano, 6 (2012) 6536-6540.

[99] Q.T. Fu, E.J. Liu, P. Wilson, Z. Chen, Ice nucleation behaviour on sol–gel coatings with different surface energy and roughness, Physical Chemistry Chemical Physics, 17 (2015) 21492-21500.

[100] S. Frankenstein, A.M. Tuthill, Ice adhesion to locks and dams: Past work; future directions?, Journal of Cold Regions Engineering, 16 (2002) 83-96.

[101] K. Li, S. Xu, J. Chen, Q. Zhang, Y. Zhang, D. Cui, X. Zhou, J. Wang, Y. Song, Viscosity of interfacial water regulates ice nucleation, Applied Physics Letters, 104 (2014) 101605.

[102] K. Li, S. Xu, W. Shi, M. He, H. Li, S. Li, X. Zhou, J. Wang, Y. Song, Investigating the effects of solid surfaces on ice nucleation, Langmuir, 28 (2012) 10749-10754.

[103] P.W. Wilson, W. Lu, H. Xu, P. Kim, M.J. Kreder, J. Alvarenga, J. Aizenberg, Inhibition of ice nucleation by slippery liquid-infused porous surfaces (SLIPS), Physical Chemistry Chemical Physics, 15 (2013) 581-585.

[104] M.A. Samaha, M. Gad-el-Hak, Polymeric slippery coatings: nature and applications, Polymers, 6 (2014) 1266-1311.

[105] R. Menini, M. Farzaneh, Advanced icephobic coatings, Journal of adhesion science and technology, 25 (2011) 971-992.

[106] A. Poynor, L. Hong, I.K. Robinson, S. Granick, Z. Zhang, P.A. Fenter, How water meets a hydrophobic surface, Physical review letters, 97 (2006) 266101.

[107] S. Chattopadhyay, A. Uysal, B. Stripe, Y.-g. Ha, T.J. Marks, E.A. Karapetrova, P. Dutta, How water meets a very hydrophobic surface, Physical review letters, 105 (2010) 037803.

[108] J. Janeček, R.R. Netz, Interfacial water at hydrophobic and hydrophilic surfaces: Depletion versus adsorption, Langmuir, 23 (2007) 8417-8429.

[109] R. Tadmor, N. Chen, J.N. Israelachvili, Thin film rheology and lubricity of hyaluronic acid solutions at a normal physiological concentration, Journal of Biomedical Materials Research Part A, 61 (2002) 514-523.

[110] B.-m.Z. Newby, M.K. Chaudhury, H.R. Brown, Macroscopic evidence of the effect of interfacial slippage on adhesion, Science, 269 (1995) 1407.

[111] A. Ghatak, L. Mahadevan, M.K. Chaudhury, Measuring the work of adhesion between a soft confined film and a flexible plate, Langmuir, 21 (2005) 1277-1281.

[112] M. Chaudhury, K. Kim, Shear-induced adhesive failure of a rigid slab in contact with a thin confined film, The European Physical Journal E: Soft Matter and Biological Physics, 23 (2007) 175-183.

[113] K. Migler, H. Hervet, L. Leger, Slip transition of a polymer melt under shear stress, Physical review letters, 70 (1993) 287.

[114] K. Vorvolakos, M.K. Chaudhury, The effects of molecular weight and temperature on the kinetic friction of silicone rubbers, Langmuir, 19 (2003) 6778-6787.

[115] Y.B. Chernyak, A. Leonov, On the theory of the adhesive friction of elastomers, Wear, 108 (1986) 105-138.

[116] A.A. Griffith, The phenomena of rupture and flow in solids, Philosophical transactions of the royal society of london. Series A, containing papers of a mathematical or physical character, 221 (1921) 163-198.

[117] N. Vogel, R.A. Belisle, B. Hatton, T.-S. Wong, J. Aizenberg, Transparency and damage tolerance of patternable omniphobic lubricated surfaces based on inverse colloidal monolayers, Nature communications, 4 (2013) 2176.

[118] T.-S. Wong, S.H. Kang, S.K. Tang, E.J. Smythe, B.D. Hatton, A. Grinthal, J. Aizenberg, Bioinspired self-repairing slippery surfaces with pressure-stable omniphobicity, Nature, 477 (2011) 443-447.

[119] J. Laforte, M. Allaire, J. Laflamme, State-of-the-art on power line de-icing, Atmospheric Research, 46 (1998) 143-158.

[120] C.C. Ryerson, Assessment of superstructure ice protection as applied to offshore oil operations safety, (2009) 49. source: https://digitalcommons.unl.edu/usarmyresearch/49/.

[121] M.J. Kreder, J. Alvarenga, P. Kim, J. Aizenberg, Design of anti-icing surfaces: smooth, textured or slippery?, Nature Reviews Materials, 1 (2016) 15003.

[122] T. Maitra, C. Antonini, M.K. Tiwari, A. Mularczyk, Z. Imeri, P. Schoch, D. Poulikakos, Supercooled water drops impacting superhydrophobic textures, Langmuir, 30 (2014) 10855-10861.

[123] X. Sun, V.G. Damle, S. Liu, K. Rykaczewski, Bioinspired Stimuli-Responsive and Antifreeze-Secreting Anti-Icing Coatings, Advanced Materials Interfaces, 2 (2015) 1400479.

[124] L. Yin, Q. Xia, J. Xue, S. Yang, Q. Wang, Q. Chen, In situ investigation of ice formation on surfaces with representative wettability, Applied Surface Science, 256 (2010) 6764-6769.

[125] Y. Han Yeong, A. Steele, E. Loth, I. Bayer, G. De Combarieu, C. Lakeman, Temperature and humidity effects on superhydrophobicity of nanocomposite coatings, Applied Physics Letters, 100 (2012) 053112.

[126] S. Kulinich, S. Farhadi, K. Nose, X. Du, Superhydrophobic surfaces: are they really ice-repellent?, Langmuir, 27 (2010) 25-29.

[127] L. Boinovich, A.M. Emelyanenko, Role of water vapor desublimation in the adhesion of an iced droplet to a superhydrophobic surface, Langmuir, 30 (2014) 12596-12601.

[128] J.D. Smith, R. Dhiman, S. Anand, E. Reza-Garduno, R.E. Cohen, G.H. McKinley, K.K. Varanasi, Droplet mobility on lubricant-impregnated surfaces, Soft Matter, 9 (2013) 1772-1780.

[129] C. Lee, H. Kim, Y. Nam, Drop impact dynamics on oil-infused nanostructured surfaces, Langmuir, 30 (2014) 8400-8407.

[130] J. Seyfi, S.H. Jafari, H.A. Khonakdar, G.M.M. Sadeghi, G. Zohuri, I. Hejazi, F. Simon, Fabrication of robust and thermally stable superhydrophobic nanocomposite coatings based on thermoplastic polyurethane and silica nanoparticles, Applied Surface Science, 347 (2015) 224-230.

[131] M. Hancer, H. Arkaz, A facile fabrication of superhydrophobic nanocomposite coating with contact angles approaching the theoretical limit, Applied Surface Science, 354 (2015) 342-346.

[132] J. Liu, Z.A. Janjua, M. Roe, F. Xu, B. Turnbull, K.-S. Choi, X. Hou, Super-hydrophobic/icephobic coatings based on silica nanoparticles modified by self-assembled monolayers, Nanomaterials, 6 (2016) 232.

[133] R. Dou, J. Chen, Y. Zhang, X. Wang, D. Cui, Y. Song, L. Jiang, J. Wang, Anti-icing coating with an aqueous lubricating layer, ACS applied materials & interfaces, 6 (2014) 6998-7003.

[134] F. Liu, F. Sun, Q. Pan, Highly compressible and stretchable superhydrophobic coating inspired by bio-adhesion of marine mussels, Journal of Materials Chemistry A, 2 (2014) 11365-11371.

[135] Y. Wang, X. Yao, J. Chen, Z. He, J. Liu, Q. Li, J. Wang, L. Jiang, Organogel as durable anti-icing coatings, Science China Materials, 58 (2015) 559-565.

[136] O. Parent, A. Ilinca, Anti-icing and de-icing techniques for wind turbines: Critical review, Cold regions science and technology, 65 (2011) 88-96.

[137] M. Mohseni, A. Amirfazli, A novel electro-thermal anti-icing system for fiber-reinforced polymer composite airfoils, Cold Regions Science and Technology, 87 (2013) 47-58.

[138] E. Andrews, H. Majid, N. Lockington, Adhesion of ice to a flexible substrate, Journal of materials science, 19 (1984) 73-81.

[139] E. Andrews, N. Lockington, The cohesive and adhesive strength of ice, Journal of materials science, 18 (1983) 1455-1465.

[140] F. Wang, W. Ding, J. He, Z. Zhang, Phase transition enabled durable anti-icing surfaces and its DIY design, Chemical Engineering Journal, 360 (2019) 243-249.

[141] E. Vazirinasab, K. Maghsoudi, R. Jafari, G. Momen, A comparative study of the icephobic and self-cleaning properties of Teflon materials having different surface morphologies, Journal of Materials Processing Technology, 276 (2020) 116415.

[142] F. Wang, S. Xiao, Y. Zhuo, W. Ding, J. He, Z. Zhang, Liquid layer generators for excellent icephobicity at extremely low temperatures, Materials Horizons, 6 (2019) 2063-2072.

[143] L. Zhu, J. Xue, Y. Wang, Q. Chen, J. Ding, Q. Wang, Ice-phobic Coatings Based on Silicon-Oil-Infused Polydimethylsiloxane, ACS Applied Materials & Interfaces, 5 (2013) 4053-4062.

[144] T. Bharathidasan, S.V. Kumar, M.S. Bobji, R.P.S. Chakradhar, B.J. Basu, Effect of wettability and surface roughness on ice-adhesion strength of hydrophilic, hydrophobic and superhydrophobic surfaces, Applied Surface Science, 314 (2014) 241-250.

[145] A.H. Work Jr, A.L. Gyekenyesi, R.E. Kreeger, J.A. Salem, M.M. Vargas, D.R. Drabiak, The adhesion strength of impact ice measured using a modified lap joint test, Proceedings of the AIAA Aviation Forum, GA, USA, (2018) 25-28.

[146] J. Soltis, J. Palacios, T. Eden, D. Wolfe, Evaluation of ice-adhesion strength on erosion-resistant materials, AIAA journal, 53 (2015) 1825-1835.

[147] J. Palacios, D. Wolfe, M. Bailey, J. Szefi, Ice testing of a centrifugally powered pneumatic deicing system for helicopter rotor blades, Journal of the American Helicopter Society, 60 (2015) 1-12.

[148] E. Tetteh, E. Loth, Reducing Static and Impact Ice Adhesion with a Self-Lubricating Icephobic Coating (SLIC), Coatings, 10 (2020) 262.

[149] Y. Zhuo, S. Xiao, V. Håkonsen, T. Li, F. Wang, J. He, Z. Zhang, Ultrafast self-healing and highly transparent coating with mechanically durable icephobicity, Applied Materials Today, 19 (2020) 100542.

[150] X. Li, G. Wang, A.S. Moita, C. Zhang, S. Wang, Y. Liu, Fabrication of bio-inspired non-fluorinated superhydrophobic surfaces with anti-icing property and its wettability transformation analysis, Applied Surface Science, 505 (2020) 144386.

[151] S. Rønneberg, J. He, Z. Zhang, The need for standards in low ice adhesion surface research: a critical review, Journal of Adhesion Science and Technology, 34 (2020) 319-347.

[152] C. Laforte, A. Beisswenger, Icephobic material centrifuge adhesion test, in: Proceedings of the 11th International Workshop on Atmospheric Icing of Structures, IWAIS, Montreal, QC, Canada, (2005) 12-16.

[153] H. Jellinek, H. Kachi, S. Kittaka, M. Lee, R. Yokota, Ice releasing block-copolymer coatings, Colloid and Polymer Science, 256 (1978) 544-551.

[154] L.-O. Andersson, C.-G. Golander, S. Persson, Ice adhesion to rubber materials, Journal of Adhesion Science and Technology, 8 (1994) 117-132.

[155] H. Saito, K.-i. Takai, G. Yamauchi, A study on ice adhesiveness to water-repellent coating, Journal of the Society of Materials Science, Japan, 46 (1997) 185-189.

[156] L. Raraty, D. Tabor, The adhesion and strength properties of ice, Proceedings of the Royal Society of London. Series A, Mathematical and Physical Sciences, (1958) 184-201.

[157] W. Bascom, R. Cottington, C. Singleterry, The adhesion of ice to hydrophobic surfaces, Naval research lab Washington DC, 1966.

[158] M. Landy, A. Freiberger, Studies of ice adhesion: I. Adhesion of ice to plastics, Journal of colloid and interface science, 25 (1967) 231-244.

[159] H. Murase, K. Nanishi, On the relationship of thermodynamic and physical properties of polymers with ice adhesion, Annals of Glaciology, 6 (1985) 146-149.

[160] H. Murase, K. Nanishi, H. Kogure, T. Fujibayashi, K. Tamura, N. Haruta, Interactions between heterogeneous surfaces of polymers and water, Journal of Applied Polymer Science, 54 (1994) 2051-2062.

[161] J. Sun, H. Li, Y. Huang, X. Zheng, Y. Liu, J. Zhuang, D. Wu, Simple and Affordable Way To Achieve Polymeric Superhydrophobic Surfaces with Biomimetic Hierarchical Roughness, ACS Omega, 4 (2019) 2750-2757.

[162] X. Wu, V.V. Silberschmidt, Z.-T. Hu, Z. Chen, When superhydrophobic coatings are icephobic: Role of surface topology, Surface and Coatings Technology, 358 (2019) 207-214.

[163] W. Cui, Y. Jiang, K. Mielonen, T.A. Pakkanen, The verification of icephobic performance on biomimetic superhydrophobic surfaces and the effect of wettability and surface energy, Applied Surface Science, 466 (2019) 503-514.

[164] Z. Zhang, L. Ma, Y. Liu, J. Ren, H. Hu, An experimental study of rain erosion effects on a hydro-/ice-phobic coating pertinent to Unmanned-Arial-System (UAS) inflight icing mitigation, Cold Regions Science and Technology, 181 (2021) 103196.

[165] X. Wu, Y. Shen, S. Zheng, Z.-T. Hu, Z. Chen, Clarifying the Correlation of Ice Adhesion Strength with Water Wettability and Surface Characteristics, Langmuir, 36 (2020) 12190-12201.

[166] L.A. Ladino Moreno, O. Stetzer, U. Lohmann, Contact freezing: a review of experimental studies, Atmospheric Chemistry and Physics, 13 (2013) 9745-9769.

[167] R. Attarzadeh, A. Dolatabadi, Icephobic performance of superhydrophobic coatings: A numerical analysis, International Journal of Heat and Mass Transfer, 136 (2019) 1327-1337.

[168] M. Balordi, A. Cammi, G. Santucci de Magistris, C. Chemelli, Role of micrometric roughness on anti-ice properties and durability of hierarchical super-hydrophobic aluminum surfaces, Surface and Coatings Technology, 374 (2019) 549-556.

[169] Y. Shen, X. Wu, J. Tao, C. Zhu, Y. Lai, Z. Chen, Icephobic materials: Fundamentals, performance evaluation, and applications, Progress in Materials Science, 103 (2019) 509-557.

[170] M.R. Haque, S.R. Das, A.R. Betz, Experimental investigation of condensation and freezing phenomena on hydrophilic and hydrophobic graphene coating, Applied Thermal Engineering, 160 (2019) 113987.

[171] A. S. Aghdam, F.Ç. Cebeci, Tailoring the Icephobic Performance of Slippery Liquid-Infused Porous Surfaces through the LbL Method, Langmuir, 36 (2020) 14145-14154.

[172] W. Cui, T.A. Pakkanen, Icephobic performance of one-step silicone-oil-infused slippery coatings: Effects of surface energy, oil and nanoparticle contents, Journal of Colloid and Interface Science, 558 (2020) 251-258.

[173] Y. Zhuo, V. Håkonsen, Z. He, S. Xiao, J. He, Z. Zhang, Enhancing the Mechanical Durability of Icephobic Surfaces by Introducing Autonomous Self-Healing Function, ACS Applied Materials & Interfaces, 10 (2018) 11972-11978.

[174] L. Valentini, S. Bittolo Bon, M. Hernández, M.A. Lopez-Manchado, N.M. Pugno, Nitrile butadiene rubber composites reinforced with reduced graphene oxide and carbon nanotubes show superior mechanical, electrical and icephobic properties, Composites Science and Technology, 166 (2018) 109-114.

[175] L. Gao, Y. Liu, H. Hu, An experimental investigation of dynamic ice accretion process on a wind turbine airfoil model considering various icing conditions, International Journal of Heat and Mass Transfer, 133 (2019) 930-939.

[176] S. Rønneberg, J. He, Z. Zhang, The need for standards in low ice adhesion surface research: a critical review, Journal of Adhesion Science and Technology, (2019) 1-29.

[177] Z.A. Janjua, The influence of freezing and ambient temperature on the adhesion strength of ice, Cold Regions Science and Technology, 140 (2017) 14-19.

[178] A. Laroche, M.J. Grasso, A. Dolatabadi, E. Bonaccurso, Tensile and Shear Test Methods for Quantifying the Ice Adhesion Strength to a Surface, in: Ice Adhesion, (2020) 237-284.

[179] K. Mirshahidi, K. Alasvand Zarasvand, W. Luo, K. Golovin, A high throughput tensile ice adhesion measurement system, HardwareX, 8 (2020) e00146.

[180] Y. Zheng, J. Wang, J. Liu, K.-S. Choi, X. Hou, Energy saving strategy for the development of icephobic coatings and surfaces, Thin Solid Films, 687 (2019) 137458.

[181] Y. Yamada, G. Onishi, A. Horibe, Sessile Droplet Freezing on Hydrophobic Structured Surfaces under Cold Ambient Conditions, Langmuir, 35 (2019) 16401-16406.

[182] X. Zhang, X. Wu, J. Min, Freezing and melting of a sessile water droplet on a horizontal cold plate, Experimental Thermal and Fluid Science, 88 (2017) 1-7.

[183] X. Yue, W. Liu, Y. Wang, Freezing delay, frost accumulation and droplets condensation properties of micro- or hierarchically-structured silicon surfaces, International Journal of Heat and Mass Transfer, 126 (2018) 442-451.

[184] K. Maghsoudi, E. Vazirinasab, G. Momen, R. Jafari, Icephobicity and durability assessment of superhydrophobic surfaces: The role of surface roughness and the ice adhesion measurement technique, Journal of Materials Processing Technology, 288 (2021) 116883.

[185] M.R. Kasaai, M. Farzaneh, A Critical Review of Evaluation Methods of Ice Adhesion Strength on the Surface of Materials, in: ASME 2004 23rd International Conference on Offshore Mechanics and Arctic Engineering, (2004) 919-926.

[186] D.t. Bishoy, C. Giuffre, A. Bastawros, Fracture Mechanics Based Approach for Ice Adhesion Characterization, in: 2018 Atmospheric and Space Environments Conference.

[187] M. Zou, S. Beckford, R. Wei, C. Ellis, G. Hatton, M.A. Miller, Effects of surface roughness and energy on ice adhesion strength, Applied Surface Science, 257 (2011) 3786-3792.

[188] Y. He, C. Jiang, X. Cao, J. Chen, W. Tian, W. Yuan, Reducing ice adhesion by hierarchical micro-nano-pillars, Applied Surface Science, 305 (2014) 589-595.

[189] S. Rønneberg, S. Xiao, J. He, Z. Zhang, Nanoscale Correlations of Ice Adhesion Strength and Water Contact Angle, Coatings, 10 (2020) 379.

[190] A. Davis, Y.H. Yeong, A. Steele, I.S. Bayer, E. Loth, Superhydrophobic Nanocomposite Surface Topography and Ice Adhesion, ACS Applied Materials & Interfaces, 6 (2014) 9272-9279.

[191] L. Gao, T.J. McCarthy, Contact Angle Hysteresis Explained, Langmuir, 22 (2006) 6234-6237.

[192] K.L. Mittal, The role of the interface in adhesion phenomena, Polymer Engineering & Science, 17 (1977) 467-473.

[193] S.A. Kulinich, M. Farzaneh, How Wetting Hysteresis Influences Ice Adhesion Strength on Superhydrophobic Surfaces, Langmuir, 25 (2009) 8854-8856.

[194] G. Jiang, L. Chen, S. Zhang, H. Huang, Superhydrophobic SiC/CNTs Coatings with Photothermal Deicing and Passive Anti-Icing Properties, ACS Applied Materials & Interfaces, 10 (2018) 36505-36511.

[195] F. Wang, T.E. Tay, Y. Sun, W. Liang, B. Yang, Low-voltage and -surface energy SWCNT/poly(dimethylsiloxane) (PDMS) nanocomposite film: Surface wettability for passive anti-icing and surface-skin heating for active deicing, Composites Science and Technology, 184 (2019) 107872.

[196] J. Schaaf, M. Kauffeld, Ice aluminum debonding with induction heating, Journal of Adhesion Science and Technology, 32 (2018) 2111-2127.

[197] F. Guerin, C. Laforte, M.-I. Farinas, J. Perron, Analytical model based on experimental data of centrifuge ice adhesion tests with different substrates, Cold Regions Science and Technology, 121 (2016) 93-99.

[198] S. Jung, M.K. Tiwari, N.V. Doan, D. Poulikakos, Mechanism of supercooled droplet freezing on surfaces, Nature Communications, 3 (2012) 615.

[199] M.A. Rahman, A.M. Jacobi, Effects of microgroove geometry on the early stages of frost formation and frost properties, Applied Thermal Engineering, 56 (2013) 91-100.

[200] M. Javan-Mashmool, C. Volat, M. Farzaneh, A new method for measuring ice adhesion strength at an ice–substrate interface, Hydrological Processes, 20 (2006) 645-655.

[201] B. Somlo, V. Gupta, A hydrophobic self-assembled monolayer with improved adhesion to aluminum for deicing application, Mechanics of Materials, 33 (2001) 471-480.

[202] H. Koivuluoto, C. Stenroos, R. Ruohomaa, G. Bolelli, L. Lusvarghi, P. Vuoristo, Research on icing behavior and ice adhesion testing of icephobic surfaces, IWAIS XVI, June, (2015) 6.

[203] L.W. Gold, Process of failure in ice, Canadian Geotechnical Journal, 7 (1970) 405-413.

[204] J. Chen, Z. Luo, Q. Fan, J. Lv, J. Wang, Anti-Ice Coating Inspired by Ice Skating, Small, 10 (2014) 4693-4699.

[205] M.P. Goertz, X.Y. Zhu, J.E. Houston, Exploring the Liquid-like Layer on the Ice Surface, Langmuir, 25 (2009) 6905-6908.

[206] Y. Zhang, L. Chen, H. Liu, Study on ice adhesion of composite anti-/deicing component under heating condition, Advanced Composites Letters, 29 (2020) 2633366X20912440.

[207] J. Ou, Q. Shi, Z. Wang, F. Wang, M. Xue, W. Li, G. Yan, Sessile droplet freezing and ice adhesion on aluminum with different surface wettability and surface temperature, Science China Physics, Mechanics & Astronomy, 58 (2015) 1-8.

[208] R. Ramachandran, M. Nosonovsky, Surface micro/nanotopography, wetting properties and the potential for biomimetic icephobicity of skunk cabbage Symplocarpus foetidus, Soft Matter, 10 (2014) 7797-7803.

[209] P. Guo, Y. Zheng, M. Wen, C. Song, Y. Lin, L. Jiang, Icephobic/Anti-Icing Properties of Micro/Nanostructured Surfaces, Advanced Materials, 24 (2012) 2642-2648.

[210] X. Gao, X. Yan, X. Yao, L. Xu, K. Zhang, J. Zhang, B. Yang, L. Jiang, The Dry-Style Antifogging Properties of Mosquito Compound Eyes and Artificial Analogues Prepared by Soft Lithography, Advanced Materials, 19 (2007) 2213-2217.

[211] M.A. Muntaha, M.M. Haider, M.A. Rahman, Modelling of frost formation and growth on microstuctured surface, AIP Conference Proceedings, 1754 (2016) 050042.

[212] R. Jafari, R. Menini, M. Farzaneh, Superhydrophobic and icephobic surfaces prepared by RF-sputtered polytetrafluoroethylene coatings, Applied Surface Science, 257 (2010) 1540-1543.

[213] S. Herminghaus, Roughness-induced non-wetting, EPL (Europhysics Letters), 52 (2000) 165.

[214] D. Öner, T.J. McCarthy, Ultrahydrophobic surfaces. Effects of topography length scales on wettability, Langmuir, 16 (2000) 7777-7782.

[215] S. Shibuichi, T. Onda, N. Satoh, K. Tsujii, Super water-repellent surfaces resulting from fractal structure, The Journal of Physical Chemistry, 100 (1996) 19512-19517.

[216] T. Onda, S. Shibuichi, N. Satoh, K. Tsujii, Super-water-repellent fractal surfaces, Langmuir, 12 (1996) 2125-2127.

[217] X. Sun, V.G. Damle, S. Liu, K. Rykaczewski, Bioinspired stimuli-responsive and antifreeze-secreting anti-icing coatings, Advanced Materials Interfaces, 2 (2015) 1400479.

[218] F. Arianpour, M. Farzaneh, On hydrophobic and icephobic properties of TiO2-doped silicon rubber coatings, International Journal of Theoretical and Applied Nanotechnology, 1 (2012) 79-85.

[219] J. Soltis, J. Palacios, T. Eden, D. Wolfe, Evaluation of ice-adhesion strength on erosion-resistant materials, AIAA journal, 53 (2014) 1825-1835.

[220] S. Rønneberg, C. Laforte, C. Volat, J. He, Z. Zhang, The effect of ice type on ice adhesion, AIP Advances, 9 (2019) 055304.

[221] S. Kulinich, M. Honda, A. Zhu, A. Rozhin, X. Du, The icephobic performance of alkyl-grafted aluminum surfaces, Soft Matter, 11 (2015) 856-861.

[222] L.B. Boinovich, A.M. Emelyanenko, K.A. Emelyanenko, E.B. Modin, Modus operandi of protective and anti-icing mechanisms underlying the design of longstanding outdoor icephobic coatings, ACS nano, 13 (2019) 4335-4346.

[223] C.S. Sharma, J. Combe, M. Giger, T. Emmerich, D. Poulikakos, Growth rates and spontaneous navigation of condensate droplets through randomly structured textures, ACS nano, 11 (2017) 1673-1682.

[224] T. Maitra, S. Jung, M.E. Giger, V. Kandrical, T. Ruesch, D. Poulikakos, Superhydrophobicity vs. ice adhesion: The quandary of robust icephobic surface design, Advanced Materials Interfaces, 2 (2015) 1500330.

[225] Z. Zhang, X.-Y. Liu, Control of ice nucleation: freezing and antifreeze strategies, Chemical Society Reviews, 47 (2018) 7116-7139.

[226] X. Liu, K. Maiwa, K. Tsukamoto, Heterogeneous two-dimensional nucleation and growth kinetics, The Journal of chemical physics, 106 (1997) 1870-1879.

[227] K. Golovin, A. Dhyani, M. Thouless, A. Tuteja, Low–interfacial toughness materials for effective large-scale deicing, Science, 364 (2019) 371-375.

[228] R.K. Moghadam, M.T. Rahni, K. Javadi, S.H. Davoudian, R. Miller, Influence of New Superhydrophobic Micro-structures on Delaying Ice Formation, Colloids and Surfaces A: Physicochemical and Engineering Aspects, (2020) 124675.

[229] F. Piscitelli, A. Chiariello, D. Dabkowski, G. Corraro, F. Marra, L.D. Palma, Superhydrophobic Coatings as Anti-Icing Systems for Small Aircraft, Aerospace, 7 (2020) 2.

[230] Y. Shen, Y. Wu, J. Tao, C. Zhu, H. Chen, Z. Wu, Y. Xie, Spraying fabrication of durable and transparent coatings for anti-icing application: dynamic water repellency, icing delay, and ice adhesion, ACS applied materials & interfaces, 11 (2018) 3590-3598.

[231] J.H. Kim, M.J. Kim, B. Lee, J.M. Chun, V. Patil, Y.-S. Kim, Durable ice-lubricating surfaces based on polydimethylsiloxane embedded silicone oil infused silica aerogel, Applied Surface Science, (2020) 145728.

[232] D. Wu, L. Ma, F. Zhang, H. Qian, B. Minhas, Y. Yang, X. Han, D. Zhang, Durable deicing lubricant-infused surface with photothermally switchable hydrophobic/slippery property, Materials & Design, 185 (2020) 108236.

[233] W. Tong, D. Xiong, N. Wang, Z. Wu, H. Zhou, Mechanically robust superhydrophobic coating for aeronautical composite against ice accretion and ice adhesion, Composites Part B: Engineering, 176 (2019) 107267.

[234] X. Wu, X. Zhao, J.W.C. Ho, Z. Chen, Design and durability study of environmental-friendly room-temperature processable icephobic coatings, Chemical Engineering Journal, 355 (2019) 901-909.

[235] Y.H. Yeong, A. Milionis, E. Loth, J. Sokhey, Self-lubricating icephobic elastomer coating (SLIC) for ultralow ice adhesion with enhanced durability, Cold Regions Science and Technology, 148 (2018) 29-37.

[236] X. Wu, Z. Chen, A mechanically robust transparent coating for anti-icing and self-cleaning applications, Journal of Materials Chemistry A, 6 (2018) 16043-16052.

[237] D.L. Beemer, W. Wang, A.K. Kota, Durable gels with ultra-low adhesion to ice, Journal of Materials Chemistry A, 4 (2016) 18253-18258.

[238] Y. Zhuo, T. Li, F. Wang, V. Håkonsen, S. Xiao, J. He, Z. Zhang, An ultra-durable icephobic coating by a molecular pulley, Soft Matter, 15 (2019) 3607-3611.

[239] J. Liu, J. Wang, L. Mazzola, H. Memon, T. Barman, B. Turnbull, G. Mingione, K.-S. Choi, X. Hou, Development and evaluation of poly (dimethylsiloxane) based

composite coatings for icephobic applications, Surface and Coatings Technology, 349 (2018) 980-985.

[240] I. Neitzel, V. Mochalin, I. Knoke, G.R. Palmese, Y. Gogotsi, Mechanical properties of epoxy composites with high contents of nanodiamond, Composites science and technology, 71 (2011) 710-716.

[241] V.N. Mochalin, Y. Gogotsi, Nanodiamond–polymer composites, Diamond and Related Materials, 58 (2015) 161-171.

[242] S. Roy, K. Mitra, C. Desai, R. Petrova, S. Mitra, Detonation nanodiamonds and carbon nanotubes as reinforcements in epoxy composites—a comparative study, Journal of Nanotechnology in Engineering and Medicine, 4 (2013).

[243] D. Cai, K. Yusoh, M. Song, The mechanical properties and morphology of a graphite oxide nanoplatelet/polyurethane composite, Nanotechnology, 20 (2009) 085712.

[244] J.D. Pampush, D.J. Daegling, A.E. Vick, W.S. McGraw, R.M. Covey, A.J. Rapoff, Technical note: Converting durometer data into elastic modulus in biological materials, American Journal of Physical Anthropology, 146 (2011) 650-653.

[245] I.M. Meththananda, S. Parker, M.P. Patel, M. Braden, The relationship between Shore hardness of elastomeric dental materials and Young's modulus, Dental Materials, 25 (2009) 956-959.

[246] B. Fiedler, F.H. Gojny, M.H.G. Wichmann, M.C.M. Nolte, K. Schulte, Fundamental aspects of nano-reinforced composites, Composites Science and Technology, 66 (2006) 3115-3125.

[247] R.E. Lavengood, L.B. Gulbransen, The effect of aspect ratio on the fatigue life of short boron fiber reinforced composites, Polymer Engineering & Science, 9 (1969) 365-369.

[248] O.G. Engel, Erosion damage to solids caused by high speed collision with rain, Journal of Research of the National Bureau of Standards, 61 (1958) 47-52.

[249] O. Gohardani, Impact of erosion testing aspects on current and future flight conditions, Progress in Aerospace Sciences, 47 (2011) 280-303.

[250] J.H. Brunton, F.P. Bowden, A discussion on deformation of solids by the impact of liquids, and its relation to rain damage in aircraft and missiles, to blade erosion in steam turbines, and to cavitation erosion - High speed liquid impact, Philosophical Transactions of the Royal Society of London. Series A, Mathematical and Physical Sciences, 260 (1966) 79-85.

[251] D. Eisenberg, S. Laustsen, J. Stege, Wind turbine blade coating leading edge rain erosion model: Development and validation, Wind Energy, 21 (2018) 942-951.

[252] H. Slot, E. Gelinck, C. Rentrop, E. Van Der Heide, Leading edge erosion of coated wind turbine blades: Review of coating life models, Renewable Energy, 80 (2015) 837-848.

[253] B. Amirzadeh, A. Louhghalam, M. Raessi, M. Tootkaboni, A computational framework for the analysis of rain-induced erosion in wind turbine blades, part II: Drop impact-induced stresses and blade coating fatigue life, Journal of Wind Engineering and Industrial Aerodynamics, 163 (2017) 44-54.

[254] M. Elhadi Ibrahim, M. Medraj, Water Droplet Erosion of Wind Turbine Blades: Mechanics, Testing, Modeling and Future Perspectives, Materials, 13 (2020) 157.

[255] M. Mahdipoor, H. Kirols, D. Kevorkov, P. Jedrzejowski, M. Medraj, Influence of impact speed on water droplet erosion of TiAl compared with Ti6Al4V, Scientific reports, 5 (2015) 14182.

[256] W. Adler, The mechanics of liquid impact, Academic Press, Treatise on Materials Science and Technology, 16 (1979) 127-183.

[257] W. Adler, R. Vyhnal, Rain erosion of Ti-6Al-4V, Proceedings, AA Fyall and RB King, eds, 2 (1974) 539-569.

[258] J.D. Buckley, D.D. Edie, Carbon-carbon materials and composites, William Andrew, 1993.

[259] F. Liu, Q. Pan, Facile Fabrication of Robust Ice-Phobic Polyurethane Sponges, Advanced Materials Interfaces, 2 (2015) 1500219.

[260] X. Sun, V.G. Damle, S. Liu, K. Rykaczewski, Bioinspired Stimuli-Responsive and Antifreeze-Secreting Anti-Icing Coatings, Advanced Materials Interfaces, 2 (2015) 1400479.

[261] T.V.J. Charpentier, A. Neville, P. Millner, R. Hewson, A. Morina, An Investigation of Freezing of Supercooled Water on Anti-Freeze Protein Modified Surfaces, Journal of Bionic Engineering, 10 (2013) 139-147.

[262] K. Kasahara, T. Waku, P.W. Wilson, T. Tonooka, Y. Hagiwara, The Inhibition of Icing and Frosting on Glass Surfaces by the Coating of Polyethylene Glycol and Polypeptide Mimicking Antifreeze Protein, Biomolecules, 10 (2020) 259.

[263] K. Koshio, T. Waku, Y. Hagiwara, Ice-phobic glass-substrate surfaces coated with polypeptides inspired by antifreeze protein, International Journal of Refrigeration, 10 (2020) 259.

[264] C. Zhou, X. Zhao, X. Zhao, H. Li, S. Zhang, W. Feng, Y. Zhang, Low Ice Adhesion Surfaces Based on Flexible Fluorinated Polymers with a Polynorbornene Backbone, ACS Applied Materials & Interfaces, 12 (2020) 53494-53502.

[265] T. Li, P.F. Ibáñez-Ibáñez, V. Håkonsen, J. Wu, K. Xu, Y. Zhuo, S. Luo, J. He, Z. Zhang, Self-Deicing Electrolyte Hydrogel Surfaces with Pa-level Ice Adhesion and Durable Antifreezing/Antifrost Performance, ACS Applied Materials & Interfaces, 12 (2020) 35572-35578.

[266] J. Gao, A. Martin, J. Yatvin, E. White, J. Locklin, Permanently grafted icephobic nanocomposites with high abrasion resistance, Journal of Materials Chemistry A, 4 (2016) 11719-11728.

[267] K. Golovin, S.P.R. Kobaku, D.H. Lee, E.T. DiLoreto, J.M. Mabry, A. Tuteja, Designing durable icephobic surfaces, Science Advances, 2 (2016) e1501496.

[268] J.K. Ling, The integument of marine mammals, Functional anatomy of marine mammals, 2 (1974) 1-44.

[269] D. Reeb, P.B. Best, S.H. Kidson, Structure of the integument of southern right whales, Eubalaena australis, The Anatomical Record, 290 (2007) 596-613.

[270] M. Mouton, A. Botha, Cutaneous lesions in cetaceans: an indicator of ecosystem status, InTech, (2012) 123-150.

[271] W. Yang, V.R. Sherman, B. Gludovatz, E. Schaible, P. Stewart, R.O. Ritchie, M.A. Meyers, On the tear resistance of skin, Nature Communications, 6 (2015) 6649.

[272] F. Van den Berg, 4.3 - Extracellular matrix, in: R. Schleip, T.W. Findley, L. Chaitow, P.A. Huijing (Eds.) Fascia: The Tensional Network of the Human Body, Churchill Livingstone, Oxford, (2012) 165-170.

[273] V. Boggarapu, R. Gujjala, S. Ojha, A critical review on erosion wear characteristics of polymer matrix composites, Materials Research Express, 7 (2020) 022002.

[274] C.J. Pfeiffer, F.M. Jones, Epidermal lipid in several cetacean species: ultrastructural observations, Anatomy and Embryology, 188 (1993) 209-218.

[275] J.A. Trejo González, M.P. Longinotti, H.R. Corti, The Viscosity of Glycerol−Water Mixtures Including the Supercooled Region, Journal of Chemical & Engineering Data, 56 (2011) 1397-1406.

[276] K.B. Storey, J.M. Storey, Biochemistry of Cryoprotectants, in: R.E. Lee, D.L. Denlinger (Eds.) Insects at Low Temperature, Springer US, Boston, MA, (1991) 64-93.

[277] M.A. Carrasco, S.A. Buechler, R.J. Arnold, T. Sformo, B.M. Barnes, J.G. Duman, Investigating the deep supercooling ability of an Alaskan beetle, Cucujus clavipes puniceus, via high throughput proteomics, Journal of Proteomics, 75 (2012) 1220-1234.

[278] C. Chen, W.Z. Li, Y.C. Song, J. Yang, Hydrogen bonding analysis of glycerol aqueous solutions: A molecular dynamics simulation study, Journal of Molecular Liquids, 146 (2009) 23-28.

[279] S. Barthwal, B. Lee, S.-H. Lim, Fabrication of robust and durable slippery anti-icing coating on textured superhydrophobic aluminum surfaces with infused silicone oil, Applied Surface Science, 496 (2019) 143677.

[280] M.J. Coady, M. Wood, G.Q. Wallace, K.E. Nielsen, A.-M. Kietzig, F. Lagugné-Labarthet, P.J. Ragogna, Icephobic Behavior of UV-Cured Polymer Networks Incorporated into Slippery Lubricant-Infused Porous Surfaces: Improving SLIPS Durability, ACS Applied Materials & Interfaces, 10 (2018) 2890-2896.

[281] Z. He, Y. Zhuo, J. He, Z. Zhang, Design and preparation of sandwich-like polydimethylsiloxane (PDMS) sponges with super-low ice adhesion, Soft Matter, 14 (2018) 4846-4851.

[282] J.H. Kim, M.J. Kim, B. Lee, J.M. Chun, V. Patil, Y.-S. Kim, Durable ice-lubricating surfaces based on polydimethylsiloxane embedded silicone oil infused silica aerogel, Applied Surface Science, 512 (2020) 145728.

[283] S.B. Subramanyam, K. Rykaczewski, K.K. Varanasi, Ice Adhesion on Lubricant-Impregnated Textured Surfaces, Langmuir, 29 (2013) 13414-13418.

[284] Mechanical Roles in Formation of Oriented Collagen Fibers, Tissue Engineering Part B: Reviews, 26 (2020) 116-128.

[285] P.B. Weisensee, Y. Wang, H. Qian, D. Schultz, W.P. King, N. Miljkovic, Condensate droplet size distribution on lubricant-infused surfaces, International Journal of Heat and Mass Transfer, 109 (2017) 187-199.

[286] M. Villegas, Y. Zhang, N. Abu Jarad, L. Soleymani, T.F. Didar, Liquid-Infused Surfaces: A Review of Theory, Design, and Applications, ACS Nano, 13 (2019) 8517-8536.

[287] A.G.M. Ferreira, A.P.V. Egas, I.M.A. Fonseca, A.C. Costa, D.C. Abreu, L.Q. Lobo, The viscosity of glycerol, The Journal of Chemical Thermodynamics, 113 (2017) 162-182.

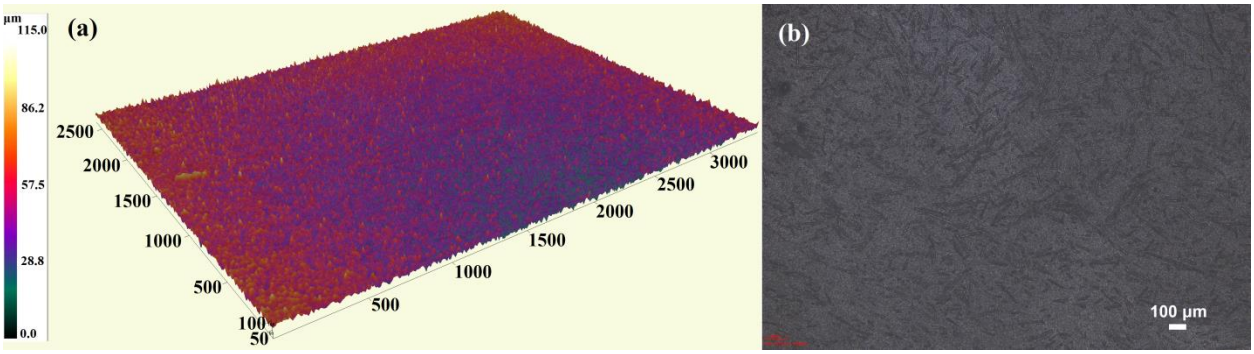
[288] X. Chen, G. Wen, Z. Guo, What are the design principles, from the choice of lubricants and structures to the preparation method, for a stable slippery lubricant-infused porous surface?, Materials Horizons, 7 (2020) 1697-1726.

[289] K. Takamura, H. Fischer, N.R. Morrow, Physical properties of aqueous glycerol solutions, Journal of Petroleum Science and Engineering, 98-99 (2012) 50-60.

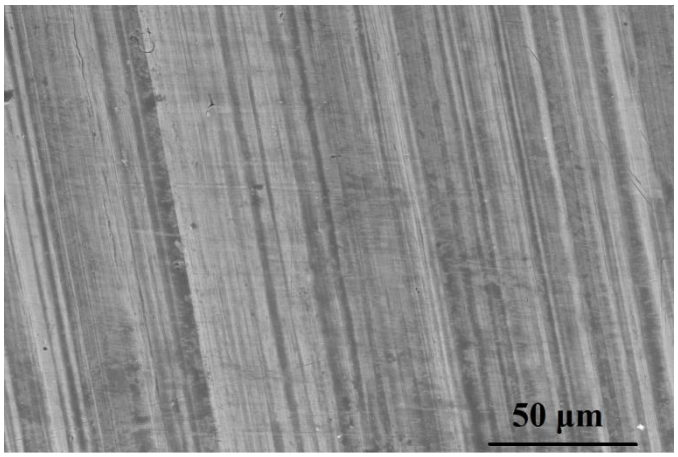
[290] M. Liu, Y. Hou, J. Li, L. Tie, Z. Guo, Transparent slippery liquid-infused nanoparticulate coatings, Chemical Engineering Journal, 337 (2018) 462-470.

Appendix A

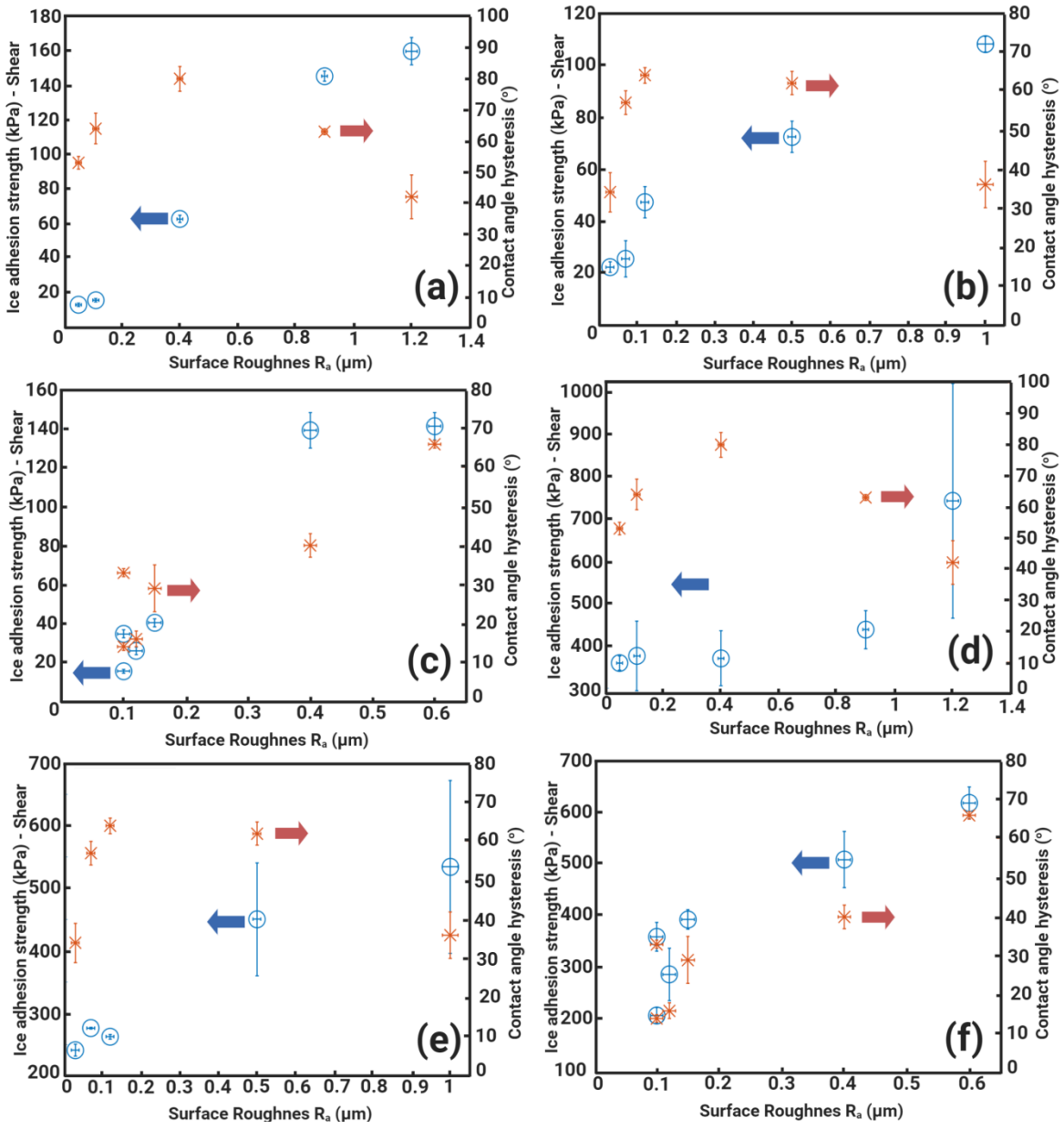
Supplementary data



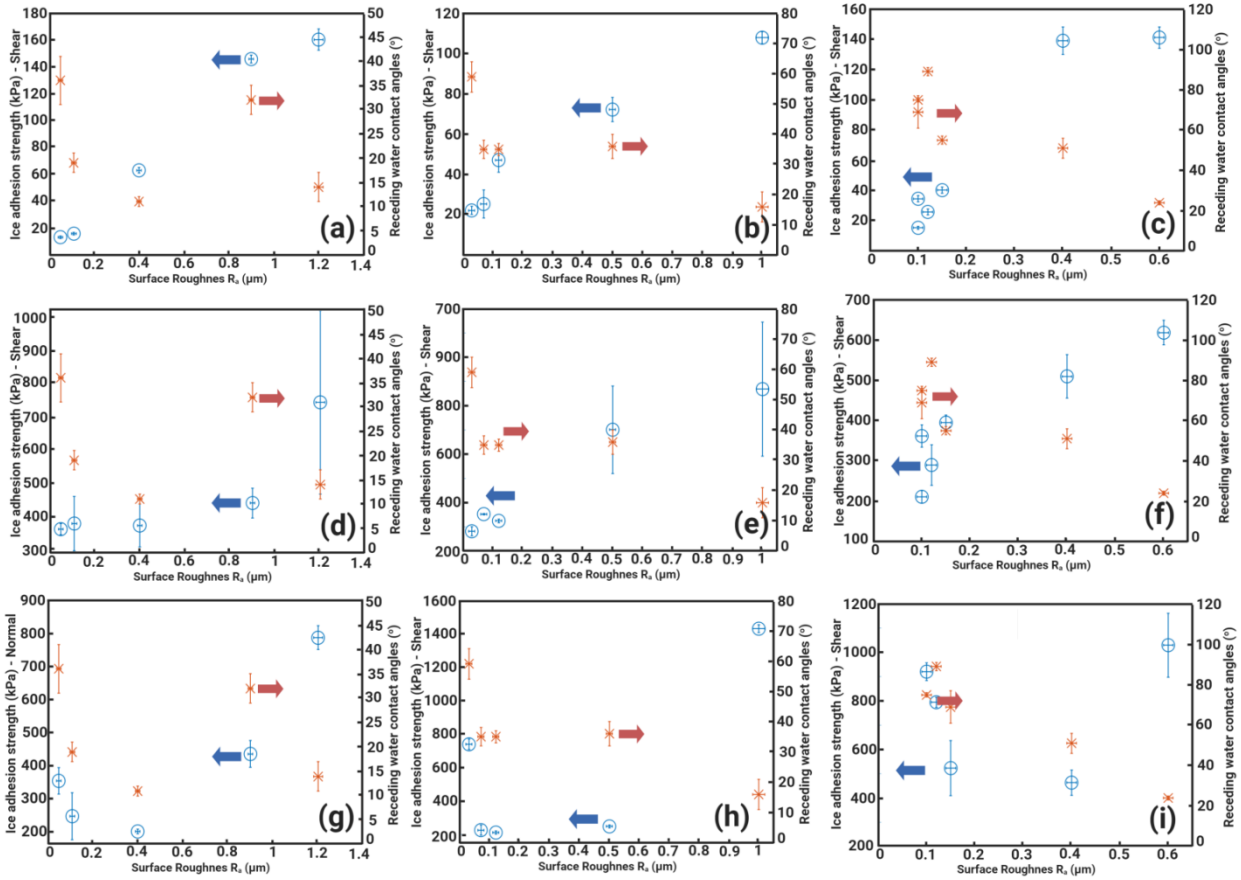
Sup. Fig. A.1: (a) 3D profile and (b) 2D image of PU-CF-20 coatings after WIETs



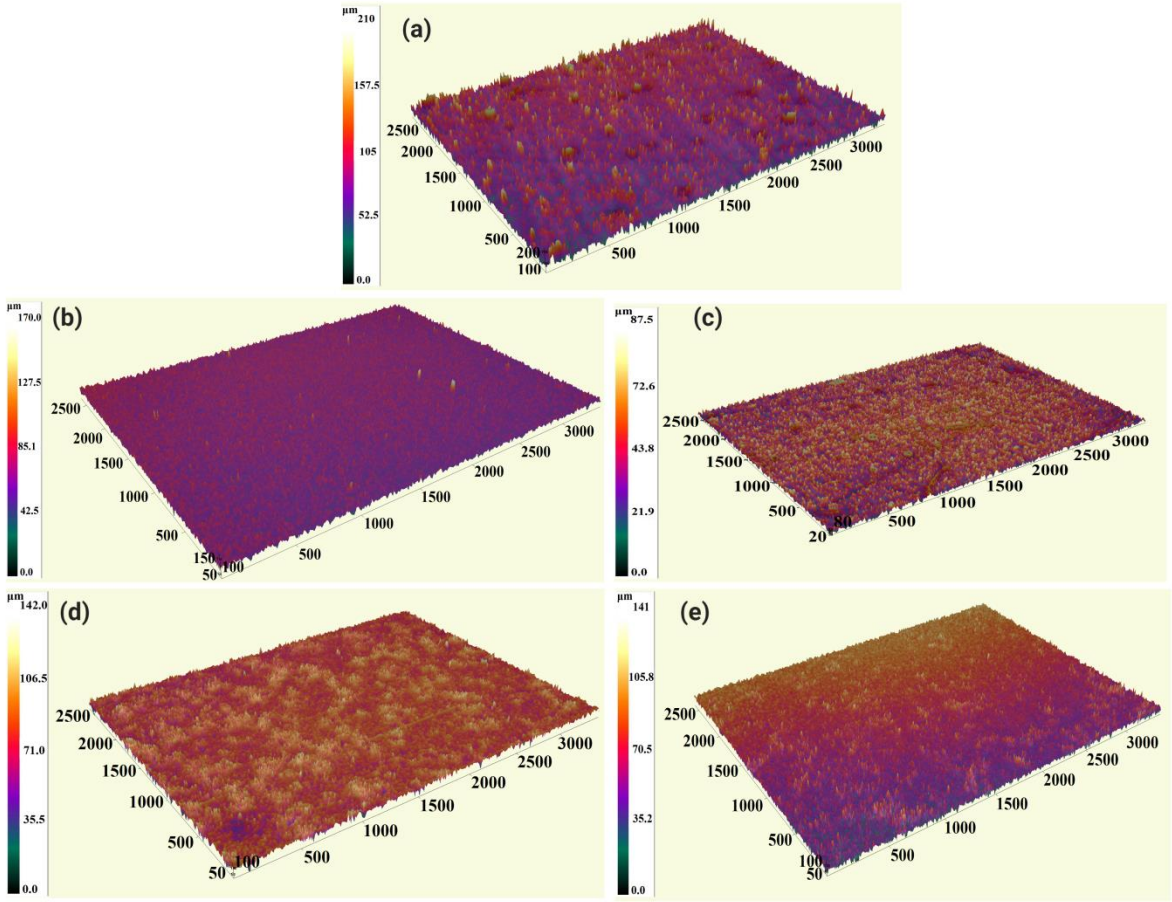
Sup. Fig. A.2: Microstructural images of the aluminium sample



Sup. Fig. A.3: Ice adhesion and CAH vs. surface roughness on the (a) aluminium samples, (b) the SS samples, and (c) TPU-BN coatings using the CAT method. Ice adhesion and CAH vs. surface roughness on the (d) aluminium samples, (e) the SS samples, and (f) TPU-BN coatings using the HPM method



Sup. fig. A.4: Ice adhesion and receding water contact angles (RWCAs) vs. surface roughness on the (a-c) using the CAT method, (d-f) using the HPM method, and (g-i) using the NTM method. Where, figures (a,d,g) are of the Al samples, (d,e,h) are of the SS samples, and (c, f, i) are of the TPU-BN coatings



Sup. fig. A.5: 3D surface profile of (a) pure PU, (b) PU-ND-3, (c) PU-GR-3, (d) PU-KV-3, and (e) PU-CF-3 coatings after WIETs. All the values are in µm

Appendix B

Complete list of results

Supplementary Table B.1: Complete list of de-icing and anti-icing evaluation data of the metallic and thermoplastic composite coatings

Coating names	Surface / substrates	Coatings / technique	Nanoparticles (wt %) / treatment	WCA (^{o})	AWCA (^{o})	RWCA (^{o})	CAH (^{o})	Ra (μm)	Ice adhesion strength (KPa)			Droplet freezing delay (s)*	Ice accumulation (mg)**	Heating melt tests**	
									Centrifugal	Force transducer	Tensile Normal			Temperature (^{o}C)^	Time (s)^
Al-AR	Al2024	-	-	78 ± 1	95 ± 2	32 ± 3	63 ± 1	0.9 ± 0.01	145.5 ± 3	438.5 ± 44.8	435.2 ± 40.4	5.2 ± 0.6	43.4 ± 6.6	4.4 ± 0.4	562 ± 11
Al-SB		Sandblasted	-	54 ± 5	56 ± 4	14 ± 3	42 ± 7	1.2 ± 0.02	>160	742 ± 276.4	786.9 ± 36.1	-	-	-	-
Al-fSB			POTS Functionalized	121 ± 2	136 ± 2	16 ± 2	120 ± 2	1.1 ± 0.02	117.3 ± 3	544.7 ± 115.7	232.8 ± 3.1	12 ± 1.2	-	-	-
Al-S1		Polished	-	87 ± 2	91 ± 5	11 ± 1	80 ± 4	0.4 ± 0.01	62.8 ± 2	370.6 ± 64.7	200.5 ± 6.8	10.7 ± 1.1	39.2 ± 4.6	4.8 ± 0.5	590 ± 9
Al-S2			-	75 ± 2	83 ± 3	19 ± 2	64 ± 5	0.11 ± 0.01	15.7 ± 1	376.6 ± 82.1	246.7 ± 71.4	12 ± 1	42 ± 7.9	4.4 ± 0.3	595 ± 7
Al-S3			-	84 ± 3	89 ± 4	36 ± 5	53 ± 2	0.05 ± 0.01	13.1 ± 1	359.7 ± 16.4	353.1 ± 40	13.7 ± 0.6	41.9 ± 6.2	4.5 ± 0.6	582 ± 8
SS-AR	SS 303	-	-	85 ± 3	98 ± 3	36 ± 4	62 ± 3	0.5 ± 0.01	72.3 ± 6	450.4 ± 90.4	248.4 ± 9.2	14.3 ± 0.6	76.6 ± 22.1	4.9 ± 0.4	562 ± 15
SS-SB		Sandblasted	-	50 ± 4	52 ± 3	16 ± 5	36 ± 6	1 ± 0.02	108 ± 3	534.3 ± 138.4	1429.9 ± 23.7	-	-	-	-
SS-fSB			POTS Functionalized	139 ± 1	147 ± 1	33 ± 1	115 ± 1	0.9 ± 0.02	30.5 ± 4	349.6 ± 22.5	115.3 ± 14.1	21.4 ± 2	-	-	-
SS-S1		Polished	-	95 ± 4	99 ± 3	35 ± 2	64 ± 2	0.12 ± 0.01	47.2 ± 6	262.4 ± 3.6	211.7 ± 9.8	16.7 ± 2.3	81.4 ± 17	5.7 ± 0.3	676 ± 14
SS-S2			-	87 ± 2	92 ± 3	35 ± 3	57 ± 3	0.07 ± 0.01	25.4 ± 7	276.3 ± 1.5	226.3 ± 31	20.1 ± 1.2	75.8 ± 12	5.5 ± 0.5	623 ± 14
SS-S3			-	90 ± 2	93 ± 3	59 ± 5	34 ± 5	0.03 ± 0.01	22.2 ± 2	240.9 ± 9.3	739.1 ± 31.5	18.7 ± 3.2	81.2 ± 12.8	5 ± 0.1	591 ± 7
TPU	Al2024	TPU	-	104 ± 1	108 ± 1	75 ± 1	33 ± 1	0.1 ± 0.01	34.6 ± 2	210.9 ± 12.6	920.7 ± 36.9	-	-	-	-
TPU-5			hBN (5%)	103 ± 1	105 ± 1	89 ± 2	16 ± 2	0.12 ± 0.01	25.9 ± 2	289.8 ± 50.3	794.4 ± 20.7	16 ± 1.1	67.2 ± 4.4	3.7 ± 0.4	532 ± 13
TPU-f5			POTS Functionalized hBN (5%)	110 ± 1	112 ± 2	98 ± 1	14 ± 1	0.1 ± 0.01	15.4 ± 1	361.6 ± 27.6	545.3 ± 65.1	26 ± 1.9	-	-	-
TPU-10			hBN (10%)	94 ± 3	98 ± 3	69 ± 8	29 ± 6	0.15 ± 0.01	40.3 ± 2	395 ± 18.6	522.6 ± 113.8	14 ± 1.7	52.3 ± 6.2	3.8 ± 0.2	532 ± 6
TPU-40			hBN (40%)	90 ± 5	96 ± 1	55 ± 2	41 ± 1	0.24 ± 0.01	67.2 ± 8	-	-	13 ± 2.4	62.9 ± 7.9	4 ± 0.3	592 ± 13
TPU-60			hBN (60%)	83 ± 4	92 ± 2	51 ± 5	40 ±3	0.4 ± 0.01	139.1 ± 9	510 ± 53.6	462.8 ± 51.8	11 ± 1.1	57.8 ± 4.6	4.5 ± 0.4	655 ± 17
TPU-80			hBN (80%)	84 ± 3	90 ± 1	24 ± 1	66 ± 1	0.6 ± 0.01	141.22 ± 7	618.5 ± 30.4	1029.9 ± 132.2	7 ± 0.6	73.9 ± 6.6	5.3 ± 0.4	699 ± 15

*at surface temperature of -10^{o}C, **at ambient temperature of -15^{o}C, and ^at time of distachment

Supplementary Table B.2: Complete list of ice adhesion strength data (including after the erosion tests), together with shore hardness measurements, of the reinforced polyurethane coatings

Coating names	Filler	Filler (wt %)	Before WIETs						After WIETs		Shore Hardness (Scale D)
			WCA (^{o})	AWCA (^{o})	RWCA (^{o})	CAH (^{o})	Ice adhesion strength (kPa)	R_a (μm)	Ice adhesion strength (kPa)	R_a (μm)	
PU	-	-	66 ± 1	68 ± 1	44 ± 1	24 ± 2	2.6 ± 1	0.08 ± 0.01	83.1 ± 11	0.45 ± 0.05	40 ± 3
PU-CF-0.5	Carbon Fiber	0.5	64 ± 1	75 ± 1	41	34 ± 1	4.1 ± 1	0.07 ± 0.01	-	-	54 ± 3
PU-CF-1	Carbon Fiber	1	64 ± 2	72	43 ± 1	28 ± 2	5.3 ± 2	0.06 ± 0.01	-	-	54± 4
PU-CF-3	Carbon Fiber	3	59 ± 5	68 ± 1	41 ± 1	27 ± 2	5.6 ± 1	0.07 ± 0.01	16.8 ± 0.5	0.27 ± 0.03	55 ± 1
PU-CF-5	Carbon Fiber	5	63 ± 3	69 ± 1	41 ± 1	28 ± 1	6.7 ± 2	0.08 ± 0.01	-	-	55 ± 3
PU-CF-20	Carbon Fiber	20	60 ± 1	66 ± 3	39 ± 2	27 ± 3	5.8 ± 1	0.12 ± 0.03	8.4 ± 1	0.15 ± 0.02	65 ± 6
PU-KV-0.5	Kevlar Fiber	0.5	72 ± 4	75 ± 2	44 ± 2	32 ± 3	12.3 ± 1	0.15 ± 0.01	-	-	58 ± 2
PU-KV-1	Kevlar Fiber	1	64 ± 1	73 ± 1	45	28 ± 1	7 ± 0.5	0.08 ± 0.01	-	-	63 ± 1
PU-KV-3	Kevlar Fiber	3	64 ± 5	73 ± 2	44	29 ± 2	5.1 ± 0.5	0.10 ± 0.01	16.1 ± 6	0.25 ± 0.02	63 ± 2
PU-KV-5	Kevlar Fiber	5	63 ± 2	68	43 ± 1	25 ± 1	6.8 ± 0.5	0.10 ± 0.01	-	-	65 ± 4
PU-KV-20	Kevlar Fiber	20	62 ± 2	66 ± 2	40 ± 4	26 ± 3	16.2 ± 1	0.12 ± 0.01	31.8 ± 4	0.22 ± 0.03	78 ± 7
PU-ND-0.5	Nanodiamond	0.5	67 ± 1	71	45 ± 1	26 ± 1	5.6 ± 0.5	0.11 ± 0.01	-	-	47 ± 1
PU-ND-1	Nanodiamond	1	65 ± 4	70 ± 1	43 ± 1	26 ± 2	3.9 ± 0.5	0.06 ± 0.01	-	-	49 ± 3
PU-ND-3	Nanodiamond	3	62 ± 1	68 ± 1	46	22 ± 1	2.7 ± 0.5	0.07 ± 0.01	45.4 ± 8	0.21 ± 0.04	55 ± 2
PU-ND-5	Nanodiamond	5	61 ± 3	67 ± 1	45 ± 1	22	2.7 ± 0.5	0.04 ± 0.01	-	-	57 ± 5
PU-ND-20	Nanodiamond	20	60 ± 1	63 ± 1	37 ± 1	26 ± 2	3 ± 0.5	0.07 ± 0.01	39.9 ± 5	0.24 ± 0.03	72 ± 8
PU-ND-40	Nanodiamond	40	54 ± 1	61 ± 1	26	35 ± 1	4.8 ± 0.5	0.11 ± 0.01	28.9 ± 7	0.17 ± 0.02	74 ± 6
PU-GR-0.5	Graphene	0.5	67 ± 5	65 ± 2	37 ± 1	28 ± 1	4 ± 0.5	0.07 ± 0.01	-	-	45 ± 1
PU-GR-1	Graphene	1	60 ± 3	64 ± 2	38	26 ± 2	3.8 ± 0.5	0.06 ± 0.01	-	-	47 ± 1
PU-GR-3	Graphene	3	60 ± 5	70 ± 1	43 ± 1	27 ± 2	2.8 ± 0.5	0.10 ± 0.01	43.3 ± 6	0.21 ± 0.03	47 ± 3
PU-GR-5	Graphene	5	69 ± 3	76 ± 1	44 ± 3	32 ± 3	11.7 ± 2	0.12 ± 0.01	-	-	48 ± 2

Supplementary Table B.3: Ice adhesion strength and static and dynamic anti-icing accumulation (before and after the durability analysis) data on the metallic and composite coatings

Coating names	Surface / substrates	Filler	Filler (wt %)	Before WIETs							After WIETs	
				WCA (^{o})	AWCA (^{o})	RWCA (^{o})	CAH (^{o})	Ice adhesion strength (KPa)	Ra (μm)	Shore Hardness (Scale D)	Ice adhesion strength (KPa)	Ra (μm)
Al2024	Al2024 T4	-	-	78 ± 1	95 ± 2	32 ± 3	63 ± 1	145.5 ± 3	0.9 ± 0.01	-	-	-
PU		-	-	66 ± 1	68 ± 1	44 ± 1	24 ± 2	2.6 ± 1	0.08 ± 0.01	40 ± 3	83.1 ± 11	0.45 ± 0.05
PU-CF-20		Carbon Fiber	20	60 ± 1	66 ± 3	39 ± 2	27 ± 3	5.78 ± 1	0.12 ± 0.03	65 ± 6	8.4 ± 1	0.15 ± 0.02
PU-gly-20		Glycerol	20	40 ± 2	48 ± 2	15 ± 3	33 ± 2	0.15 ± 0.1	0.14 ± 0.05*^	33 ± 2	5.6 ± 2	0.7 ± 0.1
PU-CF20-gly20		Carbon Fiber + Glycerol	40	43 ± 2	51 ± 3	19 ± 2	32 ± 2	0.32 ± 0.2	0.22 ± 0.04	54 ± 3	0.77 ± 0.1	0.32 ± 0.04*^{X}

Anti-icing tests - Static								
Coating names	Surface / substrates	Filler	Filler (wt %)	Testing temperature (^{o}C)	Before Water-washing (WW)		After WW	After WW- Post 24 hours
					Icing delay (sec)	Static frost accumulaton (mg)	Static frost accumulaton (mg)	Static frost accumulaton (mg)
Al2024	Al2024 T4	-	-	Icing delays (-10), Static frost formation (-15)	5.2 ± 1	76 ± 10	-	-
PU		-	-		49 ± 5	35 ± 1	-	-
PU-CF-20		Carbon Fiber	20		44 ± 3	58.9 ± 7	67.2 ± 6**	63.7 ± 7**
PU-gly-20		Glycerol	20		372 ± 14	66 ± 11	-	-
PU-CF20-gly20		Carbon Fiber + Glycerol	40		364 ± 12	96.8 ± 9	70.8 ± 10	103.2 ± 8

Anti-icing tests - Dynamic								
Coating names	Surface / substrates	Filler	Filler (wt %)	Testing temperature (^{o}C)**	Before Water-washing (WW)		After WW	After WW- Post 24 hours
					Rotating frost accumulation (mg, 300 rpm)	Rotating frost accumulation (mg, 30 rpm)	Rotating frost accumulation (mg, 30 rpm)	Rotating frost accumulation (mg, 30 rpm)
Al2024	Al2024 T4	-	-	-15	301 ± 9	41.1 ± 2	-	-
PU		-	-		210 ± 11	39 ± 1	-	-
PU-CF-20		Carbon Fiber	20		219 ± 12	40 ± 2	38.7 ± 3**	41 ± 1**
PU-gly-20		Glycerol	20		293 ± 16	42 ± 1	-	-
PU-CF20-gly20		Carbon Fiber + Glycerol	40		374 ± 11	46 ± 2	39.2 ± 1	44 ± 2

*R_a measured along the lines exluding glycerol pockets

^Including pockets 3.2 ± 0.7 μm

^{X}Including pockets 0.45 ± 0.6 μm

**The samples were not water-washed but tested along water-washed samples